Contributions to micromechanical modelling of transport and freezing phenomena within unsaturated porous media

Rong Wei Yang

THÈSE

Présentée pour obtenir le grade de

DOCTEUR DE
L'UNIVERSITÉ PARIS–EST

Domaine : Génie civil

Présentée par :

Rongwei YANG

Sujet de la thèse :

Contributions à la modélisation micromécanique du transport et des phénomènes de gel dans les milieux poreux non saturés

Contributions to micromechanical modeling of transport and freezing phenomena within unsaturated porous media

Soutenue le 23 septembre 2013 devant le jury composé de

Prof. Aza Azouni	CNRS	Président
Prof. Bernard Perrin	Université Paul Sabatier, Toulouse	Rapporteur
Prof. Albert Giraud	Université de Lorraine	Rapporteur
Dr. George Wardeh	Université de Cergy-Pontoise	Examinateur
Dr. Eric Lemarchand	Ecole nationale des ponts et chaussées	Co-Directeur
Dr. Teddy Fen-Chong	IFSTTAR	Directeur de thèse

Abstract

Numerous empirical models are employed and seem effective to investigate the transport properties and the mechanical behaviors of unsaturated porous media. However, these empirical models are phenomenological in nature because of the lack of physical foundation. Micromechanics approach seems an alternative methodology for these problems by taking account of the microstructure morphology of porous medium as well as the local physical phenomena at stake and by using homogenization procedure. This thesis deals with the transport properties and then the freezing behaviors of unsaturated porous media by means of micromechanics approach.

We first start with investigating the transport properties such as solute diffusion and liquid flow in unsaturated glass beads, sand, and sandstone. The main feature of such kind of materials lies on a mono-disperse pore size distribution, which can be taken into account by micromechanics model for one-scale microstructure. This will be the basis of all the models developed in this work, except a short development for materials with bi-disperse pore size distribution (two-scale microstructure model). Further elements of modelling are related to the physical properties of the local water distribution (e.g. the pore body water and liquid layer, the latter is defined as the intergranular layer, the wetting layer and the water film).

When the local diffusion occurs in the liquid layer treated as an interface (2-D), with no volume fraction, the homogenized solute diffusion coefficient can be derived analytically. However, the real liquid layer is an interphase (3-D), the volume fraction of which can be accounted for in an enriched micromechanics model. The latter is thus able to characterize

and take into account of the evolution of the thickness of the liquid layer during the desaturation process. The simulation results of 3-D enriched micromechanics model for solute diffusion are then compared with the experimental results in unsaturated glass beads and sand: the modelling results turn out to be good for these materials.

Taking advantage of the morphological and physical characterization of sandstone, a micromechanics model for liquid permeability in unsaturated Fontainebleau sandstone is built accounting for the intergranular layer flow, wetting layer flow, and water film flow. This micromechanics model seems effective in explaining the modified Kozeny-Carman model for saturated permeability of Fontainebleau sandstone. This micromechanics model is also applied to model the evolution of the permeability of the unsaturated Fontainebleau sandstone: the modelling results turn out to be comparable with the experimental results.

We then turn to the freezing of unsaturated porous media. Based on the local physical characterization of unsaturated freezing porous media, the disjoining pressure in unfrozen water film and surface tension effect are fully accounted for in a first micromechanics model. Then an alternative model is built by taking account of the effect of the disjoining pressure on the local elastic properties of the unfrozen water film and thus on the homogenized ones. However due to lack of data on the dependence of the disjoining pressure on temperature, use is made of the first micromechanics model to study the free swelling of a freezing cement paste. The modelling results exhibit some discrepancies with the experimental results, the reasons for this may lie in the overestimation of the ice content, which here is estimated by the pore size distribution by MIP and Gibbs-Thomson equation.

Keywords:

Porous media, Unsaturated, Diffusion, Permeability, Freezing, Micromechanics, Water film, Disjoining pressure

.

Résumé

De nombreux modèles empiriques sont utilisés et semblent efficaces pour étudier les propriétés de transport et les comportements mécaniques de milieux poreux non saturés. Toutefois, ces modèles empiriques, en l'absence de bases physiques, sont de nature phénoménologique. À l'inverse, l'approche micromécanique est une méthode alternative qui permet de formuler des problèmes prenant en compte la morphologie microstructurale des milieux poreux ainsi que les phénomènes physiques en jeu à l'échelle locale et en les intégrant par homogénéisation. Ces travaux de thèse portent sur les propriétés de transport puis le comportement au gel de milieux poreux non saturés au moyen de l'approche micromécanique.

Nous examinons d'abord les propriétés de transport telles que la diffusion de soluté et l'écoulement de liquide au sein de billes de verre, de sable, et d'un grès, en condition non-saturée. La principale caractéristique de ces matériaux réside dans la mono-dispersité de la distribution des tailles de pores, ce qui peut être pris en compte par un modèle micromécanique à une seule échelle locale de description. Ceci est la base commune à tous les modèles développés dans cette thèse, excepté une brève incursion pour des matériaux à double porosité (modèle à deux échelles locales de description). La modélisation inclue aussi des éléments supplémentaires liés aux propriétés physiques de la distribution locale de l'eau (eau libre porale et couche liquide, celle-ci désignant l'ensemble constitué par la couche inergranulaire, la couche mouillante, et le film d'eau).

Lorsque la diffusion a lieu localement dans une couche liquide assimilée à une interface (2-D), sans notion de fraction volumique, le coefficient de diffusion homogénéisé peut être

déduit analytiquement. Cependant, une couche liquide réelle est une interphase (3-D) dont la fraction volumique peut être prise en compte dans un modèle micromécanique enrichi. Ce dernier permet alors de prédire et d'intégrer l'évolution de l'épaisseur de la couche liquide durant le drainage. Les résultats numériques du modèle enrichi 3-D sont ensuite confrontés à des données expérimentales pour des billes de verre et du sable, en condition insaturée: la modélisation donne de bons résultats sur ces matériaux.

Sur la base d'une caractérisation morphologique et physique des grès, un modèle micromécanique pour la perméabilité non saturée est construit en incluant notamment l'écoulement dans une couche d'eau intergranulaire, une couche d'eau mouillante, et un film d'eau liquide. Ce modèle apparaît efficace pour expliquer le modèle modifié de Kozeny-Carman de la perméabilité saturée du grès de Fontainebleau. Ce modèle est aussi utilisé pour prédire l'évolution de la perméabilité d'un grès de Fontainebleau non saturé: les résultats obtenus sont concordants avec les résultats expérimentaux.

Nous nous intéréssons ensuite au gel de milieux poreux non saturés. Sur la base d'une caractérisation des phénomènes physiques en jeu à l'échelle locale, un premier modèle micromécanique est construit en tenant compte de la pression de disjonction et des effets de tension de surface. Un second modèle est ensuite construit pour étudier le rôle de la pression de disjonction sur les propriétés élastiques locales du film d'eau non-gelée, et donc aussi sur leurs homologues macroscopiques. Cependant, en raison d'un manque de données sur la variation de la pression de disjonction avec la température, nous utilisons le premier modèle pour analyser le gonflement libre d'une pâte de ciment. Le calcul montre un certain écart avec les résultats expérimentaux. L'une des raisons peut provenir de la surestimation de la teneur en glace dans les pores, laquelle est estimée à partir d'une distribution de tailles de pores obtenue par porosimétrie à mercure et de la relation de Gibbs-Thomson.

Mots-clés:

Milieux poreux, Non saturés, Diffusion, Perméabilité, Gel, Micromécanique, Film d'eau, Pression de disjonction

Acknowledgements

I am deeply indebted to my two advisors: Dr. Eric Lemarchand and Dr. Teddy Fen-Chong for their constant support, guidance, patience and encouragement during the study. Without their assistance, the work would never have been done. The years of study with them have been a profound experience of mine because of their effective mentoring and full support. The more I delve into the professional field, the more I appreciate their contributions and insights.

I appreciate the constructive suggestions from Prof. Bernard Perrin and Prof. Albert Giraud who are my thesis reviewers. Further thanks are due to other thesis defense committee members: Dr. George Wardeh and Prof. Aza Azouni. Special thanks are given to Prof. Aza Azouni for her warmly help and persistent encouragement during my thesis.

I have had the good fortune to benefit from the working opportunity provided by Ecole nationale des ponts et chaussées. I would like to thank every member in the Navier lab at Kepler for their constant support and excellent academic environment provided.

My gratitude is also expressed to my fellow colleagues and friends in the past four years, they are: Jiyun Shen, Haifeng Yuan, Qiang Zeng, Louisa LOULOU, Pengyun Hong, Yan Liu, Yiguo Wang, Zheng He and LinLin Wang.

Last but not least, I would like to thank my parents and my brothers. Thanks for your unconditional love and immense support!

Contents

Contents I

List of Figures V

List of Tables XI

I General introduction 1

1 Problems position 3

1.1 Research background . . . 3
1.2 Micromechanics methodology . . . 5
1.3 Phase interfaces within unsaturated porous media . . . 7
1.4 Research motivation . . . 9
1.5 Outline of the thesis . . . 10

2 Microstructural morphological characterization of porous media 13

2.1 Introduction . . . 13
2.2 Microstructure morphology of granular materials . . . 14
2.3 Microstructure morphology of non-granular materials . . . 18
2.4 Summary . . . 27

II Micromechanical modelling of transport within unsaturated porous media 29

3 Introduction to transport in unsaturated porous media 31

3.1 Evolution of water distribution within unsaturated granular materials . . . 33
3.2 Water distribution within unsaturated sandstone . . . 37
3.3 Liquid-gas interface in unsaturated porous media . . . 39
3.4 Disjoining pressure within water film . . . 43
3.5 Liquid water volume fractions at low saturation degree . . . 54
3.6 Local solute diffusion in water film . . . 61
3.7 Summary . . . 64

4 Micromechanical modelling of solute diffusion within unsaturated porous media 67
4.1 Introduction . . . 68
4.2 Empirical models for solute diffusion in unsaturated porous media . . . 70
4.3 Micromechanical modelling of solute diffusion in saturated porous media . . . 74
4.4 A first approach for solute diffusion in unsaturated porous media . . . 78
4.5 Enriched models for solute diffusion in unsaturated porous media . . . 91
4.6 Experimental results analysis . . . 114
4.7 Summary . . . 119

5 Application: micromechanical modelling of solute diffusion in unsaturated sand 121
5.1 Introduction . . . 122
5.2 Input information and assumptions . . . 122
5.3 Phase volume fractions . . . 124
5.4 Results and discussion . . . 129
5.5 Conclusion . . . 133

6 Micromechanical modelling of fluid flow in unsaturated sandstone 135
6.1 Introduction . . . 136
6.2 A review of advective transport in unsaturated porous media . . . 137
6.3 Micromechanics model for liquid flow in saturated porous media . . . 141
6.4 Micromechanics model for liquid flow in unsaturated Fontainebleau sandstone 145
6.5 Experimental analysis . . . 153
6.6 Summary . . . 161

III Micromechanical modelling of freezing behaviors within unsaturated porous media 163

7 Thermodynamics and poromechanics for freezing in porous media 165
7.1 Homogeneous nucleation and heterogeneous nucleation . . . 166
7.2 Thermodynamic equilibrium within unsaturated porous media under freezing 168
7.3 Unfrozen water film in freezing porous media . . . 178
7.4 Mechanisms and models for freezing porous media . . . 181
7.5 Poromechanics methodology for freezing in porous media . . . 187
7.6 Summary . . . 189

8 Micromechanical modelling of unsaturated freezing porous media 193
8.1 Introduction . . . 195
8.2 A thermoporoelastic model for saturated porous media . . . 196
8.3 A micromechanics model for unsaturated freezing porous media . . . 200
8.4 An alternative micromechanics model for unsaturated freezing porous media 218
8.5 Some discussion and applications . . . 221
8.6 Summary . . . 232

9 Application: Micromechanical modelling free swelling of cement paste under freezing **235**
9.1 Introduction . . . 235
9.2 Assumptions and boundary conditions . . . 236
9.3 Poroelastic properties . . . 238
9.4 Volume fractions of each phase within the cement paste sample . . . 239
9.5 Disjoining pressure . . . 242
9.6 Results and discussion . . . 242
9.7 Conclusion . . . 248

10 Conclusions **249**

Bibliography **253**

Appendix **270**

A Physical properties of water film **271**
A.1 Viscosity of the water film . . . 271
A.2 Structure and Density of water film on hydrophilic surface . . . 273
A.3 Thermodynamic definition of disjoining pressure . . . 274
A.4 Parameters for the disjoining pressure within the unfrozen water film . . . 274

B Determining average concentration tensors of each phase **277**
B.1 Eshelby's problem in Linear Diffusion within unsaturated porous media . . . 277
B.2 Solutions of auxiliary Eshelby-type problems: diffusion case . . . 278
B.3 Solutions of auxiliary Eshelby-type problems: flow permeability case . . . 282
B.4 Solutions of auxiliary Eshelby-type problems: multi scale . . . 285

C Eshelby-type problems in poroelastic porous media under freezing **287**
C.1 Eshelby's problem coupled with prestress and inhomogeneity under freezing . 287
C.2 Solution of Eshelby's problem with Mori-Tanaka scheme . . . 288

D Levin's theorem in unsaturated microporoelastic freezing porous media **291**

List of Figures

1.1 Schematic of the geometrical arrangement of each phases (a) at macroscopic, (b) at microscopic scale. . . . 6

1.2 Schematic illustration of the interface between non-wetting phase and wetting phase, α denotes non wetting phase, β denotes wetting phase. . . . 8

2.1 Two dimensional (2D) slice of morphology of the unsaturated glass bead pictured by synchrotron based X-ray microtomography [62]. . . . 15

2.2 The micro-topography of the grain of Hanford gravel with scanning electron microscope (SEM)[240]. . . . 17

2.3 Schematic illustration of several morphologies of the gravel grains [240]. . . . 18

2.4 Schematic representation of morphology of the sandstone, modified from [235]. 20

2.5 Schematic image of microstructue of clay, modified from [259]. . . . 21

2.6 Schematic representation of microscopic arrangement of clay particles and the corresponding micropores within a ped [150]. . . . 22

2.7 Schematic representation of particles which are composed of lamellas and interlayer space[150]. . . . 23

2.8 Schematic illustration of several elementary clay mineral units [172]. . . . 23

2.9 Scanning image of the polished section and the nano-indentation grid for a cement paste at $w/c = 0.5$ [217]. . . . 25

2.10 Schematic representation of LD C-S-H and HD C-S-H, after [217]. . . . 25

3.1 Schematic illustration of the evolution of water distribution within smooth glass beads at different saturation degree, after [238]. . . . 34

3.2 Capillary water resided in grooves, pits on the rough surface [181, 243]. . . . 35

3.3 Schematic illustration of influence of surface characteristic on water distribution at saturation degree 0.3, the domains surrounded by the red curves are the capillary water, the grey domains are gas and the black domains are sandstone grains [121]. . . . 38

3.4 Schematic representation of the overlapping of the two diffuse double layers when approaching the charged surface [3]: left: thick film; right: thin film. . 45

3.5 Comparison of the electrostatic, Van der Waals and structural components of the disjoining pressure of the quartz-NaCl aqueous film-air system, the parameters are given in Table(3.1), M=1mol.L^{-1}. . . . 51

3.6 Relationship of the thickness of water film with relative humidity, temperature is 293K, experimental results are for pure water film-fused quartz system, after Sumner et al. [229], the thickness of mono water molecular layer is 2.8 Å [28]. 53

3.7 Schematic illustration of the water distribution within cubic packing granular material at low saturation degree, the surface of the grains is considered as smooth. 56

3.8 Plot of evolution of the contributions of water film and pendular rings to saturation degree Sr with variation of matrix potential ψ and R_s (10 mm, 1 mm, 0.1 mm, 10 μm, 1 μm), according to Eq.(3.37). 60

4.1 Evolutions of the normalized diffusion with saturation degree for several porous materials, $D^{hom}_{Sr=1}$ is the effective diffusion coefficient in saturated porous media, while D^{hom} is the diffusion coefficient in unsaturated case, Sr is the saturation degree, a and b are the exponent cofficients, experimental results are after [6, 33, 159]. 71

4.2 The dependence of the tortuosity τ on the porosity ϕ. 78

4.3 The influence of saturation degree on normalized homogenized diffusion coefficient in one scale microstructure, notation DF denotes differential scheme, MT denotes Mori-Tanaka scheme, SC denotes self-consistent scheme. 80

4.4 Schematic illustration of morphological models for porous media with two-scale microstructure, SC denotes self-consistent scheme, MT denotes Mori-Tanaka scheme. 83

4.5 Influence of α on the evolution of D^{hom} with Sr in porous media with two-scale microstructures; MT-MT, SC-SC and MT(level II)-SC (level I) correspond to morphological models in Fig.(4.4)(a), (b) and (c), respectively; $Sr^c_1 = 0.9$, $Sr^c_2 = 0.7$, $Sr^c_3 = 0.5$. 86

4.6 Influence of ϕ on the evolution of D^{hom} with Sr in porous media with two-scale microstructures, $Sr^c_1 = 0.9$. 87

4.7 Evolution of ϕ_m with α. 88

4.8 Schematic representation of different components of water phase and their effects on solute diffusion in unsaturated porous media; the surface roughness of solid grains is disregarded in the figure; the intergranular water is decomposed into intergranular layer and pore body water; the intergranular layer, the wetting layer and the water film are represented by "liquid layer" in the following discussion. 92

4.9 2D idealization of diffusion flux in interface. 96

4.10 Morphological representation of 2D idealization of solute diffusion in unsaturated porous media 98

4.11 Eshelby problem of spherical composite made up of a solid grain and a diffusive interface. 99

4.12 Dependence of $\frac{D^{hom}_{pw}}{D^{hom}_{ll}}$ on ε, $\phi = 0.4$, the constrictive factor $\delta = 0.5$. 104

4.13 Schematic representation of unsaturated porous media with a specific matrix+inclusion morphology, this morphology corresponds to Mori-Tanaka scheme, the matrix is liquid water, the fictitious macroscopic concentration gradient $\underline{\mathrm{H}}_0$ and the real macroscopic concentration gradient $\underline{\mathrm{H}}$are linked by: $\underline{\mathrm{H}}_0$=$\underline{\mathrm{H}}$. 106
4.14 Effects on the evolution of homogenized diffusion coefficient with the saturation degree, the homogenized diffusion coefficient is determined by Mori-Tanaka scheme, Sr^{ll} is related to ϕ and ε by Eq.(4.22). 108
4.15 Schematic representation of unsaturated porous media with a specific polycrystalline microstructure, this kind of morphology corresponds to self-consistent scheme. 110
4.16 Influence of three parameters on the evolution of homogenized diffusion coefficient D^{hom} with the saturation degree, the homogenized diffusion coefficient is determined by self-consistent scheme; the curves terminate at Sr^{ll} which can be calculated by Eq.(4.22); when $Sr < Sr^{ll}$, the liquid layer governs the solute diffusion. 113
4.17 Morphological representation of water distribution in unsaturated granular material, D^{hom} and ρ^{γ} are the homogenized solute diffusion coefficient and solute concentration; the intergranular layer, the wetting layer and the water film surrounded on the solid grains are specified to characterize the evolution of the liquid layer during the desaturation process. 116
4.18 Dependence of the normalized diffusion coefficient of nitrate on the various saturation degrees. It should be noted that $Sr_1 = \frac{\varphi_f + \varphi_{wl}}{\phi}$, the green and blue points are experimental results after [211]. 118

5.1 Morphological representation of unsaturated sand. 123
5.2 Water retention curves for Beaver Creek sand (red curve) and Romkens' sand (blue curve), the curves are fitted by Eq.(5.2). The capillary pressures associated with residual saturation degrees are 20 KPa and 30 KPa for Beaver Creek sand and Romkens' sand, respectively. Experimental results are after [159, 211]. 126
5.3 Particle size distribution of Beaver Creek sand, the fitting curve are after Fredlund et al.[106], the experimental results are after Bruch et al.[31]. . . . 128
5.4 Evolution of normalized homogenized diffusion coefficient with saturation degree for Beaver Creek sand, experimental results are after [159]. 130
5.5 Evolution of normalized homogenized diffusion coefficient with saturation degree in Romkens' sand, experimental results are after [211]. 132

6.1 Schematic illustration of the intergranular water in Fontainebleau sandstone: the intergranular water is idealized as interconnected intergranular layer surrounding the solid grains, e is the thickness of the intergranular layer. 146
6.2 Schematic illustration of morphology of the unsaturated sandstone; to characterize the evolution of the intergranular layer $\rightarrow$ the wetting layer $\rightarrow$ the water film during desaturation process, all these three kinds of water are superposed on the solid grain. 147

6.3 Schematic representation of the filtration velocity profile of the water film flow on the plat plane, h is the thickness of water film. 149
6.4 The evolution of ζ with porosity ϕ at $Sr = 1$, the other parameters are given in the figure. 156
6.5 The evolution of the saturated intrinsic permeability coefficient $K^{hom}(Sr = 1)$ with porosity ϕ for Fontainebleau sandstone; the blue curve is Mavko's modified Kozeny-Carman model with fitting percolation porosity $\phi_p = 2\%$, tortuosity $\tau = 2.5$ and D=250 μm (Eq.(6.30)) [168]; the black circle points are experimental results from 240 samples with different porosities [25], the red diamond points are after [84], the green diagonal cross points are after [115]. 157
6.6 The evolution of the ζ with saturation degree Sr, $\phi = 0.095$, the other parameters are given in the figure. 159
6.7 The evolution of the relative permeability coefficient $K^{hom}/K^{hom}_{Sr=1}$ with saturation degree Sr for Fontainebleau sandstone (red curves); the fitting parameters of Brooks-Corey's model and Van Genuchten's model are given in [65]; the black circle points are from experiments in [65]. 160

7.1 Schematic illustration of unsaturated porous media under freezing. 170
7.2 Phase diagram of water, modified from [4] 174
7.3 Sketch of progressive penetration of ice in interconnected pores. 177
7.4 The disjoining pressure of the unfrozen water film between ice and fused quartz surface. The solid line is the disjoining pressure calculated by the DLVO theory (Eq.(7.19)), the dotted line is the structural component given by Eq.(3.22), the colored points are experimental results of the ice-unfrozen water film-quartz system after Churaev et al. [45]. 181
7.5 Schematic representation of crystallization pressure exerted on the cylindrical pore wall, modified from [220]. 184
7.6 Schematic illustration of disjoining pressure of water film within crystallized pores. 186

8.1 Morphological illustration of the freezing in unsaturated porous media 201
8.2 Components of the equivalent pressure $p^{eq}_{\omega}(r)$ during freezing, $\omega \in$ {f,l,g}. . . 211
8.3 Schematic representation of the crystallization in pore 230

9.1 Pore size distribution and cumulative curve of cement paste [262]. 240
9.2 Dependence of the thickness of unfrozen water film on temperature, determined by Eq.(9.11). 241
9.3 Dependence of the disjoining pressure and liquid pressure on temperature, the disjoining pressure is determined by Eq.(9.13) while the liquid pressure for the undrained case is determined by Eq.(9.2). 244
9.4 Evolution of the percentages of each phases with the temperature, the percentages of each phase are defined as their volume fractions divided by porosity. 245
9.5 Evolution of the strains of the cement paste with the temperature during freezing process. 247
9.6 Comparison of pore size distributions of mortar derived by MIP, TPM and NAD, after Sun et al. [232]. 248

A.1 The variation of viscosity within confined water film, calculated with Eq.(A.1) at temperature T= 298 K. 273

B.1 Schematic illustration of the spherical composite inclusion with three shells; C_i denotes $i-th$ domain, the quantity in the bracket is solute diffusion coefficient within i-th domain, $i \in \{$ 0, 1, 2, 3,4 $\}$; in this case $D_s \to 0$, $\underline{\mathrm{H}}_0$ is the fictitious uniform concentration gradient; e, t and h are the thicknesses of the intergranular layer, the wetting layer and the water film, respectively. 279

B.2 Schematic illustration of the spherical composite inclusion with one shell, C_i denotes i-th domain, the quantity in the bracket is solute diffusion coefficient within i-th domain, $i \in \{0, 1, 2\}$, in this case $D_s \to 0$. 281

B.3 Schematic illustration of the pore water spherical inclusion. 281

B.4 Schematic illustration of the spherical composite inclusion with two shells in flow permeability problem; C_i denotes $i-th$ domain, the quantity in the bracket is permeability coefficient of i-th domain, $i \in \{$ 0, 1, 2, 3, 4 $\}$; in this case $K_s \to 0$; ∇P_0 is the fictitious uniform pressure gradient. 283

List of Tables

2.1 Characteristics of several common elementary clay mineral units [259] 26

3.1 Parameters for the quartz-NaCl aqueous film-air system 50

4.1 Summary of material characteristics and used solutes [33, 159]. 71
4.2 Several empirical unsaturated diffusion models 73
4.3 Homogenized solute diffusion coefficient within saturated porous media with different schemes 76
4.4 Volume fractions of each phase within multi scale porous media. 85
4.5 Characteristics of two kinds of granular material [211]. 115
4.6 Volumetric fraction of each phase within unsaturated granular material. . . 117

5.1 Characteristics parameters for sand and solution[159, 211] 124
5.2 Fitting parameters for two kinds of sand 126

6.1 Several commonly used models for unsaturated permeability coefficient . . . 140
6.2 Volume fractions of each phase within unsaturated Fontainebleau sandstone 155
6.3 Characteristics of Fontainebleau sandstone [64] 158

9.1 Fitting parameters for pore size distribution function of cement paste, adopted from [262]. 240
9.2 Some parameters used in the simulation 243
9.3 The evaluated poroelastic properties by Mori-Tanaka scheme 243

A.1 Calculated parameters of disjoining pressure at different temperature ranges, after Churaev et al. [46]. 275

Part I

General introduction

Chapter 1

Problems position

Contents

1.1 Research background **3**

1.2 Micromechanics methodology **5**

1.2.1 Difference between macroscopic poromechanics and micromechanics 5

1.2.2 REV and average procedure in micromechanics 6

1.3 Phase interfaces within unsaturated porous media **7**

1.4 Research motivation **9**

1.5 Outline of the thesis **10**

1.1 Research background

Porous media are heterogeneous materials composed of solid phases as well as pore space. They can be categorized as two types: -natural materials such as rock, soil, bones and wood; -man made materials such as ceramics, plaster, cement, etc [2]. The concept of porous medium is used in many areas of applied science and engineering, such as environmental engineering, petroleum geophysics, civil engineering, geotechnical engineering, biomechanics, food industry, etc [2].

As pointed out by Coussy [58], despite the diversity of materials and fields, all porous

media have one thing in common for all applications: they may be subjected to the same chemo-physical coupled processes such as swelling induced by freezing, shrinkage induced by drying, expansion induced by osmosis, etc. Due to these phenomena, studying the behavior of porous media is interdisciplinary in nature.

Generally, the macroscopic behaviors and transport properties are the functions of saturation degree (or water content), which is determined by the pore size distribution and relative humidity.

Compared with saturated situation, the unsaturated cases are more common in engineering domains. Indeed, the mechanical behaviors and transport behaviors of unsaturated porous media have been more and more studied for decades [36, 58, 64]. Numerous investigations are devoted to understand the properties and thus the behaviors of unsaturated porous media [22, 58, 60, 82, 104]. In our work, two special cases for unsaturated porous media are specified: transport in unsaturated porous media and then freezing in unsaturated porous media.

As a special case, the hydro-mechanical behaviors of saturated porous media were extensively investigated for decades. Originally put forward by Karl von Terzaghi in 1936 [236], the effective stress $\boldsymbol{\Sigma} + \mathbf{1}P$ was introduced to study the consolidation of water saturated soil layer. According to Biot [19], a generalized effective stress can be expressed as a linear superposition of total stress $\boldsymbol{\Sigma}$ and the effect of pore pressure $\boldsymbol{B}P$ that is, $\boldsymbol{\Sigma} + \boldsymbol{B}P$. $\boldsymbol{B}$ is the Biot tensor, which accounts for the effect of the pore pressure. Indeed, Terzaghi model is a special case of Biot's model on the premise of incompressible solid skeleton, $\boldsymbol{B} = \mathbf{1}$. After the outstanding work of Biot [19], macroscopic poromechanics has been recognized as an effective tool to study the behaviors of porous media. Since then, it has been widely employed in the fields of geotechnical engineering, geological engineering and petroleum engineering [58].

1.2 Micromechanics methodology

As an alternative, micromechanics approach has be used widely in the transport and mechanics problems [79, 113, 114]. It starts at local scale where microstructure morphology and local phase behavior are explicitly characterized from a physically-based analysis. Average operations are then introduced to derive the upscaled properties which control the behaviors of porous media.

1.2.1 Difference between macroscopic poromechanics and micromechanics

The porous medium consists of different constituents such as solid and in-pore phases (the latter can here be liquid, gas or ice crystal). Within the porous medium, these phases exhibit a heterogeneous microstructure. In the context of macroscopic poromechanics, all these phases are macroscopic particles and are regarded as geometrically coincident. From the macroscopic point of view, as shown in Fig(1.1)(a), the REV is regarded as superposition of these particles in space and time [82].

On the contrary, micromechanics considers the heterogeneous structure of REV explicitly, in which the solid and fluid phases are geometrically distinct (as shown in Fig.(1.1)(b)). In other words, within the framework of the micromechanics, the refinement of the geometric description of the microstructure is required.

The difference between the Poromechanics and Micromechanics lies in treating the heterogeneous material with distinct geometric definition of representative elementary volume (REV).

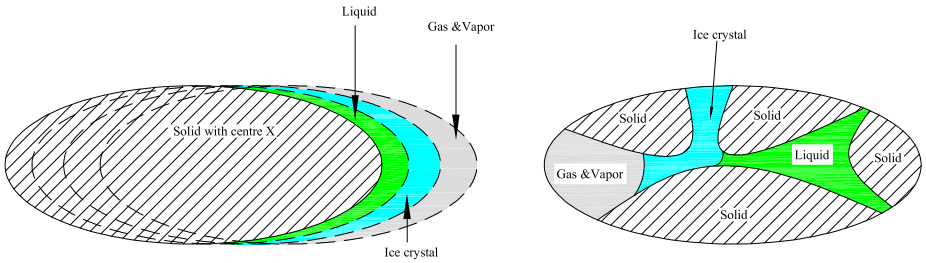

(a) Macroscale (each phase is at macro position X) **(b) Microscale**

Figure 1.1: Schematic of the geometrical arrangement of each phases (a) at macroscopic, (b) at microscopic scale.

1.2.2 REV and average procedure in micromechanics

The REV is a continuous domain of a three dimensional material which should be defined as [82]:

— Small enough at the macro scale, and can be treated as a point of macro heterogeneous material.

— Large enough at the local scale, so as to contain a large number of inhomogeneities and to be representative for the microstructure of the material.

More rigorously, if the characteristic sizes of the structure, the REV and local heterogeneities can be denoted as L, l and d, respectively, the concept of REV requires [82]:

— $l \ll L$, which makes sure the relevance of the use of the tools of differential calculus offered by a continuum description.

— $d \ll l$ so that the REV can capture all the informations in a statistical sense. The informations concern the geometrical and physical properties of porous media.

In summary, for the concept of REV to be valid, a condition for scale separation can be expressed as [82]:

$$d \ll l \ll L \tag{1.1}$$

Let Ω be the standard notation for the REV, the average of a physical quantity at local scale denoted by $a(\underline{z})$ over Ω can be expressed as [82]:

$$< a >= \frac{1}{|\Omega|} \int_{\Omega} a(\underline{z}) \mathrm{d}\Omega \tag{1.2}$$

1.3 Phase interfaces within unsaturated porous media

For unsaturated porous media, the pore space is not occupied by one single fluid phase. As shown in Fig.(1.2), during phase transition in porous media, a meniscus immediately forms at the interface between non wetting phase (denoted as α phase) and wetting phase (denoted as β phase). The surface tension along the interface induces a stress vector discontinuity ($[\boldsymbol{\sigma}].\underline{n}$) between two different phases. At local scale, the stress vector discontinuity may be derived from the momentum balance equation as [82]:

$$[\boldsymbol{\sigma}].\underline{n} + \underline{\mathrm{div}}\boldsymbol{\sigma}^m = \underline{0} \tag{1.3}$$

where $\underline{n}$ is the unit vector normal to the interface $\mathcal{I}^{\alpha\beta}$; $[\boldsymbol{\sigma}]$ is the stress difference between α phase and β phase, if we assume $\underline{n}$ orientates towards α phase, then $[\boldsymbol{\sigma}] = \boldsymbol{\sigma}^{\alpha} - \boldsymbol{\sigma}^{\beta}$, $\boldsymbol{\sigma}^{\alpha}$ and $\boldsymbol{\sigma}^{\beta}$ is the stress tensor within α phase and β phase, respectively; $\boldsymbol{\sigma}^m$ is the membrane stress tensor at the interface $\mathcal{I}^{\alpha\beta}$ between the α phase and β phase, it can be expressed as [82]:

$$\boldsymbol{\sigma}^m = \gamma^{\alpha\beta}\mathbf{1}_T \qquad \text{with:} \quad \mathbf{1}_T = \mathbf{1} - \underline{n} \otimes \underline{n} \tag{1.4}$$

With introduction of the tensor of curvature of interface, defined by $\boldsymbol{b} = -\mathbf{grad}\underline{n}$, inserting Eq.(1.4) into Eq.(1.3), we have [82]:

$$[\boldsymbol{\sigma}].\underline{n} + \gamma^{\alpha\beta}(\mathbf{1}_T : \boldsymbol{b})\underline{n} = 0 \tag{1.5}$$

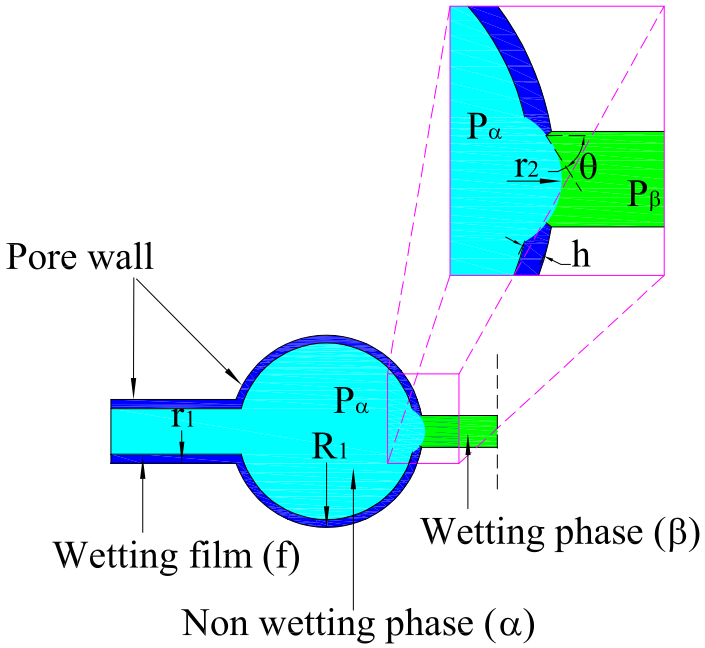

Figure 1.2: Schematic illustration of the interface between non-wetting phase and wetting phase, α denotes non wetting phase, β denotes wetting phase.

The surface tensions that are generated along the fluid-fluid and solid-fluid interfaces induces deformation, which affects the macroscopic behavior of unsaturated porous media. Two different interfaces: water-vapor interface and water-ice interface will be addressed hereafter, water being the wetting phase in both cases. In association with pore size distribution, they will play a significant role in determining the liquid saturation degree during desaturation (Chapter (3) to Chapter (6)) and the ice saturation degree during freezing

processes (Chapter (7) to Chapter (9)), respectively. This stress continuity in unsaturated transport problem (liquid-gas interface) and freezing problem (liquid-ice interface) is combined with thermodynamic equilibrium expression by Kelvin equation and Gibbs-Thomson equation, which will be introduced respectively in Section(3.3) and Section(7.2).

1.4 Research motivation

Currently, numerous empirical models are employed to analyse the transport properties and behaviors of unsaturated porous media. The drawbacks of these models lie in the fact that the basic phenomena remain poorly understood, since all of these models are phenomenological in nature. On the contrary, as stated in previous section, micromechanics approach starts at local scale where microstructural morphology and local phase behavior are explicitly characterized. Micromechanics approach is developed throughout this work to investigate the transport properties as well as freezing behaviors of unsaturated porous media.

In addition, physical characterization at local scale is greatly emphasized in this work. In order to study the transport properties and freezing behaviors of unsaturated porous media, the local physics is related to the existence of a water film (resp. unfrozen water film), which is a special phase in vicinity of the solid/pore interface within unsaturated porous media. Moreover, disjoining pressure within unfrozen water film is also incorporated in the micromechanics model to investigate the freezing behaviors of porous media.

The aim of the present research work is twofold:

— **1** Establishing a micromechanics model for transport properties (solute diffusion, flow permeability) within unsaturated porous media.

— **2** Building a thermoporoelastic model as well as a micromechanics model for freezing within unsaturated porous media.

1.5 Outline of the thesis

The present work is organized in four parts:

PartI: General introduction: After the presentation in this chapter, a review of several microstructural morphologies of granular material and non-granular material is presented and discussed in chapter 2.

PartII: Micromechanical modelling of transport within unsaturated porous media: In chapter 3, physical characterization of the transport in unsaturated porous media at local scale has been summarized and presented. In this chapter, we focus on the characterization of the evolution of water distribution with the saturation degree. The disjoining pressure in water film and local diffusion will be introduced also in this chapter. In chapter 4, we start from a review of empirical models for solute diffusion in unsaturated porous media. Then, micromechanics models for solute diffusion in unsaturated porous media are introduced and discussed. Furthermore, micromechanics models for solute diffusion are employed to analyse the experimental results. In chapter 5, micromechanics model is employed to simulate the solute diffusion in two kinds of unsaturated sand. Similarly to chapter 4, chapter 6 starts with a review of the existing empirical models for flow permeability in unsaturated porous media. Based on the introduction of water phase distribution within unsaturated porous media in chapter 4, a micromechanics model for fluid permeability in unsaturated sandstone is introduced and discussed. The micromechanics model for flow permeability is used to explain the Kozeny-Carman equation theoretically.

PartIII: Micromechanical modelling of freezing behaviors within unsaturated porous media: In chapter 7, a comprehensive knowledge of freezing is introduced and discussed. In this chapter, thermodynamic equilibrium as well as mechanisms and models for freezing porous media are presented and discussed. The poromechanics approach for freezing derived by Coussy is first reviewed; this model will be used to compare with our following micromechanics model for freezing porous media. After comprehensive knowledge of freezing porous media, chapter 8 starts with a thermoporoelastic model which accounts

for the thermal effect. Based on this thermoporoelstic model, micromechanics models for freezing porous media are introduced and discussed. In chapter 9, a micromechanics model for freezing porous media is employed to simulate the free swelling cement paste with undrained boundary condition.

A general conclusion is eventually summarized and presented.

Chapter 2

Microstructural morphological characterization of porous media

Contents

2.1 Introduction 13

2.2 Microstructure morphology of granular materials 14

2.2.1 Glass beads 14

2.2.2 Gravel 16

2.3 Microstructure morphology of non-granular materials 18

2.3.1 Sandstone 19

2.3.2 Clay 21

2.3.3 Cement paste 24

2.4 Summary 27

2.1 Introduction

Random porous materials such as geomaterials exhibit a multiphase composite nature, characterized by water-filled pores of nm- to m-scale diameter [54]. The physical characterization as well as microstructural morphology of the unsaturated porous media at local

scale are of paramount importance for investigating the macroscopic behavior of porous media by using micromechanics methodology. Microstructural studies are more and more used to improve the understanding of the macroscopic behaviors and physical properties of porous media in practical engineering. Microstructural studies involve the use of technique device to investigate the arrangement and distribution of particles, the corresponding pores as well as their contacts and connectivity at particle scale. In reality, owing to the hierarchical nature of the geomaterial, multi scale microstructure should be specified at different length scales.

In this chapter, we present morphological characterizations of several geomaterials. In the Section(2.2), the microstructural morphology of granular material is introduced. Then, a review of the more complicated morphologies of non-granular materials such as clay and cement paste will be presented and discussed in Section(2.3).

2.2 Microstructure morphology of granular materials

Compared with other sophisticated microstructure of porous media such as cement paste, microstructural morphologies of the granular materials are better characterized and less controversial. Herein, the morphologies of several granular materials such as glass beads and gravel are introduced.

The water distribution within these materials is crucial to their transport properties and behavior in the unsaturated case. This is the purpose of the Chapter 3, in which water distribution within different porous media will be presented.

2.2.1 Glass beads

Glass bead assemblages exhibit a relatively simple morphology characterized by a one-scale microstructure. This structure is classically determined by the geometric packing of the glass beads. Nowadays, thanks to the scanning device and image reconstruction techniques, a better understanding of the structure is possible [11, 184]. A slice of the cross

section of an unsaturated glass bead column, pictured by means of the synchrotron based X-ray microtomography, is presented in Fig.(2.1) [62]:

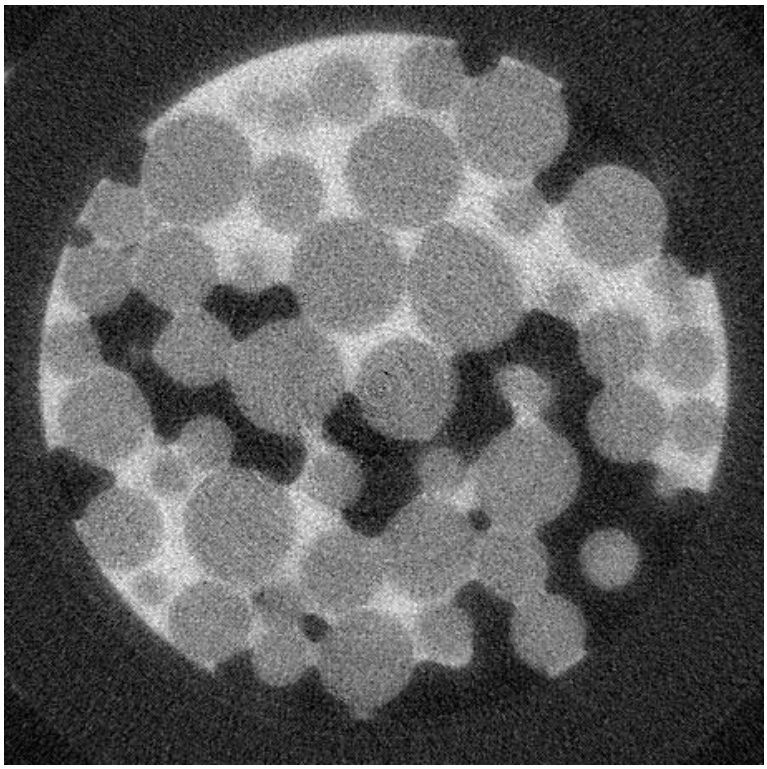

Figure 2.1: Two dimensional (2D) slice of morphology of the unsaturated glass bead pictured by synchrotron based X-ray microtomography [62].

As seen from Fig.(2.1), a morphological observation of the unsaturated glass bead may be presented according to the grayscales:

— The gray phases are glass beads, which defines the skeleton of the granular material. The grain size distribution: 1-1.4mm 30%(in weight), 0.85mm 35%, 0.6mm 35%.

— The white (lightest) phases are the KI doped solution phase which is the main mass transport pathway of porous media.

— The darkest phases (black) denote the pore spaces occupied by the gas [62].

Within the pores filled by gas, the contact areas of the grains are surrounded by menisci (pendular rings) which arise from the capillary effects.

It should be noted that, because of the limitation of the image resolution, the water film adsorbed on the surface of glass beads surrounded by the gaseous phase can not be

observed in Fig.(2.1).

Another morphological information concerning the glass beads is related to their surface roughness. Indeed, at very low water content, a certain amount of capillary water may be trapped in local menisci due to capillary effects. Hence, it may become an active pathway for mass transport at low water content. The glass beads of Fig.(2.1) were artificially polished to be smooth. However, the real geomaterials such as sand, gravel and sandstone clearly exhibit local roughness properties. Hence, the capillary water trapped in local roughness should be accounted for at low water content.

2.2.2 Gravel

Gravel is composed of unconsolidated rock fragments that generally have grain sizes ranging from 2mm to 64mm. Gravel deposits are common geological products, being formed as a result of the weathering and erosion of rocks [1]. Gravel is a substantial material that is widely used in agriculture, industry, and construction [240]. Though its substantial role in human activities, there is still little knowledge about its hydraulic and diffusive transport properties in unsaturated conditions [126, 240]. Therefore, the information about the morphology of the gravel at local scale is essential to get some new insight of its macroscopic properties.

As a kind of granular material, the distinct characteristic morphology of gravel may lie in its special external surface morphology and intra-granular porosity. Some topographic pictures of the external surface and intragranular morphologies for Hanford gravel are depicted in Fig.(2.2). Tokunaga et al. [240] used several experimental devices such as scanning electron microscope (SEM), laser profilometry and atomic force microscope (AFM) to investigate the special morphologies of the external surfaces and intragranular domain of the Hanford gravel grains. Their results can be summarized as [240]:

— Macroscopic scale:

  The gravel is granular material at macroscopic scale. The characteristic sizes of the Hanford gravel grains in two samples are 2 mm and 6 mm, respectively [240].

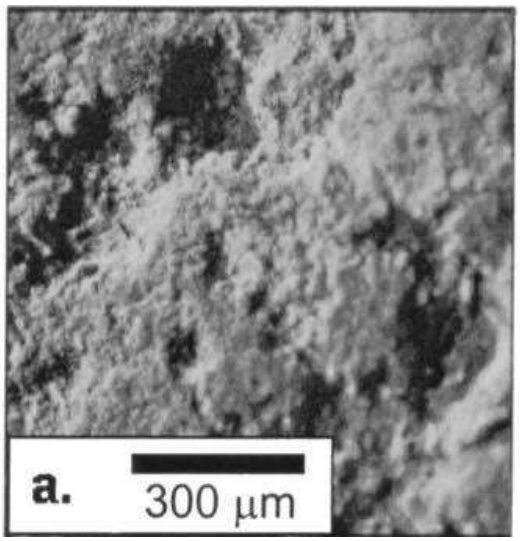

(a) The morphology of the external surface of grain.

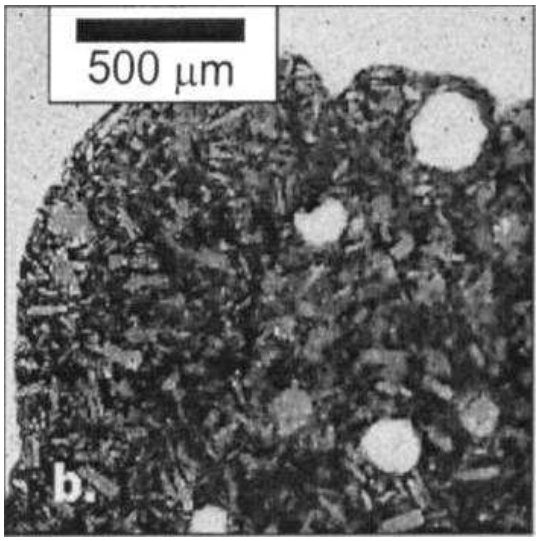

(b) The microstructure of the polished cross section of the gravel grain, where the white domain is the void, meanwhile the other parts are matrix of the grains.

Figure 2.2: The micro-topography of the grain of Hanford gravel with scanning electron microscope (SEM)[240].

Besides, the magnitude of intergranular pore size is of the same order as that of solid grains.

— Mesoscopic scale:

On the external surface of Hanford gravel, there exists a root mean-squared roughnesses (rmsr) in the micron range, with sparsely distributed deep (hundreds of micrometers) pits (as shown in periphery of the grain in Fig.(2.2)(b)).

The intraporosity of Hanford gravel is about 10% of the total porosity. As shown in Fig.(2.2)(b), the intragranular pores are composed of the sparsely distributed voids (hundreds of micron) connected by rather small pore groups. The specific surface of Hanford gravel is estimated to be about $11 m^2.g^{-1}$, which is higher than that of same material without intraporosity.

Due to the intragranular and intergranular porosity, gravel can be regarded as a dual porosity porous media.

The aforementioned morphological observation is dedicated for Hanford gravel. For

different types of gravel, by determining the intraporosity as well as characterizing the topography of the external surface, all of the morphologies of gravel grains can be categorized as the following six types in Fig.(2.3) [240].

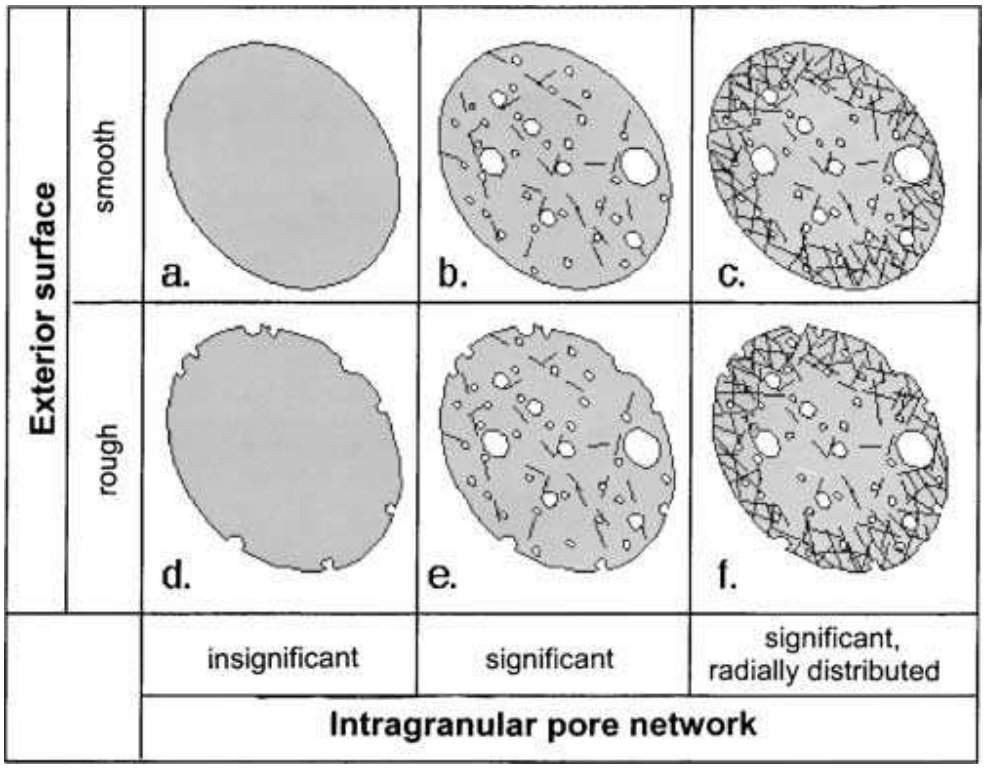

Figure 2.3: Schematic illustration of several morphologies of the gravel grains [240].

As seen from Fig.(2.3), gravel can be categorized according to the external surface roughness and intragranular pore network. Several sophisticated devices such as SEM and AFM as well as the image process technique should be employed to qualitatively characterize the morphology of gravel.

2.3 Microstructure morphology of non-granular materials

Non-granular materials commonly encountered in the practical engineering domain, exhibit more complicated morphology: multi scale microstructures and spatial configurations of the phases.

2.3.1 Sandstone

Sandstone is universally encountered in petroleum engineering and geological engineering. Sandstone may be identified as the final product of a series of complicated geological and hydrodynamical processes [11]. The processes start with erosion of the quartz-bearing rocks [11]. Then sand grains in the sandstone are transported via air, water flow and ice [11]. Finally the sand grains are deposited in sedimentary basins [11].

Sandstone is mainly composed of sand, cementing matrix, pore filling clay, interface and macro pore space. The morphology of sandstones strongly depends on its mineralogy. Based on the content of pore filling clay, sandstone can be classified as two main categories: **Arenites** which are ”clean” sandstones that are free of or have very little clay ($\leq 15\%$); **Wackes** are "dirty" sandstones that have a significant amount of clay ($\geq 15\%$) [199].

The arrangement and distribution of the sand and clay should be investigated clearly before establishing any microstructure model. A schematic model based on the picture of the backscattering electron microscope is presented for capturing the morphology of sandstone, as shown by the Fig.(2.4). The morphological characterization of sandstone can be summarized as:

— Sand grains range from 2mm to 1/16mm in diameter. The behavior of the sand grains depends on its mineral compositions which can be categorized as: quartz, feldspar and lithic fragments and other accessory minerals [23].

— Cementing matrix is mainly the quartz which is formed surrounding the sand grains owing to the geological process. Cementing matrix greatly influences the porosity of the sandstone [23].

— Pore filling clay is formed between the grains. This information (clay content) is expected to play a significant role on the transport properties of sandstone.

— Interface (cement): it is the domain where adjacent grains are bound together. Interface is a secondary mineral that forms after deposition and during the burial of sandstone [23]. There are four common types of interface: silica, limonite, calcite

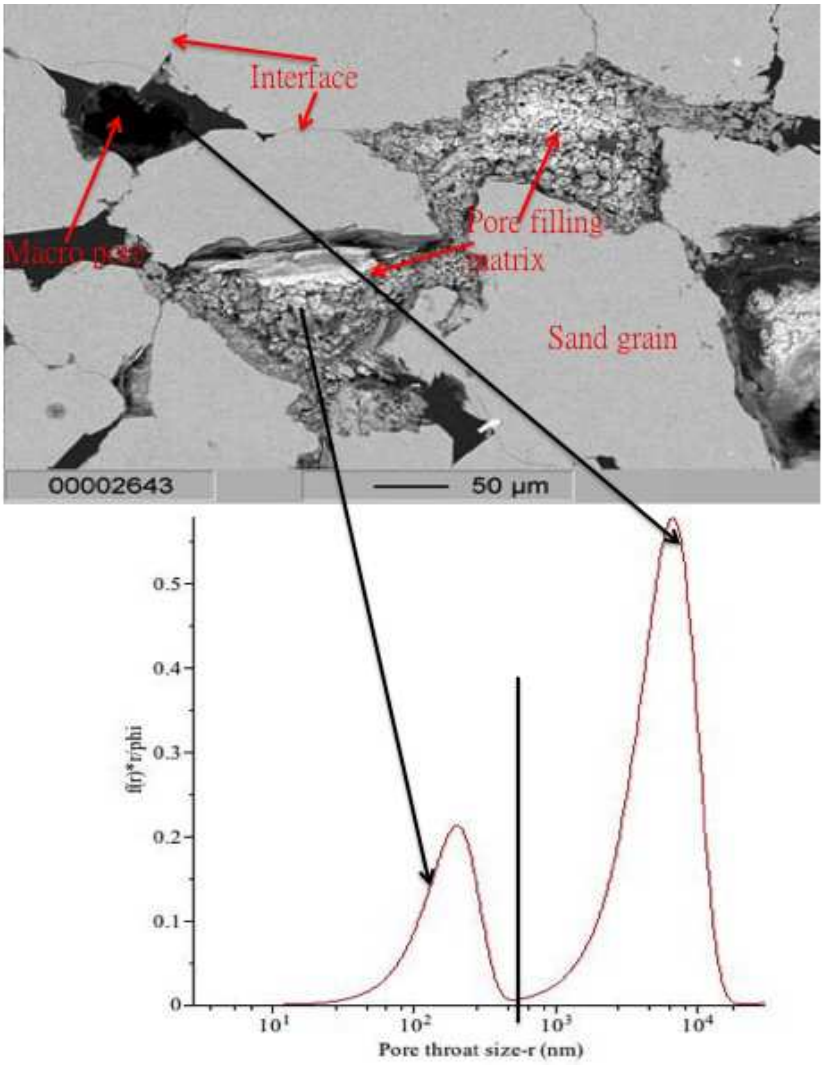

Figure 2.4: Schematic representation of morphology of the sandstone, modified from [235].

and clay minerals [23]. The mechanical behavior of sandstone is determined by the types of the interfaces.

— Pores are usually under the form of intergranular pores (macro pores) and micro-pores within the pore filling clay or interfaces. As shown in the lower part of Fig.(2.4), the pore size distribution of the sandstone presents a dual porosity property.

2.3.2 Clay

Clay is a general term covering clay minerals, metal oxides and other organic chemicals [172]. The characteristic size of solid components (particles) is finer than 2 μm in diameter as categorized by geologists [18]. Clay is a natural material which is used widely in geotechnical engineering, geological engineering and agriculture field. Clay is a complicated hierarchical porous medium the morphology of which can be analysed at the macro scale, micro scale and nano scale:

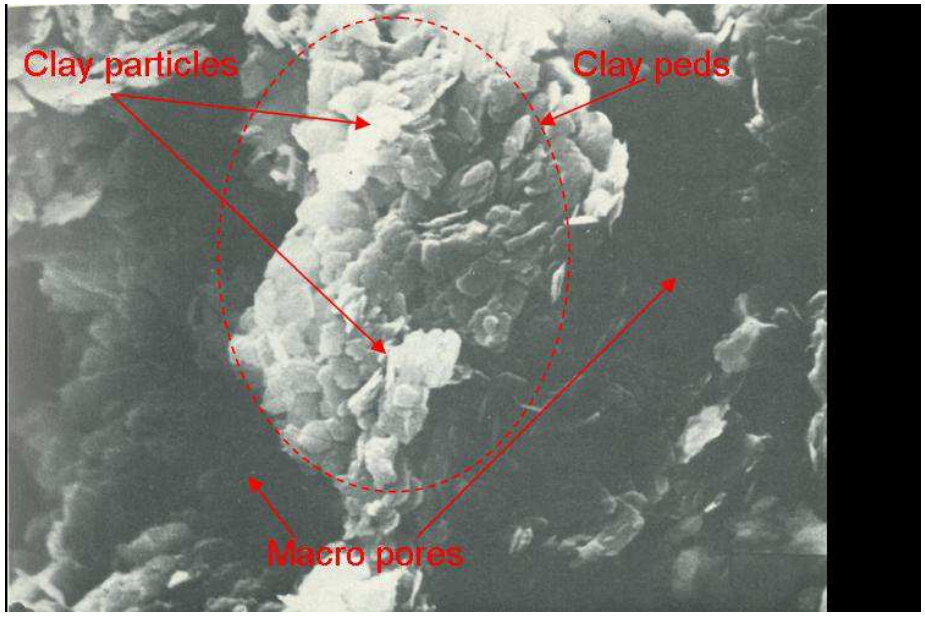

Figure 2.5: Schematic image of microstructue of clay, modified from [259].

— Macroscopic arrangement of clay [259]:

At this scale, as shown in Fig.(2.5), clay matrix is composed of the packing arrangement of the clay peds. The macro pores are the voids between these clay peds. The

size of the peds are at the order of 0.1 mm [150].

— Micro scale observation [259]:

As shown in Fig.(2.6), each clay aggregate consists of several clay particles in randomly distributed and the corresponding meso pores formed by these clay particles. As observed by Krohn et al. [150], the characteristic size of the particle is several μm.

— Nano scale observation [259]:

At this scale, each lamella is composed of interlayer with a characteristic thickness of several nanometer. In this scale, each lamella can also be specified as stacked elementary clay mineral units in parallel array (red dotted curve as shown in Fig.(2.7)). The elementary clay mineral units based on these different arrangements can be classified as four main types in the Table(2.1).

— Owing to the hierarchical nature of the clay structure, the pores in clay can be separated as macro pores formed by the packing of peds in clay matrix, micro pores formed by the packing of the particles within peds and the nano meter pores of the interlayer formed by the arranging of lamellas within particles [150]. Thus, it can be inferred that the pores size distribution of the clay appears triple porosity lying on the different scale of the pores.

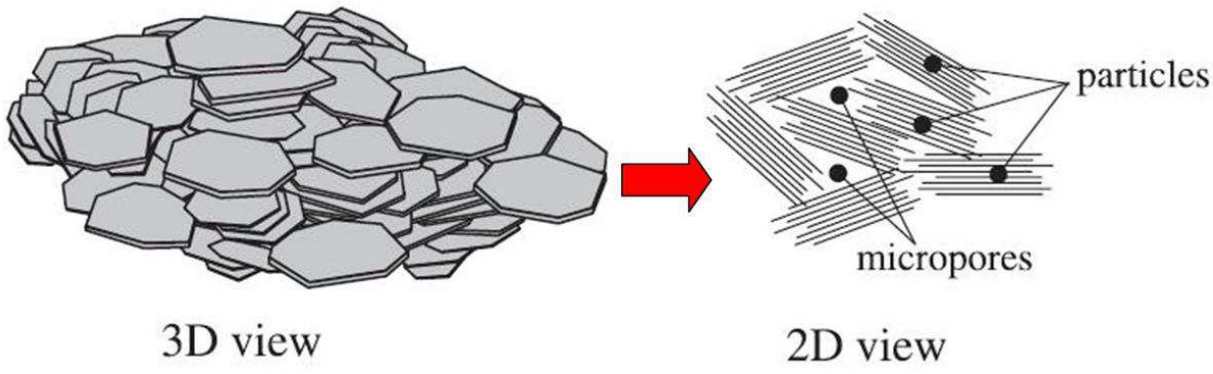

Figure 2.6: Schematic representation of microscopic arrangement of clay particles and the corresponding micropores within a ped [150].

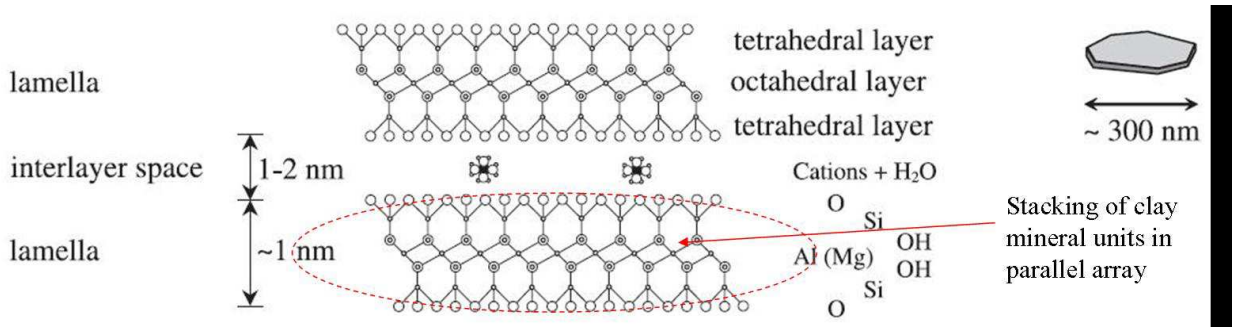

Figure 2.7: Schematic representation of particles which are composed of lamellas and interlayer space[150].

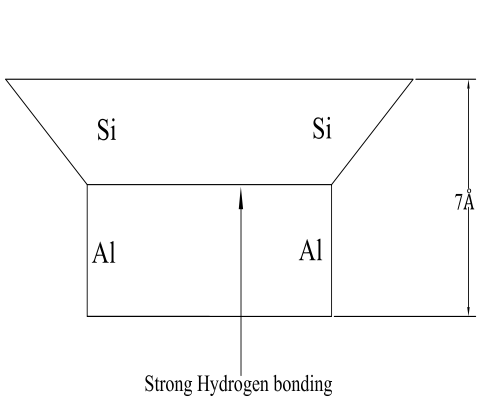

(a) Kaolinite

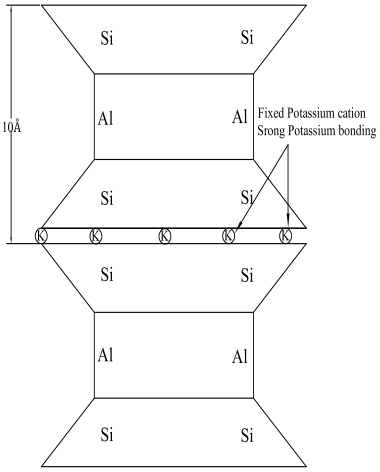

(b) Illite

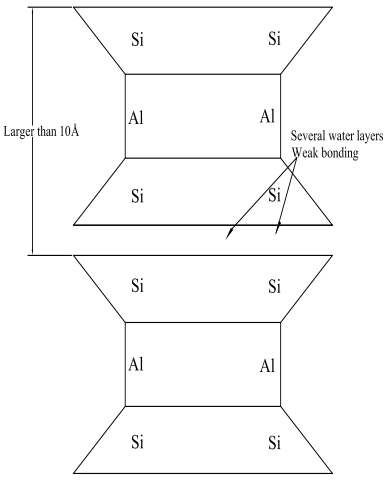

(c) Montmorillomite

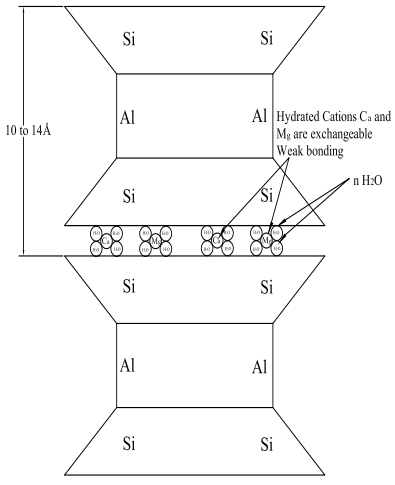

(d) Vermiculite

Figure 2.8: Schematic illustration of several elementary clay mineral units [172].

2.3.3 Cement paste

Extensive studies have increasingly focused on the microstructure of the Portland cement paste by means of non-destructive techniques such as electron optical microscope[41], X-ray diffraction techniques [41], scanning electron microscopy [48, 51], X-ray transmission microscopy [138, 209, 210], atomic force microscopy (AFM) [110]. In addition, instrumented indentation [54] is a promising technique to quantify the elastic properties of each phases of the microstructure. Based on all these experimental techniques, micromechanics should become a more and more efficient methodology.

The microstructure of the hardened cement paste is rather complex owing to its close connections with time, cement components and the curing conditions [136]. Generally, hardened Portland cement paste is the final hydration product between the cement clinkers and water [136]. Depending on the hydration degree, the microstructure of the hardened portland cement paste mainly consists of calcium silicate hydrates (C-S-H) which bind other components such as remainning anhydrous cement clinkers, Portlandite (CH), Aluminates (Al) together [136]. Taplin [234] has initially proposed a C-S-H model which specifies the hydration products (C-S-H) as outer and inner products. Outer products form in the original water filled pore space while inner products are accumulated surrounding the original cement clinkers. With the further understanding of the structure of the C-S-H, Jennings [136, 137] has proposed a more sophisticated model in which C-S-H is arranged in elements with size of 4nm. Jennings' model distinguishes the HD C-S-H (high density C-S-H) and LD C-S-H (low density C-S-H) [136, 137]. HD C-S-H is composed of the adjacent elements and small gel pores between the former [136, 137]. LD C-S-H is composed of the groups of elements and the corresponding large pores between the former [136, 137].

Therefore, owing to the multi structure of the cement paste, the morphology of the cement paste may be subdivided into the following two scales [112, 217]:

— Scale 1 (1 μm-100 μm) cement paste: as shown in Fig.(2.9), a clear phase distribution can be seen in the polished section of cement paste. At this scale, the cement paste is

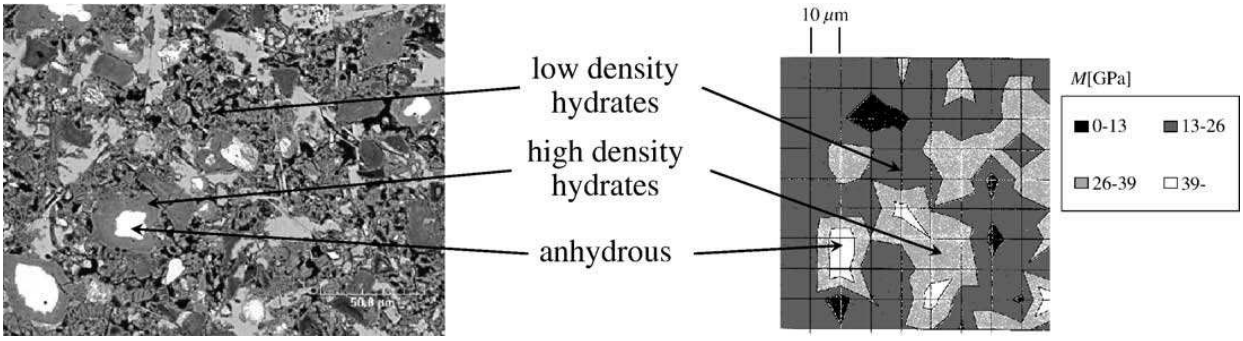

Figure 2.9: Scanning image of the polished section and the nano-indentation grid for a cement paste at $w/c = 0.5$ [217].

composed of the anhydrous cement clinkers (white domain), HD C-S-H surrounding anhydrous cement clinkers (gray areas surrounding white domain),LD C-S-H (gray and black mixed areas), portlandite crystals (light gray areas) and the macro pores (black areas in LD C-S-H) [217]. The distinct morphology of the HD C-S-H and LD C-S-H shown in the left figure of the Fig.(2.9) is verified by more sophisticated nano-indentation results shown in the right figure [217].

Scale 2 cement matrix: microstructure of CSH.

Either HD C-S-H or LD C-S-H is made up of "elementary bricks", the size of which is measured to be 60 × 30nm by 5nm thick [110]. As illustrated in Fig.(2.10), the HD and LD C-S-H come from the different spatial arrangement of the elementary bricks. The gel pores within the HD C-S-H is approximated to be ranged from 5 to 60 nm [217]. The pores within the LD C-S-H include gel pores and capillary pores, whose sizes range from 50 nm to 20 μm [217].

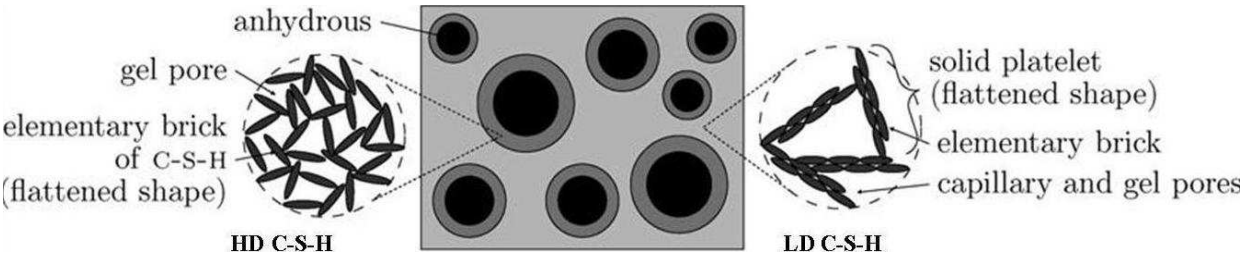

Figure 2.10: Schematic representation of LD C-S-H and HD C-S-H, after [217].

Table 2.1: Characteristics of several common elementary clay mineral units [259]

Classification	Kaolinite	Illite	Montmorillomite	Vermiculite
Composition of Layer (Silica:Alumina sheet)	1:1	2:1	2:1	2:1
Shape [1]	6-sided flakes	Flakes	Equi-dimensional Flakes	Flakes
Schematic Illustration	Fig.(2.8) a	Fig.(2.8) b	Fig.(2.8) c	Fig.(2.8) d
Interlayer Bond	Strong hydrogen bonding	Strong K^+ bonding	Weak bonding	Weak bonding
Size of particle [2]	$0.1 - 4\mu m \times 0.05 - 2\mu m$	$0.003 - 0.1\mu m \times$ up to $10\mu m$	$\geq$ 1 nm $\times$ up to $10\mu m$	Not specified

[1] After [172].
[2] Size of lamella arranged as Fig.(2.7), After [172].

2.4 Summary

Several microstructure morphologies of geomaterials are presented in this chapter. They are based on the observation by means of sophisticated technique devices. The morphology of the solid microstructure is not specially accounted for by the multi scale microstructure in this work. On the contrary, owing to the significant role of the water distribution in the transport and freezing problems, the water distribution morphology will be paid special attention to in this work and will be discussed in the next chapter. Therefore, as a first approximation, the microstructure information is interpreted by pore size distribution or grain size distribution in this work.

Part II

Micromechanical modelling of transport within unsaturated porous media

Chapter 3

Introduction to transport in unsaturated porous media

Contents

3.1 Evolution of water distribution within unsaturated granular materials 33

3.1.1 In the case of smooth surface 33

3.1.2 The effect of surface characteristics 35

3.2 Water distribution within unsaturated sandstone 37

3.3 Liquid-gas interface in unsaturated porous media 39

3.3.1 Kelvin equation 39

3.3.2 Limitations of applying Kelvin Equation 41

3.4 Disjoining pressure within water film 43

3.4.1 Definition of the disjoining pressure 43

3.4.2 Components of the disjoining pressure 44

3.4.2.1 Electrostatic component 44

3.4.2.2 Van der Waals component 46

3.4.2.3 Structural component 47

3.4.2.4 Effect of each component on disjoining pressure 49

3.4.3 Physical determination of the water film thickness 52
3.5 Liquid water volume fractions at low saturation degree 54
3.5.1 Volume contribution of pendular rings 55
3.5.2 Volume contribution of the water film 58
3.5.3 Liquid water retention 58
3.6 Local solute diffusion in water film 61
3.6.1 Pore size dependence of the diffusion coefficient 61
3.6.2 The effect of viscosity of water film 62
3.6.3 Local solute diffusion coefficient in the water film 63
3.7 Summary 64

The morphological distribution of the liquid water within a porous medium is essential to well understand and analyse the solute diffusion and advective transports within porous media. As pointed out by Tokunaga et al. [238], the distribution of water relative to other immiscible fluids is of interest in hydrogeology, subsurface water isolation using capillary barriers, petroleum engineering, and geologic carbon sequestration.

At varied saturation degree, water in porous media exhibits not only different configurations but also distinct transport mechanisms [238]. Therefore, studying the evolution of the water distribution during imbibition and drainage processes is of prior importance in transport problems. Section(3.1) and Section(3.2) are devoted to the physical characterization of the evolution of water distribution within unsaturated granular materials and sandstone at local scale. These sections show the necessity to quantify the equilibrium between liquid water and its vapor, which is described in Section(3.3). These sections also underline the influence of the water film localized on the solid/pores interface, the properties and behaviors of which are specified in the following three sections. The physical background associated with the local disjoining pressure which is likely to govern the internal state of stress within the water film is summarized and discussed in Section(3.4). In addition, a disjoining pressure model is proposed to estimate the thickness of water film. On the premise of the information about water film and pendular rings presented in the previous

sections, to quantitatively compare the volume fractions of pendular rings and water film at low saturation degree, a simple cubic packing model is proposed in Section(3.5). At last, as an introduction to the forthcoming analysis in Section(4.5), the question of the local solute diffusion in water film is addressed in Section(3.6).

3.1 Evolution of water distribution within unsaturated granular materials

This section is devoted to the physical characterization of the water distribution evolution in unsaturated granular materials. First, we consider unsaturated granular materials with smooth grain surface. The effect of pendular rings within granular materials is emphasized during desaturation process [1]. Next, the surface morphology (roughness) of the granular material is accounted for during desaturation process.

3.1.1 In the case of smooth surface

A schematic illustration of the evolution of water distribution in granular materials with smooth surface at varied saturation degree is presented in Fig.(3.1). According to the latter, Tokunaga [238] distinguished three types of water configuration and transport mechanisms in unsaturated granular materials. They are listed as follows [238]:

— Fig.(3.1)(a) illustrates the fully saturated pore network. In this case, the intergranular water is interconnected and governs the transport phenomena. Generally, the intergranular pore space may be categorized as pore body and pore throat. The latter governs the connectivity of intergranular water and the fluid transport in saturated case. To ensure the connectivity of intergranular water at high saturation degree, the intergranular water may be decomposed into intergranular layer [2] surrounded

1. In this work, to avoid discussing the hysteresis phenomena induced by progressive desaturation (drainage) and saturation (imbibition) processes, the evolution of water distribution is only characterized under drainage process.

2. Owing the polycrystalline morphology of granular material, the homogenized transport properties

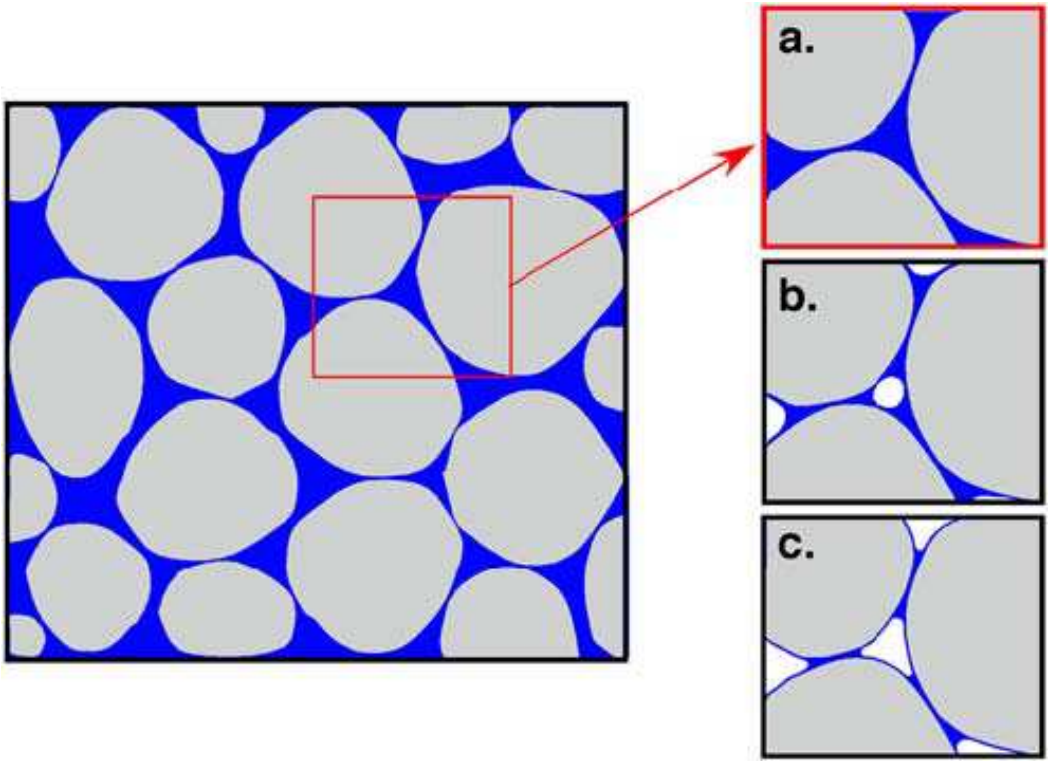

Figure 3.1: Schematic illustration of the evolution of water distribution within smooth glass beads at different saturation degree, after [238].

the solid grains and pore body water.

— Fig.(3.1)(b) depicts the water distribution at intermediate saturation degree[3]. In this case, liquid water in macro intergranular pores has been drained, while there are still pendular rings trapped in the vicinity of the grain contacts. The pendular rings are interconnected and they will play a central role in the definition of transport laws.

— Fig.(3.1)(c) illustrates water distribution at low saturation degree[4]. In this case, the pendular rings are discontinuous and connected by adsorbed water film. In this case, the adsorbed water film is expected to dominate the transport phenomena.

(e.g., homogenized diffusion coefficient and homogenized permeability coefficient) are estimated by self-consistent scheme. To ensure the connectivity of the intergranular water, part of the intergranular water is attached on the solid grain which is denoted as intergranular layer.

3. Intermediate saturation degree is a qualitative concept. It defines a range of saturation degree where the interconnected pendular rings (instead of pore water) govern the transport. Though it is not illustrated in Fig.(3.1)(b), there may be also some capillary water in smaller pores.

4. Low saturation degree characterizes a range of saturation degree in which the water film governs the transport.

3.1.2 The effect of surface characteristics

As shown in Fig.(3.1)(c), the pendular rings become discontinuous at a critical saturation degree. In the monodisperse close packing spherical grains system, the critical saturation degree is estimated as 24.3% by Fisher et al.[103].

However, in the real granular materials such as sand and sandstone, the grains surface characteristics (as shown in Fig.(3.2)) clearly influence the water retention and consequently the unsaturated transport at intermediate saturation degree. Indeed, owing to surface roughness of solid grains, in addition to the water film, capillary water trapped at grooves and concaves (depicted in Fig.(3.2)) on the solid surface will also connect the isolated pendular rings at intermediate saturation degree [181].

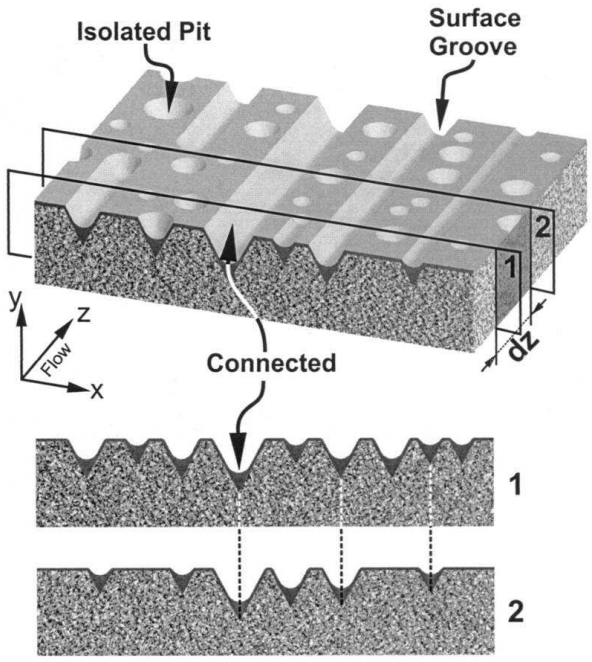

Figure 3.2: Capillary water resided in grooves, pits on the rough surface [181, 243].

The capillary water trapped at pore corner (pendular rings) and grooves on solid surface have been observed by Lenormand et al. [156]. From the thermodynamics point of view, the wetting layers trapped in pendular rings and grooves on grain surface are stabilized by capillary pressure and have a typical **thickness of the micron**, which is far smaller than the characteristic size of the grains [22]. This capillary water is considered to be

interconnected at intermediate saturation degree and can support very high flow rates [22, 152, 181, 238, 240–243, 243].

The adsorbed water film is stabilized by the surface force (or disjoining pressure which will be introduced in the sequel) and are **typically nanometers thick** [22]. When the relative humidity is low enough, the trapped capillary water on the surface grooves, pits and pendular rings will become discontinuous. In this case, the water film will interconnect the isolated trapped capillary water and play a significant role in transport.

Definition of wetting layer surrounding the solid grain

To emphasize the important role of the interconnected capillary water at intermediate saturation degree, **the interconnected capillary water which consists of pendular rings, trapped capillary water in the grooves and pits on the grains surface is denoted as wetting layer**.

Due to the size dependence of the flow permeability, at intermediate saturation degree, compared to the interconnected wetting layers (order of micron in thickness), the flux of water film (typical thickness of nanometer) seems to be negligible. However, at low saturation degree, the wetting layers become discontinuous and connected by water film, the latter thus governs the transport phenomena.

In view of clarifying our purpose in the sequel, we consider from now on that the water distribution and the corresponding flow regimes in unsaturated granular material can be summarized as:

— Intergranular water: The intergranular water comprises the pore body water and the intergranular layer surrounding the solid grain. The connectivity of the intergranular water is ensured by the intergranular layer surround the solid grains, interconnected water plays an important role in transport at high saturation degree.

— Wetting layers:

capillary water in pendular rings, grooves and pits on the grains surface are idealized

as wetting layers on the grains surface; the stability and volume quantity of wetting layers is governed by capillary pressure, they are interconnected and will play an important role in the transport at intermediate degree [181, 243].

— Water film adsorbed on grains surface:

water film will bridge the discontinuous wetting layer at low saturation degree, it will dominate the flow transport at low saturation degree.

3.2 Water distribution within unsaturated sandstone

By contrast to the granular materials introduced previously, sandstone exhibits a dual porosity microstructure (as shown in Fig.(2.4)). In this context, for simplification, clay filling in sandstone is disregarded (clean sandstone). The pore space of this clean sandstone is thus mainly composed of intergranular pore (channel pore) which can even be categorized as pore body and pore throat [161, 184]. The characteristic radius of the intergranular pore ranges from several microns to tens of microns [63, 184].

Based on this microstructure characterization, the evolution of water distribution can be characterized as:

At fully saturated case, the theoretical and experimental findings demonstrate that the transport in the fully saturated sandstone is mostly realized via intergranular water [22, 121].

At intermediate saturation degree[5], as shown in Fig.(3.3), the surface characteristic of sandstone is likely to influence the water distribution of unsaturated sandstone. The figure illustrates the capillary water localized in pendular rings, grooves and pits on grains surface. At intermediate saturation degree, the wetting layer is capillary water trapped on the solid/pore space interface and can be assumed to be continuous [22, 243]. At this regime, the water phase is thus mainly localized in pendular rings and pits on solid surface.

5. In this case, intermediate saturation degree defines a range of saturation degrees where the wetting layers (interconnected pendular rings and capillary water trapped in surface roughness) govern the transport.

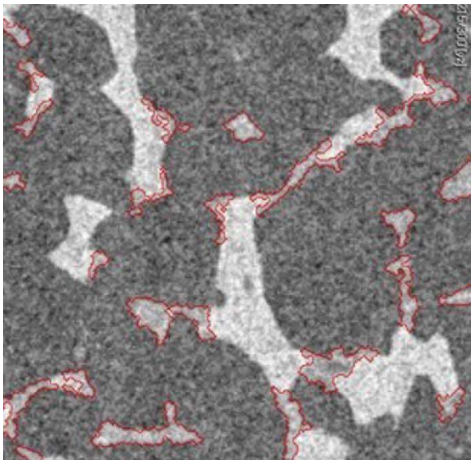

Figure 3.3: Schematic illustration of influence of surface characteristic on water distribution at saturation degree 0.3, the domains surrounded by the red curves are the capillary water, the grey domains are gas and the black domains are sandstone grains [121].

The characteristic sizes of intergranular pore, surface roughness and pendular rings are of the order of the micron.

At low saturation degree, the intergranular water as well as wetting layer (trapped capillary water) on rough surfaces and pendular rings become progressively discontinuous, so that the water film adsorbed on the solid surface is the unique water phase that is able to interconnect the isolated trapped capillary water. At this stage, the water film plays a dominant role in the transport.

In summary, the distribution of water phase in unsaturated sandstone can be divided into three regimes:

— Intergranular water. It exists at high saturation degree and at intermediate degree.

— Wetting layers:

  Wetting layers (capillary water trapped in pendular rings, grooves and pits on the grains surface) are assumed to be interconnected and will dominate the flow transport at intermediate saturation degree [121, 243].

— Water film adsorbed on grains surface:

  Water film will bridge the discontinuous wetting layers at low saturation degree, it will dominate transport at low saturation degree.

Whatever the microstructure, the definition of the transport properties of porous media is essentially a question of water distribution morphology and local physical properties for saturation regimes ranging from low to fully saturation state. This desaturation process is accompanied by the equilibrium of liquid-gas interfaces within unsaturated porous media. Indeed, the saturation degree of the porous media is closely related to the microstructure of the porous media and the equilibrium radius of the liquid-gas interface, the latter can be characterized by the Kelvin equation which is introduced in the following section.

3.3 Liquid-gas interface in unsaturated porous media

Along drainage or imbibition mechanisms within porous media, a curved interface between vapor and liquid is formed: non wetting phase is gas and wetting phase is liquid water; in Fig.(1.2), thus, $\alpha = g$, $\beta = l$. As introduced in Section(1.3), at mechanical equilibrium state, there is a pressure difference across the interface due to the surface tension. Combined with the thermodynamic equilibrium, the relation between the interface curvature radius and the relative humidity can be derived as follows.

3.3.1 Kelvin equation

As a special case, Eq.(1.5) [6] can be reorganized as classic Young-Laplace equation, that is:

$$P_{cap} = P^g - P^l = \frac{2\gamma_{lg}\cos\theta}{r_2} \tag{3.1}$$

where the curved meniscus is assumed to be hemispherical, r_2 and θ are respectively the radius of meniscus and the contact angle, as shown in the inset of Fig.(1.2); γ_{lg} is the surface tension between liquid water and vapor; P_{cap}, P^g and P^l are the capillary pressure, vapor pressure and liquid pressure, respectively.

6. In this case, $[\boldsymbol{\sigma}].\underline{n} = P^g\underline{n} - P^l\underline{n}$. When the meniscus is hemispherical in shape $(\mathbf{1}_T : \boldsymbol{b})\underline{n} = \frac{2\cos\theta}{r}\underline{n}$.

Besides mechanical equilibrium, thermodynamic equilibrium is also satisfied across the vapor-liquid interface. At equilibrium, the chemical potentials of liquid water and vapor do satisfy:

$$\mu_l(P^l, T) = \mu_g(P^g, T) \tag{3.2}$$

where $\mu_l(P^l, T)$ and $\mu_g(P^g, T)$ are the chemical potentials of liquid water and vapor at corresponding pressure (P^l or P^g) and temperature T, respectively.

Assuming sufficiently slow change, the chemical equilibrium is maintained at any time. Eq.(3.2) can then be differentiated as [58]:

$$\mathrm{d}\mu_l = \mathrm{d}\mu_g \tag{3.3}$$

According to Gibbs-Duhem equations [58]:

$$\begin{cases} \mathrm{d}\mu_l = \overline{V}_l \mathrm{d}P^l - S_l \mathrm{d}T \\ \mathrm{d}\mu_g = \overline{V}_g \mathrm{d}P^g - S_g \mathrm{d}T \end{cases} \tag{3.4}$$

where S_l and S_g are the molar entropies of liquid water and vapor phase; $\overline{V}_l$ and $\overline{V}_g$ are the molar volumes of liquid water and vapor phase; T is the temperature (in K).

At isothermal conditions (T is held constant), Eq.(3.3) together with Eq.(3.4) yield:

$$\overline{V}_l \mathrm{d}P^l - \overline{V}_g \mathrm{d}P^g = 0 \tag{3.5}$$

Consequently, when the molar volume of the vapor is assumed to be much larger than the molar volume of liquid water ($\overline{V}_g \gg \overline{V}_l$), Eq.(3.5) can be approximated as [125]:

$$\mathrm{d}(P^g - P^l) + \frac{\overline{V}_g - \overline{V}_l}{\overline{V}_l}\mathrm{d}P^g \approx \mathrm{d}(P^g - P^l) + \frac{\overline{V}_g}{\overline{V}_l}\mathrm{d}P^g = 0 \tag{3.6}$$

As the vapor is assumed to be an ideal gas, we have:

$$P^g = \frac{RT}{\overline{V}_g} \tag{3.7}$$

where R is the ideal gas constant, R=8.314 J.mol^{-1}.K^{-1}.

Substituting Eq.(3.1) and Eq.(3.7) into Eq.(3.6), followed by an integration at constant temperature constant $\overline{V}_l$, yields the so-called Kelvin equation as [58]:

$$\ln\frac{P^g}{P_{gsat}} = -\frac{2\gamma_{lg}\cos\theta\overline{V}_l}{r_2 RT} \tag{3.8}$$

where P_{gsat} is the saturation vapor pressure for a flat interface related to temperature T, P^g is the equilibrium vapor pressure over the curved interface with curvature radius r_2.

Defining the relative humidity hr as [58]:

$$hr = \frac{P^g}{P_{gsat}} \qquad hr \in [0,1] \tag{3.9}$$

Kelvin equation (Eq.(3.8)) can be rewritten in a more familiar form:

$$\ln hr = -\frac{2\gamma_{lg}\cos\theta\overline{V}_l}{r_2 RT} \tag{3.10}$$

3.3.2 Limitations of applying Kelvin Equation

In order to use the Kelvin Equation (Eq.(3.8)), it is essential to know some of its limitations.

— Surface tension is assumed to be constant, which is only valid when the curvature radius of interface is far larger than the thickness of interfacial region across interface. The magnitude of the thickness of the interfacial region is not known but it is often estimated in the range of 0.2 nm to 0.7 nm [125]. When the curvature radius of interface is small enough, a modified surface tension should be introduced, which is based on the Tolman-Koeing equation, more detailed information is given in [146].

— At curved interface typically with radius higher than 100 nm, the Kelvin equation

is valid. However, this was questioned for radius below 100 nm [91, 101]. Fisher et al. [101, 102] performed a direct measurement of the mean curvature radius of the cyclohexane condensed between crossed mica cylinders. Experimental results were compared with the curvature radius determined by Kelvin equation. It was concluded that the Kelvin equation is valid for the meniscus with radius as low as 4 nm. The Kelvin equation should be corrected when the curvature radius is lower than 4 nm.

In the following work by Fisher et al. [100], the same experimental method was employed to measure the curvature radius of liquid water trapped in wedge of fused silica surfaces. It was found that the Kelvin equation incorporating the presence of a water film (Eq.(3.11)) is valid for the meniscus with radius as low as 9 nm.

— Eventually, the assumptions that molar volume of vapor is far larger than that of liquid and the vapor is considered as an ideal gas will be out of validity when the temperature ranges between 100°C and 200°C [125].

As proposed by numerous researchers [140, 179, 225, 237], owing to the presence of the water film on the pore wall, the Kelvin equation should be modified as:

$$\ln hr = -\frac{2\gamma_{lg}\cos\theta\overline{V}_l}{(r_2-h)RT} \tag{3.11}$$

where h is the thickness of water film adsorbed on the pore wall.

Eventually, the expression for capillary pressure $P_{cap} = \dfrac{2\gamma_{lg}\cos\theta}{r_2-h}$, Eq.(3.11) can be rewritten as:

$$-\frac{RT}{V_l}\ln hr = P_{cap} \tag{3.12}$$

Thus, the effect of the water film can be accounted for in the Kelvin equation. More significantly, as introduced in Section(3.1), the low saturation regime is mainly governed by the existence of the water film adsorbed on the solid/pore space interface, the characteristic size of which is of the order of nanometer. At that scale, water phase (pore water and

wetting layer) is hardly continuous in nature. Consequently, understanding the behaviors and the transport properties at this nano-scale requires a better physical characterization. Indeed, the specific physics of the water film lies in the so-called disjoining pressure, which ensure the stability of the water film. This is the object of the following section.

3.4 Disjoining pressure within water film

Water film has been proved to be dominant in the transport at low saturation degree [121]. At nano-scale, the stability and thickness of the water film are determined by the so-called disjoining pressure [71, 75, 249]. The physics of the disjoining pressure was first proposed and verified by Derjaguin and Obuchov [75]. Later, a more formal definition from thermodynamics and mechanical equilibrium was established by Derjaguin and Churaev [71, 74]. The present section is devoted to the physical background associated with the local disjoining pressure.

3.4.1 Definition of the disjoining pressure

There are two kinds of definition of disjoining pressure: a thermodynamic related definition and a mechanical definition. Generally, the thermodynamic related definition of the disjoining pressure exhibits the essential meaning from the free energy point of view of formation of a thin layer, while a more common and intuitive alternative one is from its mechanical equilibrium. Therefore, in this section, only mechanical definition of disjoining pressure will be presented, the thermodynamic related definition of disjoining pressure is given in Appendix (A.3). Derjaguin et al. [74] argued that the internal state of stress within the water film is anisotropic and can be expressed in a tensorial form. The latter can be decomposed as a normal component P^f (to the surface) and a tangential component [7]. The normal component is interpreted as a pressure remaining constant through the

7. The tangential component will not be introduced in this section, the detailed information is given in [74, 116].

normal direction of the water film, whereas, the tangential one varies with the distance from the solid surface. In mechanical equilibrium state, the disjoining pressure is defined as the difference between the normal component (the pressure) within the water film P^f and the bulk liquid pressure P^l [71, 74, 116]:

$$\Pi(h) = P^f - P^l \tag{3.13}$$

The mechanical definition of disjoining pressure will be used widely in the following sections.

3.4.2 Components of the disjoining pressure

There are mainly three different components in the definition of the disjoining pressure. The first one is the relative long range repulsive electrostatic force which originates from the overlapping of the diffuse double layer, say $\Pi_e(h)$; the second one is the Van der Waals force between the molecules of two interfaces, say $\Pi_v(h)$; the third component is denoted as the structural force or hydration force (solvation force), say $\Pi_s(h)$.

In the following subsections, each component of the disjoining pressure will be introduced separately in order to interpret their origins and evaluate their quantity.

3.4.2.1 Electrostatic component

The electrostatic component of the disjoining pressure is investigated extensively in the colloid and interface science [74, 132, 169].

According to Churaev et al. [44], the characteristic length of the diffuse double layer, the Debye length $1/\kappa$, is used to characterize how far the electrostatic effect persists in diffuse double layer. It can be estimated by [44]:

$$\frac{1}{\kappa} = (\epsilon\epsilon_0 kT)^{1/2}(2z^2e^2n)^{-1/2} \tag{3.14}$$

where ϵ is the dielectric permittivity of water film, ϵ_0 is the permittivity of the free space,

k is the Boltzmann constant, T is the temperature (in K), n is the number density of the ions, $n = N_a \times c$, c is the concentration of the bulk electrolyte solution (in mol.ml^{-1}), N_a is Avogadro's constant ($N_a = 6.022 \times 10^{23}$), e is the elementary charge ($e = 1.602 \times 10^{-19}$ C), z is the electron charge. It can be found from Eq.(3.14) that the magnitude of the Debye length depends on the properties of the liquid instead of the properties of other media such as solid substrate or gas phase. At a given temperature, the Debye length depends solely on the ionic concentration of the solution.

As shown in the Fig.(3.4), when two negatively charged surfaces are close enough (e.g. $h \leq 2/\kappa$), the two diffuse double layers will overlap and an external pressure P_N should be exerted to maintain equilibrium. In this process, a kind of electrostatic force Π_e will arise within the water film. The pressure of the water film P^f is equal to the equilibrium bulk pressure P^l when the distance of the two solid surface h is far larger than twice of the Debye length ($1/\kappa$) [3].

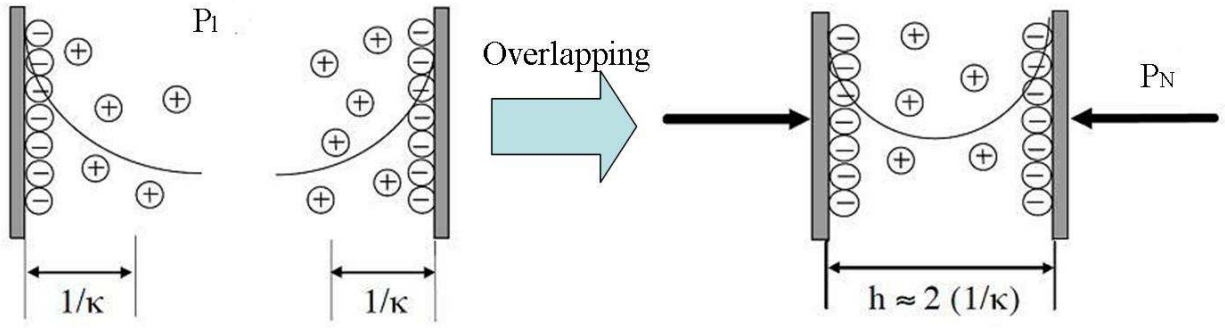

Figure 3.4: Schematic representation of the overlapping of the two diffuse double layers when approaching the charged surface [3]: left: thick film; right: thin film.

To evaluate the electrostatic pressure Π_e, the Poisson-Boltzmann equation along with certain boundary conditions such as constant surface potential or constant surface charge are widely employed [3, 74, 128, 132]. The electrostatic disjoining pressure for water film between two similarly charged surfaces, with the assumption of the monovalent electrolyte solution can be evaluated by [74]:

$$\Pi_e(h) = \frac{\epsilon\epsilon_0\psi_0^2}{8\pi}(\text{sech}^2(\kappa h)) \qquad \text{with constant surface potential} \quad \psi_0 \tag{3.15}$$

$$\Pi_e(h) = \frac{2\pi\sigma_0^2}{\epsilon}[\frac{1+\text{sech}(\kappa h/2)}{\tanh(\kappa h/2)}]^2 \qquad \text{with constant surface charge} \quad \sigma_0 \tag{3.16}$$

where ψ_0 and σ_0 are the potential and charge density of the interface.

The above electrostatic models are valid for interlayer systems which are confined between two similar charged surfaces. However, water film in unsaturated porous media has two different interfaces: water film-gas interface and water film-solid matrix interface. These two interfaces have different surface potentials[8]. In this case, the electrostatic disjoining pressure can be determined [44]:

$$\Pi_e(h) = \frac{RTc}{\text{sh}^2(\kappa h)}(2\Psi_1\Psi_2\text{ch}(\kappa h) - (\Psi_1)^2 - (\Psi_2)^2) \tag{3.17}$$

where c is the concentration of the solution (in mol.ml^{-1}), $\Psi_i = ze\psi_i/(kT)$ is the dimensionless potential of the interface i.

For low surface potential, Eq.(3.17) can be simplified as more commonly used formula[132]:

$$\Pi_e(h) = 64nkT\gamma_1\gamma_2\exp(-\kappa h) \tag{3.18}$$

in which parameters $\gamma_i = \dfrac{\exp(ze\psi_i/(2kT)) - 1}{\exp(ze\psi_i/(2kT)) + 1}$ $(i \in \{1, 2\})$; n is the concentration of the solution (in mol.L^{-1}), ψ_i denotes surface potential of water film-solid substrate interface (i=1) and surface potential of water film-gas interface (i=2).

3.4.2.2 Van der Waals component

In nanoscale confined system, besides the electrostatic interaction there is the Van der Waals interaction between the molecules of the adjacent surfaces. From the intermolecular

8. The water film-gas interface is negatively charged.

point of view, the Van der Waals force is induced by the three distinct forces: induction force, the orientation force and the dispersion force [132], each of which has a different interaction potential varying with inverse sixth power of distance. In case of plane interface, the expression obtained for the Van der Waals disjoining pressure has the following form [74, 132]:

$$\Pi_v(h) = -\frac{A}{6\pi h^3} \tag{3.19}$$

where A is the Hamaker constant that can be determined by experiment. Moreover, the non-retarded Hamaker constant can also be approximately determined from the theoretical physics arguments. For instance, the Lifshitz theory [132] yields the following theoretical definition:

$$\begin{aligned} A &= A_{\nu=0} + A_{\nu>0} \\ &\approx \frac{3}{4}kT\left(\frac{\epsilon_1-\epsilon_3}{\epsilon_1+\epsilon_3}\right)\left(\frac{\epsilon_2-\epsilon_3}{\epsilon_2+\epsilon_3}\right) + \frac{3h_p\nu_e}{8\sqrt{2}}\frac{(n_1^2-n_3^2)(n_2^2-n_3^2)}{(n_1^2+n_3^2)^{1/2}(n_2^2+n_3^2)^{1/2}((n_1^2+n_3^2)^{1/2}+(n_2^2+n_3^2)^{1/2})} \end{aligned} \tag{3.20}$$

where subscripts 1,2 and 3 represent pore wall substrate, non wetting phase and water film respectively; ϵ is the dielectric constant of the water film medium; h_p is Planck's constant ($h_p = 6.626 \times 10^{-34}$ J.s); n_i is the refractive index of the medium i; ν_e is the main electronic absorption frequency in the UV around $3 \times 10^{15}\text{s}^{-1}$; T is the temperature (in K).

3.4.2.3 Structural component

In many practical situations, it has been observed that the DLVO theory (the combination of electrostatic and Van der Waals component of disjoining pressure) can't explain all experimental results [47, 74, 132, 133, 135]. The deviation of the experimental results from the DLVO theory is even more noticeable when the water film is thin enough [47]. Besides the electrostatic and Van der Waals components, an additional component of disjoining

pressure named as structural component (or solvation component, hydration component) Π_s has been introduced in order to account for this deviation [47, 132].

Though there are still some controversies about the origin of the structural component of the disjoining pressure, the argument that the structural component of the disjoining pressure is attributed to the overlapping of boundary layers whose structure is modified, has been widely accepted [47, 74, 132, 134]. Several theoretical works are dedicated to the study of the relationship between the structural component and the thickness of the water film [147, 165, 173]. All of these theoretical models are semi-empirical: the parameters of these models have to be determined by fitting the experimental results. Because of the exponential increase of $\Pi_s(h)$ with decreasing value of h, it has been generally agreed that the structural component of the disjoining pressure can be described by the following exponential expression [47, 74, 132, 134]:

$$\Pi_s(h) = K\exp(-h/\lambda) \tag{3.21}$$

in which parameters K and λ characterize the magnitude and the acting range of the structural component. They may be determined by experiments. Generally, λ is in the range of 0.6 nm to 1.1 nm, while K ranges from 3×10^6 Pa to 5×10^7 Pa [132]. It should be noted that when the solid surface is hydrophilic, the value of K is positive: hence the structural component is repulsive; when K is negative, the structural component of disjoining pressure on the hydrophobic surface is attractive [134].

Eq.(3.21) is an approximate expression for the structural component of disjoining pressure. It is possible to take account of the different behaviors of the inner and outer parts of the water film [190]. The first several layers of water molecules (inner part) are highly bounded on the hydrophilic surface and less sensitive to the variation of the ionic concentration [190]. The outer layers of the water film are more readily affected by the change of the ionic concentration [190]. Pashley et al. [190] proposed a corrected equation to characterize the short range and long range effect for structural component of disjoining pressure:

$$\Pi_s(h) = K_{sr}\exp(-h/\lambda_{sr}) + K_{lr}\exp(-h/\lambda_{lr}) \tag{3.22}$$

The first term of the right hand side relates to the **s**hort **r**ange effect of the structural component. The second term of the right hand side corresponds to the **l**ong **r**ange effect of the structural component. K_{sr}, K_{lr}, λ_{sr} and λ_{lr} are the four corresponding fitting parameters.

Due to the lack of a fully predictive theoretical model, the structural component of the disjoining pressure is empirically determined by the difference between experimentally determined total disjoining pressure and that estimated by DLVO theory [74]. The reader should essentially keep in mind the fact that the structural component of disjoining pressure is proved to be a significant component when the thickness of water film ranges between 1.5 nm and 5 nm [135, 170].

3.4.2.4 Effect of each component on disjoining pressure

To determine the total disjoining pressure as a function of h only, $\Pi(h)$, all three components are assumed to be linearly additive [3, 47, 116, 117, 164]. Therefore, the total disjoining pressure can be expressed as:

$$\Pi(h) = \Pi_e(h) + \Pi_v(h) + \Pi_s(h) \tag{3.23}$$

To compare the contribution of the different components of the water film, a quartz-water film-air (wet air) system is adopted. The following expressions for the three components of the disjoining pressure are employed:

$$\begin{cases} \Pi_e(h) = 64nkT\gamma_1\gamma_2\exp(-\kappa h) \\ \Pi_v(h) = -\dfrac{A}{6\pi h^3} \\ \Pi_s(h) = K_{sr}\exp(-h/\lambda_{sr}) + K_{lr}\exp(-h/\lambda_{lr}) \end{cases} \tag{3.24}$$

Let us consider that the solution is an NaCl electrolyte. The parameters used are given in Table(3.1):

Table 3.1: Parameters for the quartz-NaCl aqueous film-air system

Parameters	Value (unit)	Reference
k	$1.381 \times 10^{-23} \mathrm{J \cdot K^{-1}}$	[132]
T	293K	-
Na	6.022×10^{23}	[132]
z	1	-
e	1.6×10^{-19} C	[132]
ψ_1	-100 mV	[239]
ψ_2	-25 mV	[239]
ϵ_0	$8.854 \times 10^{-12} \mathrm{C^2 J^{-1} m^{-1}}$	[132]
ϵ	80	[132]
A	-0.87×10^{-20}J	[132]
K_{sr}	3×10^8 Pa	[47]
λ_{sr}	0.3 nm	[47]
K_{lr}	2×10^6 Pa	[47]
λ_{lr}	2 nm	[47]

Using the parameters listed in Table(3.1) and treating the case as Majumdar et al. [164], the contributions of each component of the disjoining pressure are plotted in Fig.(3.5). From Fig.(3.5), it is observed that the electrostatic component near the wall decreases with increasing concentration of NaCl in the bulk solution (blue curves). Then, comparing the different components at the concentration $c = 10^{-2}$M, the structural component becomes to play a significant role for thickness $h < 12$nm. At larger range (i.e. $h > 20$nm), the effect of the structural component is rather negligible in the total disjoining pressure (black curve). The Van der Waals component of disjoining pressure (green curve) greatly influences the disjoining pressure at long range (i.e $h > 30$nm). We can conclude that when the concentration of the solution (bulk solution) is $c = 10^{-2}$M, the electrostatic component as well as Van der Waals component of disjoining pressure will be significant for thick water film, while the structural component of disjoining pressure will play a dominant effect in thin water film.

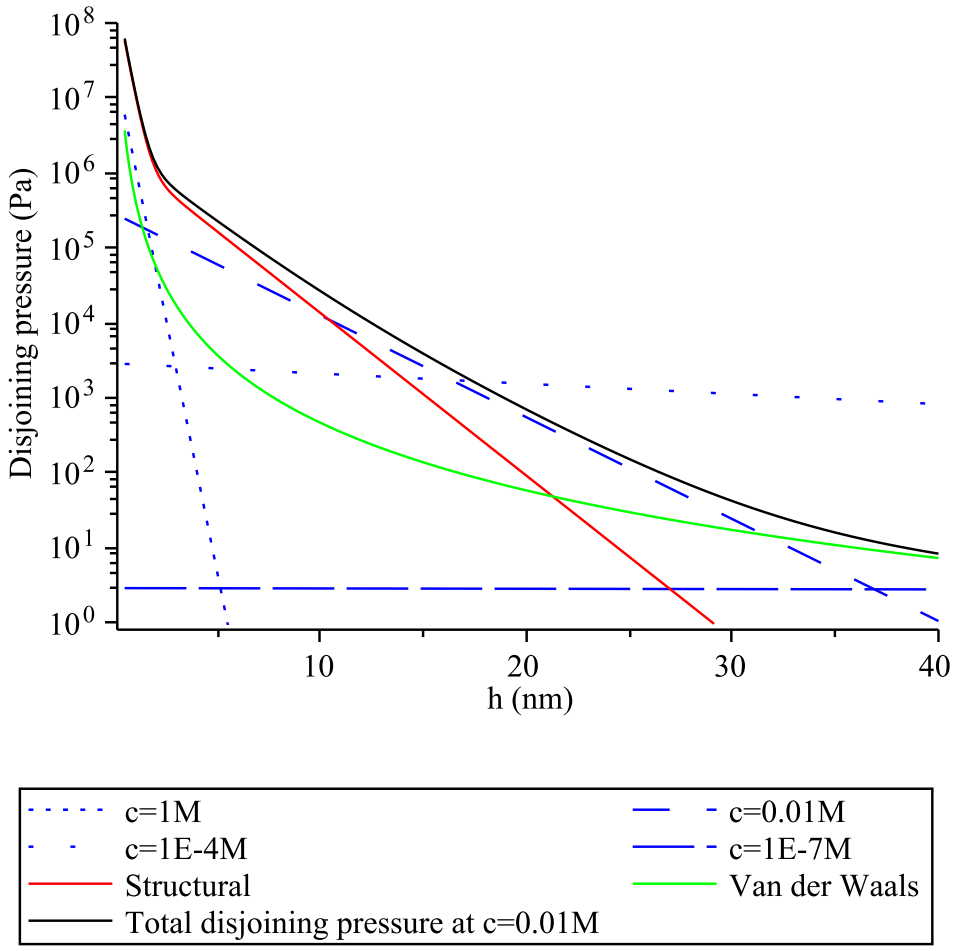

Figure 3.5: Comparison of the electrostatic, Van der Waals and structural components of the disjoining pressure of the quartz-NaCl aqueous film-air system, the parameters are given in Table(3.1), M=1mol.L^{-1}.

3.4.3 Physical determination of the water film thickness

We are interested in the physical identification of the water film thickness. Answering to this question may be done by taking advantage of the relation $\Pi(h)$. Indeed, in a micromechanics reasoning, such a new information should be identified from a physical reasoning and interpreted as a local physical quantity introduced at the scale of concern. The mechanical equilibrium for a water film separating a smooth spherical solid grain and a gas saturated pore space can be expressed as:

$$P^g - P^f = -\frac{2\gamma_{lg}}{R_s} \tag{3.25}$$

where P^g and P^f are respectively the pressure of gas and of the water film, R_s is the radius of the spherical solid grain, γ_{lg} is the surface tension along water film-gas interface [9]. Combining Eq.(3.25) and Eq.(3.13) yields:

$$\Pi(h) = P_{cap} + \frac{2\gamma_{lg}}{R_s} \tag{3.26}$$

where $P_{cap} = P^g - P^l$ is the capillary pressure in porous media. The capillary pressure can be related to the relative humidity by Eq.(3.12). Therefore, we obtain [132]:

$$\Pi(h) = \Pi_e(h) + \Pi_v(h) + \Pi_s(h) = -\frac{RT}{V_l}\ln(h_r) + \frac{2\gamma_{lg}}{R_s} \tag{3.27}$$

where V_l is the molar volume of the liquid water, R is the perfect gas constant. Uniform thickness of water film on the perfectly wetted solid surface is assumed (contact angle θ=0).

Here we investigate the evolution of the thickness of water film on flat solid surface ($R_s \to \infty$). Adopting the parameters listed in Table(3.1), the evolution of the thickness of water film with the relative humidity hr is depicted in Fig.(3.6).

As can be seen from Fig.(3.6), the results of the disjoining pressure model agree quite well with the experimental results at relative humidity hr lower than 99%. For $hr < 99\%$,

9. Here, the surface tension of water film-air interface is assumed to be equal to that of capillary water-air interface γ_{lg}.

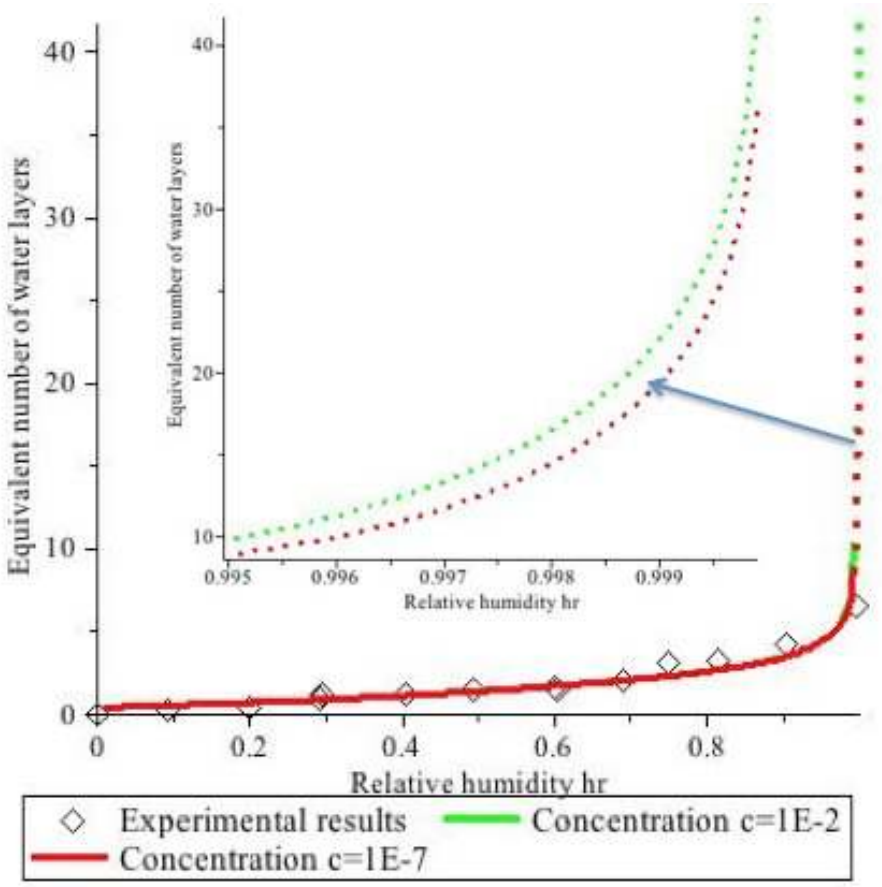

Figure 3.6: Relationship of the thickness of water film with relative humidity, temperature is 293K, experimental results are for pure water film-fused quartz system, after Sumner et al. [229], the thickness of mono water molecular layer is 2.8 Å [28].

the effect of the concentration of the solution is negligible for thin water film. This means that the electrostatic component is negligible for thin water film: the thickness of thin water film is mostly determined by the structural component. However, the influence of the concentration is notable at large thickness (as shown in the inset): the higher the concentration (green curve) the higher the thickness of the water film. This means that the electrostatic component as well as the Van der Waals component dominate the total disjoining pressure at high thickness.

3.5 Liquid water volume fractions at low saturation degree

The matrix potential is commonly used in soil mechanic and it is defined as the energy per unit volume required to extract water from a porous medium to overcome the capillary pressure and adsorptive forces (disjoining pressure) [254]. Therefore, it yields:

$$\psi = -P^{'}_{cap} - \Pi(h) \qquad \text{with } P^{'}_{cap} = P^{g} - P^{f} = -\frac{2\gamma_{lg}}{R_s} \tag{3.28}$$

where ψ is the matrix potential, $\Pi(h)$ is the disjoining pressure of water film, $P^{'}_{cap}$ is the capillary pressure of the water film-gas interface, P^{g} is the air pressure, P^{f} is the pressure of water film, R_s is the radius of the solid grain, γ_{lg} is the surface tension of gas-water film interface.

The water retention curve ($\psi(Sr)$) (saturation degree Sr dependence on the matrix potential ψ) [10] is the most common information used in the analysis of the transport properties and behaviors of unsaturated porous media [14]. Usually, due to the complex pore network, this relationship for a given porous medium can only be obtained experimentally [14]. Furthermore, owing to the extremely low fluxes and long equilibrium times associated with water film flow, the water retention curve ($\psi(Sr)$) at low saturation degree is difficult

10. It is also denoted as moisture characteristics.

to be obtained [238].

Therefore, to investigate the evolution of saturation degree Sr with matrix potential (ψ) at low saturation degree, explicit and simplified geometric models are established [14, 206, 238]. In these models, Bear's and Reinson's models just take account of the pendular rings while the effect of the water film is disregarded [14, 206]. Tokunaga [238] improved the model by taking the water film into account in the case of close packed mono disperse spheres. Our contribution focuses on the definition of the volume contribution of the pendular rings and water film with respect to matrix potential ($\psi(Sr)$) at low saturation degree in the case of cubic packing of mono disperse spheres with smooth surfaces.

At low saturation degree, the water phase within porous media is composed of water film adsorbed on the grains surface, as well as pendular rings (meniscus) trapped at the contacts of the grains (as depicted in Fig.(3.7) and discussed in Section(3.1.1)). For the sake of the simplicity, a simple geometric model in the work of Reinson et al. [206] is adopted here to calculate the volume of a pendular ring (as shown in inset of Fig.(3.7)), while the disjoining pressure model (expressed as Eq.(3.27)) is applied to estimate the thickness of the water film.

Four assumptions are adopted: (a) the solid surface is perfectly wetted by water, which means that the contact angle is $\theta_{ls} = 0$, (b) the meniscus of the pendular is hemispherical (c) the spherical grains are in contact while there is no overlap, (d) surface tension of liquid water is regarded as a constant parameter. The latter therefore disregards the modified nature of the water phase at the local level [125]. This may be a crude approximation at nanometer scale [14].

3.5.1 Volume contribution of pendular rings

To estimate the volume fraction of the pendular rings, a detailed geometric illustration of a pendular ring is depicted in inset of Fig.(3.7). The two curvature radii of the pendular rings are r_1 and r_2 respectively, β (in the unit of radian) is the angle between two straight lines, one is through the centres of the two spheres, the other is through one centre of sphere

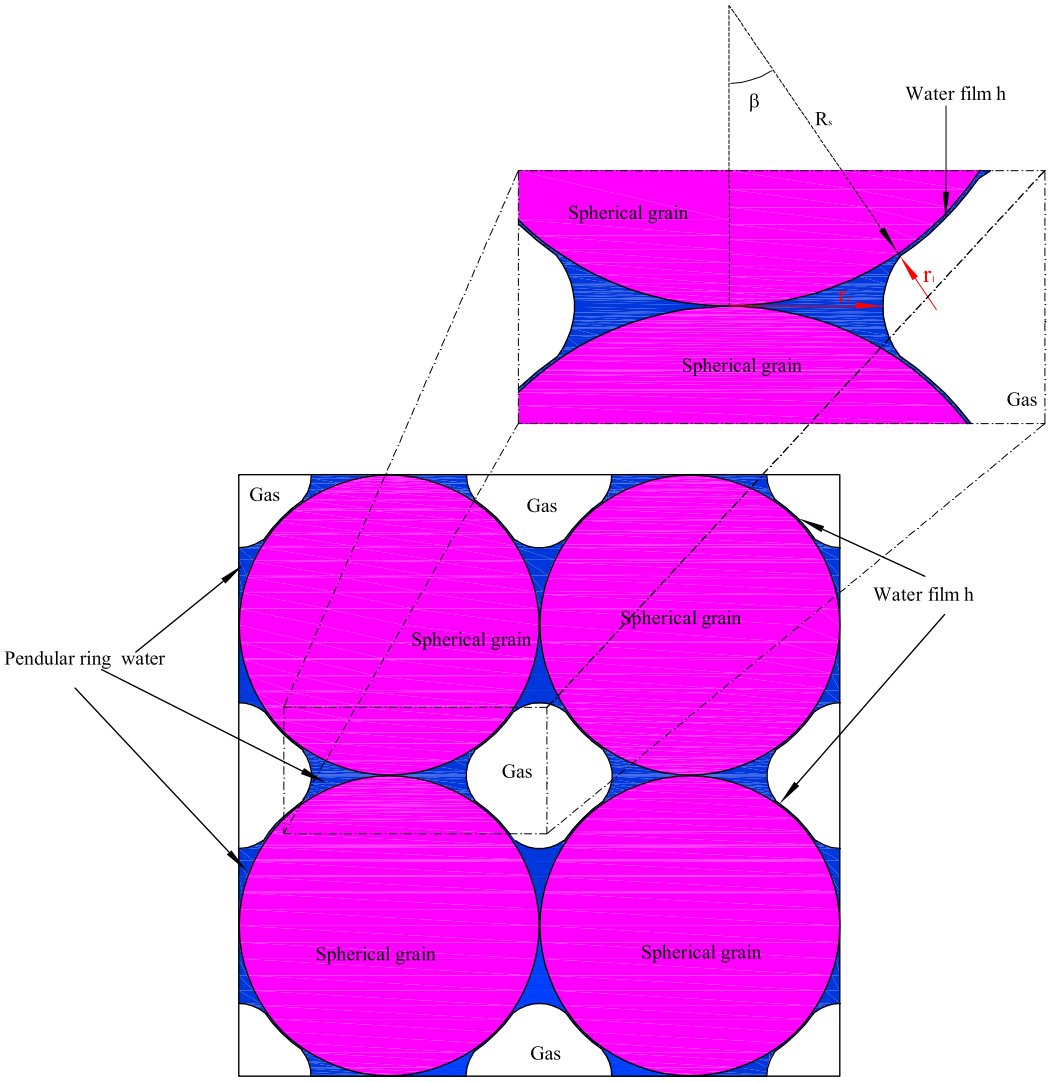

Figure 3.7: Schematic illustration of the water distribution within cubic packing granular material at low saturation degree, the surface of the grains is considered as smooth.

and the tangent point of pendular with the sphere. R_s is the radius of the spherical grain. This geometric configuration gives [206]:

$$\begin{cases} r_1 = R_s(\dfrac{1-\cos\beta}{\cos\beta}) \\ r_2 = R_s(\dfrac{\sin\beta+\cos\beta-1}{\cos\beta}) \end{cases} \tag{3.29}$$

The interface of the pendular ring can be characterized by the Young-Laplace equation [206]:

$$P_{cap} = \gamma_{lg}(\frac{1}{r_1} - \frac{1}{r_2}) \tag{3.30}$$

where γ_{lg} is the surface tension of the liquid water. Combing Eq.(3.29) and Eq.(3.30), we know that the matrix potential is related to the radius of the spherical grain and to the angle β.

Combining Eq.(3.13), Eq.(3.28) and Eq.(3.30) yields the relationship between matrix potential ψ and capillary pressure P_{cap}:

$$\psi = -P_{cap} = -\gamma_{lg}(\frac{1}{r_1} - \frac{1}{r_2}) \tag{3.31}$$

where $P_{cap} = P^g - P^l$ is the capillary pressure of liquid water-air interface (cf. P'_{cap} in Eq.(3.28)).

The volume of a pendular ring (V_p) may also be expressed as a function of R_s and β [120, 206, 213]:

$$V_p = 2\pi R_s^3[2 - 2\cos\beta - \tan\beta[2\sin\beta - \tan\beta + (\frac{\pi}{2} - \beta)(\frac{\cos\beta-1}{\cos\beta})^2]] \tag{3.32}$$

As can be readily observed in the cubic packing unit (shown in Fig.(3.7)), there are 3 pendular rings per cubic unit (V_u) [11], the volume of each cubic unit is $(2R_s)^3$. Therefore, the saturation degree contributed by pendular rings S_r^{pr} [12] can be determined by:

11. A sphere with radius R_s is circumscribed by the cubic unit, therefore, the cubic unit has length $2R_s$.
12. The saturation degree contributed by pendular rings S_r^{pr} is defined as the volume of total pendular

$$S_r^{pr} = \frac{3V_p}{V_u\varphi_c} = \frac{3\pi}{4\varphi_c}[2 - 2\cos\beta - \tan\beta[2\sin\beta - \tan\beta + (\frac{\pi}{2} - \beta)(\frac{\cos\beta - 1}{\cos\beta})^2]] \tag{3.33}$$

where φ_c is the porosity of the cubic packing which is calculated to be 0.476.

As shown in inset of Fig.(3.7), in the case of cubic packing, according to the geometric calculation, the neighbouring pendular rings will coalesce when $\beta = \frac{\pi}{4}$. At angle $\beta = \frac{\pi}{4}$ (during drainage), $Sr_c = S_r^{pr}(\beta = \frac{\pi}{4}) = 0.182$.

3.5.2 Volume contribution of the water film

The volume fraction of the water film within the monodisperse granular media in cubic packing can be estimated as:

$$\varphi_{wf} = \frac{V_{wf}}{V_s} \times (1 - \varphi_c) = \frac{(R_s + h)^3 - R_s^3}{R_s^3}(1 - \varphi_c) = [(1 + \frac{h}{R_s})^3 - 1](1 - \varphi_c) \tag{3.34}$$

where V_s is the volume of the single spherical solid grain.

As long as the thickness of the water film, which can be estimated by Eq.(3.26) and Eq.(3.27), satisfies the condition $h \ll R_s$, Eq.(3.34) may be approximated as :

$$\varphi_{wf} \approx \frac{3h}{R_s}(1 - \varphi_c) \tag{3.35}$$

3.5.3 Liquid water retention

At low saturation degree, the saturation degree which accounts for the contribution of water film and pendular rings can be expressed as:

$$Sr = S_r^{pr} + \frac{\varphi_{wf}}{\varphi_c} \tag{3.36}$$

rings within porous media over volume of pore space in porous media.

Combining Eq.(3.29)-Eq.(3.33) as well as Eq.(3.26)-Eq.(3.27), Eq.(3.35) and Eq.(3.36), the saturation degree can be related with matrix potential ψ.

$$\begin{cases} Sr = \dfrac{3\pi}{4\phi_c}[2 - 2\cos\beta - \tan\beta[2\sin\beta - \tan\beta + (\dfrac{\pi}{2} - \beta)(\dfrac{\cos\beta - 1}{\cos\beta})^2]] + \dfrac{3h(1-\phi_c)}{R_s\phi_c} \\ \psi = -P_{cap} = -\dfrac{\gamma_{lg}}{R_s}(\dfrac{\cos\beta}{1-\cos\beta} - \dfrac{\cos\beta}{\cos\beta + \sin\beta - 1}) \\ -\psi + \dfrac{2\gamma_{lg}}{R_s} = 64nkT\gamma_1\gamma_2\exp(-\kappa h) - \dfrac{A}{6\pi h^3} + K_{sr}\exp(-\dfrac{h}{\lambda_{sr}}) + K_{lr}\exp(-\dfrac{h}{\lambda_{lr}}) \end{cases} \tag{3.37}$$

Thus, during drainage of monodisperse granular material in cubic packing, the contributions of pendular rings and water film to the saturation degree can be plotted as in Fig.(3.8).

According to the Fig.(3.8), the low saturation degree starts at $Sr_c = 0.182$. The solid lines refer to the contribution of the pendular rings at different grain radii, while the dotted lines denote the contribution of the pendular rings and the water film. These results suggest two propositions: (1) the volumetric contribution of the water film shows notable size dependence on the grain size, that is, the volume fraction of water film becomes more and more dominant (as compared to the pendular rings) with decreasing grain radius; (2) In addition to size effect of grain, the volumetric contribution of the water film increases with the decrease of matrix potential (more negative). This is consistent with the difference between the characteristic sizes associated with the water film and the pendular rings, respectively.

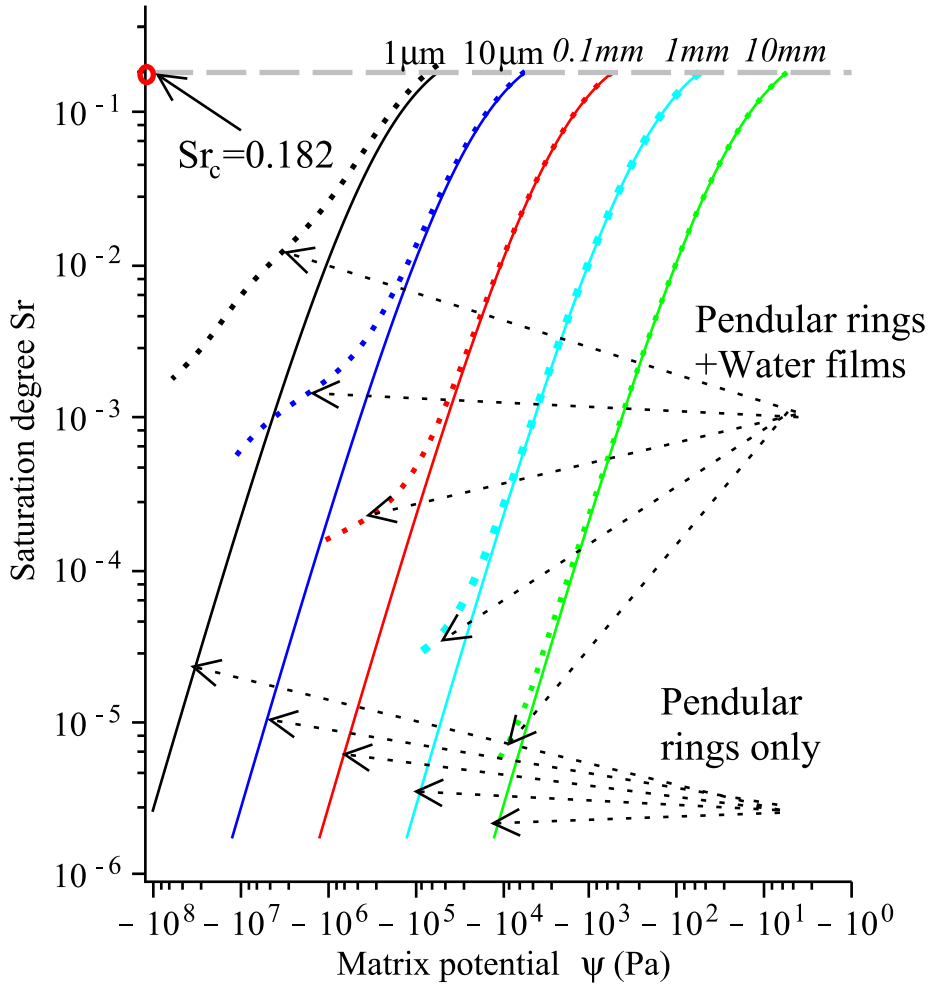

Figure 3.8: Plot of evolution of the contributions of water film and pendular rings to saturation degree Sr with variation of matrix potential ψ and R_s (10 mm, 1 mm, 0.1 mm, 10 μm, 1 μm), according to Eq.(3.37).

3.6 Local solute diffusion in water film

According to the very local confinement of the water film, it seems appropriate to derive a more specific analysis of the definition of the local solute diffusion in the water film adjacent to the solid surface. This will help us to better introduce this local transport law that is increasingly important during desaturation process.

3.6.1 Pore size dependence of the diffusion coefficient

Depending upon the characteristic size of the pore, denoted by r^p, the diffusion coefficient may be defined as [212]:

— For mesopores (i.e., pores of diameter $r^p \geq$50 nm):

The collisions between the molecules (ions) occur much more frequently than collisions with pore wall [212]. The molecule (ionic) diffusion is the dominant mechanism in mesopores. Consequently, the diffusion coefficient may be taken as that of the bulk liquid water. Theoretically, the corresponding diffusion coefficient of the molecules (ions) D^{mo} may be determined by the classic Stokes-Einstein equation [9, 153]:

$$D^{mo} = b^{\gamma} k_B T = \frac{k_B T}{6\pi\mu R^{pa}} \tag{3.38}$$

where $b^{\gamma} = \dfrac{1}{6\pi\mu R^{pa}}$ is the mobility of solute γ in the solvent [13] [9], k_B is Boltzmann constant, T is temperature, μ is the viscosity of the bulk liquid phase, R^{pa} is the radius of the solute particle. It should be noted that Stokes-Einstein equation is only valid with this assumption: the radius of solute should be larger than that of solvent in bulk system [9].

— For micropores (i.e., pores of diameter 2 nm$\leq r^p <$50 nm):

With the decrease of pore size, the collisions with the pore wall increase in microp-

13. As ions move through the solvent at a drift speed u_i, they experience a fractional retarding force F_{fric}. The mobility of solute b^{γ} is defined as the ratio of its drift speed u_i to its corresponding fractional retarding force F_{fric}, that is $b^{\gamma} = \dfrac{u_i}{F_{fric}}$ [9].

ores, therefore, Knudsen diffusion is the dominant diffusion in micropores [212]. The mobility b^{γ} in Eq.(3.38) starts to depend on the dimensions of pore.

— For nanopores (i.e., pores of diameter r^{p} <2 nm):

The characteristic size of the molecule (ion) turns out to be similar to that of micropore. Therefore, the molecule (ion) will experience interaction with the pore surface [207].

As can be seen from the diffusion in mesopores and micropores described above, the diffusion in mesopores and micropores is influenced by the viscosity of solvent, pore size and ionic adsorption and interaction with the charged pore surface.

In our purpose, the Stokes-Einstein equation is assumed to be valid whatever the scale of concern. The pore size effect is accounted for through the increase of the liquid water viscosity with decreasing pore size.

3.6.2 The effect of viscosity of water film

It has been widely stated that the viscosity of water film is greater than that of bulk water owing to its modified structure [76]. As proposed by Or et al. [181], the influence of viscosity on the fluid flow become indistinguishable for water film greater than about 10 nm. For thinner water film (<10 nm), the experimental results are summarized as follows (the detailed discussion of viscosity is given in Appendix(A.1)).

Li et al. [108] measured the viscosity of the interlayer between the hydrophilic surfaces (such as mica and glass) by means of high-resolution atomic force microscope (AFM). These authors found an increase of the viscosity of several orders of magnitude compared to the viscosity of the bulk liquid (e.g. 4 orders of magnitude higher than that of bulk water when the thickness of water film is about 0.5 nm) [108]; this result was later confirmed by Antognozzi et al. [5].

Using surface force apparatus (SFA), numerous investigators [124, 131, 143, 204, 205] have measured the viscosity of interlayers of liquid water confined between mica or silica. These authors found that the viscosity of interlayers are close to (within a factor of 3 in the

thickness range 3.5 ± 1.0 to 0.0 ± 0.4 nm) that of the bulk water [124, 131, 143, 204, 205]. The authors attributed this phenomenon (negligible increase of viscosity of interlayer water) to the abnormal solidification mechanism of water [14]. In addition, they concluded that the influence of the solute concentration on the viscosity of the confined water film is negligible [143, 205].

Considering these two rather distinct conclusions about the viscosity of the interlayers, owing to their similar experimental principle [15], the disparity may lie in the different experimental device and experimental samples (e.g., mica solid surfaces) [142]. Here, the viscosity of interlayer is taken equal to that of bulk water. In this case, the decrease of solute diffusion in water film may arise from the ionic interaction with pore wall [118].

It should be noted that the categorization of diffusivities and most of the experiments on viscosity of interlayers are carried out on interlayers confined between two negatively charged pore surface [131, 143, 204, 205]. However, pore surface-water film-gas system is asymmetrical with two distinct interfaces: pore surface-water film and gas-water film interfaces. For the pore surface-water film-gas system, not only the pore surface-water film interface but also water film-gas interface are negatively charged [132]. Moreover, similar to the interlayer, the structure of water film is modified also. Therefore, the viscosity and diffusivity of the interlayer confined between two negatively charged surface can be reasonably assumed to be similar to those of water film.

3.6.3 Local solute diffusion coefficient in the water film

As proposed by Grathwohl et al. [118], a significant solute hindrance effect in water film is expected when the thickness of water film is lower than 10 nm. This conclusion is confirmed by many experimental studies [26, 107, 127]. As introduced in Section(3.6.1),

14. In [205]. For confined interlayer water, the confinement seems primarily to suppress the formation of the highly directional hydrogen-bonded networks associated with freezing, which inhibits solidification [205].

15. $F = \eta(h)\frac{\partial v_x}{\partial y}A$ (where F is the shear force applied on the interlayer, $\eta(h)$ is the dynamic viscosity, v_x is the velocity along the direction of shear force, y is distance normal to the along the thickness of interlayer.

the reason for the reduced diffusivity within micropore may lie in the increased viscosity of water film, the ionic adsorption and interaction with the charged solid surface. Generally, a scaling constrictive factor δ for solute γ is introduced to characterize the reduced solute diffusivity within water film with respect to D^γ [26]:

$$D_f^\gamma = \delta D^\gamma \qquad \text{with} \quad \delta \leq 1 \tag{3.39}$$

where D_f^γ, D^γ are the diffusion coefficients of solute γ in water film and bulk water, respectively. To determine the constrictive factor δ, detailed knowledge about the thickness of water film (the dependence of the viscosity on thickness of water film), ionic interaction, mineralogy and surface properties of the material is required. In a special case carried out by Van Schaik et al. [248], it has been found that, for the first three layers of water film adjacent to the solid surface, the average constrictive factor of Na^+-water film-montmorillonite system $\delta_{Na} = 0.32 \pm 0.06$ [16].

3.7 Summary

In this section, the evolution of water distribution within granular material and sandstone are summarized and discussed.

— In unsaturated granular materials, the liquid water phase can be categorized as: intergranular layer, pore body water, wetting layer (trapped at interconnected pendular rings and surface roughness) and water film. Intergranular layer, wetting layer and water film are considered as surrounding the solid grain.

— In unsaturated sandstone, the liquid water phase can be categorized as: intergranular layer, wetting layer and water film. Intergranular layer, wetting layer and water film are consider as surrounding the solid grain.

The liquid-gas interface is specified in the unsaturated transport problems, the Kelvin equation is employed to characterized the equilibrium radius of the liquid-gas interface,

16. In this case, the concentrations of the NaCl solution varies from 0.0038 to 0.15 mol.L^{-3}.

that is:

$$\ln hr = -\frac{2\gamma_{lg}\cos\theta\overline{V}_l}{(r_2 - h)RT} \tag{3.11}$$

More over, the validity of the Kelvin equation at local scale is also discussed.

A disjoining pressure model is proposed to estimate the thickness of water film according to [132]:

$$\Pi(h) = \Pi_e(h) + \Pi_v(h) + \Pi_s(h) = -\frac{RT}{V_l}\ln(h_r) + \frac{2\gamma_{lg}}{R_s} \tag{3.27}$$

where each component of disjoining pressure $\Pi_e(h)$, $\Pi_v(h)$ and $\Pi_s(h)$ may be determined from physical arguments by Eq.(3.24).

A simple cubic packing (mono disperse) sphere assemblage is adopted to quantitatively compare the volume fractions of water film and pendular rings. It is found that the volumetric contribution of water film increases with decreasing matrix potential (more negative) as well as with decreasing grain size.

The solute diffusion coefficient in water film is lower than that in bulk water, an phenomenological expression for the solute diffusion coefficient (Eq.(3.39)) in water film is adopted in the sequel as [26]:

$$D_f^\gamma = \delta D^\gamma \qquad \text{with} \quad \delta \leq 1 \tag{3.39}$$

Chapter 4

Micromechanical modelling of solute diffusion within unsaturated porous media

Contents

4.1 Introduction **68**

4.2 Empirical models for solute diffusion in unsaturated porous media **70**

4.2.1 Experimental results for several unsaturated porous media 70

4.2.2 Empirical models 72

4.3 Micromechanical modelling of solute diffusion in saturated porous media **74**

4.4 A first approach for solute diffusion in unsaturated porous media **78**

4.4.1 A one-scale microstructure 79

4.4.2 A two-scale microstructure 81

4.5 Enriched models for solute diffusion in unsaturated porous media **91**

4.5.1 2-D idealization of local diffusion 95
4.5.1.1 Local diffusion at solid-pore space interface 95
4.5.1.2 Derivation of unsaturated solute diffusion coefficient . . 97
4.5.2 3-D models for solute diffusion within unsaturated porous media 105
4.5.2.1 Mori-Tanaka estimate 105
4.5.2.2 Self-consistent estimate (accounting for percolation effect) 109
4.6 Experimental results analysis 114
4.6.1 Homogenized diffusion coefficient of unsaturated granular materials 115
4.6.2 Results and discussion 118
4.7 Summary 119

4.1 Introduction

Transport phenomena in porous media are very important in agriculture production, contaminant transport, remediation, risk assessment and waste disposal [52, 53, 61, 127, 211, 215, 253]. Within this context, diffusion and advection are the most common and critical transport components. Both of them have been widely studied in fully saturated conditions.

Generally, the Fick's law is employed to characterize the solute diffusion in free water (bulk water). It has also been proposed by many studies that Fick's law is also operative in porous media [159, 171, 200], it may be expressed as:

$$\underline{J}^{\gamma} = -D^{hom} \cdot \underline{H} \tag{4.1}$$

where $\underline{J}^{\gamma}$ is the solute diffusive flux in porous media, D^{hom} is the macroscopic solute diffusion coefficient in porous media, $\underline{H}$ the macroscopic solute concentration gradient.

The solute diffusive flux $\underline{J}^{\gamma}$ in porous media is smaller that that in free water. The reason lies in the fact that, the open area available for diffusion is reduced and the diffusion pathway is more tortuous in porous media [159].

Eq.(4.1) is a phenomenological expression for the Fick's law in porous media at the macro scale. Following this law, empirical expressions for D^{hom} have been proposed based on experiment. In Section (4.3), the validity of this Fick's law at macro scale will be demonstrated with micromechanics methodology.

Indeed, micromechanics models have also been proposed in these conditions, but little has been done concerning the unsaturated case. This is the purpose of this chapter, to develop a micromechanics analysis of solute diffusion in unsaturated porous media[1]. To begin with, after a short review of the experimental results and classic empirical models in Section(4.2), micromechanics arguments are then recalled in the context of fully saturated porous media in Section(4.3). More general unsaturated models characterizing the microstructure effects on the solute diffusion are developed in Section(4.4). Based on the local physical characterization of the water distribution within unsaturated porous media, enriched models accounting for the liquid layer are developed in Section(4.5). Some experimental analysis of solute diffusion in unsaturated sand and glass beads are carried out and presented in Section(4.6) .

Herein, for clarification, the subscripts or superscripts for each phase are listed as: $\boldsymbol{g}$ is referred to as gaseous phase; $\boldsymbol{s}$ denotes the solid grains; $\boldsymbol{f}$ denotes the water film phase; $\boldsymbol{wl}$ denotes the wetting layer; $\boldsymbol{ig}$ denotes the intergranular layer; $\boldsymbol{pw}$ denotes the pore body water; γ denotes the solute (chemical species); $\boldsymbol{hom}$ is referred to as the macroscopic homogenized properties or behaviors of porous media.

1. Micromechanics analysis of flow permeability will be presented in chapter 6.

4.2 Empirical models for solute diffusion in unsaturated porous media

4.2.1 Experimental results for several unsaturated porous media

Let us first present several experimental results for diffusion coefficients of solute in unsaturated porous media. Material characteristics and the solute tracers are presented in Table.(4.1).

As expected, it is observed in Fig.(4.1) that the effective diffusion coefficient D^{hom} decreases with decreasing value of the water saturation degree Sr. This quantifies the reducing pathways for diffusion along the desaturation process. For materials such as sandstones, effective diffusion coefficients at high water saturation degree decrease gently with saturation degree. However, their effective diffusion coefficients at lower water saturation degree decrease rapidly with saturation degree (black curve in Fig.(4.1)). On the contrary, for cohesive materials such as lime mortar and brick, the effective diffusion coefficients at high water saturation degree decrease rapidly with saturation degree, while the effective diffusion coefficients at low saturation degree decreases gently (cyan curve in Fig.(4.1)).

As suggested by Archie [6], the effective diffusion coefficient within unsaturated porous media can be described by an empirical power law function of the saturation degree and the porosity. The evolution of the effective diffusion coefficients is displayed in Fig.(4.1) for two types of materials [33].

— For sandstones, the exponents of the power laws (denoted as "b" in Fig.(4.1)) are lower than one, that is $0 < b < 1$.

— For lime mortar and brick, the exponents (denoted as "a" in Fig.(4.1)) are higher than one, that is $a > 1$.

The distinct tendencies of the unsaturated diffusion coefficient are attributed to the different morphologies of the materials of concern, which will be discussed in the following section.

Table 4.1: Summary of material characteristics and used solutes [33, 159].

Material	Porosity(%)	Medium pore diameter (μm)	Saturated effective diffusivity (10^{-10}m^2.s^{-1})	Tracer
Sand	38.2	-	5.35	KCl
Sandstone1	18	0.5	3.1	Na_2SO_4
Sandstone2	23	50	2.3	Na_2SO_4
Brick	36	2	2.1	Na_2SO_4
Lime mortar	32	2&200 [1]	4.8	Na_2SO_4

[1] The lime mortar presents dual-porosity: capillary pores and big air voids.

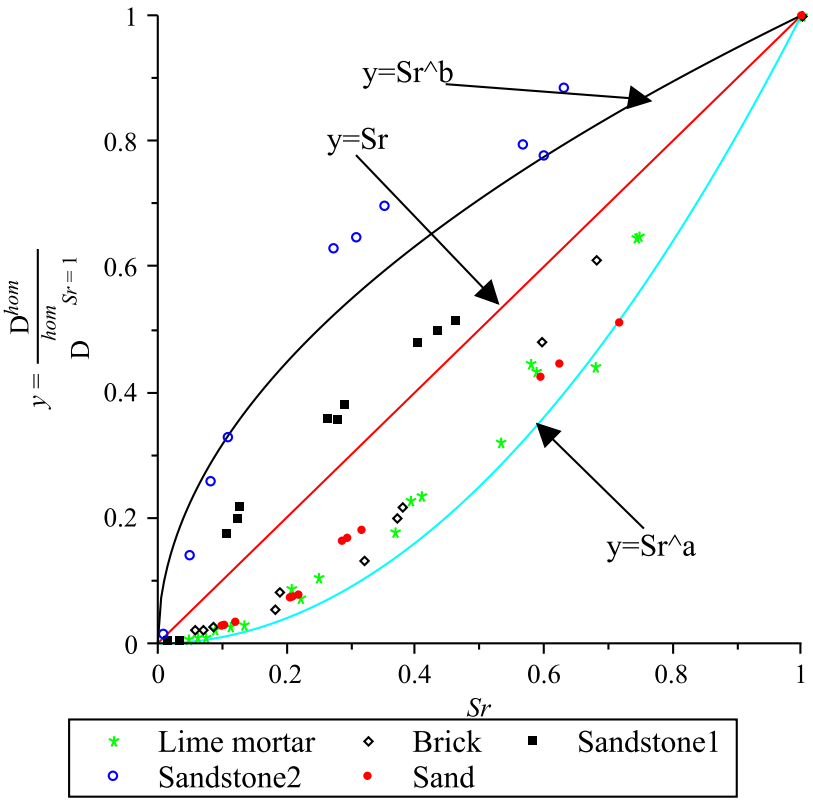

Figure 4.1: Evolutions of the normalized diffusion with saturation degree for several porous materials, $D^{hom}_{Sr=1}$ is the effective diffusion coefficient in saturated porous media, while D^{hom} is the diffusion coefficient in unsaturated case, Sr is the saturation degree, a and b are the exponent cofficients, experimental results are after [6, 33, 159].

4.2.2 Empirical models

Owing to the time-consuming and high cost of the experiments, empirical models are often used to predict the solute diffusion coefficients of unsaturated porous media. Similar to Archie's law [6], these models relate the unsaturated diffusion coefficient to the water content and total porosity [127]. There are numerous models for diffusion in various unsaturated porous media such as glass beads [144, 211], soil [13, 200, 214, 253], sand [159, 211], sandstone [33], gravel [52, 53, 126], brick [33], and cementitious materials [70, 119, 216]. Some of these models are listed in Table.(4.2).

Different theoretical perspectives have been proposed to explain Archie's law, but no universal definition of the Archie's law's exponents has been proposed so far [127].

In spite of their simplicity, all of the empirical models presented above introduce the fitting parameters that are lack of physical definition. In order to overcome this limitation inherent to the phenomenological approach, the present work builds up a micromechanics methodology incorporating local physics and microstructure morphology in view of a better understanding of the evolution of the solute diffusion in unsaturated porous media.

By using the micromechanics methodology, we expect to derive physical-based estimates, which are intrinsically able to reproduce different evolution according tot the local physical definition of diffusion laws and the specific morphology of the microstructure.

Table 4.2: Several empirical unsaturated diffusion models

Models	Materials (& species)	Reference
[1] $\frac{D^{hom}}{D^{\gamma}} = \frac{\theta_l^{10/3}}{\phi^2}$	Soils	[139]
$\frac{D^{hom}}{D^{\gamma}} = k\theta_l^3$	Soil (nutrient)	[189]
[2] $\frac{D_e}{D^{\gamma}} = 0.73(\frac{\theta_l}{\phi})^{1.98}$	7 soils with 10-51% clay (urea)	[215]
[3] $\frac{D^{hom}}{D^{\gamma}} = \phi^m S_r^n$	Sand and sandstone (NaCl)	[6]
$\frac{D_e}{D^{\gamma}} = \theta_l^{1.849}$	tuff cores, basalt, mudstone, 86 soil samples and gravel (KCl)	[61]
[4] $\frac{D_e}{D^{\gamma}} = \alpha\theta_l^n$	Sand and loam soil (Salt)	[171]
$\frac{D^{hom}}{D^{\gamma}} = \frac{0.45\theta_l(\theta_l - 0.022b)}{\phi - 0.022b}$, $\theta_l \geq 0.022b$		-
[5] $\frac{D^{hom}}{D^{\gamma}} = 0$, $\theta_l < 0.022b$.	6 soils with 11-46% clay (Cl^-, NH_4^+)	[180]
$\frac{D^{hom}}{D^{\gamma}} = 0.45\theta_l(\frac{\theta_l}{\phi})^{0.3b}$	6 soils with 11-46% clay (Cl^-, NH_4^+)	[180]

[1] $D^{hom} = \tau\delta\theta_l D^{\gamma}$ is effective diffusion coefficient, D^{γ} is the diffusion coefficient of solute in bulk water, ϕ is porosity, τ is tortuosity factor, δ is constrictive factor, this model is modified from Millington-Quirk's model [127].

[2] $D_e = D^{hom}/\theta_l = \tau\delta_l D^{\gamma}$, S_r is the water saturation degree. Constants are obtained from nonlinear regression [127].

[3] This is Archie's model, where m is cementation factor, n is saturation exponent; for unconsolidated sand m=1.3, n=2; for consolidated sandstone m ranges from 1.8 to 2.0 [6].

[4] The values of α and n are different for two stages: high and residual saturation degree.

[5] b is the slope of Campbell's soil-water characteristic curve in log-log plot [37].

4.3 Micromechanical modelling of solute diffusion in saturated porous media

Micromechanical modelling of solute diffusion in saturated porous media has already been addressed in detail and discussed in Dormieux et al. [82] and Lemarchand [153]. It should be noted that, in the following sections, we are only interested in the properties of solute diffusion in the liquid water phase, the vapor diffusion is always not considered in unsaturated porous media. Herein, the governing equations for solute diffusion in saturated cases are presented. A similar treatment will be developed in the unsaturated case.

The mass balance equation for the solute flux at micro scale is [153]:

$$\frac{\partial \rho^\gamma}{\partial t} + \mathrm{div}(\rho^\gamma \underline{V^\gamma}) = 0 \Leftrightarrow \frac{\partial \rho^\gamma}{\partial t} + \mathrm{div}[\rho^\gamma(\underline{V^\gamma} - \underline{V})] + \mathrm{div}(\rho^\gamma \underline{V}) = 0 \tag{4.2}$$

where ρ^γ is the concentration of γ solute, $\underline{V^\gamma}$ is the solute velocity, $\underline{V}$ is the velocity of the fluid phase, t is time.

To characterize the diffusion of chemical species at local scale (in the liquid water phase), linear Fick's law is assumed. The latter linearly relates the mass flux of chemical species $\underline{j^\gamma}$ to its concentration gradient $\underline{\mathrm{grad}}_z \rho^\gamma$ by [153]:

$$\underline{j^\gamma} = \rho^\gamma(\underline{V^\gamma} - \underline{V}) = -D^\gamma \underline{\mathrm{grad}}_z \rho^\gamma \tag{4.3}$$

The following assumptions are also introduced [82]:

(1) the solute diffusion is analyzed in steady state condition ($\frac{\partial \rho^\gamma}{\partial t} = 0$).

(2) no mass exchange (precipitation and dissolution) of the chemical species γ at the solid-fluid interface ($\underline{\mathrm{grad}}_z \rho^\gamma \cdot \underline{n} = 0$), where $\underline{n}$ is the unit vector normal to solid-liquid interface.

Diffusion takes place in the fluid domain. But in order to manage a local heterogeneous definition of the diffusion laws, the diffusion problem is extended from the fluid domain to the whole domain of porous media (including solid domains) by introducing a diffusion

coefficient in the solid phase satisfying $D^s \to 0$ [82]:

$$D(\underline{z}) = \begin{cases} D^s \to 0 & \forall \underline{z} \in \Omega^s \\ D^\gamma & \forall \underline{z} \in \Omega^l \end{cases} \tag{4.4}$$

where Ω^s and Ω^l are the solid and fluid domains within REV, $\Omega = \Omega^s \cup \Omega^l$.

An uniform concentration gradient $\underline{H}$ boundary condition are considered on the REV (domain Ω), which means: $\rho^\gamma(\underline{z}) = \underline{H}.\underline{z}$ when $\underline{z} \in \partial\Omega$. Consequently, the local heterogeneous diffusion problem to be solved is defined by the following equations [2] [82]:

$$\begin{cases} \mathrm{div}_z \underline{j}^\gamma = 0 & \forall \underline{z} \in \Omega \\ \underline{j}^\gamma(\underline{z}) = -D(\underline{z}) \underline{\mathrm{grad}}_z \rho^\gamma & \forall \underline{z} \in \Omega \\ \rho^\gamma(\underline{z}) = \underline{H} \cdot \underline{z} & \forall \underline{z} \in \partial\Omega \end{cases} \tag{4.5}$$

Eq.(4.5) can be treated as Eshelby based problem for diffusion, which is introduced in Appendix (B). Its solution is a linear function of the macroscopic concentration gradient $\underline{H}$. The concept of second order concentration tensor $\boldsymbol{A}(\underline{z})$ is introduced in order to express the heterogeneous solution of Eq.(4.5) as:

$$\underline{\mathrm{grad}}_z \rho^\gamma = \boldsymbol{A}(\underline{z}) \cdot \underline{H} \tag{4.6}$$

where the concentration tensor is a function of the geometrical microstructure. From the uniform boundary condition (that is third formula in Eq.(4.5)), by means of the definition of the average quantity in Eq.(1.2), we have [82]:

$$\overline{\underline{\mathrm{grad}}_z \rho^\gamma} = \underline{H} \Leftrightarrow \overline{\boldsymbol{A}} = \mathbf{1} \tag{4.7}$$

With the upscaling rule defined in Eq.(1.2), the macroscopic mass flux can be determined as $\underline{J}^\gamma = \overline{\underline{j}^\gamma(\underline{z})}$ [82]. The mass flux at local scale (Eq.(4.3)) combined with Eq.(4.6) yields a

2. In the following context, the velocity of the fluid phase $\underline{V}$ is not considered (see Eq.(4.3)).

macroscopic Fick's law [82]:

$$\underline{J}^{\gamma} = \overline{\underline{j}^{\gamma}(\underline{z})} = -\boldsymbol{D}^{hom}.\underline{H} \quad \text{with:} \quad \boldsymbol{D}^{hom} = \overline{D\boldsymbol{A}} \tag{4.8}$$

As mentioned in Section(4.1), the validity of the Fick's law for macroscopic porous media (Eq.(4.1)) is thus demonstrated by means of micromechanics methodology. For a two-phase porous medium made up of solid ($D^s \to 0$) and liquid, Eq.(4.8) yields the following result [82]:

$$\boldsymbol{D}^{hom} = \overline{D\boldsymbol{A}} = \phi D^{\gamma}\overline{\boldsymbol{A}}_l = D^{\gamma}(\mathbf{1} - (1-\phi)\overline{\boldsymbol{A}}_s) \tag{4.9}$$

where Eq.(4.7) has been used, ϕ is the pore volume fraction.

If the average concentration tensors of each phase $\overline{\boldsymbol{A}}_i$ ($i \in \{s, l\}$) are known, $\boldsymbol{D}^{hom}$ may be exactly characterized. Since the exact determination of the microstructure ($\overline{\boldsymbol{A}}_i$) is a complicated task, we rather resort to estimates. Several schemes may be used to estimate the concentration tensors. With the assumptions of isotropic microstructure as well as the spherical shape for the inclusion phases, the homogenized solute diffusion coefficient within saturated porous media can be estimated by these schemes, they are listed in Table(4.3):

Table 4.3: Homogenized solute diffusion coefficient within saturated porous media with different schemes

-	D^{hom}	**Reference**
Dilute Scheme	$(1 - \frac{3}{2}(1-\phi))D^{\gamma}$ [1] $(1-\phi \ll 1)$	Lemarchand [153]
Differential Scheme	$\phi^{3/2}D^{\gamma}$	Lemarchand [153]
Mori-Tanaka Scheme	$\frac{2\phi}{3-\phi}D^{\gamma}$	Dormieux et al. [82]
Self-Consistent Scheme	$\frac{3\phi-1}{2}D^{\gamma}$ $(\phi \geq 1/3)$	Dormieux et al. [82]

[1] ϕ is the pore volume fraction, D^{γ} is the diffusion coefficient of solute γ in liquid water phase.

Some important remarks on the different schemes (saturated case)

Whatever the solid volume fraction, liquid interconnectivity is ensured in the Differential

Scheme, the Dilute Scheme and the Mori-Tanaka Scheme:

— The dilute scheme assumes weak interaction between the solid grains. It is only valid for infinitesimal volume fraction of solid phase [82], which does not correspond to usual porous media definiton. In this case, the local concentration (ρ^γ) and the corresponding $\overline{\boldsymbol{A}_s}$ can be approximated by their values in the problem of a single spherical solid grain embedded in infinite homogeneous matrix made up of the liquid water phase (Eshelby's problem).

— The Mori-Tanaka scheme accounts for an improved interaction between the solid inclusions. Mori-Tanaka scheme is expected to be a good candidate for estimates of the homogenized diffusion coefficient when pore volume fraction is higher than 0.7.

— Differential scheme has also been developed to overcome the limitation of the dilute scheme. The idea consists of starting to a homogeneous medium identical to the fluid matrix, and introducing the solid phase by infinitesimal volume fraction in the framework of an interactive process. Detailed information is given in Dormieux et al. [82]. As presented in Fig.(4.2), differential scheme accounts for a stronger tortuosity effects for decreasing value of the porosity than Mori-Tanaka scheme. Tortuosity τ is defined as $\tau = \overline{A_l} = \dfrac{D^{hom}}{\phi D^\gamma}$ (in isotropic case). By contrast to Mori-Tanaka scheme, the differential scheme is able to correlate the decrease of the porosity and the decrease of the tortuosity coefficient. This seems consistent with the physical intuition that tortuosity effect is stronger ($\tau \to 0$) for porous material with low porosity.

By contrast, the self-consistent scheme is the sole micromechanics model able to discuss percolation effects likely to occur during the desaturation/resaturation processes of porous media. Self-consistent scheme consists in assuming that each particle of a given phase (pore or solid) reacts as if it were embedded in the equivalent homogeneous medium which is looked for [82]. For an heterogeneous medium with disordered phase arrangement, a self-consistent estimate is considered to be well adapted to represent the effective properties of the overall medium.

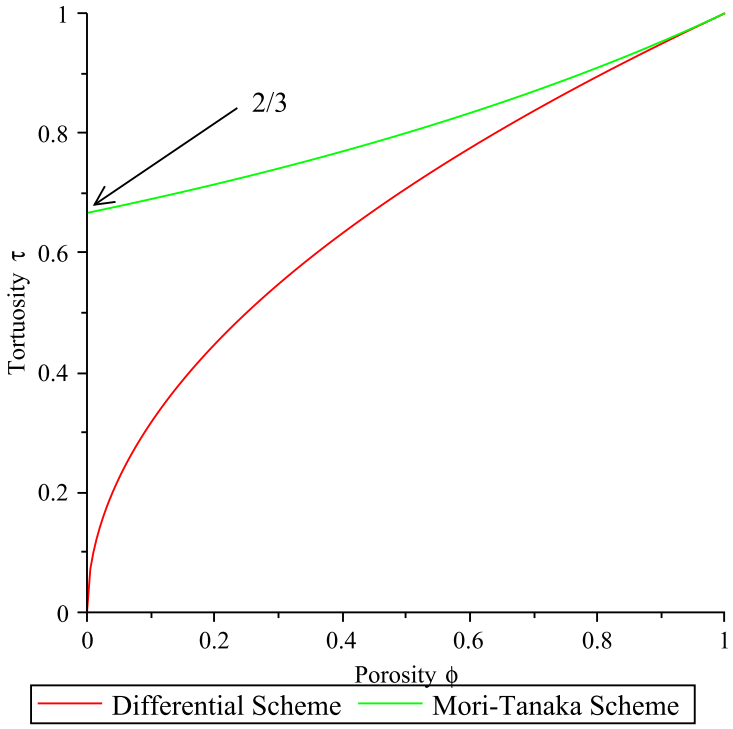

Figure 4.2: The dependence of the tortuosity τ on the porosity ϕ.

4.4 A first approach for solute diffusion in unsaturated porous media

In the previous section, the whole connected pore space of a porous medium was assumed to be fully saturated by liquid water. In this case, it has been proved that at the macroscopic scale the diffusion coefficient is affected by both the porosity and the tortuosity [3]. These two may be interpreted as pore space morphological effects at the macro scale (porosity) and at the micro scale (tortuosity $\tau = \overline{A}_l$).

The liquid phase distribution within the pore space of porous media is of great importance when dealing with the unsaturated case, and this question will be addressed in detail in next section. However, to begin with, let us consider a simplified micromechanics treatment of diffusion in unsaturated porous media based only on volume fraction of liquid information.

3. Some estimates of the tortuosity have been proposed as functions of the porosity.

4.4.1 A one-scale microstructure

When volume fraction of liquid is the only available information in a one scale homogenization procedure, the solute diffusion within unsaturated porous media is analogical to the saturated case processed by Dormieux et al. [82]. The difference lies in the existence of another phase: the gaseous phase. In solute diffusive transport problems, the gaseous phase may be interpreted as a non-diffusive phase, the diffusion coefficients of which being 0. As a consequence, this gaseous phase behaves like the solid phase when diffusion is of concern.

Hence, in an unsaturated porous medium REV, there exist three phases: the gaseous phase, the solid phase and the liquid water phase where diffusion processes occur.

To deal with this situation, one may recourse to the saturated results (Table(4.3)) by replacing the volume fraction of pores ϕ (in saturated case) by the volume fraction of liquid $\phi_l = \phi Sr$ (in the unsaturated case).

From Table(4.3), the isotropic homogenized diffusion coefficient can then be expressed as:

$$D^{hom} = \begin{cases} (1 - \dfrac{3}{2}(1 - \phi Sr))D^{\gamma}; \ \ (1 - \phi \ll 1) & \text{For Dilute scheme} \\ (\phi Sr)^{3/2} D^{\gamma} & \text{For Differential scheme} \\ \dfrac{2\phi Sr}{3 - \phi Sr} D^{\gamma} & \text{For Mori-Tanaka scheme} \\ \dfrac{3\phi Sr - 1}{2} D^{\gamma}; \quad \phi Sr \geq \dfrac{1}{3} & \text{For self-consistent scheme} \end{cases} \tag{4.10}$$

The normalized homogenized diffusion coefficient is displayed as a function of the saturation degree in Fig.(4.3) for these four micromechanics-based models.

As expected, the interconnectivity of the transport pathway is ensured at the whole saturation degree (Sr ranges from 1 to 0) within differential scheme (DF blue curves) and Mori-Tanaka scheme (MT cyan curves) procedures. The reason lies in the fact that the liquid water phase is treated as a continuous phase whatever the saturation degree when

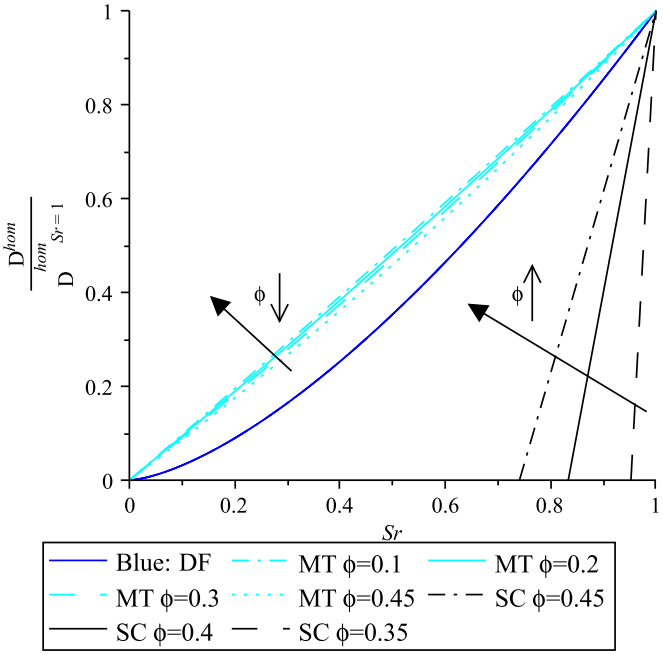

Figure 4.3: The influence of saturation degree on normalized homogenized diffusion coefficient in one scale microstructure, notation DF denotes differential scheme, MT denotes Mori-Tanaka scheme, SC denotes self-consistent scheme.

using these two schemes. It is interesting to note that the differential scheme (DF blue curves) provides a Archie-like power law defined by the exponent $\frac{3}{2}$ for both ϕ and Sr. It is important to note that the normalized homogenized diffusion coefficient coefficient derived by differential scheme (DF) is independent of the porosity ϕ. This remark is also valid for Mori-Tanaka scheme (cyan curves in Fig.(4.3)): the normalized solute diffusion coefficient weakly depends upon the porosity ($\phi \in [0.1, 0.45]$).

As expected, self-consistent estimate (SC black curves) is able to exhibit percolation effects in unsaturated case. A critical saturation degree Sr_p (solute diffusion vanishes at Sr_p: $D^{hom} = 0$ according to Eq.(4.10)) can be determined as:

$$Sr_p = \frac{1}{3\phi} \tag{4.11}$$

According to Eq.(4.11), it indicates that the percolation effects are enhanced by the value of the pore volume fraction (porosity). The higher the porosity the smaller the critical

saturation degree (see Fig.(4.3)). Therefore, the solute diffusion exists at the saturation degree ranges $[Sr_p, 1]$ in self-consistent scheme.

4.4.2 A two-scale microstructure

As discussed in Chapter 2, in practice engineering, most of porous media exhibit hierarchical structures (see Fig.(2.4)), which is defined by pore space characteristic sizes at different scales. To determine the homogenized diffusion coefficient for such microstructures, a multi-scale separation should be employed. Herein, in order to use this scale separation condition and derive the estimation by the previous schemes, a dual-porosity porous medium is considered. The idea consists in separating the pore space into two families of pores, the **m**acro **p**ores (domain Ω^{mp}) and the **s**mall **p**ores (domain Ω^{sp}). According to $\Omega^p = \Omega^{mp} \cup \Omega^{sp}$, let us define α the ratio of the **m**acro **p**ores Ω^{mp} in the whole pore space Ω^p:

$$\alpha = \frac{\Omega^{mp}}{\Omega^p} \tag{4.12}$$

The upscaling procedure for dual porosity microstructure is two fold (depending upon the saturation degree):

— At level I, the REV is made up of solid, liquid and gaseous phases.

— At level II, macro pores, either gas or liquid saturated, coexist with the homogenized medium of level I.

Detailed handling procedure of Mori-Tanaka scheme and self-consistent scheme in unsaturated cases is presented in Appendix(B). Isotropic diffusion coefficient tensors for each phase and spherical shape are assumed so that isotropic homogenized diffusion coefficients are expected. When level I (the matrix as shown in Fig.(4.4): it is denoted as domain Ω_m) and level II are dealt with different schemes, it represent different microstructures at microscopic (local) and macroscopic scales.

The morphological models are depicted in Fig.(4.4). Fig.(4.4)(a) characterizes a two-

scale matrix+inclusion microstructure: at micro scale (level I), the matrix is the liquid water (with diffusion coefficient D^{γ}) in which solid and gaseous phases are embedded; at level II, macro pores either filled with gas or liquid water are embedded in homogenized medium of level I (with homogenized diffusion coefficient D_m^{hom}).

Fig.(4.4)(b) characterizes the polycristalline microstructures at local (level I) and macro scales (level II): at micro scale, the liquid water and gas in micro pores along with solid grains are embedded in the matrix with sought homogenized diffusion coefficient D_m^{hom}; at macro scale, the homogenized medium as well as macro pores either filled with gas or liquid water are embedded in the medium with sought homogenized diffusion coefficient D^{hom}.

Fig.(4.4)(c) characterizes the polycristalline microstructure: at local scale (level I) and matrix+inclusion microstructure at macro scale (level II); at local scale, solid grain and pores filled with gas or liquid water are embedded in the matrix with sough homogenized diffusion coefficient D_m^{hom}; at macro scale, macro pores either filled with gas or liquid water are embedded in the homogenized matrix of level I.

The matrix pore space volume fraction is denoted by ϕ_m and the saturation degree Sr_m at that (local) scale are defined as:

$$\begin{cases} \phi_m = \dfrac{\Omega^{sp}}{\Omega_m} = \dfrac{\Omega^{p} - \Omega^{mp}}{\Omega - \Omega^{mp}} = \dfrac{(1-\alpha)\phi}{1-\alpha\phi} \\ Sr_m = \dfrac{\Omega_l^{sp}}{\Omega^{sp}} = \dfrac{\Omega_l^{sp}/\Omega_m}{\Omega^{sp}/\Omega_m} = \dfrac{\varphi_l}{\phi_m} \end{cases} \tag{4.13}$$

where $\Omega^{\boldsymbol{sp}}$ and $\Omega_l^{\boldsymbol{sp}}$ are the domains of **s**mall (micro) **p**ores and the liquid water in micro pores, Ω_m is the domain of the matrix (level I), φ_l is the volume fraction of the liquid water in small pores at local scale.

Thus, at level I (the matrix as shown in Fig.(4.4)), the homogenized diffusion coefficient of the matrix in the isotropic case[4] can be estimated as:

4. In isotropic case, we have $\boldsymbol{D}_m^{hom} = D_m^{hom}\mathbf{1}$, $\boldsymbol{D}^{\gamma} = D^{\gamma}\mathbf{1}$, $\overline{A_i} = \dfrac{1}{3}\mathbf{1} : \overline{\boldsymbol{A}_i}$, $i \in \{l, s, g, m\}$

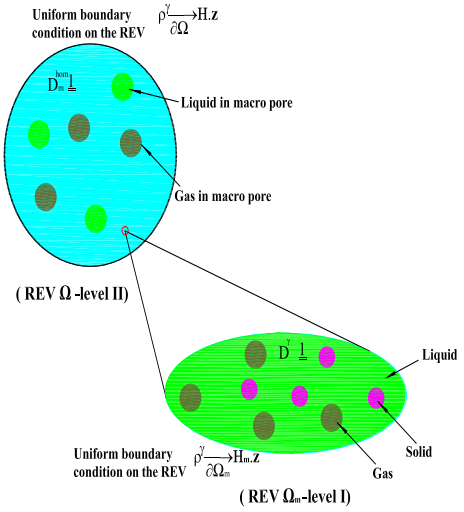

(a) Level II: MT-Level I: MT

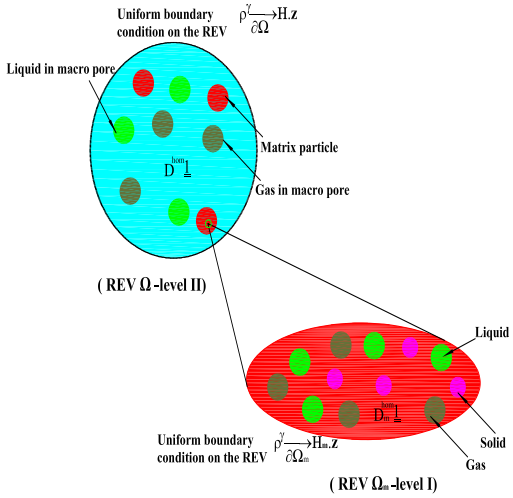

(b) Level II: SC-level I: SC

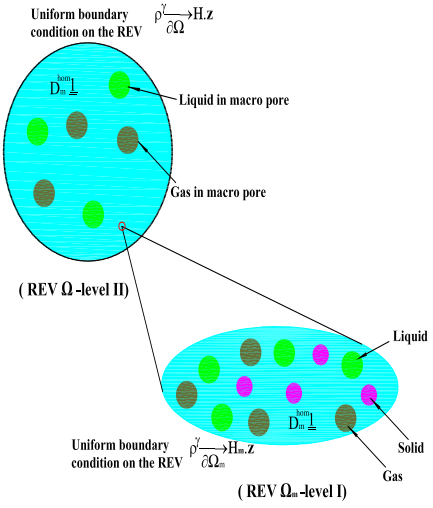

(c) Level II: MT-level I: SC

Figure 4.4: Schematic illustration of morphological models for porous media with two-scale microstructure, SC denotes self-consistent scheme, MT denotes Mori-Tanaka scheme.

$$\begin{cases} D_m^{hom} = \dfrac{2\phi_m Sr_m}{3-\phi_m Sr_m} D^\gamma & \text{with Mori-Tanaka Scheme} \\ D_m^{hom} = \dfrac{3\phi_m Sr_m - 1}{2} D^\gamma & \text{with Self-Consistent Scheme} \end{cases} \tag{4.14}$$

Similarly, at level II, in isotropic case[5], the macroscopic homogenized diffusion coefficient D^{hom} can be estimated by:

$$D^{hom} = \frac{\varphi_m D_m^{hom} \overline{A}_m + \varphi_{ml} D^\gamma \overline{A}_{ml}}{\varphi_m \overline{A}_m + \varphi_{ml} \overline{A}_{ml} + \varphi_{mg} \overline{A}_{mg}} \tag{4.15}$$

where $\overline{A}_i$ are the average concentrations of i-th phase at macro scale ($i \in \{m, mg, ml\}$). Their values are estimated by the considered schemes (e.g., Mori-Tanaka and Self-Consistent Schemes); the detailed information is given in Appendix(B.2). Correspondingly, φ_i are the volume fractions of i-th phase at macro scale ($i \in \{m, mg, ml\}$). Here, it should be clear that, φ_m is the volume fraction of the matrix at macro scale (level II) while ϕ_m is the porosity of the matrix at local scale (level I).

It has to be mentioned that α may be advantageously interpreted through the concept of a **critical macro saturation degree** Sr^c defined as:

$$Sr^c = \frac{\Omega^{sp}}{\Omega^p} = 1 - \alpha \tag{4.16}$$

This critical macro saturation degree allows to account for the saturation degree at the local scale along the progressive desaturation process.

Some remarks on α and ϕ when level I is estimated with self-consistent scheme

Let us consider porous materials defined by $1/3 \leq \phi_m \leq 1/2$ when they are estimated by self-consistent scheme. Herein, level I is estimated with self-consistent scheme (see Fig.(4.4) (b) and (c)), the pore volume fraction of the matrix ϕ_m (see Eq.(4.13)) should

5. $\boldsymbol{D}^{hom} = D^{hom}\mathbf{1}$, $\boldsymbol{D}^\gamma = D^\gamma \mathbf{1}$, $\overline{A_i} = \frac{1}{3}\mathbf{1} : \overline{\boldsymbol{A}_i}$, $i \in \{m, mg, ml\}$, subscripts m, ml and mg denote matrix, liquid water in macro pore and gas in macro pore, respectively.

obey:

$$\phi_m \geq \frac{1}{3} \Rightarrow \phi \geq \frac{1}{3-2\alpha} \geq \frac{1}{3} \tag{4.17}$$

When level I is estimated with self-consistent scheme, in order to discuss the percolation effect, the percolation threshold saturation degree Sr^p is employed, at which the macroscopic solute diffusion disappears ($D^{hom} = 0$). The quantitative expression of Sr^p is derived as:

$$Sr^p = \frac{\Omega_m^{lc}}{\Omega^p} = \frac{\Omega_m^{lc}}{\Omega^{sp}} \frac{\Omega^{sp}}{\Omega^p} = \frac{1}{3\phi_m}(1-\alpha) = \frac{1-\alpha\phi}{3\phi} \tag{4.18}$$

where Ω_m^{lc} is the critical liquid domain in matrix (solute diffusion disappears at this critical liquid domain), ϕ_m is determined by Eq.(4.13).

Taking advantage of Eq.(4.12) and Eq.(4.13), the volume fractions of each phase are listed in Table(4.4).

Table 4.4: Volume fractions of each phase within multi scale porous media.

-	$Sr \geq Sr^c$	$Sr \leq Sr^c$
[1] Solid φ_s	$\frac{1-\phi}{1-\phi(1-Sr^c)}$	$\frac{1-\phi}{1-\phi(1-Sr^c)}$
Gas in micro pores φ_g	0	$\frac{\phi(Sr^c-Sr)}{1-\phi(1-Sr^c)}$
The capillary water in micro pores φ_l	$\frac{\phi Sr^c}{1-\phi(1-Sr^c)}$	$\frac{\phi Sr}{1-\phi(1-Sr^c)}$
The capillary water in macro pores φ_{ml}	$\phi(Sr-Sr^c)$	0
Gas in macro pores φ_{mg}	$\phi(1-Sr)$	$\phi(1-Sr^c)$

[1] The volume fractions φ_s, φ_l and φ_g are defined on level I (at local scale), they can be determined by as Eq.(4.13); φ_{mg} and φ_{ml} are defined on level II (at macro scale).

Three micromechanics models are proposed in order to estimate the homogenized diffusion coefficient of two-scale porosity geomaterials (see Fig.(4.4)). They have been chosen in order to discuss the specific microstructures. The evolution of macroscopic homogenized diffusion coefficient with saturation degree is determined from Eq.(4.14) and Eq.(4.15).

The influence of α on the evolution of the macroscopic homogenized diffusion coefficient D^{hom} is depicted in Fig.(4.5) [6].

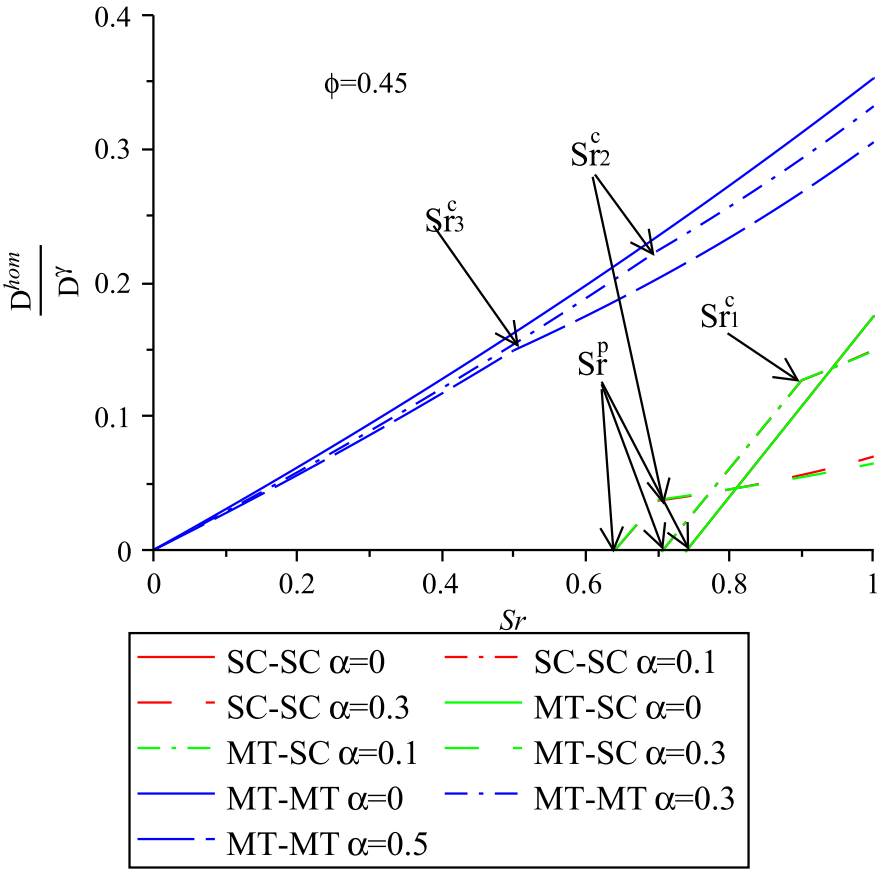

Figure 4.5: Influence of α on the evolution of D^{hom} with Sr in porous media with two-scale microstructures; MT-MT, SC-SC and MT(level II)-SC (level I) correspond to morphological models in Fig.(4.4)(a), (b) and (c), respectively; $Sr_1^c = 0.9$, $Sr_2^c = 0.7$, $Sr_3^c = 0.5$.

The influence of ϕ on the evolution of the macroscopic homogenized diffusion coefficient D^{hom} is depicted in Fig.(4.6) [7].

According to Fig.(4.5) and Fig.(4.6), these results are derived based on three morphological models (SC-SC, MT-MT and MT-SC). They deserve the following comments:

— **Effect of morphological models**

Mori-Tanaka scheme is associated to matrix+inclusion microstructure morphology.

6. Here, $\phi = 0.45$, from Eq.(4.17), $\alpha \leq 0.39$, thus, α is taken as 0, 0.1 and 0.3, respectively in this case.
7. In this case, $\alpha = 0.1$, from Eq.(4.17), $\phi \geq 0.357$, therefore, ϕ is taken as 0.36, 0.4 and 0.45, respectively.

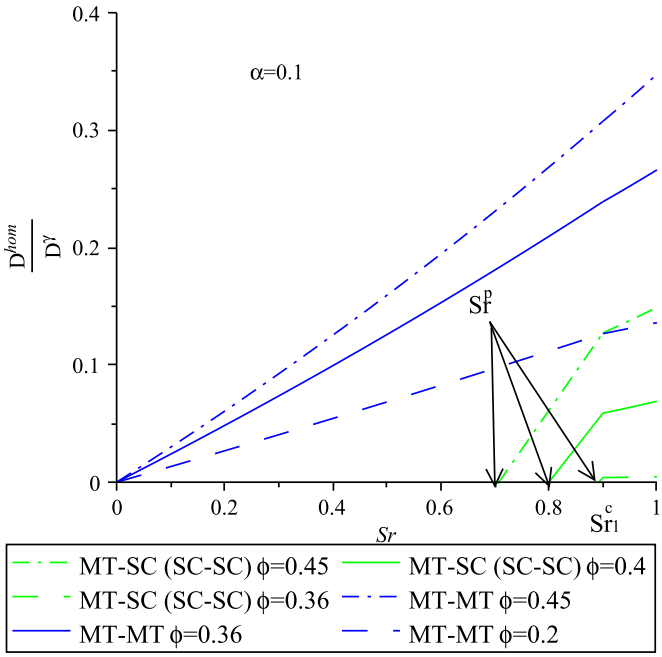

Figure 4.6: Influence of ϕ on the evolution of D^{hom} with Sr in porous media with two-scale microstructures, $Sr_1^c = 0.9$.

Nevertheless, self-consistent scheme, associated to a polycristalline microstructure, is typically used for granular materials. In addition, the crucial question of the liquid water connectedness at the different scales is addressed through the use of self-consistent scheme.

The simulation results of SC-SC and MT-SC models show great similarity (overlapping of red curves and green curves). Both of these simulation results exhibit strong percolation effects. These results emphasize the fact that macroscopic percolation effects may be attributed to percolation phenomena occurring at local scale only (in this case it is estimated with self-consistent scheme at level I).

The results of MT-MT model show that the one-scale MT model ($\alpha = 0$) is already able to account for the multi-scale (here the double scale and $\alpha > 0$) definition of the pore space. In other words, the introduction of a second pore size family does not strongly modify the result obtained by the previous MT model (see Fig.(**??**)).

— **Effect of** α

The influence of parameter α is discussed at porosity $\phi = 0.45$. Let us remind that $\alpha = \dfrac{\Omega^{mp}}{\Omega^{p}}$ defines the fraction of macro pores in the whole pore space (at macro scale). Thus, as presented in Eq.(4.13), the porosity of matrix ϕ_m (at level I) is a function of α, the evolution of the ϕ_m with α is plotted in Fig.(4.7).

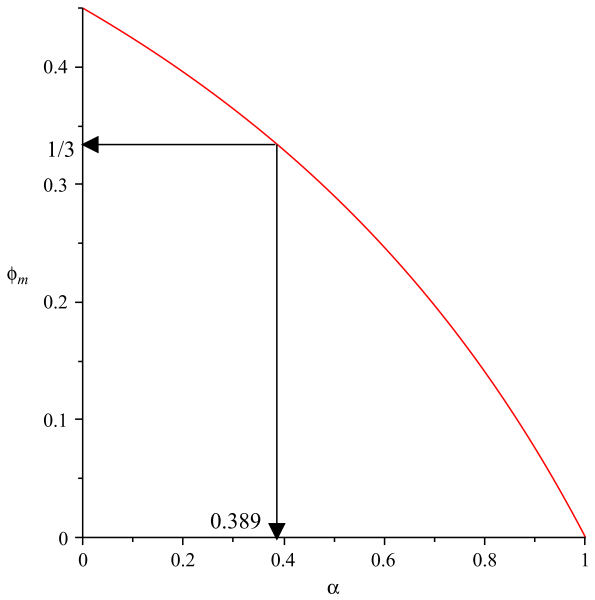

Figure 4.7: Evolution of ϕ_m with α.

1) the influence of the α on the saturated macroscopic homogenized diffusion coefficient $D^{hom}(Sr = 1)$

In self-consistent scheme (e.g., SC-SC, MT-SC models in Fig.(4.4) (b) and (c)), the porosity of the matrix ϕ_m should be higher than 1/3 to ensure the connectivity of the liquid phase in matrix (level I in Fig.(4.4)). Therefore, the maximum value of α is 0.389 (see Fig.(4.7)). As shown in Fig.(4.7), when α ranges between 0 to 0.389, ϕ_m decreases with increase of α. Therefore, from Eq.(4.14), it can be inferred that the homogenized diffusion coefficient in matrix D_m^{hom} decreases with α.

When the homogenized diffusion coefficients at level II are estimated with self-consistent or Mori-Tanaka schemes (see Fig.(4.4)(b) and (c)), the macro pore water is isolated distributed in matrix and connected by the latter. The macroscopic homogenized diffusion coefficient D^{hom} (at level II) are thus controlled by the diffusion

coefficient of the matrix D_m^{hom}. As we discussed previously, D_m^{hom} decreases with α. Therefore, in MT-SC or SC-SC models, the saturated macroscopic homogenized diffusion coefficient $D^{hom}(Sr = 1)$ also decreases with α. The simulation results are depicted in green curves and red curves in Fig.(4.5).

Similarly, in MT-MT models, the macroscopic homogenized diffusion coefficient D^{hom} is governed by the homogenized diffusion coefficient in the matrix D_m^{hom}. Therefore, D_m^{hom} also decreases with α (as shown in the blue curves in Fig.(4.5)).

2) the influence of α on the percolation effect

However, when the homogenized diffusion coefficient of matrix is estimated with self-consistent scheme, there exists strong percolation effect. The percolation effect is quantify by the value of Sr^p, the greater the Sr^p, the greater the percolation effect. Seen from Eq.(4.18), it is readily to find that Sr^p decrease with increase of α. Therefore, in MT-SC or SC-SC models, with the increase of α, percolation effect decreases, the evolution of Sr^p with α are depicted in Fig.(4.5).

As stated previously, when the homogenized diffusion coefficient of matrix (level I) is estimated with MT, the matrix is liquid water which ensures the connectivity of the diffusion pathway. Therefore, when the matrix (level I) is estimated with MT, there is no percolation effect ($Sr^p = 0$) in MT-MT (as shown in the blue curves in Fig.(4.5)).

— **Effect of porosity ϕ**

1) the influence of ϕ on the saturated macroscopic homogenized diffusion coefficient $D^{hom}(Sr = 1)$

The influence of porosity ϕ (total porosity at macro scale) on the simulation results by three morphological models is discussed at $\alpha = 0.1$. As discussed previously, the saturated macroscopic homogenized diffusion coefficient $D^{hom}(Sr = 1)$ is governed by the homogenized diffusion coefficient of the matrix D_m^{hom}. It is readily to see from Eq.(4.14), D_m^{hom} decrease with porosity of matrix ϕ_m. Moreover, from Eq.(4.13), it can be found that, the porosity of matrix ϕ_m decreases with ϕ at a given α (here

$\alpha = 0.1$). Therefore, it can be concluded that, when estimated with MT-MT, SC-SC and MT-SC, $D^{hom}(Sr = 1)$ decrease with ϕ. The simulation results are illustrated in Fig.(4.6).

2) the influence of ϕ on the percolation effect

As shown in the blue curves in Fig.(4.6) and explained previously, there is no percolation effect when MT-MT models.

For the SC-SC or MT-SC models, there exists strong percolation effect. Seen from Eq.(4.18), it is readily to find that Sr^p increases with decreasing ϕ, which means percolation effect increases with ϕ. The simulation results are depicted in the green curves in Fig.(4.6).

Therefore a general conclusion can be made: in SC-SC or MT-SC models, the saturated macroscopic homogenized diffusion coefficient $D^{hom}(Sr = 1)$ increases with decreasing α while the percolation effect decreases increases with α; in MT-MT model, the saturated macroscopic homogenized diffusion coefficient $D^{hom}(Sr = 1)$ increases with decreasing α, however there is no percolation effect in this model.

As we have discussed previously, Mori-Tanaka scheme is adopted for the matrix+inclusion microstructure morphology, the connectivity of the liquid phase is ensured in this scheme. However, the percolation effect occurred during the desaturation will not presented by this scheme. That is the reason why self-consistent scheme are introduced. Generally, the self-consistent scheme is appropriate for polycrystalline microstructures (e.g., sand, sandstone, clay particles arrangement, C-S-H particle arrangement). But this simple morphology fails since solute diffusion disappears at high saturation degree (as shown by the black curves in Fig.(4.3)), which is contradictory to the experimental results [33, 127, 159]. Therefore, in order to overcome the drawback of the self-consistent scheme, enriched models are developed accounting for the liquid layer phase, which are introduced in the following section.

4.5 Enriched models for solute diffusion in unsaturated porous media

In the previous section, different morphological representations (one-scale and two-scale microstructure) of unsaturated porous media are discussed. However, in the previous morphological representations, specific liquid water distribution within the pore space has not been considered.

The present section aims at deriving a micromechanics model for solute diffusion accounting for a more detailed morphology of the liquid water distribution within the pore space of porous media with one-scale microstructure. The evolution of water distribution within unsaturated granular material (one-scale microstructure) is introduced in Section (3.1). Based on this physical characterization, a schematic illustration of the different water components (the pore body water, the intergranular layer, the wetting layer and the water film) are depicted in Fig.(4.8).

According to Fig.(4.8), part of the "liquid water" is always attached to the pore/solid interface during the desaturation process. This "liquid water" varies from intergranular layer at high saturation degree, wetting layer at intermediate saturation degree to water film at low saturation degree. In the following context, this kind of "liquid water" with special morphology is referred to as **liquid layer** (denoted as subscript ll). Hence, liquid layer+solid grain composite morphology is sufficient to represent the morphologies of water film+solid grain, the wetting layer+solid grain and intergranular layer+solid grain within unsaturated porous medium. It will now be incorporated in the micromechanics model and discussed in the sequel.

In unsaturated porous medium, there exist the pore body water phase, the liquid layer phase, solid phase and gaseous phase. Analogical to the saturated case in Section(4.3), the local diffusion problem in this unsaturated porous medium can also be defined over a REV (domain Ω) by the following set of equations:

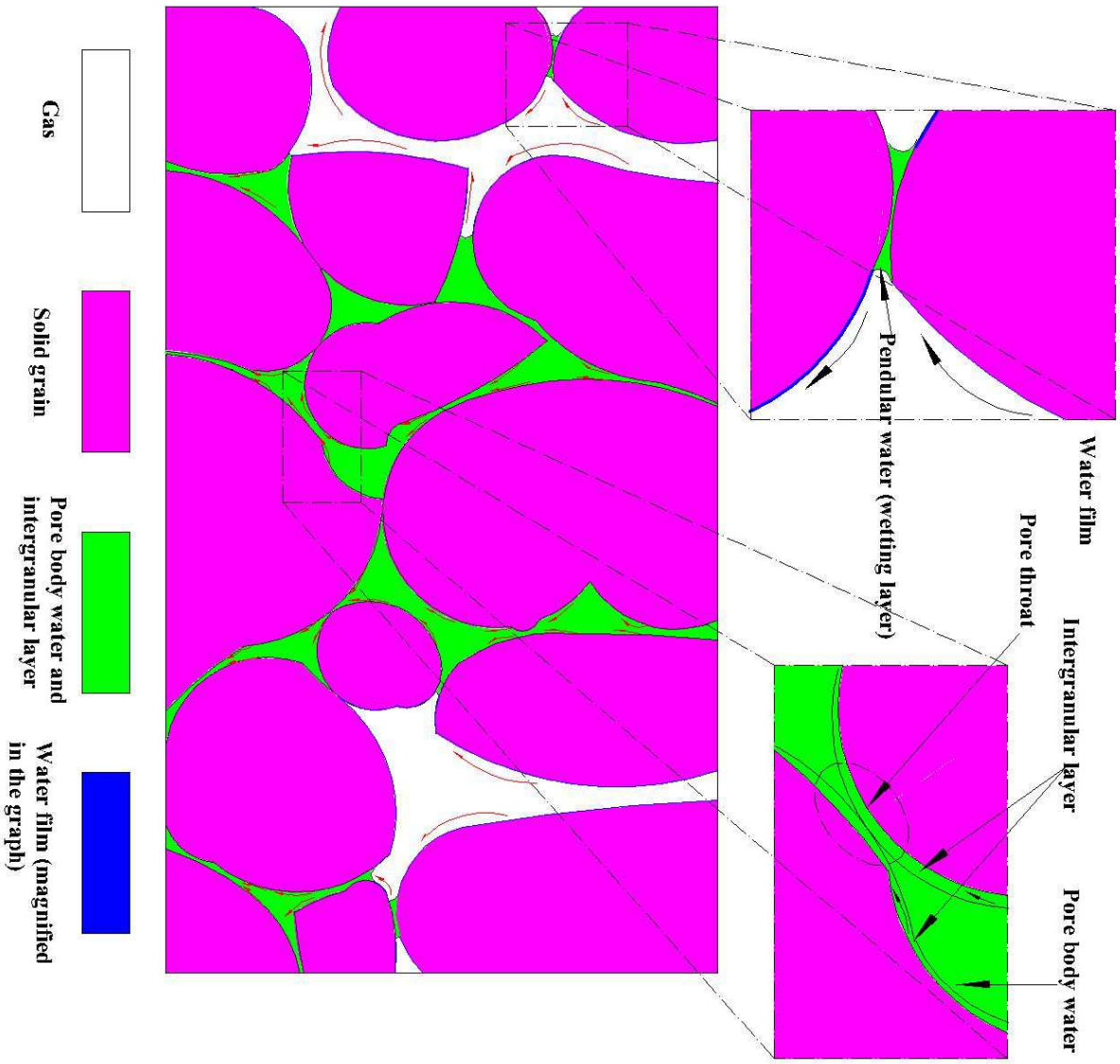

Figure 4.8: Schematic representation of different components of water phase and their effects on solute diffusion in unsaturated porous media; the surface roughness of solid grains is disregarded in the figure; the intergranular water is decomposed into intergranular layer and pore body water; the intergranular layer, the wetting layer and the water film are represented by "liquid layer" in the following discussion.

$$\begin{cases} \underline{\text{div}}\ \underline{j}^{\gamma} = 0 & (a) \\ \underline{j}^{\gamma} = -D^{\gamma}(\underline{z})\ \underline{\text{grad}}\rho^{\gamma} & (b) \\ \rho^{\gamma} = \underline{H} \cdot \underline{z} \qquad \text{when} \quad \underline{z} \in \partial\Omega & (c) \end{cases} \tag{4.19}$$

where $\underline{H}$ is the macroscopic concentration gradient applied on the boundary of the REV ($\partial\Omega$) in the sense of Hashin [122].

Here, isotropic solute diffusion coefficient tensors and spherical shape of each phase are assumed so that isotropic homogenized solute diffusion coefficients are expected. The solute diffusion coefficients of each phase can thus be expressed as:

$$D(\underline{z}) = \begin{cases} D^{s} \to 0 & \forall \underline{z} \in \Omega^{s} \\ D^{g} \to 0 & \forall \underline{z} \in \Omega^{g} \\ D^{\gamma} & \forall \underline{z} \in \Omega^{pw} \\ D^{\gamma}_{ll} = \delta D^{\gamma} & \forall \underline{z} \in \Omega^{ll} \end{cases} \tag{4.20}$$

where Ω^{s}, Ω^{pw}, Ω^{g} and Ω^{ll} are the solid, the pore body water, the gas and the liquid layer domains within REV, respectively; D^{γ}_{ll} is the diffusion coefficient of species γ within the liquid layer, δ is the constrictive factor for the solute diffusion coefficient in the liquid layer, $\delta \leq 1$ (see Section(3.6.3)).

Similar to Eq.(4.6), in order to solve Eq.(4.19), $\underline{\text{grad}}\rho^{\gamma}$ is linearly related to $\underline{H}$ by introducing the concentration tensors of each phase $\mathbf{A}_i(\underline{z})$ ($i \in \{s, g, pw, ll\}$). The latter depend on their microstructure morphologies at local scale. Generally, it is difficult to estimate the $\mathbf{A}_i(\underline{z})$. An alternative and convenient way is estimating the average concentration tensors $\overline{\boldsymbol{A}}_i$ by means of Eshelby's based solution, the detailed information is given in Appendix(B).

The evolutions of the volume fractions of pore body water and the liquid layer with relative humidity are different during drainage. The volume fraction of the liquid layer (with subscript $\boldsymbol{ll}$) can be determined by Eq.(4.21):

$$\varphi_{ll} = \frac{N\frac{4\pi[(R_s+h)^3 - R_s^3]}{3}}{N\frac{4\pi R_s^3}{3}} = [(1+\varepsilon)^3 - 1](1-\phi) \qquad \text{with, } \varepsilon = \frac{h}{R_s} \tag{4.21}$$

where N is the grain density (number of grains per unit volume), $1-\phi = \frac{4N\pi R_s^3}{3}$, ϕ is the pore volume fraction, R_s is the radius of the solid grain, h is the thickness of the liquid layer.

Therefore, the liquid layer saturation degree Sr^{ll} may be determined as:

$$Sr^{ll} = \frac{(1-\phi)}{\phi}[(1+\varepsilon)^3 - 1] \tag{4.22}$$

The saturation degree Sr may thus be defined as:

$$Sr = Sr^{pw} + Sr^{ll} \tag{4.23}$$

where $Sr^{\boldsymbol{pw}}$ is **p**ore body **w**ater saturation degree.

Hence, in this unsaturated porous media, when $\varepsilon = h/R_s \ll 1$, the volume fractions of each phase can be expressed as a function of saturation degree Sr as:

$$\begin{cases} \varphi_s = (1-\phi) \\ \varphi_g = \phi(1-Sr) \\ \varphi_{ll} = [(1+\varepsilon)^3 - 1](1-\phi) \approx 3\varepsilon(1-\phi) \\ \varphi_{pw} = \phi Sr - \varphi_{ll} = \phi Sr - [(1+\varepsilon)^3 - 1](1-\phi) \approx \phi Sr - 3\varepsilon(1-\phi) \end{cases} \tag{4.24}$$

In isotropic case, when the average concentration coefficient $\overline{A}_i$ and volume fractions of each phase φ_i ($i \in \{ll, pw, g, s\}$) are determined, the homogenized diffusion coefficient D^{hom} can be determined by revising Eq.(4.9) as:

$$D^{hom} = \sum_i \varphi_i D^i \overline{A_i} \tag{4.25}$$

Depending on the volume fraction of the liquid layer, the latter can be mathematically treated as 2-D (2 dimensional) case (in Section(4.5.1)) or 3-D case (in Section(4.5.2)).

1) 2-D case: asymptotically, when $h \ll R_s$, the liquid layer may be idealized as the diffusive interface whose volume fraction may be neglected. The saturation degree can thus be determined as:

$$Sr = Sr^{pw} + \frac{3(1-\phi)}{\phi}(\frac{h}{R_s}) \approx Sr^{pw} \qquad \text{with:} \quad h \ll R_s \tag{4.26}$$

The local solute diffusion in this asymptotic liquid layer may be idealized as a 2-D solute diffusion phenomena occurring at the solid-pore space interface.

2) 3-D case: 2-D idealization of asymptotic liquid layer is incapable of characterizing the evolution of the liquid layer during the desaturation process. To overcome this, the liquid layer which exhibits volumetric evolution is treated as a specific phase in 3-D case.

4.5.1 2-D idealization of local diffusion

4.5.1.1 Local diffusion at solid-pore space interface

Considering the local diffusion at solid-pore space interface, let us denote S_i the surface of the grain G_i. More over, S_i is the 2-D idealization of a asymptotic liquid layer of width h, the latter is infinitesimal as compared the grain size. Let $\underline{N}$ be the local unit vector normal to the tangent plane of S_i, let Z ($0 < Z < h$) denote the coordinate along an axis normal at point $\underline{z}$ of the S_i (see Fig.(4.9)).

According to Fig.(4.9) and based on the 2-D idealization of the asymptotic liquid layer, a surface flux vector of solute species $\underline{Q}^\gamma$ is defined as [79]:

$$\underline{Q}^\gamma(\underline{z}) = \int_0^h \underline{j}^\gamma(\underline{z} + Z\underline{N})\mathrm{d}Z \tag{4.27}$$

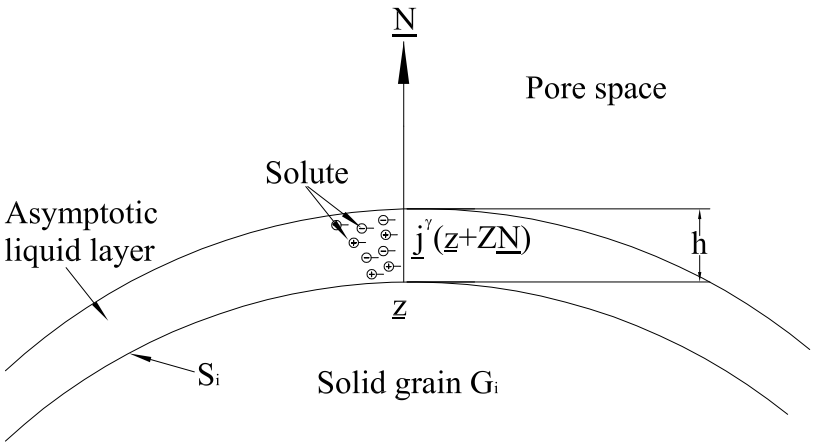

Figure 4.9: 2D idealization of diffusion flux in interface.

When the solvent velocity is negligible, the equation $\underline{j}^\gamma = \rho^\gamma \underline{v}^\gamma = -D_{ll}^\gamma \underline{\text{grad}}_z \rho^\gamma$ is also valid for the solute diffusion in diffusive interface (recalling Eq.(4.3)).

Thus, combining with Eq.(4.27), we have:

$$\underline{Q}^\gamma(\underline{z}) = -\int_0^h D_{ll}^\gamma \underline{\text{grad}}_z \rho^\gamma \mathrm{d}Z \tag{4.28}$$

where D_{ll}^γ is the diffusion coefficient of species γ within the liquid layer.

Similar to the classic 3-D Fick's law, the surface flux is assumed to be proportional to the species concentration gradient in the diffusive interface of the considered grain:

$$\underline{z} \in S_i : \qquad \underline{Q}^\gamma(\underline{z}) = -D_{sf}^\gamma \ \underline{\text{grad}}_s \rho^\gamma \tag{4.29}$$

where $\underline{Q}^\gamma$ lies within the tangent plane of S_i, D_{sf}^γ is the diffusion coefficient of the solute species on the solid surface and can be calculated from the diffusion coefficient D_{ll}^γ in the liquid layer:

$$D_{sf}^{\gamma} = \int_0^h D_{ll}^{\gamma}(\underline{z} + Z\underline{N})\mathrm{d}Z \tag{4.30}$$

As proposed in Eq.(3.39), the constrictive factor for the diffusivity in the liquid layer δ can be introduced to relate the diffusion coefficient in liquid layer D_{ll}^{γ} with the bulk diffusion coefficient D^{γ}. When δ is assumed to be constant, D_{sf}^{γ} can be defined as:

$$D_{sf}^{\gamma} = h\delta D^{\gamma} \tag{4.31}$$

Therefore, the average solute flux across the overall diffusive interfaces within the REV of porous medium $\underline{J}_{sf}^{\gamma}$ can be expressed as:

$$\underline{J}_{sf}^{\gamma} = \frac{1}{\Omega}\sum_i \int_{S_i} \underline{Q}^{\gamma}(\underline{z})\mathrm{d}S_i \tag{4.32}$$

Ω is the total volume of REV.

4.5.1.2 Derivation of unsaturated solute diffusion coefficient

The macroscopic average flux of solute species in the REV of the unsaturated porous media($\underline{J}_{tot}^{\gamma}$) involves the contribution of the solute diffusion in pore body water ($\underline{J}_{pw}^{\gamma}$) and that in the diffusive interface ($\underline{J}_{sf}^{\gamma}$) which exists in the asymptotic liquid layer (diffusive interface). That is,

$$\underline{J}_{tot}^{\gamma} = \underline{J}_{sf}^{\gamma} + \underline{J}_{pw}^{\gamma} \tag{4.33}$$

In unsaturated porous media, the solute flux in pore body water ($\underline{J}_{pw}^{\gamma}$) can be expressed as:

$$\underline{J}_{pw}^{\gamma} = \overline{\underline{j}_{pw}^{\gamma}} = -\phi Sr^{pw} D^{\gamma} \overline{\underline{\mathrm{grad}}_{pw}\rho^{\gamma}} \tag{4.34}$$

where ϕ is the porosity of porous media, Sr^{pw} is the saturation degree of pore body water, $\overline{\underline{\mathrm{grad}}_{pw}\rho^{\gamma}}$ is the average concentration gradient of the solute species in the pore body water.

Combining Eq.(4.32), Eq.(4.33) and Eq.(4.34), it yields:

$$\underline{J}^{\gamma}_{tot} = -\phi S r^{pw} D^{\gamma} \overline{\underline{\mathrm{grad}}_{pw} \rho^{\gamma}} + \frac{1}{\Omega} \sum_i \int_{S_i} \underline{Q}^{\gamma} \mathrm{d}S_i \tag{4.35}$$

$\overline{\underline{\mathrm{grad}}_{pw} \rho^{\gamma}}$ and $\underline{Q}^{\gamma}$ have to be determined. Here, we will rather perform estimates for the latters. Unsaturated porous media seem to exhibit percolation effect during the liquid water drainage, which may be accounted for by the sole self-consistent scheme.

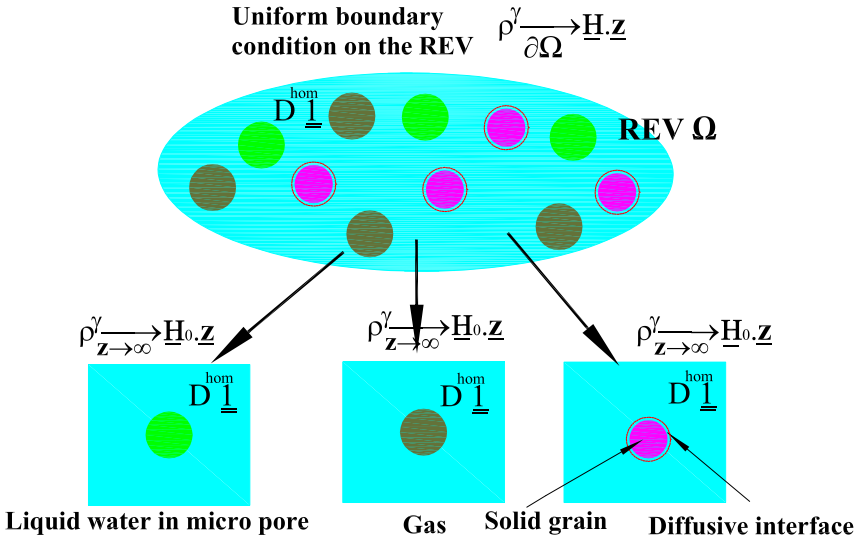

Figure 4.10: Morphological representation of 2D idealization of solute diffusion in unsaturated porous media

Following the self-consistent scheme methodology applied to the unsaturated situation, three auxiliary Eshelby problems are considered (see Fig.(4.10)). Uniform boundary conditions $\rho^{\gamma} \longrightarrow \underline{H}_0 \cdot \underline{z}$ are considered on the boundary of REV, where $\underline{H}_0$ is a fictitious uniform concentration gradient, $\underline{H}$ is a real uniform concentration gradient. According to Eq.(4.7), $\underline{H}_0$ is related to $\underline{H}$ by the following equation:

$$\underline{H}_0 = \underline{H} \tag{4.36}$$

Estimates for the liquid water phase and the gaseous phase are easily derived as a specific application of Eshelby's solution for diffusion problems. The derivation of the average concentration gradients in the pore body water ($\overline{\underline{\text{grad}}_{pw}\rho^{\gamma}}$) and gaseous phase ($\overline{\underline{\text{grad}}_{g}\rho^{\gamma}}$) is given in Appendix(B.2). Here, the concentration tensors of pore body water and gaseous phase are listed as:

$$\overline{\underline{\text{grad}}_{pw}\rho^{\gamma}} = \frac{3D^{hom}}{2D^{hom}+D^{\gamma}}\underline{H}_0 \tag{4.37}$$

$$\overline{\underline{\text{grad}}_{g}\rho^{\gamma}} = \frac{3}{2}\underline{H}_0 \tag{4.38}$$

Therefore, inserting Eq.(4.37) into Eq.(4.34) yields:

$$\underline{J}^{\gamma}_{pw} = -\phi Sr^{pw}D^{\gamma}\frac{3D^{hom}}{2D^{hom}+D^{\gamma}}\underline{H}_0 \tag{4.39}$$

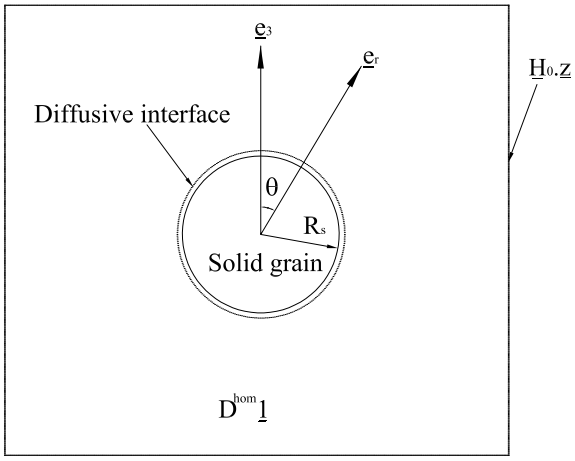

Figure 4.11: Eshelby problem of spherical composite made up of a solid grain and a diffusive interface.

The spherical composite made up of a solid grain+a diffusive interface requires an analytical resolution and it can be treated as Eshelby-based problem (see Fig.(4.11)). Taking advantage of the assumed spherical shape of the solid grains, the solute concentration (ex-

tended to the solid phase)[8] satisfies:

$$\begin{cases} r < R_s : \quad \rho^\gamma = Ar\cos\theta & (a) \\ r > R_s \quad \rho^\gamma = (\alpha r + \dfrac{\beta}{r^2})\cos\theta & (b) \end{cases} \tag{4.40}$$

where $\underline{H}_0 = H_0\underline{e}_3$ and $\underline{e}_3$ is corresponding to the axis co-linear to $\theta = 0$. Accordingly, the concentration gradient field can be shown as:

$$\begin{cases} r < R_s : \ \underline{\text{grad}}\rho^\gamma = A\underline{e}_3 & (a) \\ r > R_s : \ \underline{\text{grad}}\rho^\gamma = (\alpha - \dfrac{2\beta}{r^3})\cos\theta\underline{e}_r - (\alpha + \dfrac{\beta}{r^3})\sin\theta\underline{e}_\theta & (b) \end{cases} \tag{4.41}$$

The continuity of the concentration at $r = R_s$ reads:

$$AR_s = \alpha R_s + \frac{\beta}{R_s^2} \tag{4.42}$$

Considering the solute flux balance in the diffusive interface ($r = R_s$), it requires that:

$$\underline{\text{div}}_s\underline{Q}^\gamma = -\underline{j}^\gamma_{r|r=R_s^+} \tag{4.43}$$

Combining Eq.(4.29) and Eq.(4.43), the solute flux in the diffusive interface can be obtained by:

$$\underline{\text{div}}_s\underline{Q}^\gamma = D^\gamma_{sf}\ A\sin\theta\underline{e}_\theta \tag{4.44}$$

Meanwhile, Fick's law is applied to the interlayer ($r > R_s$) together with the use of Eq.(4.41)(b) it yields:

$$\underline{j}^\gamma_{r|r=R_s^+} = -D^{hom}((\alpha - \frac{2\beta}{r^3})\cos\theta\underline{e}_r - (\alpha + \frac{\beta}{r^3})\sin\theta\underline{e}_\theta) \tag{4.45}$$

Thus, according to the Eq.(4.43), Eq.(4.44) and Eq.(4.45), it gives:

8. The concentration gradient of the solid grain is non zero. However, owing to $D^s \to 0$, according to Fick's law, the solute flux in solid grain is 0.

$$D^{hom}(\alpha - \frac{2\beta}{R_s^3}) = 2A\frac{D_{sf}^{\gamma}}{R_s} \tag{4.46}$$

Finally, the boundary condition $\rho^{\gamma} \longrightarrow \underline{H}_0 \cdot \underline{z}$ at infinity ($r \to \infty$) together with Eq.(4.40) yields:

$$\alpha = H_0 \tag{4.47}$$

Eventually, the other two unknowns can be obtained by means of Eq.(4.42) and Eq.(4.46),

$$A = \frac{3D^{hom}R_s}{2(D^{hom}R_s + D_{sf}^{\gamma})}H_0; \qquad \beta = \frac{R_s^3}{2}\frac{D_{hom}^{\gamma}R_s - 2D_{sf}^{\gamma}}{D_{sf}^{\gamma} + D_{hom}^{\gamma}R_s}H_0 \tag{4.48}$$

From Eq.(4.41), it can be found that the concentration gradient in the solid grain is $A\mathbf{e}_3$, thus, the average concentration gradient of the solid grain $\overline{\underline{\text{grad}}_s \rho^{\gamma}}$ is estimated by:

$$\overline{\underline{\text{grad}}_s \rho^{\gamma}} = \frac{3D^{hom}R_s}{2(D^{hom}R_s + D_{sf}^{\gamma})}\underline{H}_0 \tag{4.49}$$

Similarly, combining Eq.(4.32) and Eq.(4.45), the contribution of diffusive interface can be estimated by [79]:

$$\frac{1}{\Omega}\sum_i \int_{S_i} \underline{Q}^{\gamma} \mathrm{d}S_i \approx N \int_S D_{sf}^{\gamma}\ A\ sin\theta\ \underline{e}_{\theta}\ \mathrm{d}S = -\frac{8}{3}\pi R_s^2 N D_{sf}^{\gamma}\ A\underline{e}_3 \tag{4.50}$$

where N is the grain density which is the number of grains per unit volume, the latter may be related to the volume fraction of solid grain c according to [79]:

$$c = 1 - \phi = 4\pi R_s^3 N/3 \tag{4.51}$$

Combining Eq.(4.50) and Eq.(4.51) yields:

$$\frac{1}{\Omega}\sum_i \int_{S_i} \underline{Q}^{\gamma} \mathrm{d}S_i \approx -\frac{D_{sf}^{\gamma}}{R_s}\frac{3(1-\phi)D^{hom}R_s}{D^{hom}R_s + D_{sf}^{\gamma}}\underline{H}_0 \tag{4.52}$$

Recalling Eq.(4.6), the following relationship between $\underline{H}$ and $\underline{H}_0$ is established:

$$\underline{H} = [\frac{3D^{hom}R_s(1-\phi)}{2(D^{hom}R_s + D^{\gamma}_{sf})} + \frac{3\phi Sr D^{hom}}{2D^{hom} + D^{\gamma}} + \frac{3\phi(1-Sr)}{2}]\underline{H}_0 \tag{4.53}$$

Eventually, by means of combining Eq.(4.35), Eq.(4.39), Eq.(4.52) and Eq.(4.53), it yields an analytical solution of the homogenized diffusion coefficient D^{hom}:

$$\begin{aligned} D^{hom} &= \frac{(3\phi Sr-1)D^{\gamma}}{4} + \frac{D^{\gamma}_{sf}(2-3\phi)}{2R_s} \\ &+\frac{1}{4}\sqrt{(1-3\phi Sr)^2(D^{\gamma})^2 + 4(2-3\phi)^2(\frac{D^{\gamma}_{sf}}{R_s})^2 + 4\frac{D^{\gamma}_{sf}D^{\gamma}}{R_s}[3\phi Sr(4-3\phi)+(2-3\phi)]} \\ &\approx \frac{(3\phi Sr-1)D^{\gamma}}{2} + \frac{D^{\gamma}_{sf}(2-3\phi)}{R_s} \end{aligned} \tag{4.54}$$

where $[3\phi Sr(4-3\phi)+(2-3\phi)] \approx (1-3\phi Sr)(2-3\phi)$ is applied in Eq.(4.54).

Remarks on the homogenized diffusion coefficient D^{hom}

For the convenience of discussion, the homogenized diffusion coefficient D^{hom} may be advantageously decomposed into two terms as:

$$D^{hom} \approx D^{hom}_{pw} + D^{hom}_{ll} \tag{4.55}$$

where we define two contributions:

$$D^{hom}_{pw} = \frac{(3\phi Sr-1)D^{\gamma}}{2} \qquad D^{hom}_{ll} = \frac{D^{\gamma}_{sf}(2-3\phi)}{R_s} \tag{4.56}$$

The first term accounts for the solute diffusion in the pore body water; the second term accounts for the solute diffusion in the diffusive interface.

As discussed in the Section(4.4.1), with self-consistent scheme, there is a percolation threshold for the solute diffusion in unsaturated porous media with one-scale microstructure. The critical saturation degree is $Sr^p = \frac{1}{3\phi}$, when $\phi > \frac{1}{3}$. Therefore, it is meaningful to analyse the diffusive transport phenomena with respect to the pore volume fraction of porous medium ϕ and saturation degree Sr.

— when $\phi \leq \frac{1}{3}$

Owing to the percolation threshold effect of self-consistent scheme, the pore body water becomes disconnected. Indeed, when $\phi \leq \frac{1}{3}$, even in the saturated case, the solute diffusion within pore body water (diffusion coefficient D_{pw}^{hom}) is null. The morphology of the diffusive interface (the asymptotic liquid layers surrounding the solid grains) ensures the connectivity of pathway for solute diffusion, which allows to obtain a non-zero homogenized diffusion coefficient D_{ll}^{hom}.

— when $\phi > \frac{1}{3}$ and $Sr \geq \frac{1}{3\phi}$

The homogenized unsaturated solute diffusion coefficient D^{hom} is composed of two parts: D_{pw}^{hom} contributed by pore body water as well as D_{ll}^{hom} contributed by the asymptotic liquid layer. When $Sr = 1$, the homogenized diffusion coefficient $D^{hom} = \frac{(3\phi-1)D^{\gamma}}{2} + \frac{D_{sf}^{\gamma}(2-3\phi)}{R_s}$. The ratio of the contributions of the two parts may be expressed as:

$$\frac{D_{pw}^{hom}}{D_{ll}^{hom}} = \frac{3\phi - 1}{2\varepsilon\delta(2-3\phi)} \tag{4.57}$$

where $\varepsilon = \frac{h}{R_s}$.

To quantitatively compare the dependence of the contributions of D_{pw}^{hom} and D_{ll}^{hom} on ε, parameters $\phi = 0.4$ and $\delta = 0.5$ are adopted. The results are depicted in Fig.(4.12). According to Fig.(4.12), it can readily be found that, when $\phi = 0.4$, the pore body water is interconnected, the contribution of pore body water is far greater than that of the diffusive interface ($\frac{D_{pw}^{hom}}{D_{ll}^{hom}} \gg 1$) as the thickness of liquid layer h is far smaller than the grain size R_s ($\varepsilon = h/R_s < 10^{-2}$). When $10^{-2} < \varepsilon < 10^{-1}$, the thickness of liquid layer is comparable with grain size, the contribution of liquid layer is thus comparable with that of pore body water (the same order of magnitude). It should be noted that, when $10^{-2} < \varepsilon < 10^{-1}$, the volume of the liquid layer may not be disregarded and the liquid layer can not be treated as the diffusive layer.

—

— when $\phi > \frac{1}{3}$ and $Sr < \frac{1}{3\phi}$

Similarly, the pore body water becomes discontinuous. Therefore, when $Sr < \frac{1}{3\phi}$, $D_{pw}^{hom} = 0$. In this case, the dominating contribution of solute diffusion is once again due to the diffusive interface (asymptotic liquid layer), the homogenized diffusion coefficient is thus $D^{hom} = D_{ll}^{hom}$.

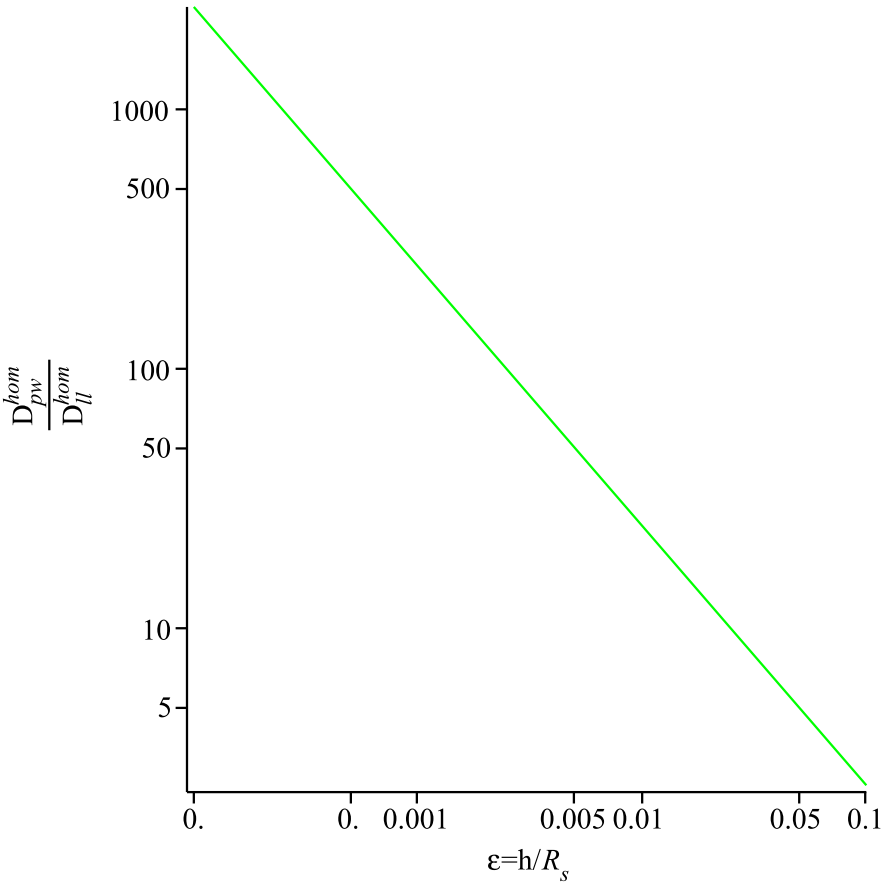

Figure 4.12: Dependence of $\frac{D_{pw}^{hom}}{D_{ll}^{hom}}$ on ε, $\phi = 0.4$, the constrictive factor $\delta = 0.5$.

In one scale microsturcture (as introduced in Section(4.4.1)), the percolation threshold proposed by self-consistent scheme is $\phi = \frac{1}{3}$. Asymptotically, from the expression of homogenized diffusion coefficient in liquid layer $D_{ll}^{hom} = \frac{D_{sf}^{\gamma}(2-3\phi)}{R_s}$, we can derive another percolation threshold $\phi = \frac{2}{3}$. It appears that for $\phi > \frac{2}{3}$, the liquid layers are not interconnected within porous medium.

4.5.2 3-D models for solute diffusion within unsaturated porous media

The 2-D idealization of the liquid layer in the previous section allows us to simplify the mathematical treatment of the asymptotic liquid layer. The volume fraction of the asymptotic liquid layer is neglected in the 2-D idealization. Indeed, the 2-D idealization of liquid layer is good for the asymptotic problem but is unable to account for the different kinds of liquid layer during desaturation process.

As depicted in Fig.(4.8), in unsaturated porous media, the liquid layer may be water film, wetting layer and intergranular layer. The volume fraction and the thickness of liquid layer decreases during desaturation process. Hence, the thickness and volume fraction of the liquid layer (superposition of water film, wetting layer and intergranular layer) has to be accounted for in the model. This the motivation of the 3-D model developed hereafter.

Depending upon the microstrcture morphologies of materials, Mori-Tanaka scheme and self-consistent scheme are used to estimate the concentration tensors of each phase.

4.5.2.1 Mori-Tanaka estimate

In the Mori-Tanaka scheme, the pore body water is treated as matrix with the diffusion coefficient D^{γ}. The morphological representation of the associated REV of an unsaturated porous medium is depicted in Fig.(4.13).

The detailed information about the determination of average concentration tensors for each phase is given in Appendix (B.2). When the porous medium is isotropic at local and macro scales, the average concentration coefficient of the i^{th} phase is estimated by Mori-Tanaka scheme and given in Eq.(4.58).

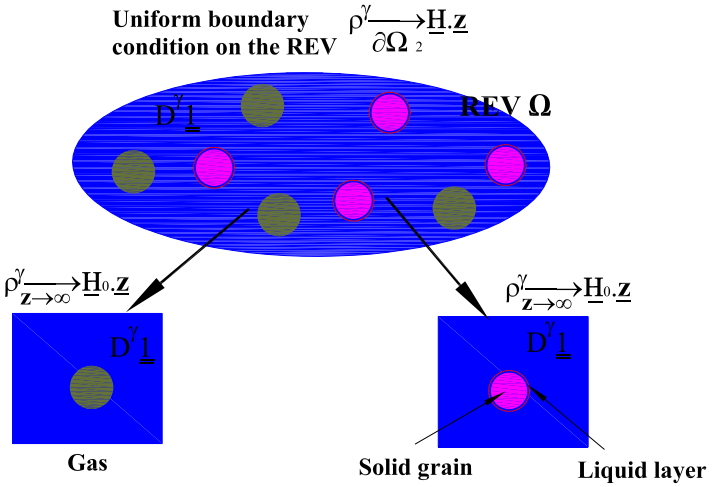

Figure 4.13: Schematic representation of unsaturated porous media with a specific matrix+inclusion morphology, this morphology corresponds to Mori-Tanaka scheme, the matrix is liquid water, the fictitious macroscopic concentration gradient $\underline{H}_0$ and the real macroscopic concentration gradient $\underline{\mathrm{H}}$ are linked by: $\underline{H}_0$=$\underline{\mathrm{H}}$.

$$\begin{cases} \overline{A}_{ll} = \dfrac{3D^\gamma(\varphi_{ll}+\varphi_s)}{3D^\gamma\varphi_s + 2D^\gamma\varphi_{ll} + D^\gamma_{ll}\varphi_{ll}} = \dfrac{3(\varphi_{ll}+\varphi_s)}{3\varphi_s + 2\varphi_{ll} + \delta\varphi_{ll}} \\ \overline{A}_s = \dfrac{3}{2}\overline{A}_{ll} = \dfrac{9(\varphi_{ll}+\varphi_s)}{2(3\varphi_s + 2\varphi_{ll} + \delta\varphi_{ll})} \\ \overline{A}_g = \dfrac{3}{2} \\ \overline{A}_{pw} = 1 \end{cases} \tag{4.58}$$

The volumetric fractions of each phase are given in Eq.(4.24). Substituting Eq.(4.24) and Eq.(4.58) into Eq.(4.25) yields the homogenized diffusion coefficient:

$$D^{hom} = \frac{-2[6(\delta-1)(1-\phi)\varepsilon^2 + (\delta+2)\phi Sr + 3(1-\phi)(\delta-1)\varepsilon + \phi Sr]}{6(\delta-1)(1-\phi)\varepsilon^2 + [-9 + (3 - 3\delta + \delta Sr + 2Sr)\phi]\varepsilon + \phi Sr - 3} D^\gamma \tag{4.59}$$

According to Eq.(4.59), the homogenized diffusion coefficient estimated by Mori-Tanaka scheme is a function of three parameters: ratio ε, the constrictive factor δ of the liquid layer and the porosity ϕ. In the following, a discussion is presented in order to provide a better understanding of the effects governed by these three parameters. The influence of these

three parameters is depicted in Fig.(4.14) on the evolution of the homogenized diffusion coefficient D^{hom}.

— **The effect of ratio ε** (with $\delta = 0.5$ and $\phi = 0.4$)

ε quantifies the volume fraction of liquid layer ($\varphi_{ll} = 3\varepsilon(1-\phi)$). At a given saturation degree, the volume fraction of pore body water increases with decreasing ε. In Mori-Tanaka scheme, the matrix is pore body water, the latter ensures the connectivity of the pathway for solute diffusion. Therefore, the homogenized diffusion coefficient D^{hom} increases with increasing volume fraction of pore body water φ_{pw}. According to Eq.(4.24)), φ_{pw} increases with decreasing ε. Hence, as depicted in Fig.(4.14)(a), D^{hom} increases with decreasing ε. Meanwhile, it can be found that, Sr^{ll} increases with ε. When $Sr < Sr^{ll}$, all of the pore body water is drained, the liquid layer plays a dominating role in the solute diffusion.

— **The effect of constrictive factor δ** (with $\varepsilon = 0.01$ and $\phi = 0.4$)

δ quantifies the solute diffusion coefficient in liquid layer, the greater the δ the greater the solute diffusion coefficient in the liquid layer. Indeed, the homogenized diffusion coefficient D^{hom} is attributed to two contributions: solute diffusion in the pore body water and in the liquid layer. When $\phi = 0.4$ and $\varepsilon = 10^{-2}$, the volume fractions of the liquid layer and the pore body water are determined. As expected, the homogenized diffusion coefficient D^{hom} increases with δ (see Fig.(4.14)(b)). It can be also found in the figure that the variations of the red curves are minor. The reason may lie in the fact that, in Mori-Tanaka scheme, the matrix is the pore body water: the liquid layer is not the main pathway for solute diffusion. However, the effect of δ will be more significant when $Sr < Sr^{ll}$ [9], since the liquid layer is the only solute diffusion pathway.

— **The effect of porosity ϕ** (with $\varepsilon = 0.01$ and $\delta = 0.5$)

Volume fraction of pore space ϕ is the property of porous medium. As shown in

9. $\mathrm{Sr}^{ll} = \dfrac{\varphi_{ll}}{\phi} = 3\dfrac{\varepsilon(1-\phi)}{\phi}, when \phi$ and ε are determined, Sr^{ll} is also determined.

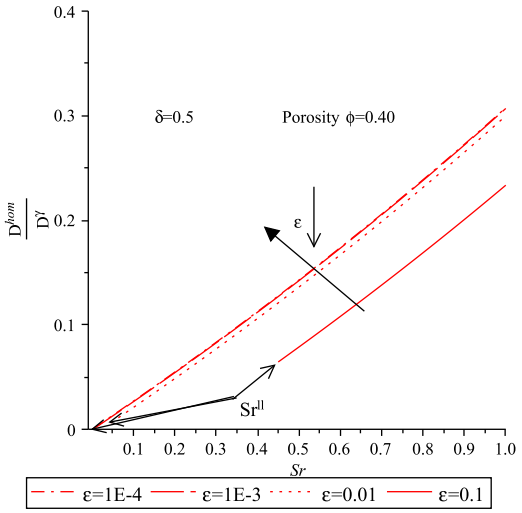

(a) The effect of ε on homogenized diffusion coefficient.

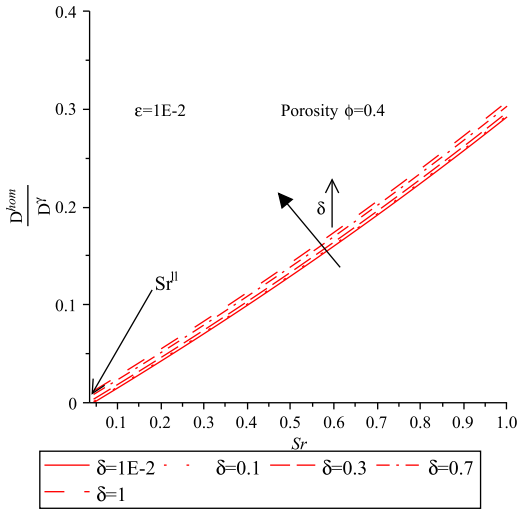

(b) The effect of δ on the homogenized diffusion coefficient.

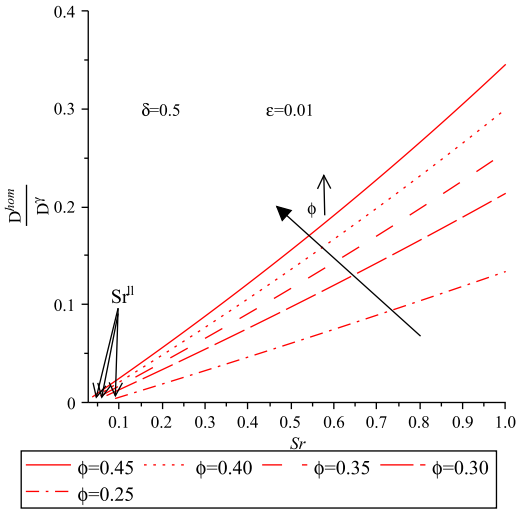

(c) The effect of ϕ on the homogenized diffusion coefficient.

Figure 4.14: Effects on the evolution of homogenized diffusion coefficient with the saturation degree, the homogenized diffusion coefficient is determined by Mori-Tanaka scheme, Sr^{ll} is related to ϕ and ε by Eq.(4.22).

Fig.(4.14)(c), the homogenized diffusion coefficient D^{hom} increases with increasing ϕ. That is because the volume fraction of pore body water φ_{pw} increases with increasing ϕ, and the former is the major pathway for solute diffusion in Mori-Tanaka scheme.

Liquid water is considered as matrix in the Mori-Tanaka scheme, which ensures the connectivity of the pathway of solute diffusion. As shown in Fig.(4.14), when the volume fraction of liquid layer is low enough (e.g. $\varepsilon \leq 0.01$), its effect is negligible in the Mori-Tanaka scheme.

4.5.2.2 Self-consistent estimate (accounting for percolation effect)

The previous section showed the Mori-Tanaka scheme does not exhibit percolation effect during desaturation process. In this section, percolation effect may be accounted for by means of the well-known self-consistent scheme. Let us now analyse the case where the a diffusive liquid layer is introduced in the one-scale morphological (see Section(4.4.1)) by means of self-consistent scheme.

A simple morphological representation of unsaturated porous media is depicted in Fig.(4.15). For the sake of simplicity, the porous medium is treated as isotropic at micro and macro scales. Uniform concentration gradient boundary conditions are considered on the REV. Three auxiliary Eshelby-type problems are introduced in order to estimate the average concentration gradient tensors in the pore body water, the liquid layer and the gaseous phase, respectively. As illustrated in Fig.(4.15), the boundary conditions of auxiliary problems are defined by an uniform auxiliary concentration gradient boundary conditions at infinity given by $\rho^{\gamma} \rightarrow \underline{H_0}.\underline{z}$ (with $\underline{z} \rightarrow \infty$).

In isotropic case, the average concentration coefficient of i^{th} phase in the auxiliary matrix is determined in Eq.(4.60). The detailed information about the determination of average concentration tensor for each phase is given in Appendix (B.2).

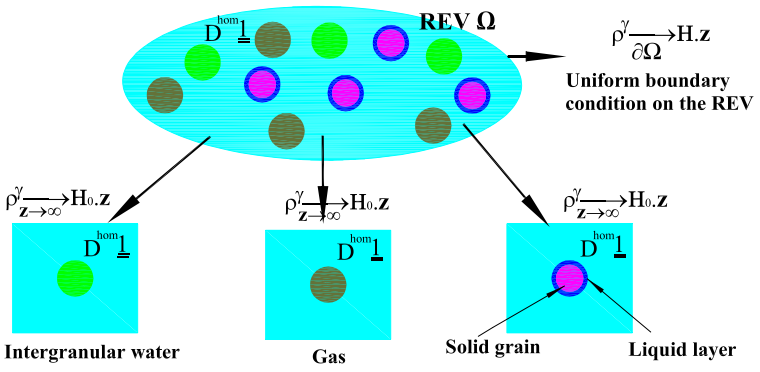

Figure 4.15: Schematic representation of unsaturated porous media with a specific polycrystalline microstructure, this kind of morphology corresponds to self-consistent scheme.

$$\begin{cases} \overline{A}_{ll} = \dfrac{3D^{hom}(\varphi_{ll}+\varphi_s)}{3D^{hom}\varphi_s + 2D^{hom}\varphi_{ll} + D^{\gamma}_{ll}\varphi_{ll}} \\ \overline{A}_s = \dfrac{3}{2}\overline{A}_{ll} = \dfrac{9D^{hom}(\varphi_{ll}+\varphi_s)}{2(3D^{hom}\varphi_s + 2D^{hom}\varphi_{ll} + D^{\gamma}_{ll}\varphi_{ll})} \\ \overline{A}_g = \dfrac{3}{2} \\ \overline{A}_{pw} = \dfrac{3D^{hom}}{2D^{hom}+D^{\gamma}} \end{cases} \tag{4.60}$$

Similarly, the volume fractions of each phase may also be estimated by Eq.(4.24). Therefore, substituting Eq.(4.24) and Eq.(4.60) into Eq.(4.25), the homogenized diffusion coefficient D^{hom} may be determined. Two limiting cases (when $\varepsilon \to 0$ and $\delta \to 0$) will be presented and discussed in the follows.

Remarks on two special cases for D^{hom}

The expressions of D^{hom} in two limiting cases are presented in Eq.(4.61).

$$\begin{cases} D^{hom}(\varepsilon \to 0) = \dfrac{3\phi Sr - 1 + \sqrt{(1-3\phi Sr)^2}}{4} D^{\gamma} & (a) \\ D^{hom}(\delta \to 0) = \dfrac{\sqrt{[9(1-\phi)\varepsilon + (1-3\phi Sr)]^2} - [9(1-\phi)\varepsilon + (1-3\phi Sr)]}{4} D^{\gamma} & (b) \end{cases} \tag{4.61}$$

As shown in Eq.(4.61)(a), when $3\phi Sr > 1$, $D^{hom}(\varepsilon \to 0) = \dfrac{3\phi Sr - 1}{2}$(while when $3\phi Sr \leq 1$, $D^{hom}(\varepsilon \to 0) = 0$). Indeed, when $\varepsilon \to 0$, the liquid layer may be neglected, it is thus the special case shown in Eq.(4.10) (for self-consistent scheme), the volume fraction of the pore body water being ϕSr.

Similarly, when $\phi Sr > \dfrac{1}{3} + 3(1-\phi)\varepsilon$, $D^{hom}(\delta \to 0)$ in Eq.(4.61)(b) can be expressed as:

$$D^{hom}(\delta \to 0) = \frac{3\phi Sr - 1 - 9(1-\phi)\varepsilon}{2} = \frac{3[\phi Sr - 3(1-\phi)\varepsilon] - 1}{2} \tag{4.62}$$

Eq.(4.62) is also a special case shown in Eq.(4.10)(for self-consistent scheme), since liquid layer is not diffusive and may be treated like the non diffusive solid phase, the volume fraction of pore body water being now $\phi(Sr - Sr^{ll})$.

Thus, we can consider that these two special cases presented in Eq.(4.61) validate the 3-D micromechanics model (with self-consistent scheme) presented in this section.

Parameters ε, constrictive factor δ and porosity ϕ are incorporated in the homogenized diffusion coefficient D^{hom} estimated by self-consistent scheme. In the follows, a discussion is presented in order to better understand the physical effects of these three parameters on D^{hom}. The effects of these three parameters on D^{hom} are plotted in Fig.(4.16).

— **The effect of ratio ε** (with $\delta = 0.5$, $\phi = 0.4$)

At given ϕ and δ, ε quantifies the volume fraction of liquid layer on the homogenized diffusion coefficient within unsaturated porous media. In self-consistent scheme, the introduction of liquid layer ensures the connectivity of the pathway for solute diffusion. From Eq.(4.54), the homogenized diffusion coefficient is superposition of

two parts: solute diffusion contributed by pore body water and solute diffusion by liquid layer. According to Eq.(4.60), we have:

$$\begin{cases} \overline{A}_{ll} = \dfrac{3D^{hom}}{3D^{hom} + (D_{ll}^{\gamma} - D^{hom})\dfrac{\varphi_{ll}}{\varphi_{ll}+\varphi_s}} \\ \overline{A}_{pw} = \dfrac{3D^{hom}}{3D^{hom} + (D^{\gamma} - D^{hom})} \end{cases} \tag{4.63}$$

It is readily found that $\overline{A}_{ll} > \overline{A}_{pw}$, since $D^{\gamma} > D_{ll}^{\gamma}$, $D^{\gamma} > D^{hom}$ and $\dfrac{\varphi_{ll}}{\varphi_{ll}+\varphi_s} < 1$. It means that in self-consistent scheme, the liquid layer is a more efficient pathway for solute diffusion than pore body water. Therefore, at given porosity (ϕ=0.4), the more volume fraction of the liquid layer, the greater the homogenized diffusion coefficient D^{hom}, as illustrated in Fig.(4.16)(a). In addition, owing to the total drainage of pore body water, the curves are terminated at Sr^{ll} (Sr^{ll} is determined by Eq.(4.22)). When $Sr < Sr^{ll}$, the liquid layer dominates the solute diffusion.

— **The effect of constrictive factor $\boldsymbol{\delta}$** (with $\varepsilon = 0.01$, $\phi = 0.4$)

δ quantifies the solute diffusivity in the liquid layer. The greater δ, the greater the solute diffusion coefficient in liquid layer. As discussed previously, the liquid layer ensures the connectivity of the pathway for solute diffusion and is a more efficient pathway for diffusion than pore body water. Therefore, as depicted in Fig.(4.16)(b), when the volume fraction of pore space ϕ and the volume fraction of liquid layer $3\varepsilon(1-\phi)$ are constant, the homogenized diffusion coefficient D^{hom} increases with increasing δ (the solute diffusion coefficient in liquid layer). Similarly, the volume fraction of liquid layer is treated as a constant during desaturation process, therefore, as illustrated in the figure, the curves terminated at Sr^{ll}.

— **The effect of volume fraction of pore space $\boldsymbol{\phi}$** (with $\varepsilon = 0.01$, $\delta = 0.5$)

The volume fraction of the liquid layer φ_{ll} is closely related to the volume fraction of pore space ϕ by $\varphi_{ll} = 3\varepsilon(1-\phi)$; φ_{ll} thus increases with decreasing ϕ. Moreover, the volume fraction of the pore body water can be estimated by $\varphi_{pw} = \phi Sr - \varphi_{ll}$ (see Eq.(4.24)), φ_{pw} thus increases with increasing ϕ.

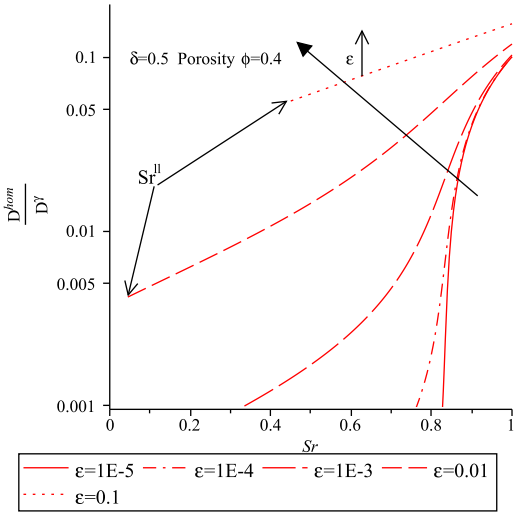

(a) The effect of ε on homogenized diffusion coefficient D^{hom}.

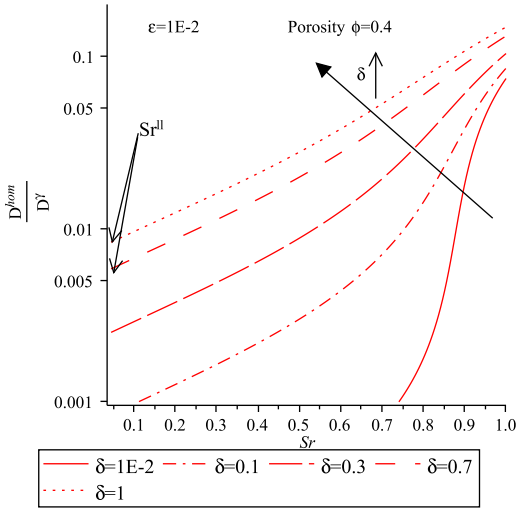

(b) The effect of δ on the homogenized diffusion coefficient D^{hom}.

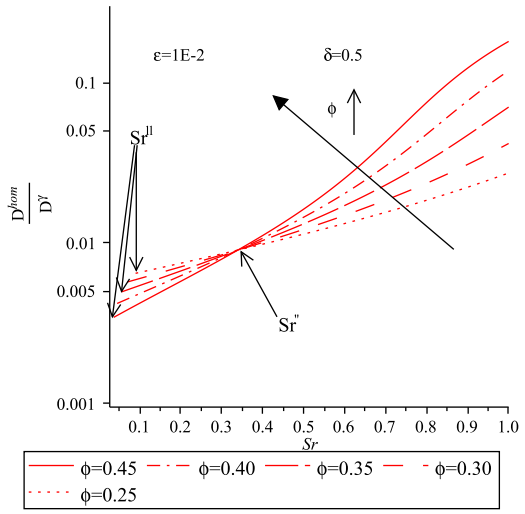

(c) The effect of ϕ on homogenized diffusion coefficient D^{hom}.

Figure 4.16: Influence of three parameters on the evolution of homogenized diffusion coefficient D^{hom} with the saturation degree, the homogenized diffusion coefficient is determined by self-consistent scheme; the curves terminate at Sr^{ll} which can be calculated by Eq.(4.22); when $Sr < Sr^{ll}$, the liquid layer governs the solute diffusion.

As discussed in Section(4.5.1.2), when $Sr > 1/(3\phi)$ and $\phi \geq 1/3$, the homogenized diffusion coefficient is the superposition of two contributions: solute diffusion in pore body water D_{pw}^{hom} and that in liquid layer D_{ll}^{hom}. Owing to percolation effect, the solute diffusion contributed by the pore body water D_{pw}^{hom} decreases greatly with decreasing saturation degree Sr. Nevertheless, the solute diffusion contributed by the liquid layers is independent on saturation degree Sr but increases with decreasing ϕ (φ_{ll} increases with decreasing ϕ). When $Sr < Sr''$ (Sr'' is depicted in Fig.(4.16)(c)) [10], the solute diffusion contributed by liquid layer prevails over that contributed by the pore body water, the liquid layer dominates the solute diffusion; the homogenized diffusion coefficient D^{hom} increases with decreasing ϕ since φ_{ll} increases with decreasing ϕ.

4.6 Experimental results analysis

Let us now try to compare the simulation results from micromechanics models with the experimental results. In the previous section, the liquid layer as local phase is accounted for in the unsaturated diffusion models. However, the characteristic thickness of the liquid layer (the intergranular layer, the wetting layer and the water film) is not specified in the theses models. As introduced previously, in unsaturated porous medium, liquid layer represents the superposition of the water film, the wetting layer and the intergranular layer.

According to the evolution of water distribution in unsaturated granular material introduced in Section(3.1), the water film is stabilized by disjoining pressure and its characteristic size is typically nanometric [22]. It dominates the solute diffusion transport at low saturation degree. In addition to the water film, owing to the special morphology of the materials (surface characteristic of sand grains), wetting layers whose characteristic thickness is micron are stabilized by capillary pressure and play a significant role in intermediate saturation degree. At high saturation degree, the intergranular water are in-

10. Sr'' is denoted as the saturation degree where the contribution of solute diffusion in the pore body water is equal to that in liquid layer.

terconnected through pore throat. Therefore, to ensure the connectivity of intergranular water in self-consistent scheme, it is thus reasonable to assume that part of intergranular water (intergranular layer) is attached on the solid grains.

In the follows, we develop a micromechanics model accounting for the different components of the liquid layer (c.f., micromechanics model in Section(4.5.2.2)) to estimate the homogenized solute diffusion coefficient. We then compare the simulation results with experimental results. Owing to the polycrystalline morphology of the granular materials, self-consistent scheme is used to estimate their homogenized diffusion coefficient.

4.6.1 Homogenized diffusion coefficient of unsaturated granular materials

First, the main characteristics of sand and glass beads are listed in Table(4.5).

Table 4.5: Characteristics of two kinds of granular material [211].

-	Unit	Glass beads	Sand
Porosity	%	38.0	42.2
Grain diameter	μ m	75	105-210
Bulk density	g.cm^{-3}	1.53	1.54
Grain density	g.cm^{-3}	2.47	2.65
Tracer	-	NO_3^{-1}	NO_3^{-1}
Saturated diffusion coefficient	$m^2 \cdot s^{-1}$	0.555×10^{-9}	0.590×10^{-9}
D^γ in bulk water [158]	$m^2 \cdot s^{-1}$	1.90×10^{-9}	1.90×10^{-9}

The overall solute diffusion consists of contributions of intergranular layer, wetting layer, water film and pore body water. In addition to these four phases, there also exist non diffusive gaseous phase and solid phase in unsaturated porous medium. When the granular material is assumed to be isotropic at local scale and macro scale, the morphology of the unsaturated solute diffusion in granular material can be depicted as in Fig.(4.17).

As presented in Section(3.1), the wetting layers (denoted as subscript wl) consist of continuous capillary water trapped in pendular rings, grooves and pits on solid grains. In this section, a parameter χ characterizing the ratio of the thickness of wetting layer t over

solid grain radius R_s is defined as:

$$\chi = \frac{t}{R_s} \tag{4.64}$$

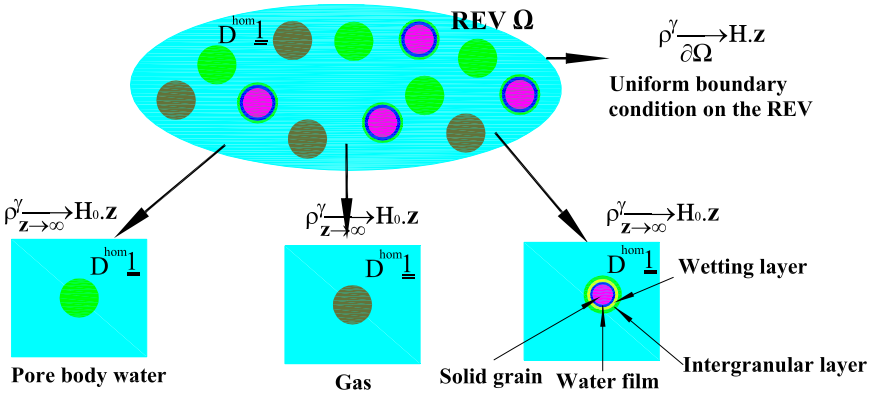

Figure 4.17: Morphological representation of water distribution in unsaturated granular material, D^{hom} and ρ^{γ} are the homogenized solute diffusion coefficient and solute concentration; the intergranular layer, the wetting layer and the water film surrounded on the solid grains are specified to characterize the evolution of the liquid layer during the desaturation process.

Since the typical characteristic size of wetting layer (micron scale [22]) is far smaller than the characteristic diameters of sand and glass beads (several hundreds microns), similar to Eq.(4.21), the volume fraction of capillary layer may be estimated as:

$$\varphi_{wl} \approx 3\chi(1-\phi) \qquad \text{when } t \ll R_s \tag{4.65}$$

In the same way, the volume fraction of water film φ_f can also be estimated by:

$$\varphi_f \approx 3\varepsilon(1-\phi) \qquad \text{when } h \ll R_s \tag{4.66}$$

where h is here the thickness of water film (in the previous sections, h was the thickness of the liquid layer), $\varepsilon = \dfrac{h}{R_s}$.

Intergranular water consists of intergranular layer and pore body water. The volume fraction of intergranular water is $\phi Sr - \varphi_{wl} - \varphi_f$. It is not easy to quantify the volume fractions of the intergranular layer and the pore body water during desaturation process. Therefore, a parameter β is introduced to quantify the volume fractions of the pore body water and the intergranular layer:

$$\begin{cases} \varphi_{ig} = \beta(\phi Sr - \varphi_{wl} - \varphi_f) \\ \varphi_{pw} = (1-\beta)(\phi Sr - \varphi_{wl} - \varphi_f) \end{cases} \tag{4.67}$$

The volume fractions of each phase are listed in Table(4.6).

Table 4.6: Volumetric fraction of each phase within unsaturated granular material.

-	Volumetric fraction
Solid φ_s	1- ϕ
Gas φ_g	ϕ (1-Sr)
Wetting layer φ_{wl}	3 $\chi(1-\phi)$
Water film φ_f	3 $\varepsilon(1-\phi)$
Intergranular layer φ_{ig}	$\beta\phi Sr - 3\chi(1-\phi) - 3\varepsilon(1-\phi)$
Pore body water φ_{pw}	(1-β)$\phi Sr - 3\chi(1-\phi) - 3\varepsilon(1-\phi)$

When the volume fractions of each phase are determined, when the diffusion coefficients and concentration tensors of each phase are isotropic, the homogenized solute diffusion coefficient can be revised from Eq.(4.9) as:

$$D^{hom} = \overline{DA} = \sum_i \varphi_i D^i \overline{A_i} \tag{4.68}$$

where $\overline{A}_i$ is the average concentration tensor for i^{th} phase ($i \in \{f, g, s, wl, ig, pw\}$), the average concentration coefficients of each phase $\overline{A}_i$ are given in Appendix(B.2),; φ_i is the volume fraction of i^{th} phase ($i \in \{f, g, s, wl, ig, pw\}$).

4.6.2 Results and discussion

The ratio ε is taken as 10^{-5} to ensure the thickness of the water film being in the order of nanometer (as the radii of solid grain of sand and glass beads are in the order of 100 μm). χ is taken as 10^{-3} to ensure the thickness of the wetting layer being in the order of microns. A value of diffusive constrictive factor of Na^+-water film system is estimated to be 0.32 [248] when water film is three molecular layers (1 nm) thick. Hence, $\delta = 0.32$ is adopted here. At various β, the evolutions of normalized homogenized solute diffusion coefficient $D^{hom}/D^{hom}(Sr = 1)$ with the saturation degree for glass beads and sand are plotted in Fig.(4.18).

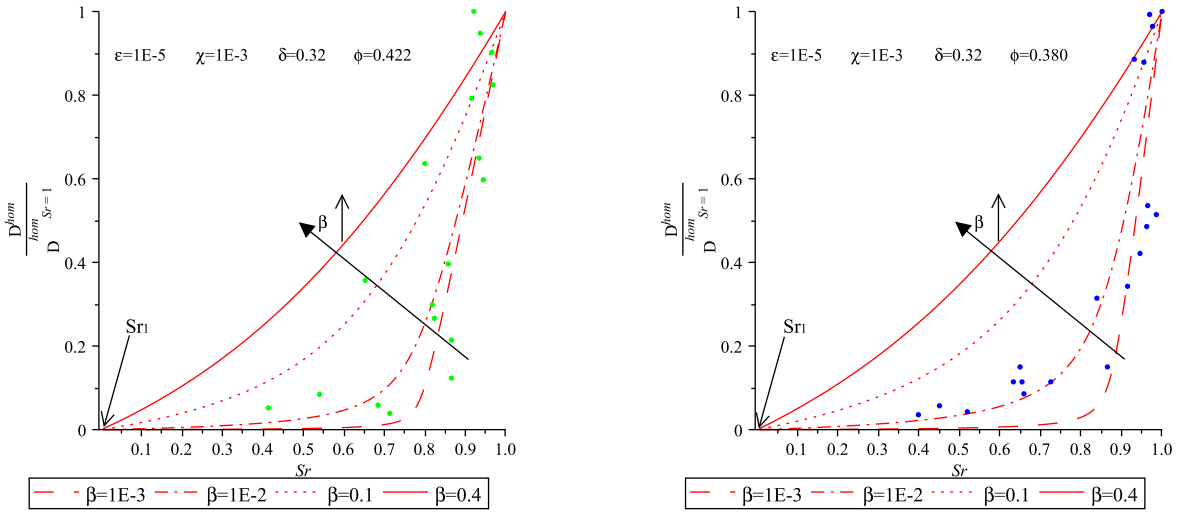

(a) Glass beads.

(b) Sand.

Figure 4.18: Dependence of the normalized diffusion coefficient of nitrate on the various saturation degrees. It should be noted that $Sr_1 = \dfrac{\varphi_f + \varphi_{wl}}{\phi}$, the green and blue points are experimental results after [211].

According to Fig.(4.18), the evolution of the diffusion coefficients of sand and glass beads exhibits notable percolation effect. The modelling results for glass beads and sand agree well with experimental results when β is taken as 10^{-2}. In this case, when $Sr = 1$, the thickness of the intergranular layer e can be estimated by:

$$e = \frac{\varphi_{ig}}{3\varphi_s} R_s = \frac{\beta\phi Sr - 3\chi(1-\phi) - 3\varepsilon(1-\phi)}{3(1-\phi)} R_s \quad \text{with } Sr = 1 \quad \text{and } \beta = 10^{-2} \tag{4.69}$$

According to Eq.(4.69), the thickness of intergranular layers in sand and glass beads is approximately $10^{-3}R_s$, R_s is the radius of the sand or glass beads. The thickness of the intergranular layer is thus nearly the same as that of wetting layer ($t = 10^{-3}R_s$). We may thus infer that there may not exist intergranular layer in these two granular materials, the intergranular layer merges with the wetting layer. Therefore, the intergranular water in these two granular materials is mainly pore body water.

The evolution of the water distribution owing to the microstructure of the materials and matrix potential is not accounted for in this simulation. In the following chapter, a simulation of the evolution of homogenized diffusion coefficient with saturation degree within unsaturated granular materials will be carried out. The water retentions of granular materials will be accounted for to determine the saturation degree.

4.7 Summary

Self-consistent estimate is considered to be well adapted to represent the polycrystalline microstructure while Mori-Tanaka estimate is expected to be good for matrix+inclusion microstructure.

In order to study the microstructure effect on the solute diffusion, several micromechanics models for solute diffusion within porous medium with one-scale and two-scale microstructures are developed and discussed. The liquid layer is not accounted for in these models. In one-scale microstructure, the homogenized solute diffusion coefficient D^{hom} exhibits strong percolation threshold when it is estimated with self-consistent scheme; which is not the case when it is estimated with differential schemes and Mori-Tanaka scheme, as the matrix in these two schemes is water. In two-scale microstructure, MT-SC (level I and

level II are estimated with self-consistent and Mori-Tanaka schemes), SC-SC and MT-MT models are developed. The influencing parameters such as volume fraction of pore space ϕ and ratio of macro pores α on the homogenized diffusion coefficient D^{hom} are discussed. The simulation results show that, in MT-SC and SC-SC models, the percolation effect decreases with increasing ϕ and ratio of macro pores α; in SC-SC and MT-MT models, the saturated homogenized diffusion coefficient $D^{hom}(Sr = 1)$ increases with increasing porosity ϕ and decreasing α. In MT-MT model, there is no percolation effect and $D^{hom}(Sr = 1)$ increases with increasing ϕ and decreasing α.

The pore water in unsaturated porous media is decomposed into the pore body water and the liquid layer. The effect of liquid layer is accounted for in the enriched micromechanics models for solute diffusion. Starting with a 2-D idealization of liquid layer (the volume fraction of water film is neglected), the effect of solute diffusion in 2-D liquid layer is discussed. The homogenized diffusion coefficient D^{hom} estimated by self-consistent scheme consists of components contributed by liquid layer and pore body water water when $Sr > \frac{1}{3\phi}$ and $\phi \geq 1/3$. The liquid layer dominates solute diffusion when $Sr \leq \frac{1}{3\phi}$ or $\phi < 1/3$.

Liquid layer is treated as 3-D phase in the following enriched micromechanics models, the volume fraction of liquid layer is considered in this model. By means of these models, the effects of ϵ (ratio of the thickness of liquid layer over the radius of solid grain), volume fraction of pore space ϕ and constrictive factor of liquid layer δ on the homogenized diffusion coefficient D^{hom} are discussed in self-consistent scheme and Mori-Tanaka scheme.

Based on the physical characterization of the water distribution in unsaturated sand and glass beads, a micromechanics model accounting for the intergranular layer, wetting layer and water film is developed for these two granular materials. The simulation results show that the normalized homogenized diffusion coefficient agrees well with the experimental results. These two materials exhibit strong percolation effects and self-consistent scheme is perfectly good for characterizing these effects. Owing to strong percolation effects, the intergranular water in these two granular materials may mainly distribute as pore body water, the volume fraction of intergranular layer is minor.

Chapter 5

Application: micromechanical modelling of solute diffusion in unsaturated sand

Contents

5.1 Introduction 122

5.2 Input information and assumptions 122

5.3 Phase volume fractions 124

5.3.1 Volume fractions of the intergranular layer and the pore body water 124

5.3.2 Volume fractions of the solid phase, gaseous phase and the water film 126

5.4 Results and discussion 129

5.4.1 Evolution of the normalized solute diffusion coefficient with saturation degree for Beaver Creek sand 130

5.4.2 Evolution of the normalized solute diffusion coefficient with saturation degree for Romkens' sand 131

5.5 Conclusion 133

5.1 Introduction

Lim et al. [159] and Romkens et al. [211] have carried out two sets of the solute diffusion experiment within unsaturated sand. A detailed description of the procedure for diffusion testing is given in their works [159, 211]. In this section, a micromechanics model for solute diffusion is employed to simulate their experimental results. To avoid the ions-surface interaction, the experimental results of nonreactive Cl^- and NO_3^{-1} instead of K^+ are adopted to compare with the simulation results.

Granular materials may exhibit pore sizes with different order depending upon their granulometry. These materials do not exhibit clear matrix+inclusion morphologies since any phase within these materials does not play the role of a cemented domain. Their apparent polycrystalline nature rather suggest a perfect disordered microstructure, which is classically accounted for by the well-known self-consistent scheme. Moreover, in order to manage the granulometry, we introduce in the model a continuous grain size distribution function. The latter will account, in a first approximation, for the specific microstructure of granular material.

For other geomaterials, the same methodology may also be feasible by accounting for the pore size distribution function, which is normally obtained by experimental apparatuses (e.g., mercury intrusion porosimetry and nitrogen adsorption).

5.2 Input information and assumptions

It is assumed that, during the desaturation (drainage) process, the pores are emptied from the bigger ones to the smaller ones in a well organized arrangement [85].

Morphological representation and concentration tensors of each phase

The evolution of the water distribution in unsaturated granular material is introduced in Section(3.1). Based on this physical characterization, a morphological model for the

unsaturated granular material is presented in Fig.(4.17).

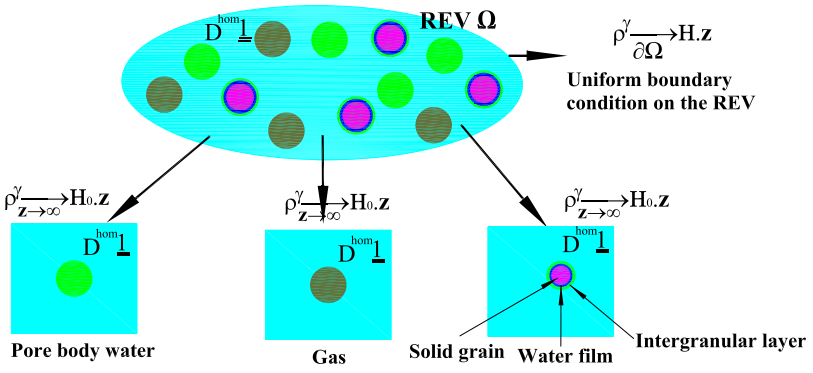

Figure 5.1: Morphological representation of unsaturated sand.

However, it is difficult to quantify and distinguish the volume fractions of the intergranular layer, the wetting layer and water film. Therefore, two assumptions are made: 1) the wetting layer is treated as a part of the intergranular layer, in other words, the wetting layer is a kind of intergranular layer at intermediate saturation degree; 2) the intergranular layers are interconnected when $Sr \geq Sr^r$, Sr^r is the residual saturation degree; the intergranular layers are discontinuous when $Sr < Sr^r$. In isotropic case, based on these simplifications, the morphology of unsaturated sand is depicted in Fig.(5.1).

The concentration tensors of each phase in isotropic case are given in Appendix(B.2).

Thickness of the water film

The thickness of the water film adsorbed on the solid grains can be estimated by Eq.(3.24), Eq.(3.26) and Eq.(3.27) [1]. The mineral of the sand is quartz, thus, the physical parameters for determining the thickness of water film are given in Table(3.1). Meanwhile, owing to the large magnitude of sand size (e.g., R_s is about several hundreds of μm), the capillary effect induced by grains size ($\frac{2\gamma_{lg}}{R_s}$) is omitted in Eq.(3.27).

Characteristics of two sands

1. The concentrations of the solution are changed in these cases.

The physical characteristics of the two sands are listed in Table(5.1).

Table 5.1: Characteristics parameters for sand and solution[159, 211]

Property	Unit	Beaver Creek sand	Romkens' sand [1]
Porosity	%	38.2 ± 0.3	42.2
Residual saturation Sr^r	%	9	7[2]
Dry bulk density	$\mathrm{Kg \cdot m^{-3}}$	1647 ± 7	1537 ± 19
Particle size distribution	-	Fig.(5.3)	105-210 μm
Tracer	-	Cl^-	NO_3^{-1}
Initial concentration of tracer	$\mathrm{mol \cdot L^{-1}}$	0.02	0.1
D^γ in bulk water [158]	$\mathrm{m^2 \cdot s^{-1}}$	2.03×10^{-9}	1.90×10^{-9}
[3] Saturated diffusion coefficient	$\mathrm{m^2 \cdot s^{-1}}$	0.535×10^{-9}	0.590×10^{-9}
Temperature	K	298	303

[1] The sand is not specified in Romkens's work, for clarification, the sand is denoted as Romkens's sand.

[2] The residual saturation degree is interpreted as the critical saturation degree where water film governs the solute diffusion. The residual saturation degree is not given in Romkens's work, it's a rough estimation from the water retention of Romkens's sand.

[3] The tracer is Cl^-, saturated diffusion coefficient has been modified in our definition for homogenized diffusion coefficient. The relation between ours (D^{hom}) and the one in literature (D_e) is: $D^{hom} = \phi D_e$, where ϕ is the porosity.

5.3 Phase volume fractions

The configuration of water phase is essential to the solute diffusion within unsaturated porous media. Therefore, estimating the volume fraction of each phase precisely is significant to determine the homogenized solute diffusion coefficient in unsaturated porous media.

5.3.1 Volume fractions of the intergranular layer and the pore body water

In the model, the intergranular water is divided into two parts: intergranular layer and pore body water. The evolution of the volume fractions of intergranular layer φ_{ig} and the pore body water φ_{pw} with capillary pressure is not easy to be determined. When the

saturation degree Sr is greater or lower that the residual saturation degree Sr^r, the pore body water and intergranular layer exhibit different regimes.

Saturation degree $Sr \geq Sr^r$

When $Sr > Sr^r$, φ_{ig} is assumed to be proportional to the total volume fraction of intergranular water $(\varphi_{pw} + \varphi_{ig})$, that is $\varphi_{ig} = \beta(\phi Sr - \varphi_f)$, where β is the proportional parameter, φ_f is the volume fraction of the water film. Correspondingly, the volume fraction of pore body water is $\varphi_{pw} = (1-\beta)(\phi Sr - \varphi_f)$.

Saturation degree $Sr < Sr^r$

When $Sr < Sr^r$, the intergranular layers are discontinuous and their effect on the solute diffusion is negligible, the water film then governs the solute diffusion. Hence, φ_{ig} should be taken to be 0 in the determination of homogenized diffusion coefficient D^{hom}. Nevertheless, in determining the saturation degree Sr, φ_{ig} is non-zero and Sr is determined by $\dfrac{\varphi_f + \varphi_{ig}}{\phi}$.

In summary, φ_{ig} and φ_{pw} can be distinguished as two regimes as:

$$Sr \geq Sr^r : \begin{cases} \varphi_{ig} = \beta(\phi Sr - \varphi_f) \\ \varphi_{pw} = (1-\beta)(\phi Sr - \varphi_f) \end{cases} \qquad Sr < Sr^r : \begin{cases} \varphi_{ig} \neq 0 & \text{In determining } Sr \\ \varphi_{ig} = 0 & \text{In determining } D^{hom} \\ \varphi_{pw} = 0 \end{cases} \tag{5.1}$$

Water retention curves

In order to relate the saturation degree Sr to capillary pressure P_c (c.f. matric suction ψ in Section(3.5)), Fredlund et al. [105] and Campbell [36] proposed two empirical relations for high saturation degree $Sr \geq Sr^r$ and low saturation degree $(Sr < Sr^r)$, respectively:

$$\begin{cases} Sr = Sr^r + (1-Sr^r)\left(\dfrac{1}{\ln[\exp(1) + (\frac{P_c}{a})^n]}\right)^m & \text{when } Sr \geq Sr^r \quad (a) \\ Sr = Sr^r\left(1 - \dfrac{\log_{10}(P_c/10)}{5}\right) & \text{when } Sr < Sr^r \quad (b) \end{cases} \tag{5.2}$$

where a, m and n are the fitting parameters for given material, the fitting parameters for

the two kinds of sand are listed in Table(5.2).

Table 5.2: Fitting parameters for two kinds of sand

Parameters	a	n	m
Beaver Creek sand [159]	3	10	2
Romkens' sand	5.4215	12.0617	1.9401

The water retention curves for Beaver Creek sand and Romkens' sand are depicted in Fig.(5.2).

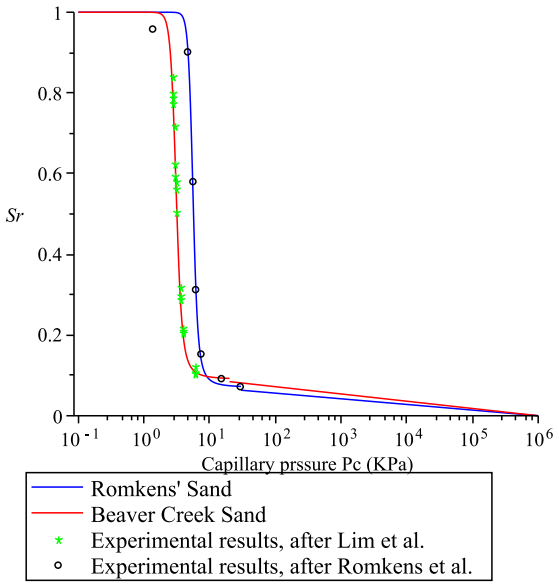

Figure 5.2: Water retention curves for Beaver Creek sand (red curve) and Romkens' sand (blue curve), the curves are fitted by Eq.(5.2). The capillary pressures associated with residual saturation degrees are 20 KPa and 30 KPa for Beaver Creek sand and Romkens' sand, respectively. Experimental results are after [159, 211].

Combining Eq.(5.1) and Eq.(5.2), φ_{pw} and φ_{ig} can be determined[2].

5.3.2 Volume fractions of the solid phase, gaseous phase and the water film

Volume fractions of solid grains and gaseous phase

2. The volume fraction of the water film φ_f will be determined in Section(5.3.2).

The volume fractions of solid grains and gaseous phase are given in Eq.(5.3):

$$\begin{cases} \varphi_s = 1 - \phi \\ \varphi_g = (1 - Sr)\phi \end{cases} \tag{5.3}$$

Volume fraction of water film

As presented in previous section, the volume fraction of the water film may be estimated by Eq.(4.21) in which $\varepsilon = \dfrac{h}{R_s}$ is introduced. In the previous chapters, ε is taken as a constant. Therefore, Eq.(4.21) is only valid in mono disperse granular material. Generally, granular materials exhibit certain granulometry (grain size distribution). Thus, to estimate the volume fraction of the water film, Eq.(4.21) should be modified to account for the grain size distribution.

An empirical grain size distribution function for Beaver Creek sand is suggested by Fredlund et al. [106] as:

$$P_p(D) = \frac{1}{\ln[\exp(1) + (\frac{g_a}{D})^{g_m}]}[1 - [\frac{\ln(1 + \frac{D_r}{D})}{\ln(1 + \frac{D_r}{D_m})}]^7] \tag{5.4}$$

where $P_p(D)$ is the percent of grains passing the diameter D; the fitting parameters for Beaver Creek sand are determined as $g_a = 0.2485$, $g_m = 4.8109$, $g_n = 1.7015$, $D_m = 0.0001$, $D_r = 36.6213$ [106].

Correspondingly, the probability density function $\nu(D)$ can be derived by differentiating the grain size distribution function $P_p(D)$ with respect to grain diameter D as:

$$\nu(D) = \frac{\mathrm{d}P_p(D)}{\mathrm{d}D} \tag{5.5}$$

The grain size distribution curve and probability density function curves are illustrated in Fig.(5.3).

At a infinitesimal diameter range $[D, D + \mathrm{d}D]$ ($\mathrm{d}D \ll D$), the volume fraction of solid grain $\mathrm{d}\varphi_s$ can be estimated:

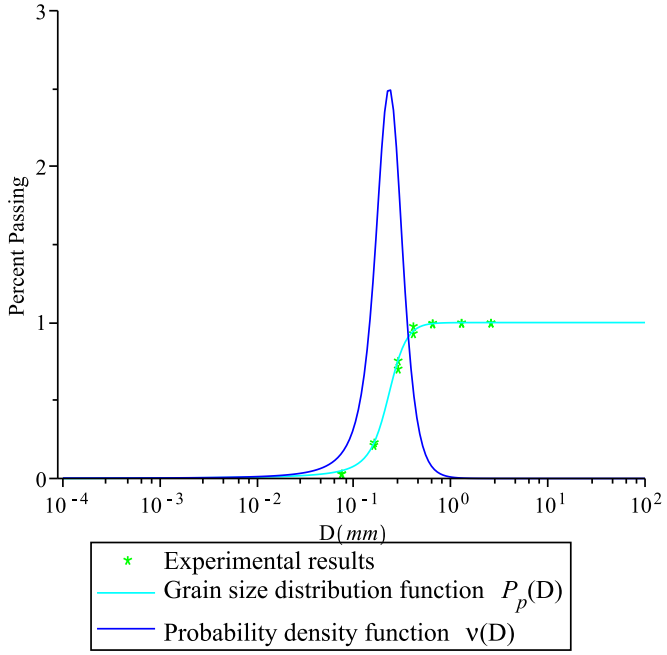

Fig 5.3: Particle size distribution of Beaver Creek sand, the fitting curve are after Fredlund et al.[106], the experimental results are after Bruch et al.[31].

$$\mathrm{d}\varphi_s = \nu(D)\mathrm{d}D \tag{5.6}$$

If the solid grains are assumed to be spherical in shape, according to Eq.(4.21), the infinitesimal volume fraction of the water film $\mathrm{d}\varphi_f$ at $[D, D+\mathrm{d}D]$ can be estimated:

$$\mathrm{d}\varphi_f = \frac{3h}{D/2}\mathrm{d}\varphi_s = \frac{6h}{D}\nu(D)\mathrm{d}D \tag{5.7}$$

The volume fraction of water film φ_s can then be evaluated by integrating Eq.(5.7):

$$\varphi_f = \int_{D_{min}}^{D_{max}} \frac{6h}{D}\nu(D)\mathrm{d}D = 6h\int_{D_{min}}^{D_{max}} \frac{\nu(D)}{D}\mathrm{d}D \tag{5.8}$$

where D_{min} and D_{max} are the minimum and maximum diameter of sand. For Beaver Creek sand, $D_{min} = 10^{-3}$ mm and $D_{max} = 10$ mm.

Unfortunately, the grain size distribution curve for Romkens' sand is not presented in Romkens' work. However, we know that the grain sizes of Romkens' sand distributed in a

narrow range of 105 μ m to 210 μ m [211]. In this case, the grain size of Romkens' sand is assumed to be mono disperse ($\nu(D) = 1$ and the magnitude of the diameter of Romkens' sand is assumed to be $D = (105 + 210)/2 \approx 150$ μm. Hence, the volume fraction of the water film in Romkens' sand can also be determined by Eq.(5.8).

5.4 Results and discussion

In the simulation, it is assumed that the solute diffusion coefficient within water film $D_f^\gamma = \delta D^\gamma$. As shown in Fig(5.2), the capillary pressures associated with the residual saturation degree for Beaver Creek sand and Romkens' sand are approximately 20 KPa and 30 KPa, respectively. At these capillary pressures (20 KPa and 30 KPa), according to Eq.(3.26) and Eq.(3.27), the corresponding thicknesses of water film for Beaver Creek sand and Romkens' sand are about 10.9 nm and 10.1 nm, respectively. As discussed in Section(3.6.3), when thickness of water film is greater than 10 nm, δ can be taken to be 1.

When the thickness of water film is less than 10 nm, the solute hindrance effect in water film is expected and thus $\delta < 1$. Generally, the constrictive factor δ is not a constant and it decreases with thickness of water film. However, for the simplification, when the thickness of water film is less than 10 nm, the constrictive factor δ is regarded as a varied parameter (<1) during the thinning of water film at low saturation degree ($Sr < Sr^r$).

As shown in Section(4.5.2), in isotropic case, the homogenized solute diffusion coefficient D^{hom} within unsaturated sand can be determined by:

$$D^{hom} = \frac{\varphi_f \overline{A}_f \delta D^\gamma + \varphi_{ig} \overline{A}_{ig} D^\gamma + \varphi_l \overline{A}_l D^\gamma}{\varphi_f \overline{A}_f + \varphi_{ig} \overline{A}_{ig} + \varphi_l \overline{A}_l + \varphi_s \overline{A}_s + \varphi_g \overline{A}_g} \tag{5.9}$$

where, $\overline{A}_i$ and φ_i are the average concentration tensors and volume fraction for i-th phase, $i \in \{f, il, l, s, g\}$.

As discussed in previous section, the self-consistent scheme is employed to estimate the concentration tensors of each phase $\overline{A}_i$, which is detailedly presented in Appendix(B.2). The volume fractions of each phase are presented in Section(5.3). Therefore, the homog-

enized diffusion coefficient D^{hom} in unsaturated sand can be estimated by Eq.(5.9). The dependency of the normalized diffusion coefficient on saturation degree for the two types of sand at varied β ($Sr \geq Sr^r$) and δ ($Sr < Sr^r$) are depicted in Fig(5.4) and Fig(5.5).

5.4.1 Evolution of the normalized solute diffusion coefficient with saturation degree for Beaver Creek sand

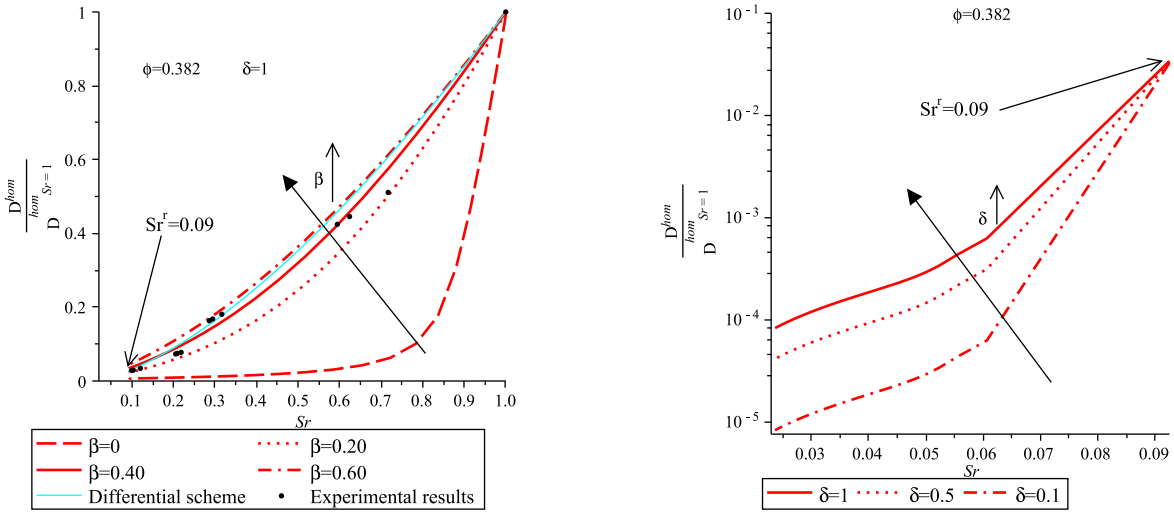

(a) $Sr \geq Sr^r$.

(b) $Sr < Sr^r$.

Figure 5.4: Evolution of normalized homogenized diffusion coefficient with saturation degree for Beaver Creek sand, experimental results are after [159].

$Sr \geq Sr^r$

Continuous intergranular layers are assumed to surround the sand grain when $Sr \geq Sr^r$. φ_{ig} decreases with saturation degree (as shown in Eq.(5.1)). Here, β quantifies the percentage of volume fraction of intergranular layers φ_{ig} over total intergranular water (intergranular layer and pore body water). When the homogenized solute diffusion coefficient D^{hom} is taken as 0.535×10^{-9} (the saturated diffusion coefficient listed in Table(5.1)), we have $\beta \approx 0.60$.

As shown in Fig(5.4)(a), the normalized homogenized diffusion increases with increasing β. When $\beta = 0.4$, the modelling result agrees well with experimental results. In the follows,

we will validate the feasibility of $\beta = 0.4$.

When $\beta = 0.4$, the average thickness of the intergranular layer is estimated to be 2.2 μm [3] in fully saturated Beaver Creek sand. The value sounds reasonable since it lies in the order of magnitude of roughness of sand (microns) [258]. Furthermore, when $\beta = 0.4$, D^{hom} determined by the model is 0.481×10^{-9} m^2.s^{-1}, which is comparable with the experimental value 0.535×10^{-9} m^2.s^{-1}.

$Sr < Sr^r$

When $Sr < Sr^r$, the pore body water is drained, the intergranular layers become discontinuous and the water films govern the solute diffusion. As presented in Eq.(5.1), the discontinuous intergranular layers contribute to the saturation degree while their contribution to the solute diffusion is neglected. Therefore, water film dominates the solute diffusion when $Sr < Sr^r$. As discussed previously, the thickness of water film is lower than 10 nm, hence the solute hindrance effect (constrictive factor δ) should be taken into account. The normalized homogenized diffusion coefficients at varied δ are depicted in Fig(5.4)(b). It can be seen from the figure that the normalized diffusion coefficients increase with increasing constrictive factor δ. Furthermore, when the water film governs the solute diffusion, the homogenized diffusion coefficient will decrease by 2 to 5 orders of magnitude with that of the saturated one. The results are comparable with the conclusion of several authors [126, 148], in which the homogenized diffusion coefficient in water film decreases by 3 orders of magnitude.

5.4.2 Evolution of the normalized solute diffusion coefficient with saturation degree for Romkens' sand

Contrary to Beaver Creek sand, the experimental results of Romkens' sand exhibit strong percolation effect. The evolution of the normalized homogenized diffusion coefficient with the saturation degree is discussed by the following two cases: $Sr \geq Sr^r$ and $Sr < Sr^r$.

3. The thickness of intergranular layers can be estimated by Eq.(5.8), in which φ_f is replaced by φ_{ig}.

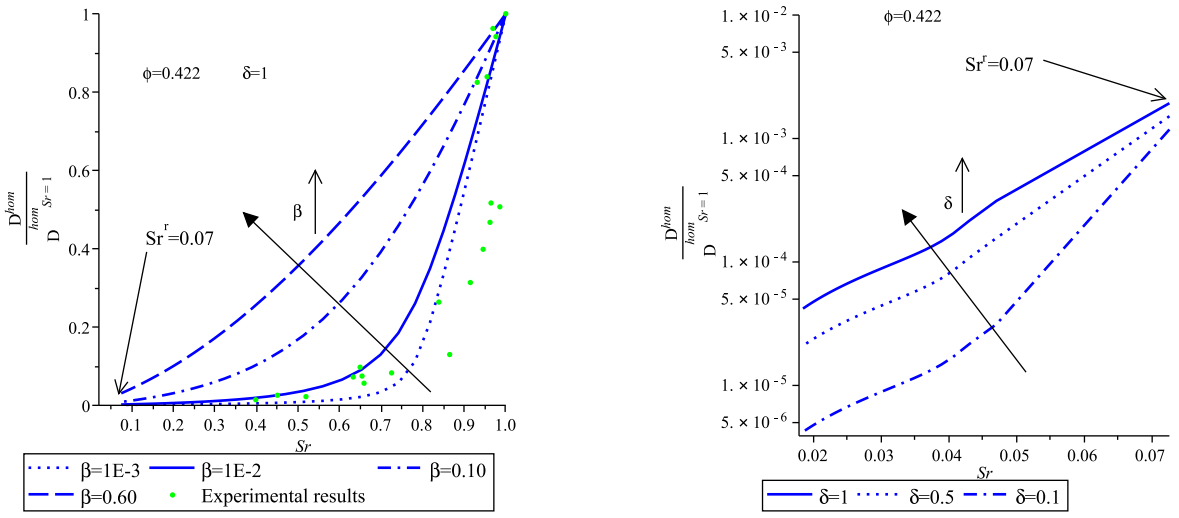

(a) $Sr \geq Sr^r$. (b) $Sr < Sr^r$.

Figure 5.5: Evolution of normalized homogenized diffusion coefficient with saturation degree in Romkens' sand, experimental results are after [211].

When $Sr > Sr^r$

As shown in Fig(5.5)(a), the normalized diffusion coefficient increases with β. When the homogenized solute diffusion coefficient D^{hom} is taken as 0.590×10^{-9} (the experimental value listed in Table(5.1)), we have $\beta \approx 0.73$ (see Fig(5.5)(a)).

When $\beta = 10^{-2}$, the modelling result agrees well with experimental results. When $\beta = 10^{-2}$, the average thickness of the intergranular layers is estimated to be 0.18 μm, which is consistent with the magnitude of roughness of sand (order of micron) [258]. However, when $\beta = 10^{-2}$, the homogenized saturated diffusion coefficient determined by the model is 0.28×10^{-9} m^2.s^{-1}, which exhibits a discrepancy with the experimental value 0.590×10^{-9} m^2.s^{-1}.

when $Sr < Sr^r$

As presented previously, the constrictive factor δ should be accounted for in this case. The evolution of normalized diffusion coefficient with saturation degree at varied δ is depicted in Fig(5.5)(b). As shown in the figure, the normalized homogenized diffusion coefficient increases with δ, owing to the increasing solute diffusion coefficient of the water film. The magnitude of the homogenized diffusion coefficient decrease by 4 to 5 orders of

magnitude comparing with saturated homogenized diffusion coefficient, which agrees well with the observation of Nakashima et al. [177].

The cyan curves in Fig(5.4)(a) and Fig(5.5)(a) are the modelling results estimated by differential scheme (shown in Eq.(4.10)). As discussed in Section(4.4.1), the porosity ϕ has no influence on the evolution of normalized solute diffusion coefficient with saturation degree (the porosity ϕ is cancelled in the normalization). From these two figures, it can also be found that the differential scheme seems applicable in Fig(5.4)(a) while it is out of validity in Fig(5.5)(a); Moreover, the cyan curves estimated by the differential scheme are rather close to those estimated by the self-consistent scheme when $\beta = 0.60$ and $\beta = 0.73$ [4]. The physical reasons for these phenomena are not clear until now.

5.5 Conclusion

Two groups of simulation on the solute diffusion in unsaturated sand are carried out to validate the micromechanics model in this section. From the experimental results, it can be found that the Romkens' sand exhibits strong percolation effect while Beaver Creek sand does not present notable percolation effect.

When $Sr \geq Sr^r$, since it is difficult to quantify the volume fraction of the interconnected intergranular layers, the volume fraction of intergranular layers is assumed to decrease linearly with saturation degree (with proportional ratio β) in the simulation. The effect of β on the evolution of normalized homogenized diffusion coefficient $D^{hom}/D^{hom}(Sr = 1)$ in these two kinds of sand is discussed. The simulation results agree well with the experimental results of Beaver Creek sand and Romkens' sand when $\beta = 0.4$ and $\beta = 10^{-2}$. At this saturation degree range, intergranular layers and pore body water dominate solute diffusion.

However, when $Sr < Sr^r$, the water film governs the solute diffusion, the magnitude of the homogenized diffusion coefficient decreases by 4 to 5 orders of magnitude when comparing with the homogenized saturated diffusion coefficient.

4. These two values for β are determined by the experimental saturated homogenized diffusion coefficient.

Owing to the lack of experimental results and microstructure information of some geo-materials such as cement and clay, the micromechanics model is not employed to simulate the solute diffusion in these materials. However, in latter work, efforts will be made to estimate the solute diffusion in these materials under unsaturated condition.

Chapter 6

Micromechanical modelling of fluid flow in unsaturated sandstone

Contents

6.1 Introduction 136

6.2 A review of advective transport in unsaturated porous media 137

6.2.1 Empirical models 138

6.2.2 Macroscopic models 138

6.2.3 Statistical models 139

6.2.4 Comments on the existing models 141

6.3 Micromechanics model for liquid flow in saturated porous media 141

6.4 Micromechanics model for liquid flow in unsaturated Fontainebleau sandstone 145

6.4.1 Idealization of intergranular water in Fontainebleau sandstone . . 145

6.4.2 Localization of liquid flow in unsaturated sandstone 146

6.4.3 The filtration velocity of the water film, the wetting layer and the intergranular layer 148

6.4.4 Estimating the homogenized permeability coefficient of the unsaturated Fontainebleau sandstone 151

6.5 Experimental analysis 153

6.5.1 Average concentration tensors of each phase within unsaturated Fontainebleau sandstone 154

6.5.2 Volume fractions of each phase within unsaturated Fontainebleau sandstone 154

6.5.3 The homogenized intrinsic permeability coefficient of Fontainebleau sandstone 155

6.5.4 Micromechanics analysis of modified Kozeny-Carman model for Fontainebleau sandstone 155

6.5.5 Evolution of the unsaturated permeability coefficient with saturation degree for Fontainebleau sandstone 158

6.6 Summary 161

6.1 Introduction

Advective transport of liquid water in porous media is a common phenomenon in several engineering fields, such as civil engineering, agricultural engineering, petroleum engineering, etc. When the pore space is fully saturated by the liquid phase, advective transport law in porous media is classically formulated by the Darcy's law [67] at the scale of a sample. The latter linearly relates the macroscopic liquid phase velocity to the macroscopic pressure gradient through the macroscopic permeability coefficient.

The advective transport of the liquid phase in unsaturated porous media is commonly described by Richards equation [198, 208]. The latter, derived in a non-linear partial differential formulation, does not have a closed-form analytical solution. In addition, the numerical procedures, required to solve this equation, need the input data: - 1) the water retention function and -2) the unsaturated permeability coefficient (evolution of unsaturated permeability coefficient with saturation degree) [198].

In this chapter, several commonly used macroscopic models for (liquid phase) advective

transport in unsaturated porous media are first introduced in Section(6.2). We then begin with the flow permeability in saturated porous media in Section(6.3). Next, a micromechanics model to characterize flow permeability in unsaturated sandstone is established in Section(6.4). The low saturation regime is analysed accounting for the existence of a liquid layer (the intergranular layer, the wetting layer and the water film) localized on the solid surface, whose transport definitions are different from that of the bulk liquid. This local liquid layer transport law is introduced and then incorporated in a micromechanics methodology. Eventually, on the premise of several assumptions of the model in Section(6.4), a micromechanics model for the the flow permeability in the Fontainebleau sandstone (clay free) is presented and discussed in Section(6.5).

6.2 A review of advective transport in unsaturated porous media

In this section, three kinds of phenomenological models for estimating the flow permeability in unsaturated porous media are reviewed and discussed. Several typical models will be used to compare with our micromechanics model results in the sequel.

The permeability coefficient of liquid water is a transport property of porous media which allows to quantitatively characterize the advective transport (of the liquid phase). Such permeability coefficient depends not only on the intrinsic permeability but also on the viscosity of the flow. The concept of relative permeability K_r is introduced when extending the single phase flow to the multiphase flow [219]. Generally, the relative permeability for water flow in unsaturated porous media is defined as the homogenized unsaturated permeability coefficient being divided by its saturated one, that is, $K_r = \dfrac{K^{hom}}{K^{hom}(Sr=1)}$. The relative permeability coefficient of liquid water is generally related to saturation degree of wetting phase as well as pore size distribution of porous media.

By means of rigid wall or flexible wall permeameter, the unsaturated permeability coefficient of liquid water in porous media can be directly measured in field or labora-

tory [34]. However, these direct measurement techniques are found to be very expensive, time consuming, error prone and sometimes impractical [218]. Therefore, based on the observed phenomenological properties, considerable efforts have been devoted to the indirect estimation of unsaturated permeability coefficient by mathematical models [29, 35, 42, 104, 109, 151, 175, 218, 244, 247]. These models may be classified as following three types [157]: empirical models [38, 109, 255], macroscopic models [175] and statistical models [35, 42, 104, 247].

6.2.1 Empirical models

In empirical models, the unsaturated permeability coefficient is expressed as the fitting equation of volumetric water content or matrix suction (capillary pressure). The fitting function depends on the shape of the experimental curves, and the fitting parameters are adjusted to match the experimental curves by means of curve fitting procedure. As concluded by Leong et al. [157], the empirical equation can be expressed as the following general form:

$$K_r = (\frac{\theta - \theta_r}{\theta_s - \theta_r})^p \tag{6.1}$$

where θ, θ_s and θ_r are the water content, saturated water content and residual water content, respectively; p is the fitting parameter.

The empirical model is intuitive and simple but its parameters lack physical meaning. Moreover, it should be aware that, at lower saturation degree, the empirical model exhibits a significant deviation with experimental results[149].

6.2.2 Macroscopic models

The macroscopic model is based on the assumption that there exists a similarity between the laminar flow at microscopic level and macroscopic flow in porous media [157]. The average macroscopic flow within unsaturated porous media is solved as the average of

microscopic laminar flow. Similar to the empirical equation (Eq.(6.1)), it has a general simplified form as [157]:

$$K_r = Sr_e^q \tag{6.2}$$

where Sr_e is the effective saturation degree which can be expressed as [29, 157]:

$$Sr_e = \frac{Sr - Sr_r}{1 - Sr_r} \tag{6.3}$$

where Sr_r is the residual saturation degree, Sr is the saturation degree, q is a constant that depends on the assumption made for the specified porous media, $q = 3.5$, $q = 2$, $q = 3$ and $q = 4$ are suggested by Averjanov et al.[10], Yuster [261], Irmay [129] and Corey et al. [55], respectively. The macroscopic model is developed disregarding the pore size distribution effect. Therefore, it leads to the controversies in assessing the value of q [29]. Hence, to account for the pore size effect, $q = (2 + 3\lambda_p)/\lambda_p$ is proposed by Brooks and Corey [29], where λ_p is a pore size distribution index.

6.2.3 Statistical models

The statistical models are the most common models used to determine the unsaturated permeability coefficient. They revealed to be efficient and can be used readily. In the practical engineering, the water retention function (relation between matric suction and water content) is easy to be determined by experiment. The statistical models are used to determine the unsaturated permeability coefficient by means of water retention functions (denoted as soil water characteristic curve in soil engineering). The statistical models for unsaturated permeability coefficient are developed on the premise of assumption of interconnected pore network. In statistical models, two major factors are specified: pore size distribution and saturation degree [176]. Three general formulas for statistical models have been reviewed by Mualem et al. [176]:

$$K_r = Sr_e^n \frac{\int_0^{\theta_w} \frac{d\theta_w}{\psi^{2+m}}}{\int_0^{\theta_s} \frac{d\theta_w}{\psi^{2+m}}} \tag{6.4}$$

$$K_r = Sr_e^n \left(\frac{\int_0^{\theta_w} \frac{d\theta_w}{\psi^{1+m}}}{\int_0^{\theta_s} \frac{d\theta_w}{\psi^{1+m}}} \right)^2 \tag{6.5}$$

$$K_r = Sr_e^n \frac{\int_0^{\theta_w} \frac{\theta_w - \nu}{\psi^{2+m}} d\nu}{\int_0^{\theta_s} \frac{\theta_w - \nu}{\psi^{2+m}} d\nu} \tag{6.6}$$

where n and m are constant, ν is the dummy variable of integration, θ_w and θ_s are the water content and the saturated water content, ψ is the matric suction (opposite of the capillary pressure), Sr_e is the effective saturation degree which may be determined by Eq.(6.3).

Table.(6.1) presents some expressions of unsaturated permeability coefficient for these 3 kinds of model.

Table 6.1: Several commonly used models for unsaturated permeability coefficient

-	**unsaturated permeability coefficient**	**reference**
Empirical model	[1] $K^{hom} = a\theta_w^b$	Gardner (1958)[109]
Empirical model	[1] $K^{hom} = K^{hom}_{(Sr=1)} \exp[b(\theta_w - \theta_s)]$	Dane et al. (1977)[66]
Macroscopic model	[2] $K^{hom} = K^{hom}_{(Sr=1)} (Sr_e)^{(2+3\lambda_p)/\lambda_p}$	Brooks et al. (1964)[29]
Statistical model	$K^{hom} = K^{hom}_{(Sr=1)} Sr_e^{1/2} [1 - (1 - Sr_e^{1/m})^m]^2$	van Genuchten (1980)[247]
	[3] $Sr_e = \frac{1}{[1 + s(\lvert\psi\rvert)^n]^m}$	

[1] K^{hom} and $K^{hom}_{(Sr=1)}$ are the homogenized unsaturated permeability coefficient and the corresponding saturated permeability coefficient; θ_w and θ_s are the volumetric water content and its corresponding saturated one; a and b are the fitting constants.

[2] Sr_e is the effective saturation degree defined by Eq.(6.3); λ_p is the pore size distribution index.

[3] s, m and n are the fitting parameters for water retention function, with $m = 1 - \frac{1}{n}$ and $n > 1$; ψ is the matric suction (opposite of the capillary pressure) (in KPa).

6.2.4 Comments on the existing models

The empirical models are obtained by fitting the experimental results. In empirical models, the relation between the unsaturated permeability coefficient and saturation degree exhibits a power law. Their applications are limited by the device capability in experiments (i.e. experimental results at low saturation degree will be inaccurate) [157]. Furthermore, the fitting parameters lack physical meaning.

The macroscopic models are based on the laminar flow at local scale and have concise formulations [157]. However, it is a rough analogy of flow between macro and micro scales [157]. Moreover, these model neglect the microstructure effect on the permeability coefficient of liquid water.

Statistical models provide an indirect determination of unsaturated permeability coefficient from water retention curve. They are commonly used in the practical engineering field. However, as can be found from the statistical model, lots of parameters are needed to fit the water retention function, which will induce errors in the calculation.

6.3 Micromechanics model for liquid flow in saturated porous media

Most of the models for unsaturated permeability introduced above are phenomenological in nature [7, 152, 198]. These phenomenological formulations for unsaturated permeability coefficient can be linked to the more fundamental micro-scale governing equations based on Stokes laws [178]. Therefore, a micromechanics model for unsaturated permeability coefficient will be developed based on fundamental physical characterization of the water distribution at local scale, in which not only the intergranular water flow but also the water film flow will be accounted for. Upscaling homogenization approach will then be employed to derive the macroscopic properties (e.g. unsaturated permeability coefficient). Here, we start with the micromechanics model for liquid permeability in saturated porous media.

Generally, Darcy's law is valid for evaluating the flow velocity at macro scale. At local scale, this law is invalid and the direct approach to such problem is the numerical solution of the Navier-Stokes equation at local scale.

The micromechanics approach was employed first to predict the homogenized flow permeability by Ene et al. [88]. In their work, Darcy's law was derived by the homogenization of the local (micro) fluid flow which is characterized by Navier-Stokes equation. This reasoning approach has been implemented in granular material and consolidated material with fractures by many researchers [27, 81, 154, 188].

To characterize the local fluid flow in porous media, several assumptions can be made to simplify the problem [22]:

— The liquid flow is laminar (Poiseuille flow) everywhere in porous media, which means the Reynolds number is small enough so that the inertial effect is negligible in the momentum balance equation of the fluid.

— All the fluids are at steady state in porous media, which means the variation of the density of liquid flow with time can be neglected in the mass balance equation ($\frac{\partial \rho}{\partial t} = 0$).

— All of the fluids are incompressible and immiscible, moreover, the liquid fluids are considered to be Newtonian fluid.

On the premise of these assumptions, the physical problems of the local liquid flow can be characterized by the simplified Navier-Stokes equation as [82]:

$$\begin{cases} -\underline{\nabla} P + \mu \underline{\nabla}^2 \underline{\mathrm{v}} = 0 & \forall \underline{z} \in \Omega^l \quad (a) \\ \underline{\nabla} \cdot \underline{\mathrm{v}} = 0 & \forall \underline{z} \in \Omega^l \quad (b) \\ \underline{\mathrm{v}} = \underline{0} & \forall \underline{z} \in \mathcal{I}^{sl} \quad (c) \end{cases} \tag{6.7}$$

where $\underline{\mathrm{v}}$ [1] denotes the filtration velocity within porous media; P is the fluid pressure; both of the filtration velocity and the liquid pressure are defined at local scale, μ is the viscosity

1. Underline letters in this work represent vectors, bold letters denote second order tensors, letters without any mark stand for scalar quantity.

of liquid, Ω^l the fluid domain in REV, $\mathcal{I}^{sl}$ is the interface between liquid and solid phases in REV.

To determine the homogenized permeability coefficient K^{hom} in the saturated porous media, a numerical solution to this simplified Navier-Stokes equation on the whole fluid domain is indispensable and time consuming. Therefore, to avoid this procedure, based on the special morphology of the saturated jointed granular rock [2], almost homogeneous liquid pressure in big pores (nearly zero pressure gradient) and only pressure drop in interface are assumed by Dormieux et al. [79, 80]. Darcy's law is thus assumed to be valid not only in interface but also in macro pore at local scale [3].

When a macroscopic fluid pressure gradient $\underline{\nabla} P$ is applied on the boundary of REV in the sense of Hashin ($P(\underline{z}) = \underline{\nabla} P \cdot \underline{z}$) [80], the liquid flow in the REV obeys the following formulas:

$$\begin{cases} \text{div } \underline{\mathrm{v}}(\underline{z}) = 0 & \forall \underline{z} \in \Omega \\ \underline{\mathrm{v}}(\underline{z}) = -\mathbf{K}(\underline{z}) \cdot \underline{\text{grad}} P(\underline{z}) & \forall \underline{z} \in \Omega \\ P(\underline{z}) = \underline{\nabla} P_0 \cdot \underline{z} & \forall \underline{z} \in \partial\Omega \end{cases} \tag{6.8}$$

where $\mathbf{K}(\underline{z})$ [4] is the permeability coefficient tensor. Owing to the size dependence of the permeability coefficient, the permeability coefficient of liquid flow in big pore K_l can be assumed to tend to infinity since the length scale of big pore is far larger than that of interface (width). The fluid in the interface can be characterized by Poiseuille flow, thus, the permeability coefficient of the liquid flow in interface is $h_i^2/12$, where h_i is the width of interface. In Dormieux's work, the liquid flow in the interface is treated as 2-D surface [5], and thus the permeability coefficient of the interface η is $h_i^3/24$. In isotropic case ($\mathbf{K}(\underline{z}) =$

2. The pore space of jointed granular rock is composed of interfaces and big pores, the latter are connected by the interfaces and the length scales of interfaces are far smaller than those of big pores. The fluid flow in the jointed granular rock is governed by the interfaces.

3. The detailed information is given in [79].

4. The intrinsic permeability depends only on the pore geometry and not on the saturating fluid phase. This allows us to get rid of the viscosity effect in the permeability coefficient. The permeability coefficient in this chapter is the intrinsic permeability coefficient.

5. The 2-D idealization is the same as that presented in Section(4.5.1).

$K(\underline{z})\mathbf{1}$), the permeability coefficients of each phase are presented in Eq.(6.9).

$$K(\underline{z}) = \begin{cases} K_l \to \infty & \forall \underline{z} \in \Omega^l \\ \eta = \dfrac{h_i^3}{24} & \forall \underline{z} \in \mathcal{I} \\ K_s \to 0 & \forall \underline{z} \in \Omega^s \end{cases} \tag{6.9}$$

where $\mathcal{I}$ is the interface between grain contacts, K_s is the permeability of liquid flow in solid phase.

From the boundary condition in Eq.(6.8), we have:

$$\overline{\underline{\text{grad}} P(\underline{z})} = \underline{\nabla} P \tag{6.10}$$

In saturated jointed granular rock, the macroscopic liquid flow filtration velocity consists of two contributions: the liquid water flow (in pore) and the flow in interface. In isotropic case ($\mathbf{K} = K\mathbf{1}$), it yields [79]:

$$-K^{hom}\underline{\nabla} P = -\phi K_l \overline{\underline{\text{grad}_l}} P_0 - \frac{1}{|\Omega|}\sum_i \int_{S_i} \eta \underline{\text{grad}_s} P_0 dS \tag{6.11}$$

where K^{hom} is the permeability coefficient of saturated porous media, K^l and η are the permeability coefficient of pore liquid and interface; $\underline{\nabla} P$ is the real macroscopic liquid pressure gradient of the saturated porous media, $\underline{\text{grad}_l} P_0$ and $\underline{\text{grad}_s} P_0$ are the two auxiliary pressure gradients of liquid water and interface, respectively; ϕ is the porosity; S_i is the surface of the solid grains; $|\Omega|$ is the volume of REV. The detailed deduction of Eq.(6.11) is given in [79].

By means of appropriate mechanical schemes (e.g. self-consistent scheme or Mori-Tanaka scheme), the quantitative relation between real macroscopic pressure $\underline{\nabla} P$ and $\overline{\underline{\text{grad}_l}} P_0$ as well as $\underline{\text{grad}_s} P_0$ can be determined by Eq.(6.10). The homogenized permeability coefficient K^{hom} in Eq.(6.11) can thus be eventually estimated [79].

6.4 Micromechanics model for liquid flow in unsaturated Fontainebleau sandstone

Fontainebleau sandstone is usually used to validate the model because of their relatively simple morphology [87, 121, 184]. The Fontainebleau sandstones are made up of well sorted monocrystalline quartz grains ranging between 350 μm and 150 μm [115] (average grain diameter D is about 200 μm [184]). They do not contain clay and their porosity displays mostly intergranular porosity [87]. The latter varies from 0.03 to roughly 0.35 without noticeable changes in grain size [25, 184].

Based on the assumptions and derivation of micromechanics model for liquid flow permeability in the saturated jointed granular rock introduced previously [79], a micromechanics model for estimating the permeability of liquid flow within unsaturated Fontainebleau sandstone is developed in this section. The water distribution in unsaturated sandstone is introduced in Section(3.2). First, we will make an idealization of the intergranular water within sandstone so as to easily determine its permeability coefficient.

6.4.1 Idealization of intergranular water in Fontainebleau sandstone

Generally, the intergranular pore space is a geometrical characteristic of sandstone. The intergranular pores of sandstone are interconnected and they can be categorized into pore bodies and pore throats. The latter connect the pore bodies and thus govern the flow transport. By means of X-ray computed micro-tomography and skeletization algorithms, the average sizes of pore bodies and pores throats of four Fontainebleau sandstones with varied porosities are determined by Lindquist et al. [160, 161]. For four Fontainebleau sandstone samples with porosities 0.075, 0.13, 0.15 and 0.22, the average radii of the pore bodies (resp. pore throats) are respectively 50.6, 45.8, 48.5 and 43.5 μm (resp. 18.4, 21.3, 24.7, 22.6 μm) [160, 161]. It can be found that, the average radii of the pore bodies

decrease slightly with porosity while the average radii of the pore throats increase with porosity. Moreover, from these data, the radii of the pore bodies and pore throats can be considered as in the same order of magnitude (several tens of microns).

Based on this geometrical information, the pore network of the Fontainebleau sandstone is always idealized as interconnected pore channels (cylindrical pores with the radius of the pore throat) [20, 21, 123, 145, 183, 185–187, 191, 192, 195, 227]. Inspired by this idealization and geometrical information (the radii of the pore body and pore throat are in the same order of magnitude), in self-consistent scheme, **to ensure the connectivity of the intergranular water, the latter is idealized as the intergranular layer which is assumed to surround the solid grains of the sandstone** (as depicted in Fig.(6.1)).

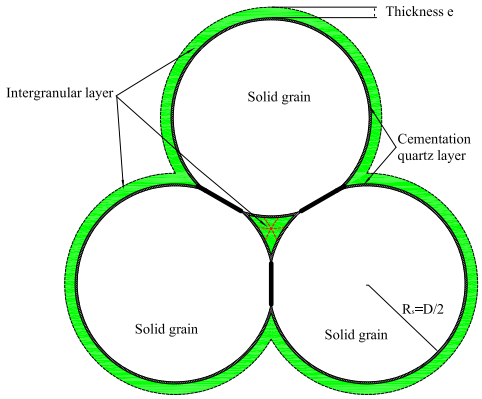

Figure 6.1: Schematic illustration of the intergranular water in Fontainebleau sandstone: the intergranular water is idealized as interconnected intergranular layer surrounding the solid grains, e is the thickness of the intergranular layer.

6.4.2 Localization of liquid flow in unsaturated sandstone

As introduced in Section(3.2), in unsaturated sandstone, there exist **s**olid phase (denoted as subscript $\boldsymbol{s}$), **g**aseous phase (denoted as subscript $\boldsymbol{g}$) and liquid water (denoted as subscript l). The latter consists of the **i**nter**g**ranular layer (denoted as subscript $\boldsymbol{ig}$), the **w**etting **l**ayer (denoted as subscript $\boldsymbol{wl}$) trapped in pendular rings and surface roughness, and the water **f**ilm (denoted as subscript $\boldsymbol{f}$) adsorbed on the solid grain. The intergranular

layers, the wetting layers, the water film and the solid grain can be regarded as a spherical composite which is embedded in the sandstone matrix. Disregarding the existence of clay filling, the morphological representation of the Fontainebleau sandstone is depicted in Fig.(6.2).

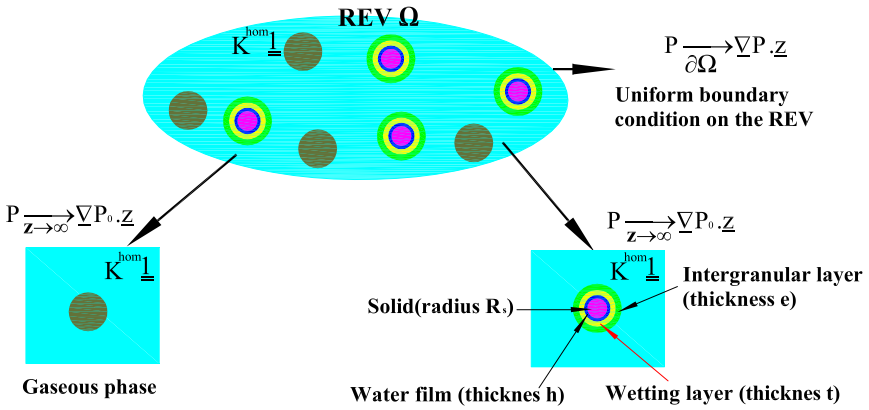

Figure 6.2: Schematic illustration of morphology of the unsaturated sandstone; to characterize the evolution of the intergranular layer → the wetting layer → the water film during desaturation process, all these three kinds of water are superposed on the solid grain.

We make use of the same assumptions on the fluid flow in Section(6.3). As illustrated in Fig.(6.2), the intergranular layer flow, the wetting layer flow and the water film flow can be treated as Poiseuille flow. Therefore, the physical laws governing the liquid flow in unsaturated sandstone can also be expressed as Eq.(6.8). The intrinsic permeability coefficient tensors of each phase can thus be expressed as[6]:

6. In this chapter, we only dedicate to studying the liquid flow. Therefore, the permeability coefficient tensor of the gaseous phase $K_g \to 0$.

$$\mathbf{K}(\underline{z}) = \begin{cases} \mathbf{K}_{ig} & \forall \underline{z} \in \Omega^{ig} \\ \mathbf{K}_{wl} & \forall \underline{z} \in \Omega^{wl} \\ \mathbf{K}_{f} & \forall \underline{z} \in \Omega^{f} \\ \mathbf{K}_{g} \to \mathbf{0} & \forall \underline{z} \in \Omega^{g} \\ \mathbf{K}_{s} \to \mathbf{0} & \forall \underline{z} \in \Omega^{s} \end{cases} \tag{6.12}$$

When the permeability coefficients (intrinsic) of each phase in sandstone are isotropic at local and macro scale, they can be simplified as:

$$\mathbf{K}_i = K_i \mathbf{1} \qquad i \in \{ig, f, wl, g, s\} \tag{6.13}$$

where $\mathbf{1}$ is the second order identity tensor.

Similar to Eq.(6.11), to estimate the homogenized intrinsic permeability coefficient, the intrinsic permeability coefficients and the average concentration tensors of each phase should be determined first, which are presented in the sequel.

6.4.3 The filtration velocity of the water film, the wetting layer and the intergranular layer

As shown in Section(6.3), in order to avoid solving the Navier-Stokes equation (see Eq.(6.7)) numerically, the water film flow, the intergranular layer flow and the the wetting layer flow, are treated as Poiseuille flow [152, 181] and assumed to obey the Darcy's law. The filtration velocity of the water film flow (channel pore water flow) on the flat plane is schematically depicted in Fig.(6.3).

As illustrated in Fig.(6.3), the water film is assumed to be Newtonian fluid with constant density and viscosity as well as to have only one none-zero velocity component v in $\boldsymbol{Z}$ axis parallel to the surface of the plane. Therefore, in one dimensional scheme, when the viscosity of water film μ_f is taken as a constant, Navier-Stokes equation (Eq.(6.7)) can be simplified

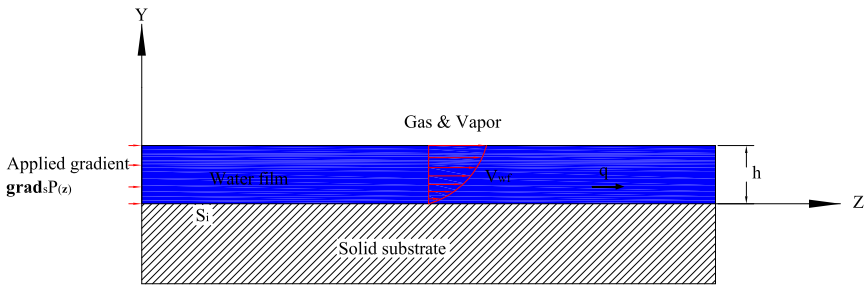

Figure 6.3: Schematic representation of the filtration velocity profile of the water film flow on the plat plane, h is the thickness of water film.

as [152, 181, 243]:

$$-\frac{1}{\mu_f}\frac{\mathrm{d}P^f(z)}{\mathrm{d}z}=\frac{\mathrm{d}^2\mathrm{v}_f(z)}{\mathrm{d}y^2}\qquad\text{with :}\qquad \frac{\mathrm{dv}_f(z)}{\mathrm{d}y}|_{y=h}=0,\quad \mathrm{v}_f(y=0)=0. \tag{6.14}$$

Thus, the classical Poiseuille solution to the viscous flow [181] may be derived from Eq.(6.14):

$$\mathrm{v}_f=\frac{h^2}{3\mu_f}(-\frac{\mathrm{d}P(\underline{z})}{\mathrm{d}(z)}) \tag{6.15}$$

Eq.(6.15) can be extended into general three dimensional form, in which $\underline{\mathrm{v}}_f(\underline{z})$ is assumed to be proportional to the fluid pressure gradient $\underline{\mathrm{grad}}_f P(\underline{z})$ in the water film as:

$$\underline{z}\in\Omega^f:\qquad \underline{\mathrm{v}}_f(\underline{z})=-\frac{K_f}{\mu_f}\underline{\mathrm{grad}}_f P(\underline{z}) \tag{6.16}$$

Comparing Eq.(6.15) and Eq.(6.16), the intrinsic permeability coefficient of water film K_f can be obtained:

$$K_f = \frac{h^2}{3} \tag{6.17}$$

According to Eq.(1.2), the average filtration velocity of the water film flow $\underline{\overline{\mathrm{v}}}_f$ may be expressed as [79]:

$$\underline{\overline{\mathrm{v}}}_f = -\varphi_f \frac{K_f}{\mu_f} \overline{\underline{\mathrm{grad}}_f} P \tag{6.18}$$

where φ_f is the volume fraction of the water film, $\overline{\underline{\mathrm{grad}}_f} P$ is the average fluid pressure gradient in water film.

The permeability coefficients and the average filtration velocities of the wetting layer flow and the intergranular layer flow can be derived similarly as water film flow. The filtration velocity of the wetting layer flow $\underline{\mathrm{v}}_{wl}(\underline{z})$ can be expressed as:

$$\underline{z} \in \Omega^{wl}: \qquad \underline{\mathrm{v}}_{wl}(\underline{z}) = -\frac{K_{wl}}{\mu_{wl}} \underline{\mathrm{grad}}_{wl} P(\underline{z}) \tag{6.19}$$

where μ_{wl} is the viscosity of the wetting layer.

The intrinsic permeability coefficient of the the wetting layer flow K_{wl} can be expressed as:

$$K_{wl} = \frac{t^2}{3} \tag{6.20}$$

where t is the thickness of the wetting layer.

The average filtration velocity of the wetting layer $\underline{\overline{\mathrm{v}_{wl}}}$ is:

$$\underline{\overline{\mathrm{v}}}_{wl} = -\varphi_{wl} \frac{K_{wl}}{\mu_{wl}} \overline{\underline{\mathrm{grad}}_{wl} P} \tag{6.21}$$

where φ_{wl} is the volume fraction of the wetting layers.

The filtration velocity of the intergranular layer flow $\underline{\mathrm{v}}_{ig}(\underline{z})$ can be expressed as:

$$\underline{z} \in \Omega^{ig} : \qquad \underline{\mathrm{v}}_{ig}(\underline{z}) = -\frac{K_{ig}}{\mu_{ig}} \underline{\mathrm{grad}}_{ig} P(\underline{z}) \tag{6.22}$$

where μ_{ig} is the viscosity of the intergranular layer.

The intrinsic permeability coefficient of the intergranular layer flow K_{ig} can be expressed as:

$$K_{ig} = \frac{e^2}{3} \tag{6.23}$$

where e is the thickness of the intergranular layer.

The average filtration velocity of the intergranular layer flow $\underline{\overline{\mathrm{v}}_{ig}}$ is:

$$\underline{\overline{\mathrm{v}}}_{ig} = -\varphi_{ig} \frac{K_{ig}}{\mu_{ig}} \underline{\overline{\mathrm{grad}}_{ig} P} \tag{6.24}$$

where φ_{ig} is the volume fraction of the intergranular layer.

6.4.4 Estimating the homogenized permeability coefficient of the unsaturated Fontainebleau sandstone

In the REV of the unsaturated sandstone, the macroscopic average filtration velocity $\underline{\overline{\mathrm{v}}}$ consists of the contributions of the intergranular layer flow $\underline{\overline{\mathrm{v}}}_{ig}$, the wetting layer flow $\underline{\overline{\mathrm{v}}}_{wl}$ and the water film flow $\underline{\overline{\mathrm{v}}}_{f}$. In this work, we dedicated to acquiring the homogenized intrinsic permeability coefficients, the viscosities of the intergranular layer, the wetting layer and the water film can thus be disregarded. Analogy to Eq.(6.11), combining Eq.(6.18), Eq.(6.21) and Eq.(6.24) yields:

$$-K^{hom} \underline{\nabla} P = -\varphi_f K_f \underline{\overline{\mathrm{grad}}_f P} - \varphi_{wl} K_{wl} \underline{\overline{\mathrm{grad}}_{wl} P} - \varphi_{ig} K_{ig} \underline{\overline{\mathrm{grad}}_{ig} P} \tag{6.25}$$

Similar to the diffusion problems introduced in Section(4.3), the second order concentration tensors $\boldsymbol{A}(\underline{z})$ is introduced to link the pressure gradients of each phase $\underline{\mathrm{grad}}_i P$ ($i \in \{s, wl, f, g, ig\}$) to the macroscopic fluid pressure gradient $\underline{\nabla} P$:

$$\underline{\text{grad}}_i P = \boldsymbol{A}_i(\underline{z}) \cdot \underline{\nabla} P \qquad i \in \{s, wl, f, g, ig\} \tag{6.26}$$

The average pressure gradients of each phase $\overline{\underline{\text{grad}}_i P}$ are related to their corresponding average concentration tensors $\overline{\boldsymbol{A}_i}$ ($i \in \{s, wl, f, g, ig\}$) by:

$$\overline{\underline{\text{grad}}_i P} = \overline{\boldsymbol{A}_i} \cdot \underline{\nabla} P \qquad i \in \{s, wl, f, g, ig\} \tag{6.27}$$

In the isotropic case $\overline{\boldsymbol{A}_i} = \overline{A_i}\mathbf{1}$ ($i \in \{s, wl, f, g, ig\}$), when inserting Eq.(6.27) into Eq.(6.25), it can be found that the estimation of the homogenized intrinsic permeability coefficient K^{hom} amounts to evaluating the volume fractions φ_i and the average concentration tensors $\overline{A_i}$ ($i \in \{s, wl, f, g, ig\}$).

Contrary to the diffusion case[7], the intrinsic permeability coefficients of the intergranular layer, the wetting layer and the water film (e.g. $K_{ig} = e^2/3$, $K_{wl} = t^2/3$ and $K_f = h^2/3$) are greatly size dependent on their thickness.

Generally, the thicknesses of the water film h, the wetting layer t and the intergranular layer e can be associated with the radius of solid grain R_s ($R_s = D/2$) by: $h = \varepsilon R_s$, $t = \chi R_s$ and $e = \zeta R_s$. Hence, the average concentration tensors of spherical composite (including the solid grain, the water film, the wetting layer and the intergranular layer) closely depend on the particle size distribution and the parameters ε, χ and ζ.

When accounting for the particle size distribution function $g(D)$ (diameter $D = 2R_s$), the average concentration tensors of each phase $\underline{A_i}$ exhibit complicated expressions. In isotropic case ($\overline{\boldsymbol{A_i}} = \overline{A_i}\mathbf{1}$, $i \in \{s, wl, f, g, ig\}$), the average concentration tensors and the filtration velocities of the solid grain, the water film flow, the wetting layer flow and the intergranular layer flow are expressed as the following two functions l_i and L_i (with self-consistent scheme):

7. Except the local diffusion coefficient in the water film, the solute diffusion coefficients in the capillary water is assumed to be constant and independent of the size of capillary pore space.

$$\begin{cases} \varphi_i \overline{A_i}(K^{hom}) = l_i(\phi, \varepsilon, \chi, \zeta, g(D), K^{hom}, Sr, \nabla P_0) & i \in \{s, wl, f, ig\} \\ \varphi_i K_i \overline{A_i}(K^{hom}) = L_i(\phi, \varepsilon, \chi, \zeta, g(D), K^{hom}, Sr, \nabla P_0) & i \in \{wl, f, ig\} \end{cases} \tag{6.28}$$

where ∇P_0 is the fictitious average concentration tensor in the auxiliary problems (as shown in the inset of Fig.(6.2)), it can be related to ∇P by Eq.(6.27).

The average concentration tensor of gas is given in Appendix(B.2.4), it can be simply expressed as:

$$\overline{A_g} = \frac{3}{2} \nabla P_0 \tag{6.29}$$

When the self-consistent scheme is adopted to estimate the concentration tensors of each phase, the homogenized permeability coefficient of the unsaturated sandstone K^{hom} can be estimated by combining Eq.(6.25), Eq.(6.27), Eq.(6.28) and Eq.(6.29).

6.5 Experimental analysis

As discussed in the previous section, owing to the size dependence of the permeability coefficients of the intergranular layer, the wetting layer and the water film flow, estimating the homogenized permeability coefficient of the unsaturated sandstone seems to be a difficult task. Therefore, in this section several simplifications are made based on the physical characteristic of Fontainebleau sandstone. They may be summarized as:

— Since the solid grains of the Fontainebleau sandstone are uniform and well sorted [184], they are thus assumed to be spherical and monodisperse, the grain size distribution function $g(D) = 1$. The diameter of sandstone D ($D = 2R_s$) is in the size range of 350 μm and 150 μm [115].

— Generally, the pore size distribution of the Fontainebleau sandstone is rather uniform and the intergranular pore size ranges from 1 μm to 100 μm [63]. For simplification,

the thickness of the intergranular layer e is assumed to be uniform during the desaturation process. The parameter ζ can thus be estimated as $\zeta = \frac{e}{D/2} = \frac{\varphi_{ig}}{3\varphi_s}$ (as Eq.(4.21)).

— The permeability coefficient here is indeed intrinsic permeability coefficient which is solely related to the microstructure of the sandstone.

— As introduced in Eq.(4.21), the thickness of the water film h is associated with the radius of the solid grain $R_s = D/2$ by a parameter ε, $h = \varepsilon D/2$. Generally, the thickness of water film is of nanometer scale [22], which is conformed in our results shown in Fig.(3.6). As the diameter of the solid grains of sandstone is several hundreds microns (order of 10^{-4} m), $\varepsilon = 10^{-5}$ may thus be assumed reasonably. Similarly, the thickness of the wetting layer is in the scale of microns [22], hence, $\chi = 10^{-3}$ may be assumed legitimately.

6.5.1 Average concentration tensors of each phase within unsaturated Fontainebleau sandstone

As illustrated in Fig.(6.2), self-consistent scheme is used to estimate the homogenized intrinsic permeability coefficient of Fontainebleau sandstone. Based on the assumptions presented previously, the physical formulas and procedures to derive the average concentration tensors of each phase are given in Appendix(B.3).

6.5.2 Volume fractions of each phase within unsaturated Fontainebleau sandstone

The volume fraction of the water film φ_f may be determined by Eq.(4.21) (since $h \ll R_s$). Similarly, the volumetric fraction of the wetting layer φ_{wl} can also be estimated by Eq.(4.21) by replacing the parameter ε by χ ($t \ll R_s$). Hence, the volume fractions of each phase in unsaturated Fontainebleau sandstone are listed in Table(6.2).

Table 6.2: Volume fractions of each phase within unsaturated Fontainebleau sandstone

-	Volume fraction
Solid φ_s	$1-\phi$
Gas in micro pores φ_g	$\phi(1-Sr)$
Water film φ_f	$3\varepsilon(1-\phi)$
Wetting layer φ_{wl}	$3\chi(1-\phi)$
Intergranular layer φ_{ig}	$\phi Sr-3\varepsilon(1-\phi)-3\chi(1-\phi)$

6.5.3 The homogenized intrinsic permeability coefficient of Fontainebleau sandstone

Based on the assumptions and volume fractions presented in the previous section, we have: volume fractions of each phase φ_i in Table(6.2), the parameters $\varepsilon = 10^{-5}$, $\chi = 10^{-3}$, particle size distribution function $g(D) = 1$) in Eq.(6.28). Inserting these parameters into Eq.(6.25), the evolution of homogenized permeability coefficient K^{hom} with porosity ϕ, saturation degree Sr and the grain size D can be determined.

6.5.4 Micromechanics analysis of modified Kozeny-Carman model for Fontainebleau sandstone

ζ ($\zeta = \dfrac{e}{(D/2)} \approx \dfrac{\varphi_{ig}}{3(1-\phi)}$ [8]) characterizes the size effect of the intergranular layer. When $Sr = 1$ (fully saturated), the evolution of ζ is depicted in Fig.(6.4). As shown in the figure, when the parameters ε (characterizing the size effect of water film) and χ (characterizing the size effect of the wetting layer) are taken to be constant, ζ decreases nearly linearly with decreasing porosity ϕ. In other words, the thickness of the intergranular pore e decreases nearly linearly with decreasing porosity ϕ.

The saturated intrinsic permeability coefficient $K^{hom}(Sr = 1) = g(\phi) \times D^2$ [9]. It is interesting to find that D^2 dependence of saturated intrinsic permeability coefficient is similar to that of the modified Kozeny-Carman model, in which the saturated intrinsic

8. It can be determined by Eq.(4.21).
9. The expression is so lengthy that we use $g(\phi)$ (the function of porosity ϕ) to represent the expression.

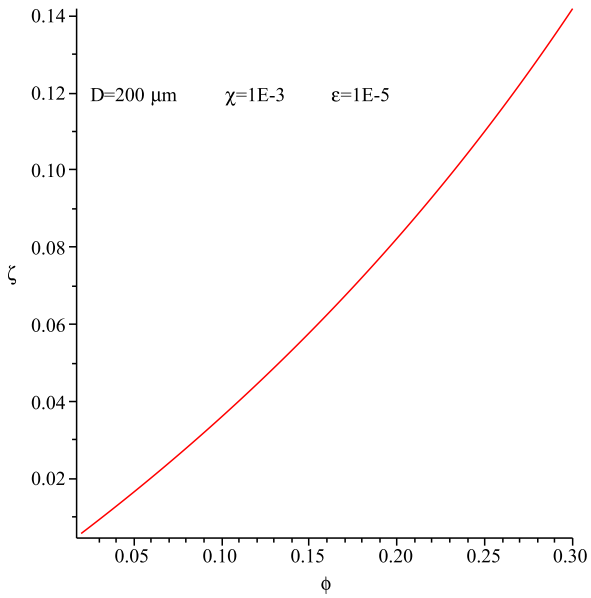

Figure 6.4: The evolution of ζ with porosity ϕ at $Sr = 1$, the other parameters are given in the figure.

permeability coefficient is expressed as [115]:

$$K^{hom}(Sr = 1) = \frac{(\phi - \phi_p)^3}{72[1 - (\phi - \phi_p)]^2\tau^2} D^2 \tag{6.30}$$

where ϕ_p is the percolation porosity, τ is the tortuosity factor, D is the radius of solid grain of sandstone.

Indeed, the D^2 dependence of the saturated intrinsic permeability $K^{hom}(Sr = 1)$ has been experimentally verified for clean, well sorted natural sands [15, 95, 256] and sandstones [24, 168].

For Fontainebleau sandstone, the influence of D on the evolution of the saturated intrinsic permeability coefficient $K^{hom}(Sr = 1)$ with the porosity ϕ is illustrated in Fig.(6.5)(a). As can be seen from the figure, the modelling results agree well with experimental results when the porosity is higher than 0.08 at $D = 150$ μm and 200 μm. However, the modelling results are higher than the experimental results when porosity is lower than 0.08. The main reason may lie in the fact that, some of pores such as dead end pores and stagnant pockets will not contribute to the flow permeability [115, 167]. The porosity of dead end pores and

stagnant pockets is denoted as percolation porosity ϕ_p in Mavko's modified Kozeny-Carman model (Eq.(6.30)).

Like Mavko et al. [168], when the percolation porosity $\phi_p = 2\%$ is accounted for in our model (replacing ϕ by $\phi - \phi_p$ in the micromechanics model), it can be found that the modelling results perfectly agree with experimental results, as shown in Fig.(6.5)(b).

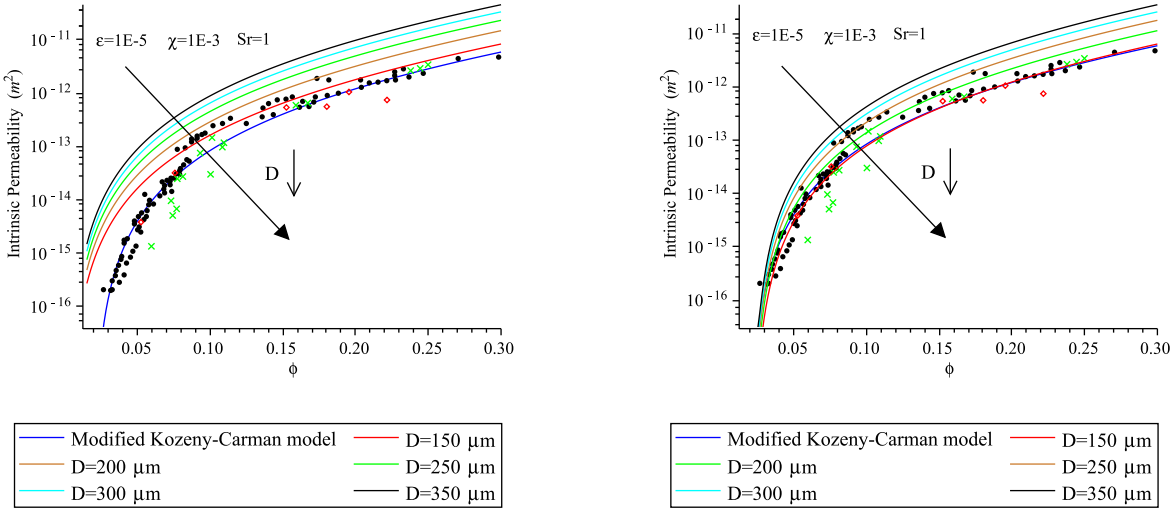

(a) Original micromechanics model.

(b) Modified micromechanics model: replacing ϕ by $\phi - \phi_p$ in the model, $\phi_p = 2\%$.

Figure 6.5: The evolution of the saturated intrinsic permeability coefficient $K^{hom}(Sr = 1)$ with porosity ϕ for Fontainebleau sandstone; the blue curve is Mavko's modified Kozeny-Carman model with fitting percolation porosity $\phi_p = 2\%$, tortuosity $\tau = 2.5$ and D=250 μm (Eq.(6.30)) [168]; the black circle points are experimental results from 240 samples with different porosities [25], the red diamond points are after [84], the green diagonal cross points are after [115].

The perfect agreement between simulation results and experiment results (see Fig.(6.5)(b)) demonstrates the feasibility of the assumptions aforementioned (e.g. $\zeta = \dfrac{\varphi_{ig}}{3(1-\phi)}$) and the validity of the micromechanics model for Fontainebleau sandstone.

6.5.5 Evolution of the unsaturated permeability coefficient with saturation degree for Fontainebleau sandstone

Dana et al. [64, 65] has carried out an experiment to measure the unsaturated permeability coefficient of Fontainebleau sandstone (for liquid water flow). The characteristics of the Fontainebleau sandstone are listed in Table(6.3):

Table 6.3: Characteristics of Fontainebleau sandstone [64]

-	ρ_b ($g.cm^{-3}$)	ρ_s ($g \cdot cm^{-3}$)	ϕ (%)	S_{BET} ($m^2.g^{-1}$)	Pore size (μm)	K (m^2)
Fontainebleau sandstone	2.36	2.60	9.5	0.03	1–200	2.0×10^{-13}

[1] ρ_b and ρ_s are the bulk density and skeletal density of sandstone, ϕ is the porosity, S_{BET} is the specific surface area measured by BET method, pore size ranges from 1 to 200 μm and mainly lies in 10 μm, K is the intrinsic permeability coefficient.

The micromechanics model based on the several assumptions (in Section(6.5.3)) is used to simulate this experiment. Owing to the pore size distribution of the Fontainebleau sandstone, the pores are drained from the bigger ones to the smaller ones in a well organized arrangement during the desaturation process. To simplify the problem, we assume that during the desaturation process, the thicknesses of the water film h and the wetting layer t remain constant while the thickness of the intergranular layer e decreases uniformly with saturation degree Sr according to:

$$e = \zeta R_s \approx \frac{\varphi_{ig}}{3(1-\phi)} R_s = \frac{\phi Sr - \varphi_f - \varphi_{wl}}{31 - \phi} R_s \tag{6.31}$$

In this case, the evolution of ζ ($\zeta = e/R_s$) with saturation degree Sr is illustrated in Fig.(6.6). As shown in the figure, ζ decreases linearly with saturation degree Sr.

When $\varepsilon = 10^{-5}$, $\chi = 10^{-3}$ and $\phi = 0.095$ are taken as input in the function of K^{hom} introduced in Section(6.5.3), the evolution of the relative homogenized permeability coefficient $K^{hom}/K^{hom}(Sr = 1)$ with the saturation degree Sr and grain size D is depicted in Fig.(6.7). The connectivity of the liquid flow is ensured by the intergranular layer surround-

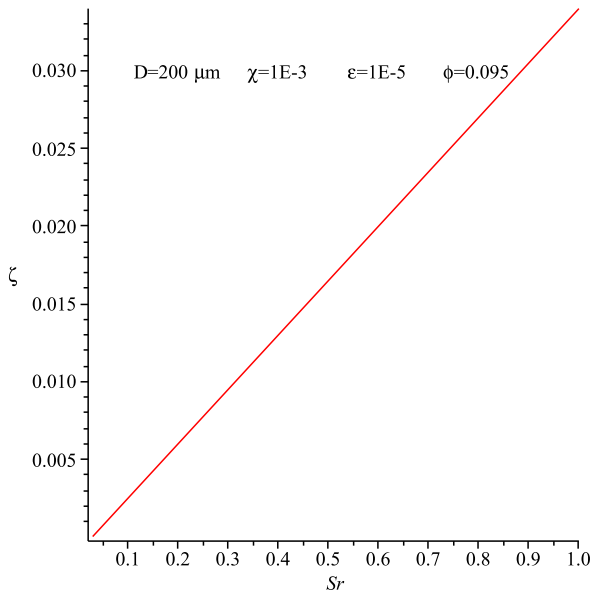

Figure 6.6: The evolution of the ζ with saturation degree Sr, $\phi = 0.095$, the other parameters are given in the figure.

ing the solid grains. The relative homogenized permeability coefficient is thus governed by the intergranular layer at this stage. As can be seen from Fig.(6.7), our modelling results agree better with the experimental results than the empirical models such as Brooks-Corey's model and Van Genuchten's model.

From our modelling [10], when $D = 270$ μm (at the range of 350 μm to 150 μm), we have $K^{hom}(Sr = 1) = 2 \times 10^{-13}$ m^2 (the measured value shown in Table(6.3)). As shown in the figure, the four curves with different grain sizes merge together. Indeed, in the simulation, when χ and ε are taken as constant value, the unsaturated permeability coefficient $K^{hom}(Sr) = f(Sr, \phi) \times D^2$ (the real expression is so long that it is simplified as a function $f(Sr, \phi)$ here), the term D^2 will be cancelled during the normalization. Thus, there is no influence of diameter of solid grains D on relative permeability coefficient $(K^{hom}/K^{hom}_{Sr=1})$.

10. The percolation porosity 2% is taken into account in the modelling.

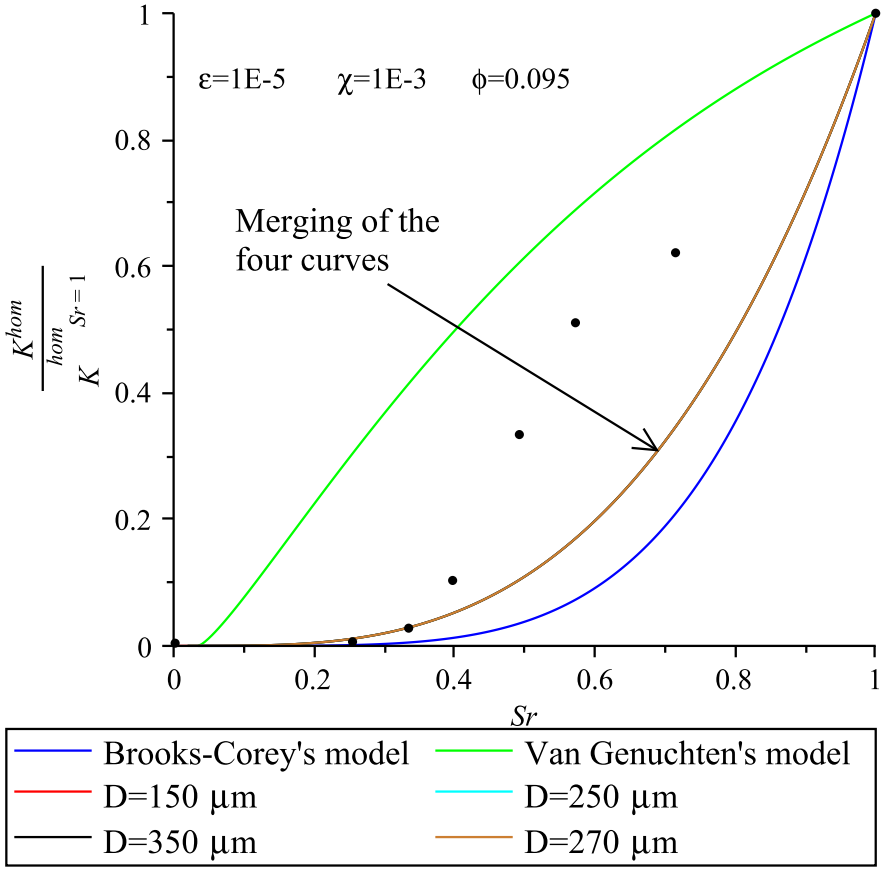

Figure 6.7: The evolution of the relative permeability coefficient $K^{hom}/K^{hom}_{Sr=1}$ with saturation degree Sr for Fontainebleau sandstone (red curves); the fitting parameters of Brooks-Corey's model and Van Genuchten's model are given in [65]; the black circle points are from experiments in [65].

6.6 Summary

Three types of empirical models are reviewed and discussed. A micromechanics model for liquid flow in unsaturated sandstone is developed based on several simplifications of Navier-Stokes solution for flow at local scale. It is applied to predict the saturated intrinsic permeability and then the unsaturated relative permeability of Fontainebleau sandstone.

Fontainebleau sandstone are used in the model owing to its relative simple microstructure. All of the intergranular water within this sandstone is idealized as the intergranular layer surrounded on the solid grains. The thickness of the intergranular layer e can be estimated as $e = \zeta D/2 \approx \dfrac{\varphi_{ig}}{3(1-\phi)} = \dfrac{\phi Sr - \varphi_f - \varphi_{wl}}{3(1-\phi)}$. The thickness of the intergranular layer e varies with ϕ and Sr. The thicknesses of the water film and the wetting layer are assumed to be constant.

When $Sr = 1$, we can obtain the relation between saturated intrinsic permeability $K^{hom}(Sr = 1)$ and porosity ϕ from this micromechanics model. The simulation results perfectly agree with the experimental results. Moreover, this micromechanics model is able to explain the D^2 dependence of the saturated intrinsic permeability coefficient according to the modified Kozeny-Carman model.

The micromechanics model is also used to predict the relationship between the relative permeability coefficient and saturation degree for Fontainebleau sandstone. In this case, $\phi = 0.095 - \phi_p$ is taken to be constant, where $\phi_p = 2\%$ is the percolation porosity. The thickness of intergranular layer e within the Fontainebleau sandstone decreases linearly with the saturation degree Sr. The relative permeability of the unsaturated sandstone is governed by the intergranular layer at intermediate saturation degree and at high saturation degree. The simulation results sound more comparable with the experimental results than Brooks-Corey's model and Van Genuchten's model.

Part III

Micromechanical modelling of freezing behaviors within unsaturated porous media

Chapter 7

Thermodynamics and poromechanics for freezing in porous media

Contents

7.1 Homogeneous nucleation and heterogeneous nucleation 166

7.1.1 Homogeneous nucleation 166

7.1.2 Heterogeneous Nucleation 167

7.2 Thermodynamic equilibrium within unsaturated porous media under freezing 168

7.2.1 Thermodynamic condition for the coexistence of each phase . . . 169

7.2.2 Crystallographic structure of ice within porous media 173

7.2.3 Depression of the freezing temperature owing to capillary effect . 175

7.2.4 Ice propagation within the pore network 176

7.3 Unfrozen water film in freezing porous media 178

7.3.1 Disjoining pressure in unfrozen water film 178

7.3.1.1 DLVO theory 178

7.3.1.2 Hamaker constant for unfrozen water film 179

7.3.1.3 Structural component of disjoining pressure 179

7.3.2 Dominant effect of structural component 180

7.4 Mechanisms and models for freezing porous media 181
7.4.1 Hydraulic model 182
7.4.2 Osmotic model and cryo-suction effect 183
7.4.3 Crystallization pressure 184
7.4.4 Disjoining pressure model 185
7.5 Poromechanics methodology for freezing in porous media . . . 187
7.6 Summary 189

Superscripts or subscripts such as $\boldsymbol{c}$, $\boldsymbol{l}$, $\boldsymbol{f}$, $\boldsymbol{g}$, $\boldsymbol{v}$, $\boldsymbol{s}$ denote ice crystal, liquid water, unfrozen water film, gas, vapour and solid substrate, respectively. Moreover, the coupled two alphabets represent the interface between these two phases, e.g., $\boldsymbol{cl}$ refers to the interface between ice crystal $\boldsymbol{c}$ and pore water $\boldsymbol{l}$.

7.1 Homogeneous nucleation and heterogeneous nucleation

Before the ice propagation process, the water in porous media is usually in the state of supercooling. The primary reason for the existence of the supercooling water lies in energy barrier [262]. The nucleation occurs when the energy barrier is overcome. There are two types of nucleation, one is homogeneous nucleation and the other is heterogeneous nucleation.

7.1.1 Homogeneous nucleation

Homogeneous nucleation begins with hydrogen atoms bonding together and creating clusters at nearly random positions [226]. When the temperature is low enough, the clusters will become thermodynamically stable and combine together to form a nucleus [8]. The stability of a nucleus is governed by two parts: -1) the volume free energy ΔG_v (named as bulk free energy by Coussy [58]), which is the energy released during liquid-ice transfor-

mation and is the driving force for ice formation; -2) the surface free energy ΔG_s, which is the energy cost for the formation of the liquid-ice interface and inhibits nucleus formation [40]. Therefore, the total free energy for the formation of nucleus ΔG_{hom} can be expressed as [58]:

$$\Delta G_{hom} = \Delta G_v + \Delta G_s = -\frac{4}{3}\pi r^3 \Delta g_v + 4\pi r^2 \gamma_{cl} \tag{7.1}$$

where r is the radius of nucleus, γ_{cl} is the surface tension for ice-liquid water interface, Δg_v is the volume free energy per unit volume, which can be determined by $\Delta g_v = \frac{\Delta h_m \Delta T}{T_0}$ [40], T_0 is the reference freezing temperature (273.15 K), $\Delta T = T_0 - T$ is the supercooling temperature, Δh_m is the latent heat of fusion per volume. To derive a critical radius of and critical total free energy for a nucleus, a derivative of ΔG_{hom} is taken with respect to radius of nucleus r [40]:

$$\frac{\mathrm{d}\Delta G_{hom}}{\mathrm{d}r} = 0 \tag{7.2}$$

From Eq.(7.2), the critical radius of the nucleus r^* is derived as [40]:

$$r^* = \frac{2\gamma_{cl}}{\Delta g_v} = \frac{2\gamma_{cl} T_0}{\Delta h_m \Delta T} \tag{7.3}$$

Rasmussen et al. [203] have shown that the rate of homogeneous nucleation is only significant around $-38°$C, which corresponds to a critical ice nucleus radius $r^* = 1.6$nm. At higher temperature, it is unlikely to form ice nucleus with larger radius because of thermal fluctuations [203]. Therefore it is impossible for the ice nucleation to occur randomly in large pores by such process.

7.1.2 Heterogeneous Nucleation

Instead of nucleating at the supercooling as low as $-38°$C, heterogeneous nucleation happens at the surfaces of impurities within solution or at the surfaces of the solid parti-

cles, where the activation energy required to form a nucleus is greatly lowered down [203]. The relationship between the total free energy needed by homogeneous and heterogeneous nucleation is [40]:

$$\Delta G_{het} = f(\theta)\Delta G_{hom} = (\frac{2 - 3cos\theta + cos^3\theta}{4})\Delta G_{hom} \tag{7.4}$$

where ΔG_{het} is the total free energy induced by heterogeneous nucleation, θ is the wetting angle of the nucleus and substrate; for instance, when the ice wets perfectly ($\theta \rightarrow 0$), $\Delta G_{het} \rightarrow 0$ [40]. Combining Eq.(7.2) and Eq.(7.4), it can be inferred that the supercooling temperature at the same critical radius as for homogeneous nucleation, can be written as the follows [40]:

$$\Delta T_{het} = f(\theta)\Delta T = (\frac{2 - 3cos\theta + cos^3\theta}{4})\Delta T \tag{7.5}$$

where ΔT_{het} is the supercooling temperature induced by heterogeneous nucleation.

Heterogeneous nucleation within porous media is the process in which ice nucleates somewhere in large pores, and then penetrates into small pores until the thermodynamic equilibrium as well as mechanical equilibrium between the ice crystal and liquid water are reached.

In practical engineering or lab experiments, based on the theory of heterogeneous nucleation, nucleation agents are often employed in the freezing porous media in order to rise or control the magnitude of the freezing temperature [230].

7.2 Thermodynamic equilibrium within unsaturated porous media under freezing

Generally all pores in porous media under freezing are considered to be totally filled with water, which is obviously unrealistic in almost all practical cases [193]. Therefore, in order to be consistent with realistic engineering situations, another vapour phase is introduced

in freezing problems by several investigators [193, 194, 222, 264]. However, as indicated by Brun et al. [32], the Gibbs-Duhem equation which governs the freezing in unsaturated porous media can not be solved with closed form solutions except in the special case where the ice-gas interface is assumed to be a plane [193]. Following Penttala et al. [193], the thermodynamic problem of freezing in unsaturated porous media is presented in the sequel.

7.2.1 Thermodynamic condition for the coexistence of each phase

Besides the lower freezing temperature by nucleation, freezing temperature can be depressed by the ions in solution or by the capillary effect of pores. In the normal case, pore water within porous media is aqueous solution rather than pure water. However, for simplifying, the effect of the ions will not be considered here, only the phase transformations between the pure unfrozen water (denoted as $\boldsymbol{l}$), ice $\boldsymbol{c}$ and vapour $\boldsymbol{v}$ will be discussed.

For the pure water in an unsaturated freezing system, as shown in Fig.(7.1), there coexist four kinds of water at different states: liquid water ($\boldsymbol{l}$), ice crystal ($\boldsymbol{c}$), unfrozen water film $\boldsymbol{f}$ on the ice crystal and vapour ($\boldsymbol{v}$). Here, the temperature is considered to be homogeneous whereas the pressure is only homogeneous in each phase.

The thermodynamic equilibriums between the unfrozen liquid water ($\boldsymbol{l}$), ice crystal ($\boldsymbol{c}$), unfrozen water film $\boldsymbol{f}$ on the ice crystal and vapour ($\boldsymbol{v}$) are expressed by the equality of their chemical potentials:

$$\begin{cases} \mu_l(T, P^l) = \mu_c(T, P^c) = \mu_f(T, P^f) = \mu_v(T, P^v) \\ \mu_l^0(T_0, P_0) = \mu_c^0(T_0, P_0) = \mu_f^0(T_0, P_0) = \mu_v^0(T_0, P_0) \end{cases} \tag{7.6}$$

From the Gibbs-Duhem equation, the chemical potential of the i^{th} ($i = \{c, l, f, v\}$) phase is expressed as:

$$\mathrm{d}\mu_i(T, P^i) = V_i \mathrm{d}P^i - S_i \mathrm{d}T \tag{7.7}$$

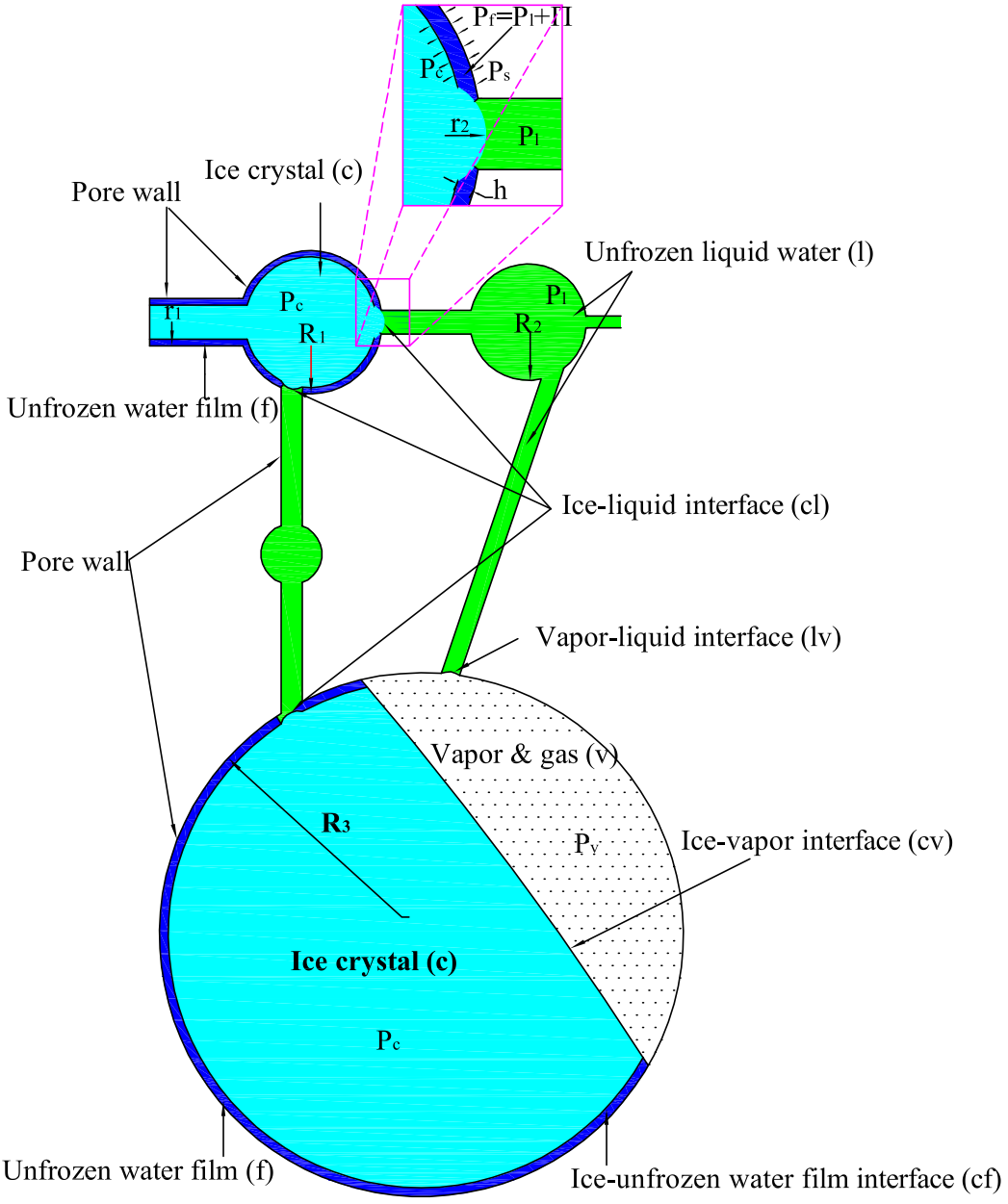

Figure 7.1: Schematic illustration of unsaturated porous media under freezing.

where $\mu_i(T, P^i)$ is the chemical potential of the i^{th} phase at temperature T and internal partial pressure P^i ($i \in \{c, l, f, v\}$), S_i (in J.mol^{-1}.K^{-1}) is the molar entropy of the i^{th} phase ($i \in \{c, l, f, v\}$) , V_i (in m^3.mol^{-1}) is molar volume of the i^{th} ($i \in \{c, l, f, v\}$) phase, while taking atmospheric pressure ($P_0 = 10^5$ Pa) and the corresponding freezing point $T_0 = 273.15$ K as the reference equilibrium state. Integrating Eq.(7.7), the chemical potential μ_i of each phase can be expressed as:

$$\mu_i(T, P^i) = \mu_i^0(T_0, P_0) - \int_{T_0}^{T} S_i \mathrm{d}T + \int_{P_0}^{P^i} V_i \mathrm{d}P \tag{7.8}$$

where $\mu_i^0(T_0, P_0)$ is the chemical potential of the i^{th} phase ($i \in \{c, l, f, v\}$) in the reference equilibrium bulk state.

In unsaturated freezing porous media, the thermodynamic equilibriums between ice and other three components $i = \{l, f, v\}$ are specified, based on the assumption of constant molar volume of liquid water, unfrozen water film and ice. From Eq.(7.8) and Eq.(7.6), it yields:

$$\begin{cases} V_c(P^c - P_0) - V_l(P^l - P_0) + \int_{T_0}^{T}(S_l - S_c)\mathrm{d}\tau = 0 \\ V_c(P^c - P_0) - V_f(P^f - P_0) + \int_{T_0}^{T}(S_f - S_c)\mathrm{d}\tau = 0 \\ V_c(P^c - P_0) - RT\ln(\dfrac{P^v}{P_0}) + \int_{T_0}^{T}(S_v - S_c)\mathrm{d}\tau = 0 \\ V_l(P^l - P_0) - RT\ln(\dfrac{P^v}{P_0}) + \int_{T_0}^{T}(S_v - S_l)\mathrm{d}\tau = 0 \end{cases} \tag{7.9}$$

where the vapour is assumed to behave like an ideal gas and we have $\int_{P_0}^{P^v} V_v \mathrm{d}P = RT\ln(\dfrac{P^v}{P_0})$; R is gas constant.

The molar entropy S_i in Eq.(7.9) can be calculated [193]:

$$S_i = S_i^0(T_0) + \int_{T_0}^{T} \frac{\partial S(T_0)}{\partial \tau}\mathrm{d}\tau = S_i^0(T_0) + \int_{T_0}^{T} \frac{C_{P,i}}{\tau}\mathrm{d}\tau \tag{7.10}$$

where $S_i^0(T_0)$ is the molar entropy of the i^{th} ($i \in \{c, l, f, v\}$) component of water in the reference equilibrium sate; $C_{P,i}$ is the heat capacity of the i^{th} component of water (in J.mol^{-1}).

Heat capacity of the i^{th} component of water depends upon the temperature, pressure[1] [193, 262]. However, as indicated by [93, 98, 262], the variation of the heat capacity with temperature is negligible in drained case when the temperature ranges between $-38°$C and $0°$C [98]. $C_{P,i}$ can thus be taken as a constant value. Therefore, from Eq.(7.10), we have:

$$\begin{cases} S_l - S_c = (S_l^0(T_0) - S_c^0(T_0)) + \int_{T_0}^{T} \dfrac{C_{P,l} - C_{P,c}}{\tau} \mathrm{d}\tau = \dfrac{\Delta H_{fus}^0}{T_0} + (C_{P,l} - C_{P,c}) \ln(\dfrac{T}{T_0}) \\ S_f - S_c = (S_f^0(T_0) - S_c^0(T_0)) + \int_{T_0}^{T} \dfrac{C_{P,f} - C_{P,c}}{\tau} \mathrm{d}\tau = \dfrac{\Delta H_{fus}^{f0}}{T_0} + (C_{P,f} - C_{P,c}) \ln(\dfrac{T}{T_0}) \\ S_v - S_c = (S_v^0(T_0) - S_c^0(T_0)) + \int_{T_0}^{T} \dfrac{C_{P,v} - C_{P,c}}{\tau} \mathrm{d}\tau = \dfrac{\Delta H_{sub}^0}{T_0} + (C_{P,v} - C_{P,c}) \ln(\dfrac{T}{T_0}) \\ S_v - S_l = (S_v^0(T_0) - S_l^0(T_0)) + \int_{T_0}^{T} \dfrac{C_{P,v} - C_{P,l}}{\tau} \mathrm{d}\tau = \dfrac{\Delta H_{eva}^0}{T_0} + (C_{P,v} - C_{P,l}) \ln(\dfrac{T}{T_0}) \end{cases} \tag{7.11}$$

where $\Delta H_{fus}^0 = (S_l^0(T_0) - S_c^0(T_0))T_0$ is the enthalpy change of fusion of ice (for capillary water) at reference state; $\Delta H_{fus}^{f0} = (S_f^0(T_0) - S_c^0(T_0))T_0$ is the enthalpy change of fusion of ice (for unfrozen water film) at reference state; $\Delta H_{sub}^0 = (S_v^0(T_0) - S_c^0(T_0))T_0$ is the enthalpy change of sublimation of ice at reference state; $\Delta H_{vap}^0 = (S_v^0(T_0) - S_l^0(T_0))T_0$ is the enthalpy change of vaporization of ice at reference state.

Integrating the Eq.(7.11) with temperature, it derives:

$$\begin{cases} \int_{T_0}^{T} (S_l - S_c) \mathrm{d}\tau = S_{fus}(T - T_0) + (C_{P,l} - C_{P,c})(T_0 - T + T\ln(\dfrac{T}{T_0})) \\ \int_{T_0}^{T} (S_f - S_c) \mathrm{d}\tau = S_{fusf}(T - T_0) + (C_{P,f} - C_{P,c})(T_0 - T + T\ln(\dfrac{T}{T_0})) \\ \int_{T_0}^{T} (S_v - S_c) \mathrm{d}\tau = S_{sub}(T - T_0) + (C_{P,v} - C_{P,c})(T_0 - T + T\ln(\dfrac{T}{T_0})) \\ \int_{T_0}^{T} (S_v - S_l) \mathrm{d}\tau = S_{eva}(T - T_0) + (C_{P,v} - C_{P,l})(T_0 - T + T\ln(\dfrac{T}{T_0})) \end{cases} \tag{7.12}$$

where $S_{fus} = S_l^0(T_0) - S_c^0(T_0)$ is defined as molar fusion entropy (in J.K^{-1}.mol^{-1}) at reference state (for capillary water); $S_{fusf} = S_f^0(T_0) - S_c^0(T_0)$ is defined as molar fusion entropy

1. The effect of salt concentration is neglected here.

(in J.K^{-1}.mol^{-1}) at reference state (for unfrozen water film); $S_{sub} = S_v^0(T_0) - S_c^0(T_0)$ is the molar sublimation entropy (in J.K^{-1}.mol^{-1}) at reference state; S_{eva} is the molar vaporization entropy (in J.K^{-1}.mol^{-1}) at reference state.

Substituting Eq.(7.12) into Eq.(7.9), we have:

$$\begin{cases} P^c - P^l = (\frac{V_l}{V_c} - 1)(P^l - P_0) + \frac{S_{fus}(T_0 - T)}{V_c} + \frac{C_{P,l} - C_{P,c}}{V_c}(T - T_0 + T\ln(\frac{T_0}{T})) & (a) \\ P^c - P^f = (\frac{V_f}{V_c} - 1)(P^f - P_0) + \frac{S_{fusf}(T_0 - T)}{V_c} + \frac{C_{P,f} - C_{P,c}}{V_c}(T - T_0 + T\ln(\frac{T_0}{T})) & (b) \\ P^c - P_0 = \frac{RT}{V_c}\ln(\frac{P^v}{P_0}) + \frac{S_{sub}(T_0 - T)}{V_c} + \frac{C_{P,c} - C_{P,v}}{V_c}(T - T_0 + T\ln(\frac{T_0}{T})) & (c) \\ P^l - P_0 = \frac{RT}{V_l}\ln(\frac{P^v}{P_0}) + \frac{S_{eva}(T_0 - T)}{V_l} + \frac{C_{P,l} - C_{P,v}}{V_l}(T - T_0 + T\ln(\frac{T_0}{T})) & (d) \end{cases} \tag{7.13}$$

7.2.2 Crystallographic structure of ice within porous media

Substituting $P^c = P^l$ in Eq.(7.13) (a) yields a Clapeyon-like equation:

$$P^l - P_0 = \frac{1}{V_c - V_l}[S_{fus}(T_0 - T) + (C_{P,l} - C_{P,c})(T - T_0 + T\ln(\frac{T_0}{T}))] \tag{7.14}$$

Eq.(7.14) allows predicting the boundary of the ice-liquid water phase diagram with temperature (shown as red lines in Fig.(7.2)).

Fig.(7.2) also presents different types of bulk ice with varied pressure and temperature. Nevertheless, the structure of ice within porous media is still under dispute. Numerous researches have indicated that the confined supercooled water in pores is transformed into cubic crystal ice instead of ordinary hexagonal ice (denoted as Ih in Fig.(7.2))), the detailed discussion is presented in [17, 86, 111, 174, 228, 233, 263]. However, it should be noted that for cement-based material, the supercooled water freezes via hexagonal structure generally [96, 221, 263]. The reasons lies in two factors: 1)- the temperature in normal atmospheric environment for cold region is rarely lower than 230K; 2)-the rough surface of solid skeleton of cement base material acts as nucleation agent [263]. Thus, the hexagonal ice is the usual

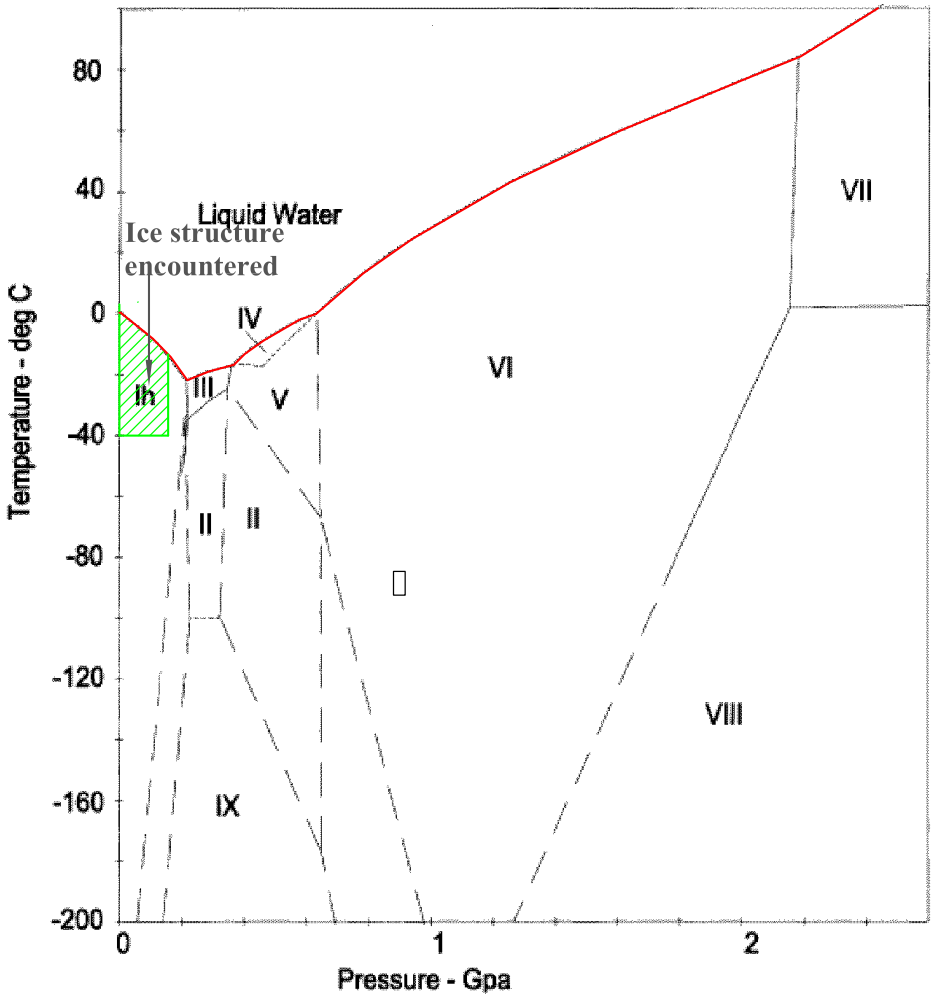

Figure 7.2: Phase diagram of water, modified from [4]

crystal form encountered in freezing cement based materials: in Fig.(7.2) it is shown as the green strip region (0℃∼ -40℃, several hundreds bar [265]).

7.2.3 Depression of the freezing temperature owing to capillary effect

As introduced in the Section(7.1), besides bulk supercooling, capillary effect can also depress the freezing temperature. The depression of the temperature arising from the capillary effect can be determined by the thermodynamic equilibrium and the mechanical equilibrium of the ice crystal-liquid water interface. Therefore, by means of Young-Laplace equation, Eq.(7.13) (a) can be rearranged as:

$$P^c - P^l = \kappa_{cl}\gamma_{cl} = (\frac{V_l}{V_c} - 1)(P^l - P_0) + S_m\Delta T + C_{fu}(-\Delta T + T\ln(\frac{T_0}{T})) \tag{7.15}$$

where $\Delta T = T_0 - T$ is the supercooling temperature, T_0 and T is the reference temperature (273 K) and the current freezing temperature, respectively; $S_m = S_{fus}/V_c$ (in J.K^{-1}. m^{-3}) is the fusion entropy when per unit volume ice transferring to liquid water, $C_{fu} = (C_{P,l} - C_{P,c})/V_c$ (in J.K^{-1}.m^{-3}) is the fusion heat capacity when per unit volume of water transforming to ice; κ_{cl} is the curvature of the ice-water interface, γ_{cl} is the surface tension of ice-water interface. As presented in [32], S_m=1.2 MPa.K^{-1}, C_{fu}=2.14 MPa.K^{-1}.

Since $(\frac{V_l}{V_c} - 1) \approx -0.09$ is a very low value, the term $(\frac{V_l}{V_c} - 1)(P^l - P_0)$ is usually neglected, Eq.(7.15) thus reduces to [98]:

$$\kappa_{cl}\gamma_{cl} = P^c - P^l = S_m\Delta T - C_f\frac{(\Delta T)^2}{2T_0} \tag{7.16}$$

As discussed in [98], Eq.(7.16) is usually satisfactory when the temperature is as low as −40°C, especially in drained condition.

In the case of spherical ice-liquid interface, $\kappa_{cl} = 2\cos\theta/r_c$ and making the first order ap-

proximation of temperature effect, Eq.(7.16) can be simplified as the classic Gibbs-Thomson equation:

$$\frac{2\gamma_{cl}\cos\theta}{r_c} = S_m \Delta T \tag{7.17}$$

where θ is the contact angle between ice crystal and unfrozen water film; r_c is the radius of spherical ice crystal filled with pore (with radius r_p), thus, $r_c = r_p - h$, h is the thickness of unfrozen water film.

However, it should be noted that, in undrained case, the pressure in freezing porous media can reach hundreds of MPa [60]. Consequently, in this case, the depressed effect induced by liquid pressure should be taken into account, the term $(\frac{V_l}{V_c} - 1)(P^l - P_0)$ should not be neglected. Consequently, Eq.(7.17) should be rewritten as:

$$P^c - P^l = \frac{2\gamma_{cl}\cos\theta}{r_c} = (\frac{V_l}{V_c} - 1)(P^l - P_0) + S_m \Delta T \tag{7.18}$$

7.2.4 Ice propagation within the pore network

At a given temperature below freezing point, ice crystals as well as unfrozen water films will form in the large capillary pores, while due to the freezing point depression, the water in smaller pores remains unfrozen.

On the premise of the equilibrium of ice crystal-liquid water interface at each temperature step, the classic Gibbs-Thomson equation (Eq.(7.17)) is commonly utilized to characterize the propagation of ice crystals in pores network, a schematic representation of the ice formation in simple pores network is illustrated in Fig.(7.3).

Let us assume that ice has formed in the channel with radius $r_1 + h(T_1)$ and the spherical pore with radius $R_1 + h(T_1)$ at temperature T_1, $h(T_1)$ being the thickness of the unfrozen water film at temperature T_1. From Eq.(7.17), r_2 will decrease from R_1 with decreasing T until $r_2 = r_3$, then allowing ice propagation into smaller channel pores. Note that the thickness of unfrozen water film h decreases with decreasing T and that the porous network

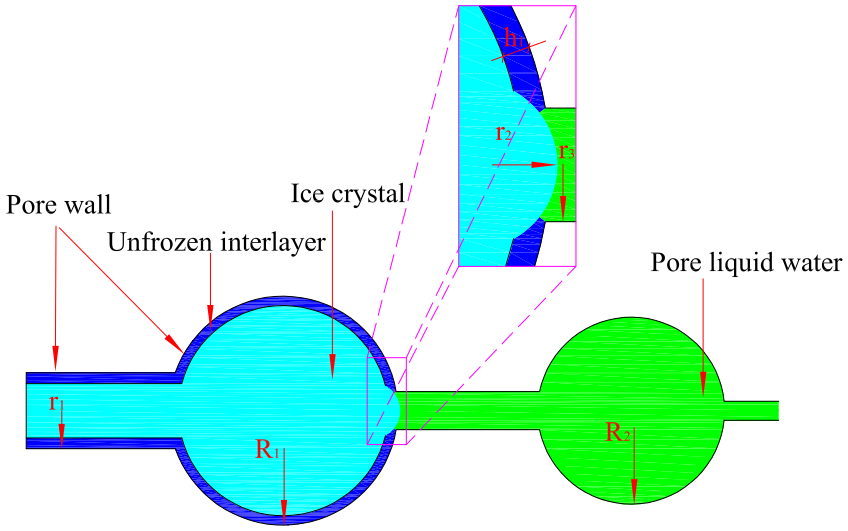

Figure 7.3: Sketch of progressive penetration of ice in interconnected pores.

radii are susceptible to change due to the mechanical effects.

7.3 Unfrozen water film in freezing porous media

The existence of the unfrozen water film on the surface of the ice crystal has been observed for more than 150 years since the pioneering work of Faraday [97]. Since then, numerous studies have focused on investigating the properties as well as behaviors of such peculiar unfrozen water film within freezing porous media [45, 46, 49, 50, 68, 69, 92, 130]. From all of these works on the unfrozen water film, it can be found that the disjoining pressure plays a central role in the stability and the thickness of the unfrozen water film [46].

7.3.1 Disjoining pressure in unfrozen water film

7.3.1.1 DLVO theory

It has been pointed out by Derjaguin and Churaev [46] that the Van der Waals dispersion pressure and electrostatic pressure are less sensitive to the temperature than the structural part. Hence, in unfrozen water film, the electrostatic and Van der Waals disjoining pressure can be determined by the DLVO theory at room temperature:

$$\Pi_{DLVO}(h) = \Pi_e(h) + \Pi_v(h) \tag{7.19}$$

Π_{DLVO}, Π_e, Π_v are the disjoining pressure determined by the DLVO theory, the electrostatic pressure and the Van der Waals pressure, respectively.

For the unfrozen water film in freezing porous media, owing to the different surface potential of interfaces (i.e., unfrozen water film-pore wall interface and unfrozen water film-ice crystal interface), the electrostatic pressure can be calculated by the model proposed by Churaev [46] [2]. Therefore, the disjoining pressure determined from the DLVO theory can be expressed as [46]:

2. The electrostatic component of disjoining pressure is determined based on this boundary condition: the surface charge remains constant when the two interfaces become closer and closer (from infinity distance). With this condition, the surface potential of interface ψ can be linked to the surface potential of interface at infinite distance ψ_∞.

$$\Pi_{DLVO}(h) = \frac{\epsilon\epsilon_0\kappa^2}{8\pi}\frac{[2\psi_{1\infty}\psi_{2\infty}\cosh(\kappa h) + \psi_{1\infty}^2 + \psi_{2\infty}^2]}{\sinh^2(\kappa h)} - A/(6\pi h^3) \tag{7.20}$$

ψ_1, ψ_2 (in V) are the surface potentials of the two interfaces (unfrozen water film-solid substrate interface and unfrozen water film-ice crystal interface), A is the Hamaker constant of the unfrozen water film between the pore wall and ice crystal.

7.3.1.2 Hamaker constant for unfrozen water film

Unfortunately, the Hamaker constant for the quartz pore wall-unfrozen water film-ice crystal system is still unknown [50]. Churaev et al. [50] has proposed that the Hamaker constant for quartz-water film-quartz (1.0×10^{-21} J) can be used for the quartz pore wall-unfrozen water film-ice crystal system.

There is another alternative solution: Eq.(3.20) can be used to estimate the value of Hamaker constant for quartz pore wall-unfrozen water film-ice crystal system. All constants of Eq.(3.20) can be determined as: $k = 1.381 \times 10^{-23}$ J.K^{-1}, $h = 6.626 \times 10^{-34}$ J s, $\nu_e = 3 \times 10^{15}$ s^{-1}, $\epsilon_1 = 3.8$, $\epsilon_2 = 4.15$ [132], $\epsilon_3 = 88$, $n_1 = 1.46$, $n_2 = 1.309$, $n_3 = 1.333$[132], $T = 272.13$ K. The Hamaker constant for quartz pore wall-unfrozen water film-ice crystal system is found to be 1.51×10^{-21} J, a slightly higher value than that suggested by Churaev et al. [50].

7.3.1.3 Structural component of disjoining pressure

Extensive investigations [45, 46, 49, 50] have found that the structural component of the disjoining pressure may play a dominant role in unfrozen water film due to the molecular structure modification of the unfrozen water film. Though the origin of the structural component of disjoining pressure is still disputed [50], its magnitude obeys the exponential form as in Eq.(3.21).

As discussed by Churaev et al. [46], the parameters K and λ are temperature-dependent: with decreasing temperature, the value of K increases and the value of λ decreases. It is

also found by Churaev et al. [46] that the parameters K and λ are of the same order for hydrophilic surface of mica, quartz, silica and glass, at room temperature. To describe all of the experimental results in the whole temperature range, a general empirical function [50, 190] including two exponential terms was proposed, it can be expressed by Eq.(3.22). The detailed analysis of the experimental results can be found in Appendix (A.4).

7.3.2 Dominant effect of structural component

As introduced in the previous section, due to the lack of the theoretical model for the structural component, its value is always determined by the difference between the total disjoining pressure and the disjoining pressure calculated by the DLVO theory.

As shown in Fig.(7.4), the combination of the electrostatic and Van der Waals components of the disjoining pressure (calculated by DLVO) is depicted as solid line, the experimental points stand for the measured total disjoining pressure. Here, we have, $A^{'} = 1.51 \times 10^{-21}$ J, $\psi_1 = -100$ mV for quartz surface, $\psi_2 = -60$ mV for ice interface, $\kappa = 10^8$ m^{-1} [46].

It can be found from Fig.(7.4) that the disjoining pressure determined by DLVO theory is far smaller than the total disjoining pressure, which means that the structural component plays a dominant role in the disjoining pressure of the unfrozen water film. The reason for such dominance may arise from the significantly modified structure of unfrozen water film, as discussed by Churaev et al. [50].

Therefore, as suggested by Churaev et al. [45, 50] the electrostatic and Van der Waals components of disjoining pressure are negligible and the disjoining pressure of the unfrozen water film can be calculated by two-terms exponential equation shown in Eq.(3.22) ($K_{sr} = 22.6$ MPa, $K_{lr} = 4.9$ MPa, $\lambda_{sr} = 3.1$ nm, $\lambda_{lr} = 20.3$ nm [50]), which is illustrated as dotted line in Fig.(7.4).

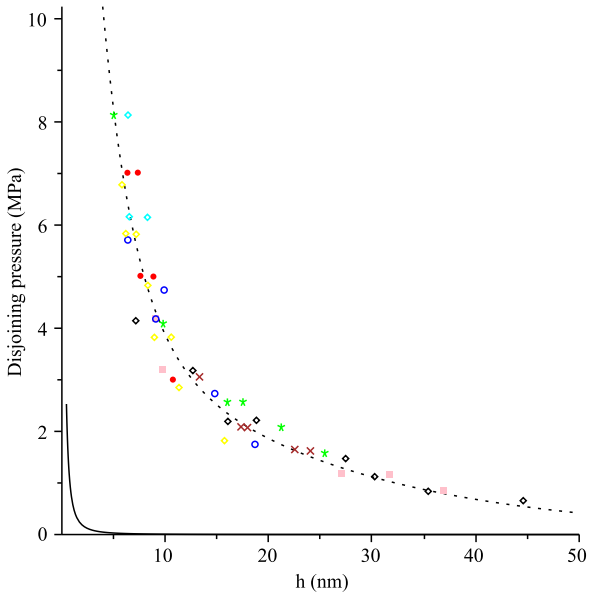

Figure 7.4: The disjoining pressure of the unfrozen water film between ice and fused quartz surface. The solid line is the disjoining pressure calculated by the DLVO theory (Eq.(7.19)), the dotted line is the structural component given by Eq.(3.22), the colored points are experimental results of the ice-unfrozen water film-quartz system after Churaev et al. [45].

7.4 Mechanisms and models for freezing porous media

Frost and surface scaling damage are the two main deteriorating phenomena of concrete structure in cold region [40, 230, 246, 265]. Intensive investigations upon porous media under freezing have been conducted for decades[40, 99, 230, 246, 265], numerous models and mechanisms for the deterioration of freezing porous media have been proposed [40, 60, 90, 99, 201, 202, 220, 222–224, 230, 246, 265]. However, none of them can account for all of the deterioration phenomena occurring in the field practice or laboratory experiments. To better understand and compare the advantages and disadvantages of certain models and mechanisms, we will briefly review several classic models and mechanisms for freezing in porous media, and potential subsequent damage process.

7.4.1 Hydraulic model

The hydraulic model for the freezing porous media is firstly introduced by Powers et al. [202] in their milestone study for the effect of air void in concrete. In this work, Powers attributed the damage of concrete under freezing to the hydraulic pressure. The latter arises from the following arguments: during freezing, liquid water within the pore will have a volumetric expansion of about 9% owing to the water-ice transformation; if there is not enough empty pore space within the material to act as expansion reservoir, hydraulic pressure will emerge [230]. Based on this argument, Powers suggested air voids be introduced into the concrete, in order to offer additional space for the expansion of ice. This is supported by experiment on air-entrained voids concrete which are less damaged during freezing. Therefore, the hydraulic pressure model for freezing porous media is widely accepted as an effective model for the internal frost damage [230]. Furthermore, by means of this model, the effect of the air-entrained voids can be quantitatively discussed [230]. In certain boundary conditions, such as fully saturated pore space conditions, while the external boundary is sealed well, the magnitude of the hydraulic pressure can be evaluated using the formula by Coussy et al. [58]:

$$P^l - P_{atm} = \frac{V_c - V_l}{V_c} \frac{Sr_c}{Sr_c/K_c + (1 - Sr_c)/K_l} \tag{7.21}$$

where P_{atm} is the atmospheric pressure,V_i $(i = l, c)$ is the molar volume of the i^{th} phase. Sr_i is the saturation degree of the i^{th} phase (here, $Sr_c + Sr_l = 1$), K_i is the bulk modulus of the i^{th} phase.

However, in following studies, Powers et al. [16, 201] found that the hydraulic model seemed imperfect to explain some of the frost phenomena, the pressure causing the damage of concrete under freezing being not necessary the hydraulic pressure. In the experiment, it was found that the samples without air voids continue to expand during freezing when the temperature kept constant [230]. This observation couldn't be explained by hydraulic pressure model as the hydraulic pressure here should be constant for constant value of the

temperature [230]. Furthermore, the samples with air voids during freezing shrank instead of simply not expanding [230].

The second experimental observation made by Beaudoin et al.[16] was more clearly showed the contradiction with the hydraulic pressure. Beaudoin performed an experiment by saturating concrete samples with benzene instead of with water. Benzene contracts during freezing, therefore there should be no hydraulic pressure in the concrete samples during freezing [230]. Correspondingly, there will be no expansion of the samples during freezing. Nevertheless, the benzene filled concrete samples were found to expand during freezing. From this experimental observations, the authors argued that there exists another crystallization pressure responsible for the damage of porous media during freezing [16] (see subsection (7.4.3)).

7.4.2 Osmotic model and cryo-suction effect

As presented in the previous subsection, due to the the obvious limitations of the hydraulic pressure model, Powers and and Helmuth [201] proposed a second model based on the physics related to osmosis phenomena. This osmotic model can be presented as follows: the pore water within porous media is electrolyte instead of pure water. During freezing, most of the capillary water in big pores is transformed into ice, the residual unfrozen solution (unfrozen water film) in the same capillary pores is concentrated simultaneously, while the pore solution of the thin capillary pores nearby stay at low concentration. The different concentrations of pore solution lead to different chemical potentials, which results in osmotic pressure within porous media accompanying the water migrating from the lower concentration (thin capillary pores) to higher concentration (big capillary pores) [262]. This model is indeed able to give an explanation to the unexpected experimental observation (continual expansion without air voids and continual shrinkage with air void) made by Powers [202].

Similarly, as proposed by Coussy et al. [60], the principle of the cryo-suction is induced by the different chemical potential of the ice and supercooling water. During freezing, if

the air void is filled with water, the latter will freeze first, the chemical potential of which is lower than that of supercooling water nearby, therefore, the ice in air voids tends to suck the supercooling water nearby, which results in a negative pressure likely to support the continual shrinkage of the entrained air void concrete samples [60].

It should be noted that, though the osmotic pressure and cryo-suction effect give rise to significant improvements allowing to explain qualitatively several unexpected experimental observation, they are still not easy to be taken into account quantitatively.

7.4.3 Crystallization pressure

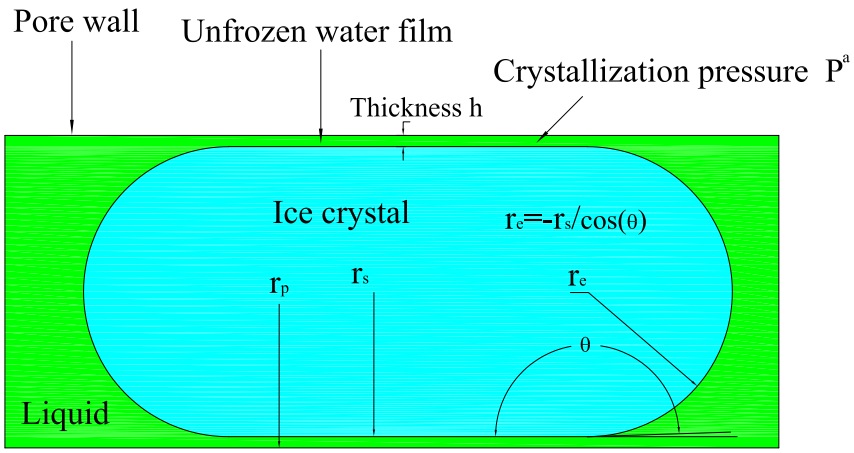

Figure 7.5: Schematic representation of crystallization pressure exerted on the cylindrical pore wall, modified from [220].

According to Scherer and co-workers [220, 230, 246], the crystallization pressure rather than hydraulic pressure is proved to be the real reason for the damage of the concrete under freezing. As depicted in Fig.(7.5), when ice crystallized in the capillary pores, at the pore end (with radius r_e) the interface of ice crystal-liquid water exhibits hemispherical configuration interface; while at the pore wall, the interface of ice crystal-unfrozen water film exhibits cylindrical shape (with radius r_s). The interfaces being in equilibrium and the

curvatures of the two interfaces being different, to ensure the uniformity of the pressure within the ice crystal, another pressure must be exerted on the crystal side along the pore wall. This pressure is the crystallization pressure P^a. For detailed discussion and application of crystallization pressure, the reader may refer to [220, 230, 246]. In the simple configuration of the cylindrical pores as shown in Fig.(7.5), with assumption of $\theta = 180°$ the magnitude of the crystallization pressure P^a can be estimated by [230]:

$$P^a = \gamma_{cl}(\kappa_{cl}^e - \kappa_{cl}^s) = \frac{\gamma_{cl}}{r_e} - \frac{\gamma_{cl}}{r_s} = \frac{\gamma_{cl}}{r_e} - \frac{\gamma_{cl}}{r_p - h} \tag{7.22}$$

where γ_{cl} is the surface tension of ice-liquid water interface, κ_{cl}^e and κ_{cl}^s are curvatures of the pore ends (hemispherical side) and pore sides (cylindrical side), r_e is the radius of ice crystal at the pore ends, r_s is the radius of the pore sides, r_p is the radius of the cylindrical pore, h is the thickness of unfrozen water film.

7.4.4 Disjoining pressure model

As developed by Derjaguin et al. [72, 73], an additional pressure within the unfrozen water film, named as disjoining pressure, emerges owing to the overlapping of two boundary layers: pore wall boundary layer and ice crystal boundary layer. Disjoining pressure plays a key role not only in formation of the unfrozen water film but also in the phenomenon of frost destruction of porous media [73]. Detailed information about the unfrozen water film can go back to Section.(7.3.2).

A schematic of the disjoining pressure effect is shown in Fig.(7.6). As illustrated in the inset of Fig.(7.6), ice-unfrozen water film interface and unfrozen water film-solid interface being in equilibrium:

$$\begin{cases} P^f - P^c = -\dfrac{2\gamma_{cl}}{R_1 - h} \\ P^f = P^l + \Pi(h) \\ P^c - P^l = \dfrac{2\gamma_{cl}}{r_2} \end{cases} \tag{7.23}$$

where r_2 is the radius of the ice-liquid water interface, R_1 is the radius of the spherical pore filled with ice and $\Pi(h)$ is the disjoining pressure which depends on the thickness of the unfrozen water film h (see Section(7.3)). In Eq.(7.23), the surface tension between ice crystal and unfrozen water film interface is taken the same as that between ice crystal and liquid water interface.

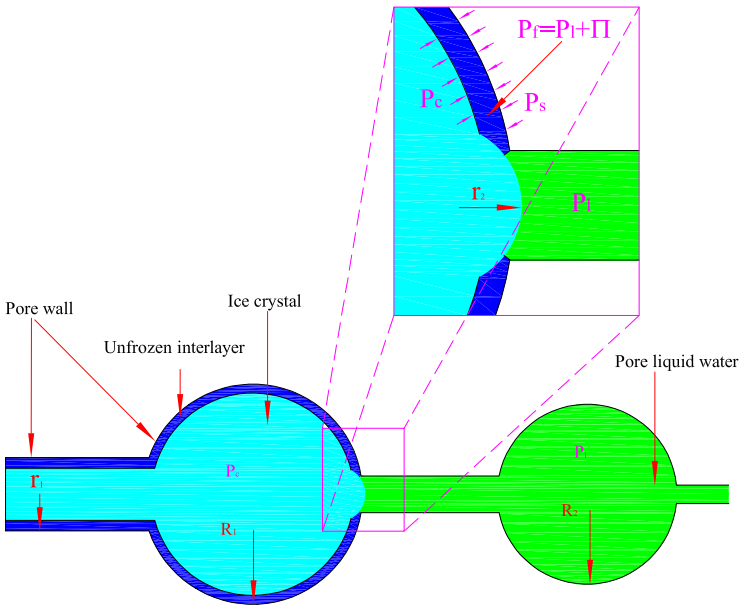

Figure 7.6: Schematic illustration of disjoining pressure of water film within crystallized pores.

From Eq.(7.23), the magnitude of the disjoining pressure can be estimated by:

$$\Pi(h) = \frac{2\gamma_{cl}}{r_2} - \frac{2\gamma_{cl}}{R_1 - h} \tag{7.24}$$

Eq.(7.24) is exactly the same expression as in Eq.(7.22) for $r_e = r_2$ and $r_p = R_1$. Thus, the disjoining pressure $\Pi(h)$ is indeed equal to the crystallization pressure P^a.

7.5 Poromechanics methodology for freezing in porous media

The differences between poromechanics and microporomechanics have been addressed in the Chapter 1. Unsaturated poroelasticity was employed into the freezing problems by Coussy et al. [57, 58, 60, 93, 99], Zuber et al. [267] and Wardeh and Perrin [250–252]. In poroelastic freezing model, there are two main internal pressures within freezing porous media: liquid pressure P^l and ice crystal pressure P^c. Use of P^c instead of $\Pi(h)$ lies in the assumption that: $R_1 - h \gg r_2$. From Eq.(7.24), it gives $\Pi(h) \approx \frac{2\gamma_{cl}}{r_2}$. When this expression for disjoining pressure is inserted into Eq.(7.23), we have:

$$P^c \approx \Pi(h) + P^l = P^f = P^s \tag{7.25}$$

The pressure of ice crystal P^c is thus the pressure exerted on the solid matrix P^s.

$$P^c \approx \Pi + P^l = P^f = P^s \tag{7.26}$$

Therefore, ice crystal pressure P^c instead of disjoining pressure $\Pi(h)$ is taken into account in the freezing poroelastic model [58, 60].

P^c and P^l can be linked by the thermodynamic equilibrium Eq.(7.13)(a) or its first order expression Eq.(7.18).

Based on Coussy's work [56, 58], in isotropic case, two state equations for freezing porous media which take into account of initial stress and interface stress can be revised as :

$$\begin{cases} \sigma - \sigma_0 = K\epsilon - b_l[P^l - P_0^l - (T^l - T_0^l)] - b_c[P^c - P_0^c - (T^c - T_0^c)] - K\alpha_s\delta T \\ \varphi_c - \varphi_{c0} = b_c\epsilon + \dfrac{Sr_c[(P^c - T^c) - (P_0^c - T_0^c)]}{N_{cc}} + \dfrac{Sr_l[(P^l - T^l) - (P_0^l - T_0^l)]}{N_{cl}} - \alpha_{\varphi_c}\delta T \\ \varphi_l - \varphi_{l0} = b_l\boldsymbol{\epsilon} + \dfrac{Sr_c[(P^c - T^c) - (P_0^c - T_0^c)]}{N_{cl}} + \dfrac{Sr_l[(P^l - T^l) - (P_0^l - T_0^l)]}{N_{ll}} - \alpha_{\varphi_l}\delta T \end{cases} \tag{7.27}$$

where σ is the macro stress, σ_0 is the initial macro stress tensor; K is the macroscopic bulk modulus; ϵ is the strain; b_i ($i \in \{l, c\}$) are the Biot coefficient for the pores filled with i^{th} phase; α_s is the thermal dilation coefficient tensor of the solid phase, α_{ϕ_i} are the volumetric thermal dilation coefficients of pore space filled with i^{th} phase; T^i are the average interface stresses for the i^{th} phase-solid interfaces, T_0^i are their corresponding initial interface stresses; $\delta T = T - T_0$ (cf. supercooling $\Delta T = T_0 - T$ in Eq.(7.15)); Sr_i are saturation degree for the i^{th} phase ($Sr_l + Sr_c = 1$); P^i are the internal pressure of the i^{th} phase, N_{ij} are poroelastic modulus relating the pore pressure P^i linearly to the porosity variation $\varphi_i - \varphi_{i0}$ when $\epsilon = 0$, $i \in \{l, c\}$; φ_i and φ_{i0} are the current and initial porosity occupied by the i^{th} phase.

The average interface stresses for the i^{th} phase-solid interfaces T^i within Eq.(7.27) can be determined by [58]:

$$T^i = \frac{1}{Sr_i} \int_{R_{min}}^{R_{cri}} \frac{2\gamma_{si}}{r} \frac{\mathrm{d}Sr_i(r)}{\mathrm{d}r} \mathrm{d}r \tag{7.28}$$

in which, γ_{si} stands for the surface tension between the solid matrix and the i^{th} phase (i$\in \{c, l\}$), R_{cri} is the critical radius of ice crystal, R_{min} is the minimum radius of porous media, $\mathrm{d}Sr_i(r)$ represents the infinitesimal fraction of porous volume occupied by the i^{th} phase.

The poroelastic freezing model needs the macroscopic poroelastic properties as input parameters. They can be measured by experiment as proposed by Sun[231, 232] and Zuber [266, 267].

They can also be estimated as proposed by Coussy et al. [58]. In isotropic case, the macroscopic poroelastic properties of porous media can be related to the macroscopic poroelastic properties of the solid matrix by the following expressions [57, 58]:

$$\begin{cases} \alpha_{\varphi_c} = \alpha_s(b_c - \phi_0 Sr_c) \\ \alpha_{\varphi_l} = \alpha_s(b_l - \phi_0 Sr_l) \\ \dfrac{1}{N_c} + \dfrac{1}{N_{cl}} = \dfrac{(b_c - \phi_0 Sr_c)}{K_s} \\ \dfrac{1}{N_l} + \dfrac{1}{N_{cl}} = \dfrac{(b_l - \phi_0 Sr_l)}{K_s} \\ b_l + b_c = b = 1 - \dfrac{K^{hom}}{K_s} \\ b_i = bS_i \end{cases} \tag{7.29}$$

where b is the Biot coefficient of the porous medium, $b_i (i = l, c)$ are the Biot coefficients for the i^{th} phase within isotropic porous media; K^{hom} and K_s are the bulk modulus of porous media and the corresponding solid skeleton, respectively.

Remark:

With the undrained boundary condition, free swelling ($\sigma = 0$) and the assumption of the absence of initial stress, from Eq.(7.27) and Eq.(7.17), we have:

$$\varepsilon = \frac{b_l[P^l - T^l] + b_c[P^l + S_m \Delta T - T^c] + K\alpha_s \delta T}{K} \tag{7.30}$$

It can be noted that the strain arising from the undrained free swelling of freezing porous media can be attributed to the following: -1) the hydraulic pressure P^l owing to the volumetric change of ice formation; -2) the interface stress arising from the surface tension effect; -3) thermal dilation (i.e. α_{ϕ_i} $(i = l, c)$ and α_s); -4) the pressure caused by fusion heat (i.e. $S_m \Delta T$).

7.6 Summary

In this chapter, some basic knowledge of the freezing is presented, which are essential to the micromechanics model for freezing porous media in the next chapter. The main information which will be used in sequel is summarized as follows:

— Some thermodynamic relations for the ice, liquid water and unfrozen water film are presented in this chapter. Besides the bulk supercooling effect, the depression of temperature $\Delta T = T_0 - T$ owing to capillary effect can be determined by Eq.(7.18).

— Several classic models and mechanisms for freezing in porous media are reviewed and discussed. Inspired by disjoining pressure for freezing porous media, the unfrozen water film as well as disjoining pressure within which will be introduced in the following micromechanics model for freezing porous media. The relation shown in Eq.(7.31) links the pressure in crystallized pore and the pore liquid pressure, it will be employed in the following micromechanics model for freezing porous media.

$$P^f = P^s = \Pi(h) + P^l \tag{7.31}$$

where P^f, P^s and P^l are the pressure of unfrozen water film (crystallized pore), pressure exerted on pore wall and liquid pressure, respectively; $\Pi(h)$ is the disjoining pressure of unfrozen water film.

— According to the experimental results of Churaev et al. [45, 46, 50], the Van der Waals component and electrostatic component of the disjoining pressure within unfrozen water film are negligible with respect to its structural component. Therefore, the total disjoining pressure may be fitted as a two-term exponential expression:

$$\Pi(h) = K_{sr}\exp(-h/\lambda_{sr}) + K_{lr}\exp(-h/\lambda_{lr}) \tag{3.22}$$

where K_{sr}, K_{lr}, λ_{sr} and λ_{lr} are the four corresponding fitting parameters, which are temperature dependent.

— Poromechanics methodology for freezing in porous media was discussed. The limitation of poromechanics methodology lies in its incapability of estimating the poroelastic properties theoretically. The difference of the poromechanics model and micromechanics model for freezing porous media lies in the dissimilar treatment of crystallized pore. Ice crystal pressure P^c is treated as internal pressure of crystal-

lized pore in poromechanics model, while $P^f = P^l + \Pi$ is considered as internal pressure of ice crystallized pore in micrmechanical model. A more detailed comparison between poromechanics model and micromechanics model for freezing porous media will be presented in Section(8.5.1.1).

Chapter 8

Micromechanical modelling of unsaturated freezing porous media

Contents

8.1 Introduction 195

8.2 A thermoporoelastic model for saturated porous media 196

8.2.1 Thermoporoelastic local behaviors 196

8.2.2 Macroscopic state equations 197

8.2.2.1 First state equation for thermoporoelasticity 198

8.2.2.2 Second thermoporoelastic state equation 199

8.3 A micromechanics model for unsaturated freezing porous media 200

8.3.1 Physical characterization of local phases within unsaturated freezing porous media 201

8.3.2 Localized behaviors in unsaturated freezing porous media 204

8.3.2.1 The initial state of the freezing in unsaturated porous media 204

8.3.2.2 The current state of freezing in unsaturated porous media 205

8.3.3 First poroelastic state equation for unsaturated freezing porous media 206

8.3.3.1 Dependence of the membrane stresses on the pore size distribution . . . 207
8.3.3.2 First state equation accounting for pore size effect . . . 210
8.3.3.3 Evolution of the macroscopic equivalent pressure during freezing process . . . 211
8.3.4 Second poroelastic state equation for unsaturated freezing porous media . . . 214
8.4 An alternative micromechanics model for unsaturated freezing porous media . . . 218
8.4.1 Localization of unfrozen water film accounting for its stiffness tensor 219
8.4.2 Homogenization of poroelastic properties . . . 220
8.5 Some discussion and applications . . . 221
8.5.1 A comparison between micromechanics model and poromechanics model for freezing . . . 222
8.5.1.1 Poromechanics model for freezing . . . 222
8.5.1.2 Micromechanics model for freezing . . . 222
8.5.2 Application: determining the liquid pressure with second state equation . . . 224
8.5.3 Application: estimating the evolution of mass quantity of ice within the air voids during freezing . . . 227
8.5.4 Application: a micromechanics approach to determine the thickness of unfrozen water film . . . 229
8.5.4.1 Strain of ice crystal . . . 229
8.5.4.2 Strain of ice-unfrozen water film spherical composite inclusion . . . 231
8.5.4.3 Determination of thickness of unfrozen water film . . . 232
8.6 Summary . . . 232

8.1 Introduction

Freezing within porous media is a thermoelastic problem coupled with phase transformation. It is likely to develop damage within the microstructure. The coalescence of these local damage may then yield to the macroscopic fracture of the material. To begin with, based on local phases characterization, a thermoporoelastic model for saturated porous media is proposed in Section(8.2).

A micromechanics model for unsaturated freezing porous media is developed in Section(8.3). When phase transformation (water to ice) is accounted for in the thermoporoelastic model. In crystallized pores, the unfrozen water film instead of ice crystal directly exerts pressure on the pore wall. Based on this local physical characterization, the internal pressure of unfrozen water film is taken as internal pressure of crystallized pores in this micromechanics model. As a comparison, ice crystal pressure is always taken as internal pressure of crystallized pores in poromechanics models [60, 99, 231, 267]. As introduced in Section(7.3), in addition to the liquid pressure, due to the overlapping of the boundary layers (here, boundary layers attached on the solid-unfrozen water film interface and ice-unfrozen water film interface), an additional disjoining pressure $\Pi(h)$ originates from the repulsive or attractive surface force emerges. In essence, the disjoining pressure is a local physical term which is related to thermodynamic equilibrium between the bulk liquid water and the unfrozen water film.

A more detailed micromechanics model for unsaturated freezing porous media will be introduced in Section(8.4), from the very definition of the disjoining pressure as a function of the thickness of the unfrozen water film, a stiffness of the unfrozen water film is accounted for in the micromechanics model.

In the last part, the poroelastic properties derived from the micromechanics model are discussed. Several applications will be also presented.

8.2 A thermoporoelastic model for saturated porous media

By means of micromechanics methodology, a poroelastic model for the saturated porous media has been developed by Dormieux et al. [82]. When the local thermal stress [1] is accounted for in this poroelastic model, a thermoporoelastic model has to be derived.

8.2.1 Thermoporoelastic local behaviors

In the REV of a saturated thermoporoelastic porous medium, the microscopic stress $\boldsymbol{\sigma}$ [2] , strain $\boldsymbol{\varepsilon}(\underline{z})$ and displacement $\underline{\xi}$ which characterize the response of the REV to the three loading parameters: the macroscopic strain tensor $\boldsymbol{E}$, the variation of the temperature δT ($\delta T = T - T_0$) and the uniform pore liquid pressure P should obey the following physical formulas:

$$\begin{cases} \mathrm{div}\boldsymbol{\sigma} = 0 & \underline{z} \in \Omega \\ \boldsymbol{\sigma} = \mathbb{C}^s : \boldsymbol{\varepsilon}(\underline{z}) - \boldsymbol{\kappa}^s \delta T & \underline{z} \in \Omega^s \\ \boldsymbol{\sigma} = -P\mathbf{1} & \underline{z} \in \Omega^p \\ \underline{\xi} = \boldsymbol{E} \cdot \underline{z} & \underline{z} \in \partial\Omega \end{cases} \tag{8.1}$$

where $\mathbb{C}^s$ and $\boldsymbol{\kappa}^s$ [3] are the elastic tensor and the thermal stress coefficient tensor of the solid phase, Ω^s and Ω^p are respectively the solid domain and pore space domain in the REV (domain Ω), $\Omega = \Omega^s \cup \Omega^p$.

Owing to the heterogeneity of porous media, solid phase (domain Ω^s) and pore space (domain Ω^p) exhibit distinct internal state of stress (see Eq.(8.1)). To make the physical

1. In this context, we assume the variation of temperature δT to be uniform throughout the overall REV.

2. In this text, for convenience, $\boldsymbol{\sigma}$ is concise expression of $\boldsymbol{\sigma}(\underline{z})$. In the following context, we always use $\boldsymbol{\sigma}$ instead of $\boldsymbol{\sigma}(\underline{z})$.

3. In this text, curlicue letters represent fourth order tensor, bold letters denote second order tensor while letters with underlines denote the vectors (first order tensor).

formulas be valid in the whole REV, Eq.(8.1) may be reorganized into the following general formulas:

$$\begin{cases} \mathrm{div}\boldsymbol{\sigma} = 0 & \underline{z} \in \Omega \\ \boldsymbol{\sigma} = \mathbb{C} : \boldsymbol{\varepsilon} + \boldsymbol{\sigma}^p - \boldsymbol{\kappa}\delta T & \underline{z} \in \Omega \\ \underline{\xi} = \boldsymbol{E} \cdot \underline{z} & \underline{z} \in \partial\Omega \end{cases} \tag{8.2}$$

with:

$$(\mathbb{C}, \boldsymbol{\kappa}, \boldsymbol{\sigma}^p)(\underline{z}) = \begin{cases} (\mathbb{C}^s, \boldsymbol{\kappa}^s, 0) & \underline{z} \in \Omega^s \\ (0, 0, -P\mathbf{1}) & \underline{z} \in \Omega^p \end{cases} \tag{8.3}$$

The problem in Eq.(8.2) may be processed as Levin's theorem. Given the linearity with respect to the three loadings $\boldsymbol{E}$, $\boldsymbol{\sigma}^p$ and δT, it is possible to take advantage of the decomposition of the linear problem into three loading subproblems as follows:

$$\begin{cases} (P^{'} : \boldsymbol{E} \neq 0, \delta T = 0, P = 0) \rightarrow (\boldsymbol{\sigma}^{'}, \boldsymbol{\varepsilon}^{'}) : \ \boldsymbol{\sigma}^{'} = \mathbb{C}^s : \boldsymbol{\varepsilon}^{'} \quad (\Omega^s), \\ \boldsymbol{\sigma}^{'} = 0 \quad (\Omega^p), \quad \underline{\xi}^{\prime} \rightarrow \boldsymbol{E} \cdot \underline{z} \quad (\partial\Omega) \\ (P^{''} : P \neq 0, \boldsymbol{E} = 0, \delta T = 0) \rightarrow (\boldsymbol{\sigma}^{''}, \boldsymbol{\varepsilon}^{''}) : \boldsymbol{\sigma}^{''} = \mathbb{C}^s : \boldsymbol{\varepsilon}^{''} \quad (\Omega^s), \\ \boldsymbol{\sigma}^{''} = -P\mathbf{1} \quad (\Omega^p), \quad \underline{\xi}^{''} \rightarrow 0 \quad (\partial\Omega) \\ (P^{'''} : \delta T \neq 0, \boldsymbol{E} = 0, P = 0) \rightarrow (\boldsymbol{\sigma}^{'''}, \boldsymbol{\varepsilon}^{'''}) : \boldsymbol{\sigma}^{'''} = \mathbb{C}^s : \boldsymbol{\varepsilon}^{'''} - \boldsymbol{\kappa}\delta T \quad (\Omega^s), \\ \boldsymbol{\sigma}^{'''} = 0 \quad (\Omega^p), \quad \underline{\xi}^{'''} \rightarrow 0 \quad (\partial\Omega) \end{cases} \tag{8.4}$$

8.2.2 Macroscopic state equations

The two poroelastic state equations are now derived from Eq.(8.4). They relate the macroscopic stress tensor and Lagrangian porosity variation $(\phi - \phi_0)$ to the loading parameters $\boldsymbol{E}$, δT and P. They correspond to the two poroelastic state equations which will be

presented in the follows.

8.2.2.1 First state equation for thermoporoelasticity

As introduced in Eq.(1.2), the macroscopic stress tensor $\boldsymbol{\Sigma}$ is defined as the average of the local stress tensor $\boldsymbol{\sigma}(\underline{z})$ over Ω:

$$\boldsymbol{\Sigma} = \langle \boldsymbol{\sigma}(\underline{z}) \rangle_{\Omega} \tag{8.5}$$

With the introduction of strain concentration tensor $\overline{\mathbb{A}}^{i}$ $(i \in \{s, p\})$ [4] [82] , the first thermoporoelastic state equation could be derived:

$$\boldsymbol{\Sigma} = \mathbb{C}^{hom} : \boldsymbol{E} - \boldsymbol{B}P - \boldsymbol{\kappa}^{hom}\delta T \tag{8.6}$$

with:

$$\begin{cases} \mathbb{C}^{hom} = (1-\phi_0)\mathbb{C}^s : \overline{\mathbb{A}}^s = \mathbb{C}^s : (\mathbb{I} - \phi_0 \overline{\mathbb{A}}^p) \\ \boldsymbol{\kappa}^{hom} =< \boldsymbol{\kappa} : \mathbb{A} >= \boldsymbol{\kappa}^s : (\mathbb{I} - \phi_0 \overline{\mathbb{A}}^p) = \boldsymbol{\kappa}^s : \mathbb{S}^s : \mathbb{C}^{hom} = \boldsymbol{\alpha}^s : \mathbb{C}^{hom} \\ \boldsymbol{B} = \phi_0 \mathbf{1} : \overline{\mathbb{A}}^p = \mathbf{1} : (\mathbb{I} - \mathbb{S}^s : \mathbb{C}^{hom}) \end{cases} \tag{8.7}$$

in which $\mathbb{C}^{hom}$, $\boldsymbol{\kappa}^{hom}$ and $\boldsymbol{B}$ are respectively the homogenized elastic tensor, the homogenized thermal stress coefficient tensor and the Biot tensor, $\mathbb{S}^s$ is the compliance tensor of solid phase ($\mathbb{S}^s = (\mathbb{C}^s)^{-1}$); $\boldsymbol{\alpha}^s$ is the volumetric thermal dilation coefficient tensor of the solid phase, $\overline{\mathbb{A}}^p$ and $\overline{\mathbb{A}}^s$ are the average strain concentration tensors over the pore space and the solid phase, respectively.

The homogenized volumetric thermal dilation coefficient tensor can be defined as

4. In this context, superscripts s and p represent as follows: s: solid phase, p: pore space.

$\boldsymbol{\alpha}^{hom} = \mathbb{S}^{hom} : \boldsymbol{\kappa}^{hom}$ and it may be deduced as follows:

$$\begin{aligned}\boldsymbol{\alpha}^{hom} = \mathbb{S}^{hom} : \boldsymbol{\kappa}^{hom} = \boldsymbol{\kappa}^{hom} : \mathbb{S}^{hom} = \boldsymbol{\kappa}^{s} : (\mathbb{I} - \phi_0 \overline{\mathbb{A}}^{p}) : ((1-\phi_0)\mathbb{C}^{s} : \overline{\mathbb{A}}^{s})^{-1} \\ = ((1-\phi_0)\boldsymbol{\kappa}^{s} : \overline{\mathbb{A}}^{s}) : ((1-\phi_0)\mathbb{C}^{s} : \overline{\mathbb{A}}^{s})^{-1} = \boldsymbol{\kappa}^{s} : \mathbb{S}^{s} = \boldsymbol{\alpha}^{s}\end{aligned} \tag{8.8}$$

In may be concluded that the homogenized volumetric thermal dilation coefficient of porous media is only related to the volumetric thermal dilation coefficient of solid phase.

A remark for a special case:

According to Eq.(8.6), when a porous medium with drained boundary condition ($P = 0$) is under free swelling ($\boldsymbol{\Sigma} = \mathbf{0}$), the macroscopic strain is determined by:

$$\boldsymbol{E} = \mathbb{S}^{hom} : \boldsymbol{\kappa}^{hom}\delta T = \boldsymbol{\alpha}^{hom}\delta T = \boldsymbol{\alpha}^{s}\delta T \tag{8.9}$$

In this case, the macroscopic strain tensor $\boldsymbol{E}$ is strictly controlled by the thermal properties of the solid phase $\boldsymbol{\alpha}^s$, $\mathbb{S}^{hom}$ is the homogenized compliance tensor of porous media.

8.2.2.2 Second thermoporoelastic state equation

Concerning the second state equation, the applied loadings may also be decomposed into three subproblems as Levin's theorem, (as shown in Eq.(8.4)). Hence, the variation of porosity $\phi - \phi_0$ may be decomposed into the following three components:

$$\phi - \phi_0 = \phi_0 \mathbf{1} : \overline{\boldsymbol{\varepsilon}}^{p} = \phi_0 \mathbf{1} : (\overline{\boldsymbol{\varepsilon}'}^{p} + \overline{\boldsymbol{\varepsilon}''}^{p} + \overline{\boldsymbol{\varepsilon}'''}^{p}) \tag{8.10}$$

— **Subproblem 1** (P'), $\boldsymbol{E} \neq 0$, $\delta T = 0$,$P = 0$: with $\overline{\boldsymbol{\varepsilon}'}^{p} = \overline{\mathbb{A}}^{p} : \boldsymbol{E}$, we have $\phi_0 \mathbf{1} : \overline{\boldsymbol{\varepsilon}'}^{p} = \phi_0 \mathbf{1} : \overline{\mathbb{A}}^{p} : \boldsymbol{E} \Rightarrow \phi_0 \mathbf{1} : \overline{\boldsymbol{\varepsilon}'}^{p} = \boldsymbol{B} : \boldsymbol{E}$

— **Subproblem 2** (P''), $P \neq 0$, $\boldsymbol{E} = 0$, $\delta T = 0$: with $\phi_0 \overline{\boldsymbol{\varepsilon}''}^{p} + (1-\phi_0)\overline{\boldsymbol{\varepsilon}''}^{s} = 0$ and $\boldsymbol{\Sigma}'' = (1-\phi_0)\mathbb{C}^{s} : \overline{\boldsymbol{\varepsilon}''}^{s} - \phi_0 P \mathbf{1} = -\boldsymbol{B}P$, we have $-\phi_0 \mathbb{C}^{s} : \overline{\boldsymbol{\varepsilon}''}^{p} - \phi_0 P \mathbf{1} = -\boldsymbol{B}P \Rightarrow$

$\phi_0\mathbf{1} : \overline{\boldsymbol{\varepsilon}''^p} = \mathbf{1} : \mathbb{S}^s : (\boldsymbol{B} - \phi_0\mathbf{1})P = \dfrac{1}{N}P$

— **Subproblem 3** (P'''), $\delta T \neq 0$, $\boldsymbol{E} = 0$, $P = 0$: with $\phi_0\overline{\boldsymbol{\varepsilon}'''^p} + (1-\phi_0)\overline{\boldsymbol{\varepsilon}'''^s} = 0$ and $\boldsymbol{\Sigma}''' = (1-\phi_0)\mathbb{C}^s : \overline{\boldsymbol{\varepsilon}'''^s} - (1-\phi_0)\boldsymbol{\kappa}^s\delta T = -\boldsymbol{\kappa}^{hom}\delta T$, we have $-\phi_0\mathbb{C}^s : \overline{\boldsymbol{\varepsilon}'''^p} - (1-\phi_0)\boldsymbol{\kappa}^s\delta T = -\boldsymbol{\kappa}^{hom}\delta T \Rightarrow \phi_0\mathbf{1} : \overline{\boldsymbol{\varepsilon}'''^p} = \mathbf{1} : \mathbb{S}^s : [\boldsymbol{\kappa}^{hom} - (1-\phi_0)\boldsymbol{\kappa}^s]\delta T = (\phi_0\mathbf{1} - \boldsymbol{B}) : \boldsymbol{\alpha}^s\delta T = -\alpha_\phi\delta T$

Inserting the results of the three subproblems into Eq.(8.10) yields the second thermo-poroelastic state equation as:

$$\phi - \phi_0 = \boldsymbol{B} : \boldsymbol{E} + \frac{1}{N}P - \alpha_\phi\delta T \tag{8.11}$$

with:

$$\begin{cases} \boldsymbol{B} = \mathbf{1} : (\mathbb{I} - \mathbb{S}^s : \mathbb{C}^{hom}) \\ \dfrac{1}{N} = \mathbf{1} : \mathbb{S}^s : (\boldsymbol{B} - \phi_0\mathbf{1}) \\ \alpha_\phi = (\boldsymbol{B} - \phi_0\mathbf{1}) : \boldsymbol{\alpha}^s \end{cases} \tag{8.12}$$

It is interesting to note that, the homogenized volumetric thermal dilation coefficient tensor α_ϕ is closely related to the volumetric thermal dilation coefficient tensor of solid phase $\boldsymbol{\alpha}^s$, Biot coefficient tensor $\boldsymbol{B}$ and initial porosity ϕ_0. Nevertheless, it is irrelevant to the thermal properties of fluid within porous media [5].

8.3 A micromechanics model for unsaturated freezing porous media

Generally, the traditional models for freezing porous media often neglect the effect of the unfroze water film [57, 201, 220]. As introduced in chapter 7, the disjoining pressure within unfrozen water film plays a significant role in the internal pressure of crystallize pores (the internal pressure of unfrozen water film). Herein, the special physics of the unfrozen water

5. However, the liquid pressure within the porous media is closely related to the thermal properties of the fluid [58].

film [6] is accounted for in the micromechanics model.

8.3.1 Physical characterization of local phases within unsaturated freezing porous media

As presented in Fig.(8.1), a REV of unsaturated freezing porous media is made up of a **s**olid matrix (domain $\Omega^{\boldsymbol{s}}$) and a **p**ore space (domain $\Omega^{\boldsymbol{p}}$). The latter may be filled with three kinds of immiscible phase depending on its size (see the pore size distribution in Fig.(8.1)): unfrozen pores liquid (domain Ω^{l}), ice crystal **s**pherical **c**omposite inclusion (domain $\Omega^{\boldsymbol{sc}}$) [7] and the gas phase (domain Ω^{g}). The initial configuration of these domains are denoted as Ω_0^{l}, Ω_0^{sc}, and Ω_0^{g}, respectively. The ice crystal spherical composite inclusion may be divided into two components: ice crystal (domain Ω^{c}) and unfrozen water film (domain Ω^{f}).

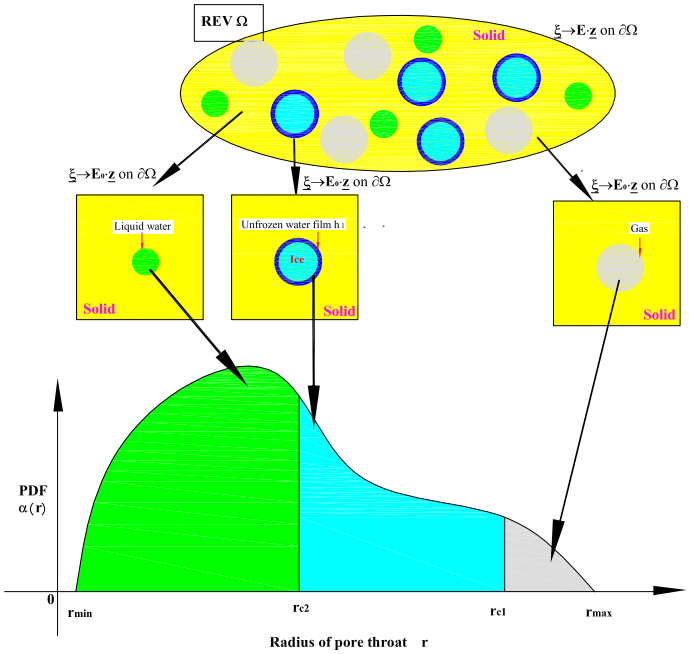

Figure 8.1: Morphological illustration of the freezing in unsaturated porous media

Physically, unsaturated freezing porous media may be treated as an unsaturated ther-

6. The internal pressure of the water film P^f is the combination of liquid pressure P^l and the disjoining presure $\Pi(h)$, $P^f = P^l + \Pi(h)$.

7. In ice crystallized pore, ice crystal coupled with the unfrozen water film may be treated as spherical composite inclusion (as presented in Fig.(8.1)).

moporoelastic problem. Therefore, as introduced in the previous section, the thermal stress induced by the variation of temperature δT as well as internal pore pressures should be taken into account during progressive freezing process. Depending on the pore sizes (see the pore size distribution in Fig.(8.1)), the internal pore pressures may be specified as follows:

— Liquid pressure P^l:

In freezing porous media, the liquid pressure P^l is closely related to the boundary condition. In drained freezing porous media, the liquid pressure remains to be atmospheric pressure. However, in undrained freezing porous media, the liquid pressure is induced by the phase transformation of liquid water to ice crystal and plays a significant role in freezing problem.

— Gas pressure P^g:

As introduced in Section(7.2), when the pore space coexists three immisible phases such as gas (vapor), unfrozen liquid and ice-unfrozen water film composite inclusion, the pressures of each phase will not have closed form solution. Hence, several assumptions should be made to determine the internal pressures of gas, liquid and ice crystal composite in this unsaturated freezing problem.

For example, in the air-entrained voids cement paste, the gas pressure is always assumed to be equal to the internal pressure of ice crystal (the interface between gas and ice crystal is assumed to be a flat plane). Both of them are assumed to equal to the atmospheric pressure in air void cement paste [231].

— Membrane stress:

Membrane stress in unsaturated freezing porous media is ascribed by surface tension of different interfaces, it leads to the stress vector discontinuity between different phases. The detailed information of membrane stress is given in Section(1.3).

— Internal pressure within unfrozen water film P^f:

The internal pressure of unfrozen water film can be determined in the form of:

$$P^f \mathbf{1} = P^l \mathbf{1} + \Pi(h) \underline{n} \otimes \underline{n} \tag{8.13}$$

where P^f is the internal pressure of unfrozen water film, P^l are the internal pressure of the liquid water, $\Pi(h)$ is the disjoining pressure within unfrozen water film, h is the thickness of unfrozen water film.

As introduced in Section(3.3), P^g and P^l may be linked by Kelvin equation (Eq.(3.11)). P^c and P^l may be linked by Gibbs-Thomson equation (Eq.(7.18)), P^c and P^f ($P^f = P^l + \Pi(h)$) may also be linked by Eq.(7.23). In these three equations, an additive disjoining pressure $\Pi(h)$ is introduced needs to be explicitly determined.

Currently, there is no theoretical model to explicitly determine the disjoining pressure. Nevertheless, as introduced and discussed in Section(7.3), the structural component of the disjoining pressure sufficiently represents the total disjoining pressure in the unfrozen water film. The disjoining pressure of unfrozen water film may thus be estimated as a function of the thickness of the unfrozen water film by the following two-term exponential formula [190]:

$$\Pi(h) = K_{sr}\exp(-\frac{h}{\lambda_{sr}}) + K_{lr}\exp(-\frac{h}{\lambda_{lr}}) \tag{8.14}$$

where K_{sr}, K_{lr}, λ_{sr} and λ_{lr} are fitting parameters which characterize the acting range of surface force in unfrozen water film.

The current volume fraction of the i^{th} phase ($i \in \{s, l, g, c, sc, f\}$) is denoted by φ_i. The saturation degrees of ice crystal composite inclusion Sr_{sc}, liquid water Sr_l and gas Sr_g may be defined as:

$$\begin{cases} Sr_l = \dfrac{|\Omega^l|}{|\Omega^p|} = \dfrac{\varphi_l}{\phi}; \quad Sr_{sc} = \dfrac{|\Omega^{sc}|}{|\Omega^p|} = \dfrac{\varphi_{sc}}{\phi}; \quad Sr_g = \dfrac{|\Omega^g|}{|\Omega^p|} = \dfrac{\varphi_g}{\phi}; \\ \varphi_{sc} = \varphi_f + \varphi_c; \quad \phi = \varphi_l + \varphi_{sc} + \varphi_g \end{cases} \tag{8.15}$$

where ϕ is the porosity.

Several assumptions are made for unsaturated freezing porous media: 1)-in the overall REV, the pore network is assumed to be hydraulically interconnected to ensure the uniformity of the pore pressures in each phase. P^l, P^f and P^g are assumed to be uniform in

each phase at equilibrium state; 2)-thermodynamic equilibrium and mechanical equilibrium between each phase are assumed; 3)-the displacement and transformation of the freezing porous media is infinitesimal at micro and macro scale so that the mechanical behaviors of the freezing porous media lie in the poroelastic regime; 4)-the variation of the temperature δT is assumed to be uniform throughout the overall REV.

8.3.2 Localized behaviors in unsaturated freezing porous media

The present section is an extension of the previous saturated case to the behavior of the unsaturated freezing porous media. The initial and current states of the unsaturated freezing porous media will also be specified in this section.

8.3.2.1 The initial state of the freezing in unsaturated porous media

As encountered in many engineering applications, an initial prestress $\boldsymbol{\sigma}_0$ prevails within porous media. The initial configuration of porous medium is here the reference state and the initial macroscopic strain of porous media is considered to be 0. By analogy to Eq.(8.2), the physical formulas for this initial state problem can be expressed as:

$$\begin{cases} \mathrm{div}\boldsymbol{\sigma}_0 = 0 & \underline{z} \in \Omega_0 \\ \boldsymbol{\sigma}_0(\underline{z}) = \mathbb{C}(\underline{z}) : \boldsymbol{\varepsilon}_0 - \boldsymbol{\kappa}\delta T_0 + \boldsymbol{\sigma}_0^p & \underline{z} \in \Omega_0 \\ \underline{\xi}_0 = 0 & \underline{z} \in \partial\Omega_0 \end{cases} \tag{8.16}$$

where Ω_0 and $\partial\Omega_0$ are the initial REV domain and its corresponding boundary surface; $\boldsymbol{\varepsilon}_0$, δT_0, $\boldsymbol{\sigma}_0^p$ and $\underline{\xi}_0$ are initial local strain, initial temperature variation, initial internal pore pressure and initial boundary displacement, respectively. Correspondingly, the initial poroelastic properties can be summarized as:

$$(\mathbb{C},\boldsymbol{\kappa},\boldsymbol{\sigma^p})(\underline{z})=\begin{cases}(\mathbb{C}^s,\boldsymbol{\kappa}^s,\boldsymbol{\sigma_0}) & \forall\underline{z}\in\Omega_0^s\\ (0,0,-P_0^f\mathbf{1}) & \forall\underline{z}\in\Omega_0^{sc}\\ (0,0,-P_0^g\mathbf{1}) & \forall\underline{z}\in\Omega_0^g\\ (0,0,-P_0^l\mathbf{1}) & \forall\underline{z}\in\Omega_0^l\\ (0,0,\gamma^{ac}\mathbf{1}_T\delta_{ac}) & \forall\underline{z}\in\mathcal{I}_0^{ac}\end{cases}\tag{8.17}$$

In which, the physical quantities with subscript "0" correspond to its initial value; γ^{ac} is the surface tension within the initial interface $\mathcal{I}_0^{ac}$, δ_{ac} is dirac distribution function $((a,c)\in\{f,l,c,g,s,sc\})$.

8.3.2.2 The current state of freezing in unsaturated porous media

The microscopic stress, strain and displacement and boundary condition in the REV at uniform boundary condition obeys the following physical formulas:

$$\begin{cases}\mathrm{div}\boldsymbol{\sigma}=0 & \underline{z}\in\Omega\\ \boldsymbol{\sigma}=\mathbb{C}:\boldsymbol{\varepsilon}+\boldsymbol{\sigma}^p-\boldsymbol{\kappa}\delta T & \underline{z}\in\Omega\\ \underline{\xi}=\boldsymbol{E}\cdot\underline{z} & \underline{z}\in\partial\Omega\end{cases}\tag{8.18}$$

with:

$$(\mathbb{C},\boldsymbol{\kappa},\boldsymbol{\sigma^p})(\underline{z})=\begin{cases}(\mathbb{C}^s,\boldsymbol{\kappa}^s,0) & \forall\underline{z}\in\Omega^s\\ (0,0,-P^f\mathbf{1}) & \forall\underline{z}\in\Omega^{sc}\\ (0,0,-P^g\mathbf{1}) & \forall\underline{z}\in\Omega^g\\ (0,0,-P^l\mathbf{1}) & \forall\underline{z}\in\Omega^l\\ (0,0,\gamma^{ab}\mathbf{1}_T\delta_{ab}) & \forall\underline{z}\in\mathcal{I}^{ab}\end{cases}\tag{8.19}$$

where γ^{ab} is the surface tension within the current interface $\mathcal{I}^{ab}$, δ_{ab} is dirac distribution function $((a,b)\in\{f,l,c,g,s,sc\})$.

8.3.3 First poroelastic state equation for unsaturated freezing porous media

The macroscopic stress tensor $\boldsymbol{\Sigma}$ may be derived by average of the local stress over REV domain Ω (see Eq.(8.5)). Treating the homogenization by means of Levin's theorem [82], the macroscopic stress tensor may be decomposed into four loading cases: 1)-the initial stress $\boldsymbol{\sigma}_0$ (corresponding to macroscopic stress $\boldsymbol{\Sigma}^{'}$), 2)-the macroscopic strain $\boldsymbol{E}$ (corresponding to macroscopic stress $\boldsymbol{\Sigma}^{''}$), 3)-the thermal stress tensor $\boldsymbol{\kappa}\delta T$ (corresponding to macroscopic stress $\boldsymbol{\Sigma}^{'''}$) and 4)-the prestress tensor $\boldsymbol{\sigma}^p$ (corresponding to macroscopic stress $\boldsymbol{\Sigma}^{''''}$). The macroscopic stress $\boldsymbol{\Sigma}$ is thus derived by linearly superposing the four loading cases in the form of [8]:

$$\begin{aligned}\boldsymbol{\Sigma} &= \boldsymbol{\Sigma}^{'} + \boldsymbol{\Sigma}^{''} + \boldsymbol{\Sigma}^{'''} + \boldsymbol{\Sigma}^{''''} \\ &= \boldsymbol{\Sigma}_0 + \mathbb{C}^{hom} : \boldsymbol{E} - \boldsymbol{\kappa}^{hom}\delta T - (\varphi_l P^l \mathbf{1} : \overline{\mathbb{A}}^{l} + \varphi_{sc} P^f \mathbf{1} : \overline{\mathbb{A}}^{sc} + \varphi_g P^g \mathbf{1} : \overline{\mathbb{A}}^{g}) \\ &\quad + [(\gamma_{ab}\int_{\mathcal{I}^{ab}} \mathbf{1}_T : \mathbb{A}\frac{dS}{\Omega}) - (\gamma_{ac}\int_{\mathcal{I}_0^{ac}} \mathbf{1}_T : \mathbb{A}\frac{dS}{\Omega})]\end{aligned} \tag{8.20}$$

where $\boldsymbol{\Sigma}_0$ and $\boldsymbol{\Sigma}$ are the initial and current macroscopic stresses; $\mathbb{C}^{hom}$ and $\boldsymbol{\kappa}^{hom}$ are the homogenized elastic tensor (stiffness tensor) and homogenized thermal stress coefficient tensor, respectively; $\overline{\mathbb{A}}^{l}$, $\overline{\mathbb{A}}^{sc}$ and $\overline{\mathbb{A}}^{g}$ are average strain concentration tensors of liquid water phase, ice crystal spherical composite inclusion and gas phase, respectively; $(\gamma_{ac}\int_{\mathcal{I}_0^{ac}} \mathbf{1}_T : \mathbb{A}\frac{dS}{\Omega})$ and $(\gamma_{ab}\int_{\mathcal{I}^{ab}} \mathbf{1}_T : \mathbb{A}\frac{dS}{\Omega})$ are the initial and current membrane stresses, respectively, where $\mathcal{I}_0^{ac}$ $\mathcal{I}^{ab}$ are the initial and current interface.

Indeed, Eq.(8.20) may be rewritten as concise incremental form [9] as:

8. The detailed derivation is suggested to refer to Appendix(D)

9. It should bear in mind that the initial macroscopic strain $\boldsymbol{E}_0$ is taken as the reference strain and equal to 0.

$$\delta\boldsymbol{\Sigma} = \mathbb{C}^{hom} : \boldsymbol{E} - \boldsymbol{\kappa}^{hom}\delta T - (\varphi_l \delta P^l \mathbf{1} : \overline{\mathbb{A}}^{l} + \varphi_{sc}\delta P^f \mathbf{1} : \overline{\mathbb{A}}^{sc} + \varphi_g \delta P^g \mathbf{1} : \overline{\mathbb{A}}^{g}) + \delta(\gamma_{ab}\int_{\mathcal{I}^{ab}} \mathbf{1}_T : \mathbb{A}\frac{dS}{\Omega}) \tag{8.21}$$

where $\delta\boldsymbol{\Sigma} = \boldsymbol{\Sigma} - \boldsymbol{\Sigma}_0$, $\delta T = T - T_0$ (cf. supercooling temperature $T_0 - T$), $\delta P^i = P^i - P_0^i$ ($i \in \{l, sc, g\}$), $\delta(\gamma_{ab}\int_{\mathcal{I}^{ab}} \mathbf{1}_T : \mathbb{A}\frac{dS}{\Omega}) = \gamma_{ab}\int_{\mathcal{I}^{ab}} \mathbf{1}_T : \mathbb{A}\frac{dS}{\Omega} - \gamma_{ac}\int_{\mathcal{I}_0^{ac}} \mathbf{1}_T : \mathbb{A}\frac{dS}{\Omega}$ denotes the variation of the membrane stress induced by the transformation of the phase c to phase b ($(a, b, c) \in \{f, l, c, g, s, sc\}$).

Here, it is reasonable to assume that there are no morphological differences between Ω^l, Ω^{sc} and Ω^g [39, 82]. Hence, the average strain concentrations of the liquid, gas and ice crystal composite inclusion are expected to be equal to that of pore space [39, 82]:

$$\overline{\mathbb{A}}^{l} \approx \overline{\mathbb{A}}^{sc} \approx \overline{\mathbb{A}}^{g} \approx \overline{\mathbb{A}}^{p} \tag{8.22}$$

Substituting Eq.(8.22) into the third term of the right hand side of Eq.(8.21) yields:

$$\begin{aligned}\varphi_l \delta P^l \mathbf{1} : \overline{\mathbb{A}}^{l} + \varphi_{sc}\delta P^f \mathbf{1} : \overline{\mathbb{A}}^{sc} + \varphi_g \delta P^g \mathbf{1} : \overline{\mathbb{A}}^{g} &\approx (Sr_l \delta P^l + Sr_{sc}\delta P^f + Sr_g \delta P^g)\phi \mathbf{1} : \overline{\mathbb{A}}^{p} \\ &= \boldsymbol{B}(Sr_l \delta P^l + Sr_{sc}\delta P^f + Sr_g \delta P^g) = \boldsymbol{B}\delta P^{eq}\end{aligned} \tag{8.23}$$

where Eq.(8.23) suggest to introduce the macroscopic equivalent pressure δP^{eq} can be defined as:

$$\delta P^{eq} = Sr_l \delta P^l + Sr_{sc}\delta P^f + Sr_g \delta P^g \tag{8.24}$$

8.3.3.1 Dependence of the membrane stresses on the pore size distribution

As shown in Fig.(8.1), the pore space morphology within unsaturated freezing porous media may be categorized as three types: 1)-pores saturated with liquid water, 2)-pores

filled with ice crystal composite inclusion and 3)-pores occupied by gas. At equilibrium state, the critical pore radii between 3 different pores may be determined by Young-Laplace equation and Gibbs-Thomson equation (go back to Section(1.3)). Similar to the unsaturated case processed by Cariou [39], the surface tension effects of the interfaces between pore wall and i^{th} ($i \in \{l, g, sc, f\}$) are accounted for while the surface tension effect of interfaces $\mathcal{I}_{lg} = \mathcal{I}_{cl} = \mathcal{I}_{cg}$ are assumed to be negligible. All of the pores and interfaces within unsaturated freezing porous media are classified and listed according to:

$$\begin{cases} r \leq r_{c2} & \text{pores filled with liquid water} \\ r_{c2} \leq r \leq r_{c1} & \text{pores filled with ice-unfrozen water film composite} \\ r_{c1} \leq r & \text{pores filled with gas} \\ r_{c1} = \dfrac{2\gamma_{lg}}{P_g - P_l}; \qquad r_{c2} = \dfrac{2\gamma_{cl}}{P_c - P_l} = \dfrac{2\gamma_{cl}}{-S_m \delta T} & \\ \mathcal{I}_{lg} = \mathcal{I}_{cl} = \mathcal{I}_{cg} = \mathcal{O} & \end{cases} \tag{8.25}$$

It can be found that, the last term of the right hand side of Eq.(8.21) (membrane stress) is closely depended on the pore size. Hence, in order to determine the membrane stresses within unsaturated freezing porous media, a pore size size distribution function $\alpha(r)$ is introduced first. Where $\alpha(r)dr$ represents the volume fraction of the pores within the radius range $[r, r + dr]$. Outside the range of the $[r_{min}, r_{max}]$, $\alpha(r) = 0$, where r_{max} and r_{min} are the maximum and minimum pore radii of porous media.

From the definition of the pore size distribution function, we have:

$$\int_{r_{min}}^{r_{max}} \alpha(r)dr = 1; \quad Sr_l = \int_{r_{min}}^{r_{c2}} \alpha(r)dr; \quad Sr_{sc} = \int_{r_{c2}}^{r_{c1}} \alpha(r)dr \quad Sr_g = \int_{r_{c1}}^{r_{max}} \alpha(r)dr. \tag{8.26}$$

where, r_{c1} is the critical radius between ice crystal and gas phase, r_{c2} is the critical radius between ice crystal and liquid water phase (see Fig.(8.1)).

Membrane stress

When the pore size distribution function $\alpha(r)$ is clearly determined, membrane stress of **s**olid-ice crystal composite inclusion (unfrozen water **f**ilm) interface (denoted as superscript $\boldsymbol{sf}$), **s**olid-**g**as interface (denoted as superscript $\boldsymbol{sg}$) and **s**olid-**l**iquid interface (denoted as superscript $\boldsymbol{sl}$) can be derived. Combining with Eq.(8.22), the membrane stress within interface $\mathcal{I}_{ab}$ (the last term of the right hand side of Eq.(8.21)) can be rewritten as [39]:

$$\gamma_{ab}\int_{\mathcal{I}^{ab}}\mathbf{1}_T:\mathbb{A}\frac{dS}{\Omega}=\frac{\gamma_{ab}}{|\Omega|}\int_{\mathcal{I}^{ab}}\mathbf{1}_T dS:\overline{\mathbb{A}}^p \tag{8.27}$$

In order to evaluate Eq.(8.27), the tangent plane identity tensor $\mathbf{1}_T$ is integrated on a single sphere with radius r first, it gives [82]:

$$\frac{1}{V(r)}\int_{S(r)}\mathbf{1}_T dS=\frac{2}{r}\mathbf{1} \tag{8.28}$$

where $V(r)$ is the volume of a sphere with radius r. Thus, Eq.(8.27) may be rewritten as [39]:

$$\int_{\mathcal{I}^{ab}}\mathbf{1}_T dS=\int_{r_2}^{r_1}\mathcal{N}(r)(\frac{2V(r)}{r})dr\mathbf{1} \tag{8.29}$$

where $\mathcal{N}(r)dr=\dfrac{\phi|\Omega|\alpha(r)dr}{V(r)}$ is the number of the pores within the range $[r,r+dr]$, $(r_1,r_2)\in\{r_{c1},r_{c2},r_{min},r_{max}\}$, $r_1\geq r_2$. Combining Eq.(8.27) and Eq.(8.29) yields [39]:

$$\frac{\gamma_{ab}}{|\Omega|}\int_{\mathcal{I}^{ab}}\mathbf{1}_T:\overline{\mathbb{A}}^p dS=\gamma_{ab}\int_{r_2}^{r_1}(\frac{2\alpha(r)}{r})\phi\mathbf{1}:\overline{\mathbb{A}}^p dr=\gamma_{ab}\int_{r_2}^{r_1}(\frac{2\alpha(r)}{r})dr\boldsymbol{B} \tag{8.30}$$

Therefore, the average membrane stresses of each interface may be derived from Eq.(8.30):

$$\begin{cases}\gamma_{sl}\int_{\mathcal{I}^{sl}}\mathbf{1}_T:\mathbb{A}\dfrac{dS}{\Omega}=\gamma_{sl}\int_{r_{min}}^{r_{c2}}(\dfrac{2\alpha(r)}{r})dr\boldsymbol{B} & \text{in interface}\quad \mathcal{I}_{sl}\\ \gamma_{sf}\int_{\mathcal{I}^{sf}}\mathbf{1}_T:\mathbb{A}\dfrac{dS}{\Omega}=\gamma_{sf}\int_{r_{c2}}^{r_{c1}}(\dfrac{2\alpha(r)}{r})dr\boldsymbol{B} & \text{in interface}\quad \mathcal{I}_{sf}\\ \gamma_{sg}\int_{\mathcal{I}^{sg}}\mathbf{1}_T:\mathbb{A}\dfrac{dS}{\Omega}=\gamma_{sg}\int_{r_{c1}}^{r_{max}}(\dfrac{2\alpha(r)}{r})dr\boldsymbol{B} & \text{in interface}\quad \mathcal{I}_{sg}\end{cases} \tag{8.31}$$

where γ_{sl}, γ_{sf} and γ_{sg} are the surface tensions of **s**olid-**l**iquid water interface, **s**olid-unfrozen water **f**ilm interface and **s**olid-**g**as interface, respectively.

8.3.3.2 First state equation accounting for pore size effect

Combining Eq.(8.14), Eq.(8.21), Eq.(8.24) and Eq.(8.31), the first poroelastic state equation for unsaturated freezing porous media is rewritten as:

$$\delta\boldsymbol{\Sigma} = \mathbb{C}^{hom} : \boldsymbol{E} - \boldsymbol{\kappa}^{hom}\delta T - \delta(P^{eq})\boldsymbol{B} \tag{8.32}$$

in which,

$$P^{eq} = \int_{r_{min}}^{r_{max}} p^{eq}(r)\alpha(r)dr \tag{8.33}$$

with:

$$\begin{cases} \mathbb{C}^{hom} = \mathbb{C}^{s} : (\mathbb{I} - \phi_0\overline{\mathbb{A}}^{p}) \\ \boldsymbol{\kappa}^{hom} =< \boldsymbol{\kappa} : \mathbb{A} >= \boldsymbol{\kappa}^{s} : (\mathbb{I} - \phi_0\overline{\mathbb{A}}^{p}) \\ \boldsymbol{B} = \phi_0\mathbf{1} : \overline{\mathbb{A}}^{p} \end{cases} \tag{8.34}$$

and:

$$p^{eq}(r) = \begin{cases} (P^{l} - \dfrac{2\gamma_{sl}}{r}) & r_{min} \leq r \leq r_{rc2} \\ P^{f} - \dfrac{2\gamma_{sf}}{r} = P^{l} - \dfrac{2\gamma_{sf}}{r} + \Pi(h) & r_{c2} \leq r \leq r_{rc1} \\ (P^{g} - \dfrac{2\gamma_{sg}}{r}) & r_{c1} \leq r \leq r_{max} \\ r_{c1} = \dfrac{2\gamma_{lg}}{P_g - P_l} & \\ r_{c2} = \dfrac{2\gamma_{cl}}{P_c - P_l} & \end{cases} \tag{8.35}$$

Here, P^{eq} is the macroscopic equivalent pressure which accounts for liquid pressure,

disjoining pressure and membrane stress induced by surface tension effect. As shown in Eq.(8.35), the equivalent pressure $p^{eq}(r)$ consists of fluid pressure of ω phase P^{ω} ($\omega \in \{f, l, g\}$) and its surface tension effect $2\gamma_{s\omega}/r$ (depicted in Fig.(8.2)). The critical radius r_{c1} between the gas and liquid may be determined by the Young-Laplace equation (Eq.(3.1)); the critical radius r_{c2} between ice crystal and liquid water may be determined by Gibbs-Thomson equation Eq.(7.17).

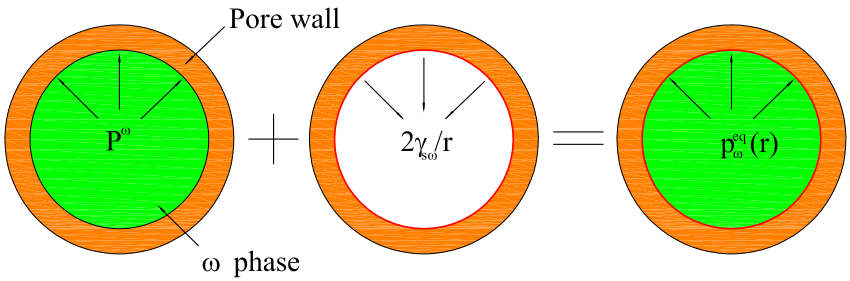

Figure 8.2: Components of the equivalent pressure $p_{\omega}^{eq}(r)$ during freezing, $\omega \in$ {f,l,g}.

8.3.3.3 Evolution of the macroscopic equivalent pressure during freezing process

When freezing takes place in fully liquid saturated porous media from T_c to T_c^* ($T_c < T_c^* < 0°C$), the corresponding radius of the crystallized pore r_c (resp. r_c^*) at T_c (resp. T_c^*) is determined by Eq.(7.17), $r_c < r_c^*$. The evolution of the macroscopic equivalent pressure may be determined from Eq.(8.24) as[10]:

10. In this case, if γ_{sf} and γ_{sl} are assumed to be independent on the temperature T.

$$\delta P^{eq} = \int_{r_{min}}^{r_c} (P^l - P_0^l)\alpha(r)\mathrm{d}r + \int_{r_c}^{r_c^*} [(P^f - \frac{2\gamma_{sf}}{r}) - (P_0^l - \frac{2\gamma_{sl}}{r})]\alpha(r)\mathrm{d}r + \int_{r_c^*}^{r_{max}} (P^f - P_0^f)\alpha(r)\mathrm{d}r \tag{8.36}$$

Eq.(8.36) characterizes the variation of the equivalent pressure within pore network during freezing ($r_c < r_c^*$):

— For the pores initially filled with ice crystal composite inclusion ($r > r_c^*$), a variation of the equivalent pressure $P^f - P_0^f$ (variation of the pressure in unfrozen water film) during freezing can be found.

— For the pores range between r_c and r_c^* ($r_c < r < r_c^*$), during freezing, the pores initially occupied by liquid with an equivalent pressure of $(P_0^l - \frac{2\gamma_{sl}}{r})$ is replaced by ice crystal composite inclusion with an equivalent pressure of $(P^f - \frac{2\gamma_{sf}}{r})$. Therefore, a variation of the equivalent pressure $[(P^f - \frac{2\gamma_{sf}}{r}) - (P_0^l - \frac{2\gamma_{sl}}{r})]$ emerges in these pores.

— For the pores initially filled with liquid ($r < r_c$), a variation of the equivalent pressure $P^l - P_0^l$ during freezing can be found.

Indeed, Eq.(8.36) can be reorganized as follows:

$$\begin{aligned}\delta P^{eq} &= \int_{r_{min}}^{r_c} (P^l - P_0^l)\alpha(r)\mathrm{d}r + \int_{r_c}^{r_c^*} (P^l - P_0^l)\alpha(r)\mathrm{d}r + \int_{r_c^*}^{r_{max}} (P^l - P_0^l)\alpha(r)\mathrm{d}r \\ &+ \int_{r_c}^{r_c^*} (\frac{2\gamma_{sl}}{r} - \frac{2\gamma_{sf}}{r})\alpha(r)\mathrm{d}r + \int_{r_c}^{r_c^*} \Pi(h)\alpha(r)\mathrm{d}r + \int_{r_c^*}^{r_{max}} (\Pi(h) - \Pi_0(h_0))\alpha(r)\mathrm{d}r \\ = \underbrace{P^l - P_0^l}_{\text{Liquid pressure}} &+ \underbrace{2(\gamma_{sl} - \gamma_{sf}) \int_{r_c}^{r_c^*} \frac{1}{r}\alpha(r)\mathrm{d}r}_{\text{Membrane stress by surface tension}} + \underbrace{\int_{r_c}^{r_{max}} \Pi(h)\alpha(r)\mathrm{d}r - \int_{r_c^*}^{r_{max}} \Pi_0^f(h_0)\alpha(r)\mathrm{d}r}_{\text{disjoining pressure}}\end{aligned} \tag{8.37}$$

It can be found from Eq.(8.37), the variation macroscopic equivalent pressure can be decomposed into three contributions:

— The variation of liquid pressure throughout the overall pore network during freezing.

— The variation of the membrane stress induced by the liquid water-ice crystal trans-

formation, the latter is physico-chemical process.

— The variation of disjoining pressure which is induced by the physico-chemical process.

Effect of surface tensions

For surface tensions γ^{ab} between $\boldsymbol{a}$ phase and $\boldsymbol{b}$ phase ($\{a,b\} \in \{\text{f,l,s,c, g}\}$), their relations are not independent. They are related to Young equation in the form [9]:

$$\begin{cases} \gamma_{sl} = \gamma_{cl}\cos\theta_{cl} + \gamma_{cs} \\ \gamma_{sf} = \gamma_{cf}\cos\theta_{cf} + \gamma_{cs} \end{cases} \tag{8.38}$$

where θ_{cl} is the contact angle between ice-liquid interface and ice-solid interface, θ_{cf} is the contact angle between ice-unfrozen water film interface and ice-solid interface.

From Eq.(8.38), with the assumption of $\theta_{cl} = \theta_{cf} = 180°$, it yields:

$$\gamma_{sl} - \gamma_{sf} = \gamma_{cf} - \gamma_{cl} \tag{8.39}$$

If $\gamma_{cf} \approx \gamma_{cl}$, the membrane stress (surface tension effect) in Eq.(8.37) can be neglected. Thus, disjoining pressure plays a significant role in the equivalent pressure.

A remark on a special case

In this special case, porous medium is fully liquid saturated and it is taken as an initial state ($\Sigma_0 = 0$). Moreover, the freezing porous medium is under free swelling ($\Sigma = 0$). Assuming that the microscopic and macroscopic elasticity tensor are isotropic, the macroscopic strain of freezing porous medium E may be written as:

$$E = \alpha_s/3\delta T + b\delta(P^{eq})/(3K^{hom}) \tag{8.40}$$

where α_s is the dilation coefficient of the solid matrix, K^{hom} is the bulk modulus of the freezing porous media, b is the Biot coefficient, $\delta T = T - T_0 < 0$.

— In the right hand side of Eq.(8.40), the first term is negative ($\alpha_s\delta T < 0$).

— As the the porous medium is initially liquid saturated (absent of gaseous phase), concerning the second term in the right hand side of Eq.(8.40), the macroscopic

equivalent pressure in Eq.(8.37) may thus be rewritten as:

$$\delta P^{eq} = P^l - P_0^l + \int_{r_c}^{r_{max}} [2(\gamma_{sl} - \gamma_{sf})\frac{1}{r} + \Pi(h)]\alpha(r)\mathrm{d}r \tag{8.41}$$

For the sake of simplification, the distribution of pore radii is assumed to be uniform ($r = R$, $\alpha(r) = \delta_R$), δ_R is the Dirac distribution function [11]. Eventually, if $\gamma_{sl} \approx \gamma_{sf}$ is also assumed, the macroscopic equivalent pressure yields:

$$\delta P^{eq} = P^l - P_0^l + \Pi(h) \tag{8.42}$$

The value of the equivalent pressure depends on the boundary condition of the freezing porous medium (e.x. drained or undrained). Inserting Eq.(8.42) into Eq.(8.40) yields:

$$E = \frac{\alpha_s}{3\delta T} + b(P^l - P_0^l + \Pi(h))/(3K^{hom}) \tag{8.43}$$

The sign of the strain during the progressive freezing process depends on the weighted values of thermal strain $\frac{\alpha_s}{3\delta T} < 0$ and strain induced by equivalent pressure $b(P^l - P_0^l + \Pi(h))/(3K^{hom}) > 0$. If the thermal strain prevails over that induced by equivalent pressure, the total strain will be negative; on the contrary, when the stress induced equivalent pressure prevails over thermal stress, the total strain will be positive. The first case corresponds to swelling, the latter to shrinkage at the macroscopic scale.

8.3.4 Second poroelastic state equation for unsaturated freezing porous media

With the progressive freezing process in connected pore network, a variation of the pore volume has to be accounted for. Thus, we turn to the second poroelastic state equation. Lagrangian porosity is adopted to express the variation of the porosity, since the variation of which is proportional to the pore volume change (or variation of the average strain field

11. $\delta_R = 1$ when $r = R$ and $\delta_R = 0$ when $r \neq R$.

in the pore space) in the form of:

$$\phi - \phi_0 = \frac{\Omega - \Omega_0}{|\Omega_0|} = \varphi_0 \mathrm{tr}\bar{\boldsymbol{\varepsilon}}^p \tag{8.44}$$

where ϕ is the current porosity, $\phi_0 = \varphi_0$ is the initial porosity.

The REV may be considered to be subjected to four loading parameters, they are: initial stress $\boldsymbol{\sigma}_0$, uniform macroscopic strain tensor $\boldsymbol{E}$ on the boundary, thermal stress loading $\boldsymbol{\alpha}\delta T$ and the microscopic prestress tensor $\boldsymbol{\sigma}^p$. On the premise of the linear elasticity, by means of Levin's theorem, the overall variation of porosity can be decomposed into contributions of four subproblems:

$$\phi - \phi_0 = \varphi_0 \mathrm{tr}\bar{\boldsymbol{\varepsilon}}_1^p + \varphi_0 \mathrm{tr}\bar{\boldsymbol{\varepsilon}}_2^p + \varphi_0 \mathrm{tr}\bar{\boldsymbol{\varepsilon}}_3^p + \varphi_0 \mathrm{tr}\bar{\boldsymbol{\varepsilon}}_4^p \tag{8.45}$$

— **Loading case 1**: $\boldsymbol{E} \neq 0$, $\boldsymbol{\sigma}_0 = 0$, $\delta T = 0$, $\delta p^{eq}(r) = 0$.

This loading case can be treated as the micromechanics problem for drained porous media. The REV is subjected to a uniform macroscopic $\boldsymbol{E}$ on the boundary, the variation of the porosity induced by this loading can be determined by:

$$\varphi_0 \mathrm{tr}\bar{\boldsymbol{\varepsilon}}_1^p = \varphi_0 \mathbf{1} : \bar{\boldsymbol{\varepsilon}}_1^p = \varphi_0 \mathbf{1} : \overline{\mathbb{A}}^p : \boldsymbol{E} = \boldsymbol{B} : \boldsymbol{E} \tag{8.46}$$

— **Loading case 2**: $\boldsymbol{\sigma}_0 \neq 0$, $\boldsymbol{E} = 0$, $\delta T = 0$, $\delta p^{eq}(r) = 0$.

For mechanical compatibility, $p_0^{eq}(r) \neq 0$ is indispensable. Therefore, it is readily found that, $\forall \underline{z} \in \Omega$, $\boldsymbol{\sigma}_2(\underline{z}) = \boldsymbol{\sigma}_0$ and displacement field $\underline{\xi}_2 = 0$. it yields:

$$\varphi_0 \mathrm{tr}\bar{\boldsymbol{\varepsilon}}_2^p = \varphi_0 \mathbf{1} : \bar{\boldsymbol{\varepsilon}}_2^p = 0 \tag{8.47}$$

— **Loading case 3**: $\delta T \neq 0$, $\boldsymbol{\sigma}_0 = 0$, $\boldsymbol{E} = 0$, $\delta p^{eq}(r) = 0$.

Thermal dilation effect can be processed as thermoporoelastic case presented in previous section. According to Eq.(8.11) and Eq.(8.12), we have:

$$\varphi_0 \mathrm{tr}\bar{\boldsymbol{\varepsilon}}_3^p = \varphi_0 \mathbf{1} : \overline{\boldsymbol{\varepsilon}_3}^p = (\phi_0 \mathbf{1} - \boldsymbol{B}) : \boldsymbol{\alpha}^s \delta T = -\alpha_\phi \delta T \tag{8.48}$$

— **Loading case 4**: $\delta p^{eq}(r) \neq 0$, $\boldsymbol{\sigma}_0 = 0$, $\boldsymbol{E} = 0$, $\delta T = 0$.

From the boundary condition $\boldsymbol{E} = 0$, the homogenized macroscopic strain can be expressed in the form of:

$$\boldsymbol{E} = \bar{\boldsymbol{\varepsilon}}_4 = (1 - \varphi_0)\bar{\boldsymbol{\varepsilon}}_4^s + \varphi_0 \overline{\boldsymbol{\varepsilon}_4}^p = 0 \tag{8.49}$$

where $\overline{\boldsymbol{\varepsilon}_4}^{p(r)}$ is the average strain tensor ascribed by equivalent pressure for pores with radius r, $\bar{\boldsymbol{\varepsilon}}_4^s$ and $\overline{\boldsymbol{\varepsilon}_4}^p$ are the macroscopic strain of solid phase and pore space induced by the equivalent pressure.

Equivalent pressure consists of three components: internal liquid pressure P^l, disjoining pressure and membrane stress. Similarly, owing to the size effect of membrane stress, a representation of the pore network (pore size distribution) as well as a mechanical scheme are required for estimating the homogenized surface tension effect.

In this section, to ensure the micromechanics model be feasible in the following cementitious materials (in chapter 9), a Mori-Tanaka scheme with auxiliary strain $\boldsymbol{E}_{aux}$ is used to estimate poroelastic parameters. Pores and solid grains are assumed to be spherical in shape. $\overline{\boldsymbol{\varepsilon}_4}^{p(r)}$ can be determined by:

$$\overline{\boldsymbol{\varepsilon}_4}^{p(r)} = (\mathbb{I} - \mathbb{P}^s \mathbb{C}^s)^{-1} : (\boldsymbol{E}_{aux} + \delta P^{eq}(r)) = (\mathbb{I} - \mathbb{S})^{-1} : (\boldsymbol{E}_{aux} + \delta P^{eq}(r)\mathbb{P}^s : \mathbf{1}) \tag{8.50}$$

where $\mathbb{P}^s$ is the Hill tensor of spherical inclusion in an solid matrix, $\mathbb{S}$ is the corresponding Eshelby tensor. The detailed derivation of $\mathbb{P}^s$ and $\mathbb{S}$ is given in Appendix(C.1).

when pore size distribution $\alpha(r)$ is incorporated in Eq.(8.50), the variation of the

porosity ascribed by equivalent pressure can be determined as:

$$\varphi_0 \overline{\boldsymbol{\varepsilon}_4}^p = \varphi_0 \int_{r_{min}}^{r_{max}} \overline{\boldsymbol{\varepsilon}_4}^{p(r)} \alpha(r) dr = \varphi_0 (\mathbb{I} - \mathbb{S})^{-1} : (\boldsymbol{E}_{aux} + \delta(P^{eq}) \mathbb{P}^s : \mathbf{1}) \tag{8.51}$$

with:

$$\delta(P^{eq}) = \int_{r_{min}}^{r_{max}} \delta(p^{eq}(r)) \alpha(r) dr \tag{8.52}$$

With Mori-Tanaka scheme, the homogenized strain of solid phase can be estimated by:

$$(1 - \varphi_0) \overline{\boldsymbol{\varepsilon}_4}^s = (1 - \varphi_0) \boldsymbol{E}_{aux} \tag{8.53}$$

Substituting Eq.(8.53) and Eq.(8.51) into Eq.(8.49), the expression of the $\boldsymbol{E}_{aux}$ can be determined.

$$\boldsymbol{E}_{aux} = -\varphi_0 \delta(P^{eq}) [\mathbb{I} - (1 - \varphi_0) \mathbb{S}]^{-1} : \mathbb{P}^s : \mathbf{1} \tag{8.54}$$

Thus, combining with Eq.(8.51), it yields:

$$\varphi_0 \mathbf{1} : \overline{\boldsymbol{\varepsilon}_4}^p = \varphi_0 \delta(P^{eq}) (\mathbf{1} - \boldsymbol{B}) : (\mathbb{I} - \mathbb{S})^{-1} : \mathbb{P}^s : \mathbf{1} \tag{8.55}$$

Using the identity $(\mathbb{I} - \mathbb{S})^{-1} : \mathbb{S} = (\mathbb{I} - \mathbb{S})^{-1} - \mathbb{I}$ [82], we thus obtain:

$$\varphi_0 \mathbf{1} : \overline{\boldsymbol{\varepsilon}_4}^p = \delta(P^{eq}) (\mathbf{1} - \boldsymbol{B}) : [\varphi_0 (\mathbb{I} - \mathbb{S})^{-1} - \varphi_0 \mathbb{I}] : \mathbb{S}^s : \mathbf{1} \tag{8.56}$$

The homogenized stiffness tensor $\mathbb{C}^{hom}$ can be readily determined with Mori-Tanaka scheme, it can be expressed as:

$$\mathbb{C}^{hom} = (1 - \varphi_0) \mathbb{C}^s : [(1 - \varphi_0) \mathbb{I} + \varphi_0 (\mathbb{I} - \mathbb{S})^{-1}]^{-1} \tag{8.57}$$

From Eq.(8.57), we have the following expression:

$$\varphi_0(\mathbb{I}-\mathbb{S})^{-1}-\varphi_0\mathbb{I}=(1-\varphi_0)\mathbb{S}^{hom}:\mathbb{C}^s-\mathbb{I} \tag{8.58}$$

Therefore, Inserting Eq.(8.58) into Eq.(8.56), it gives:

$$\varphi_0\mathbf{1}:\overline{\boldsymbol{\varepsilon}_4}^p=\delta(P^{eq})(\mathbf{1}-\boldsymbol{B}):[(1-\varphi_0)\mathbb{S}^{hom}-\mathbb{S}^s]:\mathbf{1} \tag{8.59}$$

Here, the Biot tensor estimated with Mori-Tanaka scheme can be shown as:

$$\boldsymbol{B}=\varphi_0\mathbf{1}:\overline{\mathbb{A}}^p=\varphi_0\mathbf{1}:(\mathbb{I}-(1-\varphi_0)\mathbb{S})^{-1} \tag{8.60}$$

In summary, the second poroelastic state equation (cf. Eq.(8.45)) can be rewritten as:

$$\phi-\phi_0=\underbrace{\boldsymbol{B}:\boldsymbol{E}}_{\text{Boundary strain}}-\underbrace{(\boldsymbol{B}-\phi_0\mathbf{1}):\boldsymbol{\alpha}^s\delta T}_{\text{Thermal dilation effect}}+\underbrace{\delta(P^{eq})(\mathbf{1}-\boldsymbol{B}):[(1-\varphi_0)\mathbb{S}^{hom}-\mathbb{S}^s]:\mathbf{1}}_{\text{The Internal pressure and surface effect}} \tag{8.61}$$

It should be noted that the variation of the porosity is here determined under the Mori-Tanaka scheme. Therefore, compliance tensor $\mathbb{S}^{hom}$ and Biot tensor $\boldsymbol{B}$ can be determined by Eq.(8.57) and Eq.(8.60), respectively.

8.4 An alternative micromechanics model for unsaturated freezing porous media

The unfrozen water film confined within the solid pore wall and ice crystal is a kind of quasi liquid, which exhibits certain stiffness property. In this section, unfrozen water film is specified as a special phase with stiffness (cf. solid matrix). By means of disjoining pressure concept, the stiffness tensor and internal prestress of unfrozen water film will be derived in the follows. Inspired by Dormieux et al. [83], an improved micromechanics freezing model

accounting for the stiffness of unfrozen water film will be presented.

8.4.1 Localization of unfrozen water film accounting for its stiffness tensor

At equilibrium state, the variation of the disjoining pressure for the initial $\Pi_0(h_0)$ and current state $\Pi(h)$ can be presented as:

$$-(\Pi(h)-\Pi_0(h_0))\underline{n}\otimes\underline{n}=-h_0\times\frac{h-h_0}{h_0}\frac{\partial\Pi}{\partial h}|_{h_0}\underline{n}\otimes\underline{n}\qquad\text{with}\quad\frac{h-h_0}{h_0}\ll 1\tag{8.62}$$

The normal strain $\boldsymbol{\varepsilon}_f$ for unfrozen water film can be defined as [83]:

$$\frac{h-h_0}{h_0}=\underline{n}\otimes\underline{n}:\boldsymbol{\varepsilon}_f\tag{8.63}$$

From Eq.(8.62) and Eq.(8.63), it yields:

$$(\Pi(h)-\Pi_0(h_0))\underline{n}\otimes\underline{n}=h_0\times\frac{\partial\Pi_0}{\partial h}|_{h_0}\underline{n}\otimes\underline{n}\otimes\underline{n}\otimes\underline{n}:\boldsymbol{\varepsilon}_f\qquad\text{with}\quad\frac{h-h_0}{h_0}\ll 1\tag{8.64}$$

Therefore, the disjoining pressure $\Pi(h)$ within the unfrozen water film can be expressed as:

$$-\Pi(h)\underline{n}\otimes\underline{n}=-\Pi_0(h_0)\underline{n}\otimes\underline{n}-h_0\times\frac{\partial\Pi}{\partial h}|_{h_0}\underline{n}\otimes\underline{n}\otimes\underline{n}\otimes\underline{n}:\boldsymbol{\varepsilon}_f=\mathbb{C}^f:\boldsymbol{\varepsilon}_f-\Pi_0(h)\underline{n}\otimes\underline{n}\tag{8.65}$$

where the stiffness tensor of unfrozen water film is :

$$\mathbb{C}^f=-h_0\times\frac{\partial\Pi(h)}{\partial h}|_{h_0}\underline{n}\otimes\underline{n}\otimes\underline{n}\otimes\underline{n}\tag{8.66}$$

Eq.(8.65) is a generalization of the disjoining pressure in Eq.(8.14) where an elastic "physical-based" contribution of the unfrozen water film has been identified.

At uniform boundary condition, the local stress in the REV of unsaturated freezing porous media still obeys the following physical formulations:

$$\begin{cases} \mathrm{div}\boldsymbol{\sigma} = 0 & \underline{z} \in \Omega \\ \boldsymbol{\sigma} = \mathbb{C} : \boldsymbol{\varepsilon} + \boldsymbol{\sigma}^p - \boldsymbol{\kappa}\delta T & \underline{z} \in \Omega \\ \underline{\xi} = \boldsymbol{E} \cdot \underline{z} & \underline{z} \in \partial\Omega \end{cases} \tag{8.67}$$

with the new local behaviors:

$$(\mathbb{C}, \boldsymbol{\kappa}, \boldsymbol{\sigma^p})(\underline{z}) = \begin{cases} (\mathbb{C}^s, \boldsymbol{\kappa}^s, 0) & \forall \underline{z} \in \Omega^s \\ (\mathbb{C}^f, 0, -P^l\mathbf{1} - \Pi_0(h_0)\underline{n} \otimes \underline{n}) & \forall \underline{z} \in \Omega^{sc} \\ (0, 0, -P^g\mathbf{1}) & \forall \underline{z} \in \Omega^g \\ (0, 0, -P^l\mathbf{1}) & \forall \underline{z} \in \Omega^l \\ (0, 0, \gamma^{ab}\mathbf{1}_T\delta_{ab}) & \forall \underline{z} \in \mathcal{I}^{ab} \end{cases} \tag{8.68}$$

where $(a, b) \in \{f, g, l, s\}$.

8.4.2 Homogenization of poroelastic properties

Processing similarly as previous subsection, two state equations can be presented as [4] :

$$\begin{cases} \boldsymbol{\Sigma} - \boldsymbol{\Sigma}_0 = \mathbb{C}^{hom} : \boldsymbol{E} - \boldsymbol{\kappa}^{hom}\delta T - \delta P^{eq}\boldsymbol{B} \\ \phi - \phi_0 = \boldsymbol{B} : \boldsymbol{E} - (\boldsymbol{B} - \phi_0\mathbf{1}) : \boldsymbol{\alpha}^s\delta T + \delta(P^{eq})(\mathbf{1} - \boldsymbol{B}) : [(1 - \varphi_0)\mathbb{S}^{hom} - \mathbb{S}^s] : \mathbf{1} \end{cases} \tag{8.69}$$

4. It should be kept in mind that, the macroscopic equivalent pressure $\delta(P^{eq})$ is determined under Mori-Tanaka scheme, therefore, the other poroelastic properties should be also estimated by Mori-Tanaka scheme, the poroelastic tensors can refer to Appendix C.

In which,

$$P^{eq} = \int_{r_{min}}^{r_{max}} p^{eq}(r)\alpha(r)dr \tag{8.70}$$

$$p^{eq}(r) = \begin{cases} (P^l - \dfrac{2\gamma_{sl}}{r}) & r_{min} \le r \le r_{rc2} \\ (P^l + \Pi_0(h_0) - \dfrac{2\gamma_{sf}}{r}) & r_{c2} \le r \le r_{rc1} \\ (P^g - \dfrac{2\gamma_{sg}}{r}) & r_{c1} \le r \le r_{max} \\ r_{c1} = \dfrac{2\gamma_{lg}}{P_g - P_l} & \\ r_{c2} = \dfrac{2\gamma_{cl}}{P_c - P_l} & \end{cases} \tag{8.71}$$

The homogenized poroelastic properties can be derived:

$$\begin{cases} \mathbb{C}^{hom} = (1-\varphi_0)\mathbb{C}^s : \overline{\mathbb{A}}^s + \varphi_f \mathbb{C}^f : \overline{\mathbb{A}}^{sc} \\ \boldsymbol{\kappa}^{hom} =< \boldsymbol{\kappa} : \mathbb{A} >= (1-\phi)\boldsymbol{\kappa}^s : \overline{\mathbb{A}}^s \\ \boldsymbol{B} = \varphi_0 \mathbf{1} : \overline{\mathbb{A}}^p \end{cases} \tag{8.72}$$

Comparing the expressions of the homogenized elastic tensor $\mathbb{C}^{hom}$ within Eq.(8.57) and Eq.(8.72), it can be found that, the homogenized stiffness as well as homogenized thermal stress coefficient of porous media are strengthened owing to the ice crystal-unfrozen water film composite inclusion.

8.5 Some discussion and applications

Though the alternative micromechanics model for unsaturated freezing will better characterize the freezing behavior for unsaturated porous media, owing to the lack of information

about the unfrozen water film (i.e., the precise model for disjoining pressure in terms of thickness of unfrozen water film and lacking the initial thickness of unfrozen water film h_0), the model introduced in Section(8.3) will be discussed and used in the sequel.

8.5.1 A comparison between micromechanics model and poromechanics model for freezing

8.5.1.1 Poromechanics model for freezing

After outstanding works of Biot, poromechanics is usually used when studying the behaviors of porous media. Coussy and his co-workers [58] consummate this method with thermodynamic viewpoint, which makes the poromechanics more comprehensive and meaningful from energy viewpoint. Coussy et al. [57–60] derived a comprehensive theoretical framework for freezing porous media. A more detailed information is presented in Section(7.5).

A linear poroelatic state equation for isotropic freezing porous media [58], whose initial state is taken to be atmosphere pressure (zero reference pressure), can be simplified from Eq.(7.27) along with Eq.(7.29), it may be as [12]:

$$\begin{cases} \sigma = K\varepsilon - b[Sr_c(P^c - T^c) + Sr_l(P^l - T^l)] - \alpha^s K\delta T \\ \phi - \phi_0 = b\varepsilon + \dfrac{b-\phi_0}{K_s}[Sr_c(P^c - T^c) + Sr_l(P^l - T^l)] - \alpha^s(b-\phi_0)\delta T \end{cases} \tag{8.73}$$

It should be aware that, Eq.(8.73) is the special case of unsaturated freezing porous media, in which there is no gas, that means, $Sr_l + Sr_c = 1$.

8.5.1.2 Micromechanics model for freezing

As presented in the Section(8.3), in micromechanics model, two state equations for unsaturated freezing porous media can be expressed as:

12. In this subsection, for simplification, all of the formulations are expressed in isotropic case.

$$\begin{cases} \delta\boldsymbol{\Sigma} = \mathbb{C}^{hom} : \boldsymbol{E} - \boldsymbol{\kappa}^{hom}\delta T - \delta(P^{eq})\boldsymbol{B} \\ \phi - \phi_0 = \boldsymbol{B} : \boldsymbol{E} - (\boldsymbol{B} - \phi_0\mathbf{1}) : \boldsymbol{\alpha}^s\delta T + \delta(P^{eq})(\mathbf{1} - \boldsymbol{B}) : [(1-\varphi_0)\mathbb{S}^{hom} - \mathbb{S}^s] : \mathbf{1} \end{cases} \tag{8.74}$$

In which,

$$P^{eq} = \int_{r_{min}}^{r_{max}} p^{eq}(r)\alpha(r)dr \tag{8.75}$$

$$p^{eq}(r) = \begin{cases} (P^l - \dfrac{2\gamma_{sl}}{r}) & r_{min} \le r \le r_{rc2} \\ (P^l + \Pi(h) - \dfrac{2\gamma_{sf}}{r}) & r_{c2} \le r \le r_{rc1} \\ (P^g - \dfrac{2\gamma_{sg}}{r}) & r_{c1} \le r \le r_{max} \\ r_{c1} = \dfrac{2\gamma_{lg}}{P_g - P_l} & \\ r_{c2} = \dfrac{2\gamma_{cl}}{P_c - P_l} & \end{cases} \tag{8.76}$$

In the deduction of the second state equation, Mori-Tanaka scheme is employed. Here, the poroelastic tensors estimated with Mori-Tanaka are listed as[13]:

$$\begin{cases} \mathbb{C}^{hom} = (1-\phi)\mathbb{C}^s : ((1-\phi)\mathbb{I} + \phi(\mathbb{I} - \mathbb{S})^{-1})^{-1} \\ \boldsymbol{\kappa}^{hom} = <\boldsymbol{\kappa} : \mathbb{A}> = (1-\phi)\boldsymbol{\kappa}^s : ((1-\phi)\mathbb{I} + \phi(\mathbb{I} - \mathbb{S})^{-1})^{-1} = \boldsymbol{\alpha}^s : \mathbb{C}^{hom} \\ \boldsymbol{B} = \phi\mathbf{1} : (\mathbb{I} - (1-\phi)\mathbb{S})^{-1} \end{cases} \tag{8.77}$$

where $\mathbb{C}^s$ and $\mathbb{S}^s$ are the elastic tensor and compliance tensor of the solid matrix; $\boldsymbol{\kappa}^s$ is the thermal stress coefficient tensor for solid matrix; $\mathbb{S} = \mathbb{P} : \mathbb{C}^s$ is the Eshelby tensor of spherical inclusion within solid matrix.

When the elastic tensors are assumed to be isotropic at local (micro) and macro scale,

13. The detailed derivation of poroelastic tensors is given in Appendix(C.2).

Eq.(8.74) can then be expressed as:

$$\begin{cases} \delta\sigma = K^{hom}\varepsilon - b\delta P^{eq} - \alpha^s K^{hom}\delta T \\ \phi - \phi_0 = b\varepsilon - (b-\phi_0)\kappa^s\delta T + \delta P^{eq}(1-b)(\dfrac{1-\phi_0}{K^{hom}} - \dfrac{1}{K^s}) \end{cases} \tag{8.78}$$

Comparing the poromechanics model (Eq.(8.73)) with micromechanics model (Eq.(8.78)), it can be found that, all of the terms in these two equations are nearly identical except the terms associated with the internal pressure.

The different of the internal pressure lies in the absence of disjoining pressure in poromechanics model, which seems significant in unfrozen water film. The other difference lies in that: the poromechanics model can not directly estimate the macroscopic poroelastic properties while micromechanics model is able to estimate these poroelastic properties with mechanical schemes (e.g., self-consistent or Mori-Tanaka scheme).

8.5.2 Application: determining the liquid pressure with second state equation

In Section (8.3), we derive two state equations, in which two macroscopic state quantities Σ and $\phi - \phi_0$ are expressed as functions of macroscopic strain $\boldsymbol{E}$ and P and δT. However, for certain cases such as freezing in porous media, it involves the phase transformation of water and the corresponding complicated volume change. Therefore, an alternative second state equation which expresses variation of the mass, instead of volume for fluid phase within porous media would be feasible.

In the REV of freezing porous media, when crystallization occurring in one pore, some of the water is expelled out of the crystallized pore from the channel pores or unfrozen water films. Thus, the mass of water as well as liquid pressure in one pore are imbalance at local scale. However, at equilibrium state, the deviation of the local liquid pressure field around its average in the REV is negligible [82]: $P^l = \overline{P^l(\underline{z})} \approx P^l(\underline{z})$. A similar assumption can be made about the density of the each pahse in pores: $\rho_i = \overline{\rho_i(\underline{z})} \approx \rho_i(\underline{z})$ $(\forall \underline{z} \in \Omega_i)$,

where $i \in \{l, c, g, f\}$. These are the theoretical premise of the determination of macroscopic liquid pressure in the freezing porous media.

The mass content m is defined as the total fluid mass (different components) contained in pore space $|\Omega_p|$ divided by the initial volume $|\Omega_0|$ of the REV [82]:

$$m = \frac{1}{|\Omega_0|} \int_{\Omega^p} \rho(\underline{z}) \mathrm{d}V_z \tag{8.79}$$

Indeed, in freezing porous media, the fluid mass content change per initial total volume of the REV can be expressed in terms of the Lagrangian porosity [82]:

$$m - m_0 = \varphi_c \rho_c + \varphi_f \rho_f + \varphi_l \rho_l + \varphi_g \rho_g - \phi_0 \rho_l^0 \tag{8.80}$$

where φ_i is the current volume fraction of the i^{th} phase ($i \in \{c, f, l, g\}$) .

Generally, the density of vapor is far smaller than those of other liquid phase or ice crystal. Hence, the fourth term of Eq.(8.80) can be omitted. Furthermore, for simplification, the unfrozen water film can be treated as liquid phase. Thus, it gives:

$$m - m_0 \approx \varphi_c \rho_c + \varphi_l \rho_l - \phi_0 \rho_l^0 \tag{8.81}$$

From Eq.(8.81), it then yields:

$$\frac{m - m_0}{\rho_l^0} \approx \varphi_c + \varphi_l - \phi_0 + \phi_l^0 \frac{\rho_l - \rho_l^0}{\rho_l^0} + \varphi_c^0 \left(\frac{\rho_c - \rho_c^0}{\rho_c^0} \frac{\rho_c^0}{\rho_l^0} + \frac{\rho_c^0}{\rho_l^0} - 1 \right) \tag{8.82}$$

In order to ensure the linearity of the macroscopic state equation in terms of $\boldsymbol{E}$ and $m - m_0$, it is necessary to assume that the variation of the density of fluid (including ice) around a reference value are small: $\frac{\delta \rho_i}{\rho_i^0} \ll 1$, $i \in \{c, l\}$ [82]. Therefore, a linear form of fluid state equation liking the density and the pressure and temperature can be employed:

$$\frac{\delta \rho_i}{\rho_i} = \frac{P^i}{K_i} - \alpha^i \delta T \qquad i \in \{l, c\} \tag{8.83}$$

where K_i is the bulk modulus of the i^{th} phase, α^i is the volumetric thermal dilation coefficient of the i^{th} phase, $i \in \{l, c\}$.

Inserting Eq.(8.83) into Eq.(8.82), we obtain:

$$\frac{m-m_0}{\rho_l^0} \approx \phi - \phi_0 + \varphi_l^0(\frac{P^l}{K_l} - \alpha^l \delta T) + \varphi_c^0[(\frac{P^c}{K_c} - \alpha^c \delta T)\frac{\rho_c^0}{\rho_l^0} + \frac{\rho_c^0}{\rho_l^0} - 1] \tag{8.84}$$

Here, $\phi = \varphi_c + \varphi_l$ is the current porosity. The internal pressure of ice crystal P^c is related to liquid pressure P^l by Eq.(7.18). Therefore, inserting Eq.(8.61) into Eq.(8.84) yields the expression of liquid pressure:

$$\begin{aligned} P^l \approx M^{-1}\{(\frac{m-m_0}{\rho_l^0}) - \boldsymbol{B} : \boldsymbol{E} + (\boldsymbol{B} - \phi_0 \mathbf{1}) : \boldsymbol{\alpha}^s \delta T + \varphi_l^0 \alpha^l \delta T + \varphi_c^0 \alpha^c \delta T \frac{\rho_c^0}{\rho_l^0} - \varphi_c^0(\frac{\rho_c^0}{\rho_l^0} - 1) \\ + \varphi_c^0 \frac{S_m \delta T}{K_c}\frac{\rho_c^0}{\rho_l^0} - (\Pi \frac{\phi_c^0}{\phi_0} - \int_{r_{min}}^{r_{max}} \delta(\frac{2\gamma_s l}{r})\alpha(r)dr)(\mathbf{1} - \boldsymbol{B}) : [(1-\varphi_0)\mathbb{S}^{hom} - \mathbb{S}^s] : \mathbf{1}\} \end{aligned} \tag{8.85}$$

with:

$$M^{-1} = \{\frac{\phi_l^0}{K_l} + \frac{\phi_c^0}{K_c} + (\mathbf{1} - \boldsymbol{B}) : [(1-\varphi_0)\mathbb{S}^{hom} - \mathbb{S}^s] : \mathbf{1}\}^{-1} \tag{8.86}$$

From Eq.(8.85), it can be found that, the liquid pressure within freezing porous media is induced by six contributions. They are: **1**)- liquid pressure induced by mass change $m - m_0$ in porous media system; **2**)- liquid pressure induced by external macroscopic $\boldsymbol{B} : \boldsymbol{E}$; **3**)- liquid pressure induced by thermal dilation of each phase, i.e., $(\boldsymbol{B} - \phi_0 \mathbf{1}) : \boldsymbol{\alpha}^s \delta T + \varphi_l^0 \alpha^l \delta T + \varphi_c^0 \alpha^c \delta T \frac{\rho_c^0}{\rho_l^0}$; **4**)- liquid pressure induced by the density difference between ice and liquid during freezing, i.e., $\varphi_c^0(\frac{\rho_c^0}{\rho_l^0} - 1)$; **5**)- liquid pressure induced by entropy of melting, i.e., $\varphi_c^0 \frac{S_m \delta T}{K_c}\frac{\rho_c^0}{\rho_l^0}$, as proposed by Coussy [60], this part of contribution is the origin of micro-cryo- suction process; **6**)- liquid pressure inhibited by other internal pressure component,

i.e., the disjoining pressure $\Pi(h)$ and membrane stress induced by surface tension.

8.5.3 Application: estimating the evolution of mass quantity of ice within the air voids during freezing

Powers et al. [202] first observed that the distributed network of the air voids in cement paste material could enhance its frost resistance. Spacing air voids within cement pastes act as reservoirs which relax the pressure build up, as liquid water is expelled into the air voids whose pressure is atmospheric. The expelled liquid water is not in the confined situation and freezes instantaneously.

Indeed, due to its negative pressure (ice crystals in air void being atmospheric pressure), the liquid water is progressively sucked towards the air voids. Hence, the efficiency of the air voids is two fold: the reservoirs effect for the expelling water as well as the cryosuction effect [58].

In this section, when porous medium entrained with air voids is subjected to low temperature, Eq.(8.84) is used to estimate the evolution of mass change of ice crystal in air voids. Moreover, porous medium is assumed be free swelling during freezing. Hence, the initial conditions and boundary conditions for porous medium entrained with air voids can be expressed as:

— There are no water in the air voids at initial state, all of water is resided in small capillary pores before freezing.

— Freezing porous media is assumed to be free swelling ($\boldsymbol{\Sigma} = 0$ and thus $\delta\boldsymbol{\Sigma} = 0$). Therefore, the macroscopic strain E can be determined by first state equation in Eq.(8.74).

— The boundary of porous media is sealed, therefore, the water will not be expelled outside porous media during freezing. On the contrary, the water is only expelled into the air voids during freezing.

— The length scale of air voids is far larger than that of capillary pores. Therefore, it

is reasonable to assume that the pressure of ice crystals in air voids are atmospheric pressure. Moreover, the atmospheric pressure is taken as zero reference pressure. Hence, we have,

$$P^c = P^g = 0 \tag{8.87}$$

— At the vicinity of air void, the liquid water is greatly depressurized owing to the liquid-ice crystal equilibrium. Therefore, the liquid pressure can be determined by the following expression [58]:

$$P^c - P^l = \frac{V_c^0}{V_l^0}\Delta S_m(T_m - T), \quad \text{with} \quad P^c = 0 \tag{8.88}$$

— The temperature and the variation of the temperature are assumed to be uniform throughout the overall porous media so as to avoid the temperature gradient.

As stated previously, from the boundary condition of free swelling, we have $\boldsymbol{\Sigma} = 0$. Therefore, the macroscopic strain tensor and the variation of the porosity can be estimated by:

$$\begin{cases} \boldsymbol{E} = (\mathbb{S}^{hom})^{-1}(\boldsymbol{\kappa}^{hom}\delta T + \delta(P^{eq})\boldsymbol{B}) \\ \phi - \phi_0 = \boldsymbol{B} : \boldsymbol{E} - (\boldsymbol{B} - \phi_0\mathbf{1}) : \boldsymbol{\alpha}^s\delta T + \delta(P^{eq})(\mathbf{1} - \boldsymbol{B}) : [(1-\varphi_0)\mathbb{S}^{hom} - \mathbb{S}^s] : \mathbf{1} \end{cases} \tag{8.89}$$

Combining Eq.(8.84), Eq.(8.87), Eq.(8.88) and Eq.(8.89), the mass change of ice within air voids $m - m_0$ can be determined. The poroelastic properties in these equations are given in Eq.(8.77) and Eq.(8.37).

8.5.4 Application: a micromechanics approach to determine the thickness of unfrozen water film

Generally, the thickness of the unfrozen water film is determined by the thermodynamic approaches [46, 68, 130], which are considered as macroscopic methods. Based on the localization information in the previous sections, a micromechanics approach is used to determine the thickness of unfrozen water film at the local scale.

8.5.4.1 Strain of ice crystal

The volume of liquid water expands about 9% with respect to ice crystal under free swelling condition. In isotropic case, the strain of the ice crystal will be $\boldsymbol{\varepsilon}_L = \epsilon_L/3\mathbf{1}$, where $\epsilon_L = 0.09$.

However, within the freezing porous media, water will transform into ice crystal under confined condition when lowing down the temperature. Thus, a prestress equalling to the stress of the ice crystal (the negative value of the pressure of ice crystal) will exert on the the ice surface. In addition, the thermal dilation caused by the temperature variation δT will induce thermal stress.

The local stress of the ice crystal (shown in cyan circle region in Fig.(8.3) (b)) which induces from the crystallization of the liquid water (shown in red circle region in Fig.(8.3) (a)), can be expressed as:

$$(\forall z \in \Omega_c) \qquad \boldsymbol{\sigma}_c(\underline{z}) = \mathbb{C}^c(\underline{z}) : (\boldsymbol{\varepsilon}_c(\underline{z}) - \boldsymbol{\varepsilon}_L - \boldsymbol{\kappa}^c \delta T) = -P^c \mathbf{1} \tag{8.90}$$

where $\boldsymbol{\varepsilon}_c$ is the strain tensor of the ice crystal, $\boldsymbol{\kappa}^c$ is the dilation coefficient tensor of the ice crystal, P^c is the internal pressure of ice crystal. From Eq.(8.90), the strain of the ice crystal can be derived:

$$(\forall \underline{z} \in \Omega_c) \qquad \boldsymbol{\varepsilon}_c(\underline{z}) = -P^c \mathbb{S}^c(\underline{z}) : \mathbf{1} + \boldsymbol{\varepsilon}_L + \boldsymbol{\kappa}^c \delta T \tag{8.91}$$

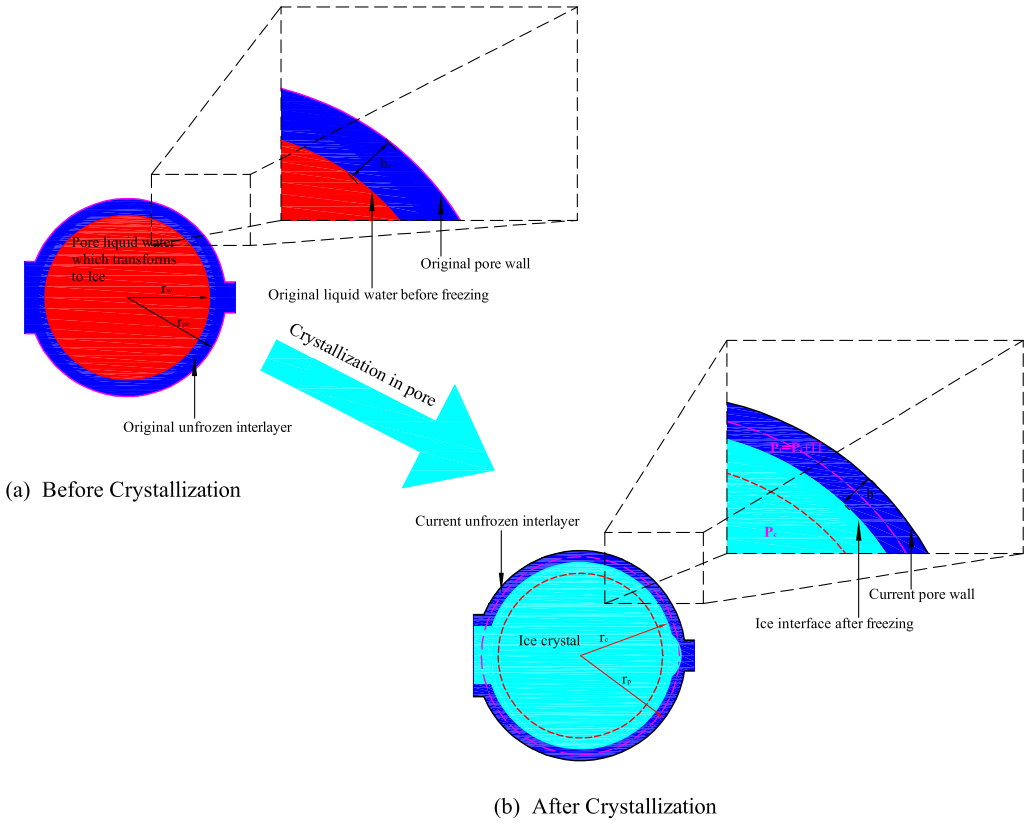

Figure 8.3: Schematic representation of the crystallization in pore

Young-Lapalace equation is used to characterize mechanical equilibrium betweem ice crystal and the unfrozen water film:

$$P^c - P^f = \frac{2\gamma_{cf}}{r_c} \tag{8.92}$$

with:

$$P^f = P^l + \Pi(h) \tag{8.93}$$

where r_c is the radius of the ice crystal, γ_{cf} is the surface tension between the ice crystal and unfrozen water film. Here, for simplification, it is taken to be identical to the surface tension between the ice and bulk liquid water γ_{cl} .

In addition to mechanical equilibrium, Gibbs-Thomson equation is used to characterized the thermodynamic equilibrium between the ice and bulk water [58]:

$$\frac{2\gamma_{cl}}{r_m} = P^c - P^l = -S_m \delta T - (1 - \frac{V_l}{V_c})P^l \tag{8.94}$$

where $\delta T = T - T_0$, T_0 is the melting point of bulk water; V_l and V_c are the molar volumes of liquid water (supercooling water) and ice crystal; r_m is the radius of ice meniscus (cf. r_c in Eq.(8.92)); S_m is the melting entropy of water.

8.5.4.2 Strain of ice-unfrozen water film spherical composite inclusion

As shown in Fig.(8.3) (b), the ice-unfrozen water film spherical composite inclusion embedded in the solid matrix can be treated as Eshelby-based problem. The total strain in the specified crystallized pore cased by the internal pressure of the unfrozen water and the macro strain $\boldsymbol{E}$ can be evaluated by :

$$\boldsymbol{\varepsilon}_{sc} = \{\overline{\mathbb{A}}_s : \boldsymbol{E} + \mathbb{P} : [(P_l - \frac{2\gamma_{sf}}{r_c + h})\mathbf{1} + \Pi \underline{n} \otimes \underline{n})]\} \tag{8.95}$$

where $\boldsymbol{E}$ is the macro strain tensor applied on the boundary of the porous medium, γ_{sf} is the surface tension between unfrozen water film and solid matrix, h is the thickness of

the unfrozen water film, $\underline{n}$ is the unit normal vector, $\overline{\mathbb{A}}_s$ is the average stain concentration tensor of the solid matrix, $\mathbb{P}$ is the Hill tensor. In isotropic case, the detailed information about $\overline{\mathbb{A}}_s$ and $\mathbb{P}$ is given in Appendix(C.1).

8.5.4.3 Determination of thickness of unfrozen water film

The displacement continuity of unfroze water film can be expressed as:

$$\boldsymbol{\varepsilon}_{sc}.(r_c + h)\underline{e}_r = \boldsymbol{\varepsilon}_c.r_c\underline{e}_r + h\underline{n} \tag{8.96}$$

where $\underline{e}_r$ is the radial vector.

When the poroelastic properties are known, combining Eq.(8.91), Eq.(8.95) and Eq.(8.96), the thickness of unfrozen water film h can be determined with the micromechanics approach.

8.6 Summary

In this chapter, based on local physical characterization, several micromechanics models for thermoporoelastic porous media and unsaturated freezing porous media were presented.

— Thermoporoelastic model for saturated porous media is developed first in Eq.(8.6) and Eq.(8.11). In addition to macroscopic strains $\boldsymbol{E}$ and prestress tensor $\boldsymbol{\sigma}^p$, thermal stress as an independent loading parameter is accounted for in the state equations. The homogenized volumetric thermal dilation coefficient $\boldsymbol{\alpha}^{hom}$ is equal to that of solid phase $\boldsymbol{\alpha}^s$.

— Different from poromechanics model for unsaturated freezing porous media, the micromechanics model for unsaturated freezing porous media specifies the unfrozen water film surrounding the ice crystal at local scale. From the physico-chemical point of view, an additional disjoining pressure should be considered in the micromechanics model. Thus, a comprehensive micromechanics model for unsaturated freezing porous media is established. The state equations are shown in Eq.(8.32) and Eq.(8.61), in which macroscopic strain on the boundary, the thermal effect, the

initial stress, the equivalent pressure (including liquid pressure, gas pressure, the membrane stress and the disjoining pressure) are accounted for.

Analysing the equivalent pressure in Eq.(8.37) and Eq.(8.39), the membrane surface tension seems negligible when surface tensions $\gamma_{cf} \approx \gamma_{cl}$ is assumed. This is quite different from the conclusion of Coussy's poromechanics model [60], in which surface tension effect should be taken into account. The reason for this different may lie in the different treatment of ice-solid interface in poromechanics model and the micromechanics model. In the micromechanics model, the unfrozen water film between the ice and solid matrix is specified, hence, the disjoining pressure within the unfrozen water film is accounted for in this model. However, ice crystal interacts directly with solid matrix in the poromechanics model, therefore, the variation of surface tension $\gamma_{cs} - \gamma_{sl}$ have to been taken into account in the poromechanics model.

— An alternative micromechanics model for unsaturated freezing porous media which accounts for the stiffness property of the unfrozen water film is presented. The homogenized elastic tensor of the unsaturated freezing porous media increases owing to the disjoining pressure in the unfrozen water film.

Chapter 9

Application: Micromechanical modelling free swelling of cement paste under freezing

Contents

9.1 Introduction 235
9.2 Assumptions and boundary conditions 236
9.3 Poroelastic properties 238
9.4 Volume fractions of each phase within the cement paste sample 239
9.5 Disjoining pressure 242
9.6 Results and discussion 242
9.7 Conclusion 248

9.1 Introduction

In this chapter, the micromechanics model presented in Section(8.3) will be used to simulate the free swelling of undrained freezing cement paste. The free swelling of cement paste have been performed by Zeng et al. [262], all of the experimental procedures are

suggested to his work [262].

9.2 Assumptions and boundary conditions

The assumptions and boundary conditions for the cement paste samples are listed in the follows:

— **1** The sample is filled with liquid water before freezing. 0°C is taken as initial temperature and the reference internal pressure is also taken as 0.

— **2** The temperature is uniform through the overall sample, the variation of the temperature is sufficient slow so that the sample is always in equilibrium state.

— **3** The sample is free swelling during freezing, it gives: $\boldsymbol{\Sigma} = 0$.

— **4** The boundary of sample is sealed so that it is undrained. Therefore, the mass balance of water (liquid water and ice crystal) within sample is always satisfied during freezing, it yields: $m - m_0 = 0$, where m_0 and m are the initial and current mass of the water in overall sample.

— **5** The macroscopic and local strains of sample are infinitesimal, the sample can thus be treated as poroelastic case.

— **6** Each phase of the cement paste sample is isotropic at local and macro scales.

— **7** The physical properties of unfrozen water film are assumed to be identical to those of supercooling water.

Based on these conditions and assumptions, we have the following expressions:

With assumption 7, the surface tension of unfrozen water film-solid matrix interface γ_{sf} is equal to supercooling water-solid matrix γ_{sl}. Therefore, the membrane stress (induced by surface tension) can be disregarded (go back to Eq.(8.37)). From Eq.(8.37) as well as condition 1, we have:

$$\delta P = P^l + \varphi_{sc}^0 \Pi^f \tag{9.1}$$

where φ_{sc}^0 is the volume fraction of the pore space occupied by ice crystal-unfrozen water film spherical composite (the variation of the volume induced by the internal pressure is not accounted for).

With the assumption 7, the density of unfrozen water film is assumed to be identical to that of supercooling water. Moreover, we know the boundary of sample is sealed and can be considered as undrained (condition 4). Therefore, from Subsection(8.5.2), in isotropic case (assumption 6), the liquid pressure P^l can be determined as:

$$\begin{aligned} P^l \approx M^{-1}\{-3b\epsilon + [(b-\phi_0)\alpha^s + \varphi_l^0\alpha_l + \varphi_c^0\alpha_c\frac{\rho_c^0}{\rho_l^0}]\delta T - \varphi_c^0(\frac{\rho_c^0}{\rho_l^0} - 1) + \varphi_c^0\frac{S_m\delta T}{K_c}\frac{\rho_c^0}{\rho_l^0} \\ -(\Pi^f\frac{\varphi_{sc}^0}{\phi_0})(1-b)[\frac{1-\varphi_0}{K^{hom}} - \frac{1}{K^s}]\} \end{aligned} \tag{9.2}$$

with:

$$M^{-1} = \{\frac{\varphi_l^0}{K_l} + \frac{\varphi_c^0}{K_c} + (1-b)[\frac{1-\varphi_0}{K^{hom}} - \frac{1}{K^s}]\}^{-1} \tag{9.3}$$

With the condition 3 and assumption 6, the total linear strain of the freezing cement paste sample can be determined by Eq.(8.32) as:

$$\epsilon = \epsilon_{P^l} + \epsilon_\Pi + \epsilon_{th} = \frac{bP^l}{3K^{hom}} + \frac{\varphi_{sc}^0 b\Pi^f}{3K^{hom}} + \frac{\kappa^{hom}\delta T}{3K^{hom}} \tag{9.4}$$

with:

$$\begin{cases} \epsilon_{P^l} = \dfrac{bP^l}{3K^{hom}} \\ \epsilon_\Pi = \dfrac{\varphi_{sc}^0 b\Pi^f}{3K^{hom}} \\ \epsilon_{th} = \dfrac{\kappa^{hom}\delta T}{3K^{hom}} \end{cases} \tag{9.5}$$

Combining Eq.(9.2) and Eq.(9.5), the liquid pressure P^l and total linear strain ϵ can be determined. According to Eq.(9.2) and Eq.(9.5), P^l and ϵ are the functions of poroelastic properties ,volume fractions of each phase φ_i^0 $(i \in \{s, c, f, l, sc\})$ and disjoining pressure

Π^f. In the following sections, poroelastic properties, the volume fractions of each phase and disjoining pressure will be respectively determined.

9.3 Poroelastic properties

Generally, cement paste exhibits complex microstructure and it is a multi-scale porous medium. As we have discussed in Section(2.4), owing to the significant role of the water distribution in the freezing problems, the water distribution morphology other than the solid morphology should be paid special attention to. Therefore, the cement paste sample may be considered to simply consist of solid matrix, liquid water and ice crystal-unfrozen water film spherical composite inclusion. The latter two phases are embedded in the solid matrix. Cement paste exhibits notable matrix+inclusion morphology and its macroscopic properties can be estimated with Mori-Tanaka scheme. Hence, the simplified morphology of cement paste can also be represented by Fig.(8.1).

The poroelastic properties of the freezing porous media are estimated with Mori-Tanaka scheme and shown in Eq.(8.77). In isotropic case, the poroelastic properties are listed as follows:

$$\begin{cases} K^{hom} = \dfrac{(1-\phi)K^s}{(1-\phi)+\dfrac{\phi}{1-\alpha}} \\ b = \dfrac{\phi}{1-(1-\phi)\alpha} \\ \kappa^{hom} = K^{hom}\alpha^s \\ \alpha = \dfrac{3K^s}{3K^s+4\mu^s} \end{cases} \tag{9.6}$$

According to Eq.(9.6), when the porosity of the cement paste ϕ, the bulk modulus and volumetric dilation coefficient of solid matrix of cement paste (K^s and α^s) are known, the macroscopic poroelastic properties can then be estimated.

9.4 Volume fractions of each phase within the cement paste sample

With assumption 5 shown in Section(9.2), the current volume fractions of each phase is assumed to be identical to their corresponding initial value. The latter can be estimated by the pore size distribution function of cement paste. The pore size distribution of the cement paste is determined by means of Mercury intrusion porosimetry (MIP) and the pore size distribution function $\alpha(r)$ is fitted by Zeng [262]:

$$\alpha(r) = f_0 + \sum_i^N [\frac{\sqrt{2}A_i}{w_i\sqrt{\pi}}\exp(\frac{-2(\log(r) - \log(r_i))^2}{w_i^2})] \tag{9.7}$$

where f_0, A_i and w_i are the fitting parameters. From Eq.(8.26), we have:

$$\int_{r_{min}}^{r_{max}} \alpha(r) = 1 \tag{9.8}$$

where r_{max} and r_{min} are the maximum and minimum pore radii of cement paste, for this cement paste sample, $r_{min} = 3nm$ and $r_{max} = 4 \times 10^5\ nm$ [262].

The cumulative curve of the cement paste can be expressed as logarithmic form [262]:

$$\varphi(r) = \int_{\log(r_{max})}^{\log(r)} \{f_0 + \sum_i^N [\frac{\sqrt{2}A_i}{w_i\sqrt{\pi}}\exp(\frac{-2(\log(r) - \log(r_i))^2}{w_i^2})]\}\mathrm{d}(\log(r)) \tag{9.9}$$

The fitting parameters for the pore size distribution of the cement paste are listed in Table(9.1).

At certain temperature variation $\delta T = T - T_0$ ($T < T_0$, c.f., supercooling temperature $T_0 - T$), ice crystal and liquid pore water are in mechanical and thermodynamic equilibrium. The equilibrium critical pore radius $r_c^{'}$ can be determined by means of Eq.(8.94):

$$r_c^{'} = h - \frac{2\gamma_{cl}}{S_m\delta T + (1 - \frac{V_l}{V_c})P^l} \tag{9.10}$$

where T_0 is the melting point of bulk water ($T_0 = 0°\mathrm{C}$); V_l and V_l are the molar volume of

Table 9.1: Fitting parameters for pore size distribution function of cement paste, adopted from [262].

Peaks	f_0 [1]	A_i	w_i	log$r_i(r_i)$ (nm)	Coefficients
1		0.0109	0.432	5.515 (327340)	
2	0.00477	0.180	0.727	1.190 (15.488)	0.999
3		0.530	0.647	0.0145 (1.0304)	

[1] On the vertical axis of original pore size curve, the unit of the pore volume is ml per gram cement paste sample in Zeng's thesis. In our study, to make sure the vertical axis be the volume fraction (ml pore space per ml cement paste sample), the original value of A_i and f_0 are modified by multiplying density of the sample and dividing by its porosity.

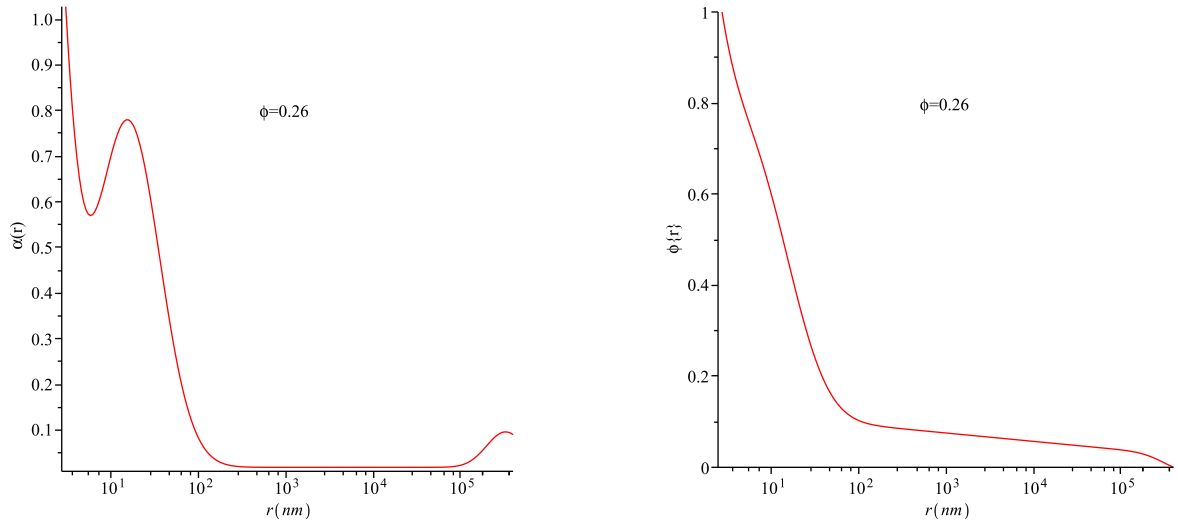

(a) Pore size distribution

(b) Cumulative curve

Figure 9.1: Pore size distribution and cumulative curve of cement paste [262].

water and ice crystal; S_m is the melting entropy of water; γ_{cl} is the surface tension of ice crystal-liquid pore water interface; h is the thickness of unfrozen water film.

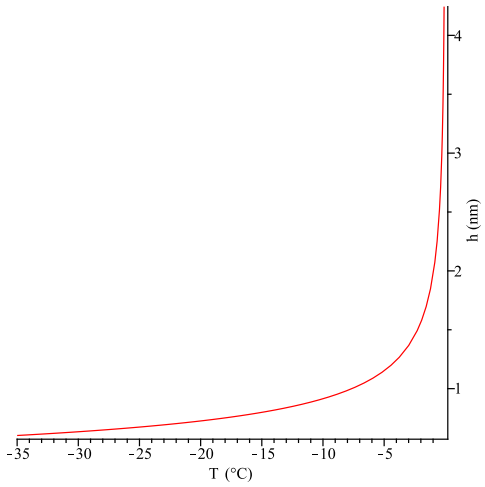

Figure 9.2: Dependence of the thickness of unfrozen water film on temperature, determined by Eq.(9.11).

An empirical equation proposed by Fagerlund et al. [94] is employed to determine the thickness of unfrozen water film in cement based materials:

$$h = 1.97(T_0 - T)^{-1/3} = 1.97(-\delta T)^{-1/3}(\text{nm}) \tag{9.11}$$

The dependence of the thickness of unfrozen water film on temperature can be plotted in Fig.(9.2).

Therefore, during freezing, the volume fractions of each phase can be evaluated as:

$$\begin{cases} \varphi_{sc} \approx \varphi_{sc}^0 = \phi_0 \int_{r_c'}^{r_{max}} \alpha(r)dr \\ \varphi_f \approx \varphi_f^0 = \phi_0 \int_{r_c'}^{r_{max}} \dfrac{3h}{r}\alpha(r)dr \\ \varphi_c \approx \varphi_c^0 = \phi_0 \int_{r_c'}^{r_{max}} (1 - \dfrac{3h}{r})\alpha(r)dr \\ \varphi_l \approx \varphi_l^0 = \phi_0 \int_{r_{min}}^{r_c'} \alpha(r)dr \end{cases} \tag{9.12}$$

where r_c' is determined by Eq.(9.10), h is determined by Eq.(9.11).

9.5 Disjoining pressure

As introduced in Section(7.3), the disjoining pressure in the unfrozen water film can be expressed as a two-term formula in whole temperature range. However, there are still lack of experimental data for disjoining pressure within unfrozen water film until now. Therefore, the structural component of water film at room temperature (isothermal condition) [47] is adopted to characterize the disjoining pressure of the unfrozen water film, it follows [190]:

$$\Pi(h) = K_{sr}\exp(-\frac{h}{\lambda_{sr}}) + K_{lr}\exp(-\frac{h}{\lambda_{lr}}) \tag{9.13}$$

with [47]:

$$K_{sr} = 300 \text{ MPa} \qquad \lambda_{sr} = 0.3 \text{ nm} \qquad K_{lr} = 2 \text{ MPa} \qquad \lambda_{lr} = 2 \text{ nm} \tag{9.14}$$

It should be borne in mind that, as discussed in Section(7.3), the values of parameters K (K_{sr} and K_{lr}) and λ (λ_{sr} and λ_{lr}) are temperature dependent: K increases with the decreasing temperature while λ decreases with temperature. Thus, it is reasonable to infer that the value of disjoining pressure in unfrozen water film is probable to be underestimated when the parameters in Eq.(9.14) are adopted.

9.6 Results and discussion

The parameters used in the simulation are listed in Table(9.2):

Taking advantage of the elastic properties of solid matrix and the porosity of cement paste in Table(9.2), the homogenized poroelastic properties of cement paste can be estimated by Eq.(9.6). These estimated poroelastic properties are compared with those obtained by Zeng et al. [262] in Table(9.3).

As can be seen from Table(9.3), the homogenized poroelastic properties estimated by Mori-Tanaka scheme are comparable to those estimated by Zeng [262]. Therefore, it is feasible to use the homogenized poroelastic properties in the simulation.

Table 9.2: Some parameters used in the simulation

Parameters	Value (unit)	Reference
Initial porosity ϕ_0	0.26	Zeng et al. [262]
Skeleton Desity of cement paste	2.38 g.cm^{-3}	Zeng et al. [262]
K^s	31.8 GPa	Ulm et al. [245]
μ^s	19.1 GPa	Ulm et al. [245]
K^c	7.81 GPa	Coussy et al.[60]
K^l	1.79 GPa	Coussy et al.[60]
γ_{cl}	$0.0409 + 3.9 \times 10^{-4}(\ \mathrm{T} - \mathrm{T}_0)\mathrm{J} \cdot \mathrm{M}^{-2}$	Sun et al.[232]
ρ_c^0	0.917 g.cm^{-3}	Coussy et al.[60]
ρ_l^0	0.999 g.cm^{-3}	Coussy et al.[60]
K_{sr}	300 MPa	Churaev et al. [47]
K_{lr}	2 MPa	Churaev et al. [47]
λ_{sr}	0.3 nm	Churaev et al. [47]
λ_{lr}	2 nm	Churaev et al. [47]
α^s	54×10^{-6}	Coussy et al.[60]
α^c	155×10^{-6}	Coussy et al.[60]
α^l	$[\ 68.7 + 24.732(\mathrm{T}\text{-}\mathrm{T}_0)]\times 10^{-6}$	Zeng et al. [262]
S_m	1.2MPa.K^{-1}	Coussy et al.[60]

Table 9.3: The evaluated poroelastic properties by Mori-Tanaka scheme

	This study	Zeng's work [262] [1]
Bulk modulus K^{hom}(GPa)	17.76	17.39
Biot coefficient b	0.44	0.49
Biot modulus N_{hom}(GPa)	175.3	122.2
Volumetric thermal dilation coefficient α^{hom}	5.40×10^{-5}	5.54×10^{-5}

[1] In Zeng's work, the homogenized poroelastic properties are determined by multi-scale homogenization. The cement paste are divided into three scale levels, the detailed procedure is given in [262].

Taking $r_c^{'}$ (as shown in Eq.(9.10)) as a variable which ranges between maximum pore radius (4×10^5 nm) and minimum pore radius (3 nm), by means of Eq.(9.12), the volume fractions of each phase can be determined.

With a given $r_c^{'}$ and the corresponding volume fractions of each phase, combining with Eq.(9.2), Eq.(9.5) and Eq.(9.10) yields the liquid pressure P^l and the corresponding supercooling δT (and T).

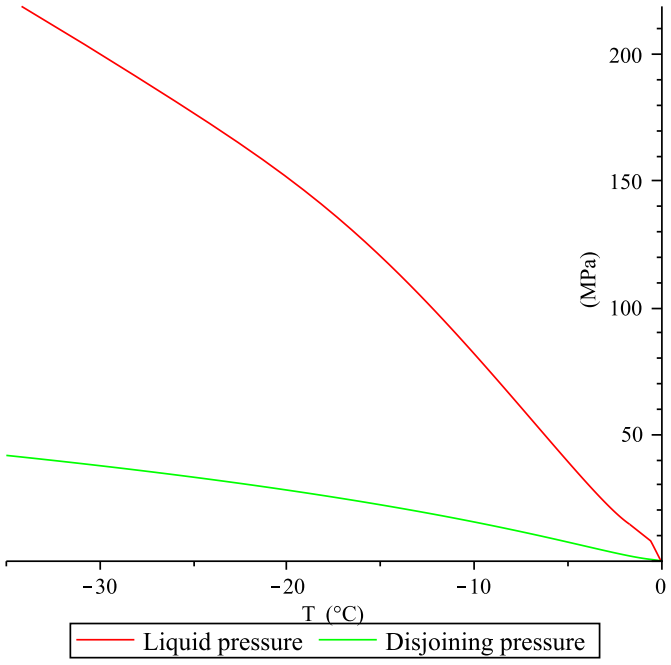

Figure 9.3: Dependence of the disjoining pressure and liquid pressure on temperature, the disjoining pressure is determined by Eq.(9.13) while the liquid pressure for the undrained case is determined by Eq.(9.2).

The dependence of the disjoining pressure and liquid pressure on the temperature is plotted in Fig.(9.3). It can be seen from the figure, both of the disjoining pressure and liquid pressure increase with the decrease of temperature (increase of supercooling). During the freezing, liquid pressure is always larger than disjoining pressure. Moreover, the liquid pressure can reach as much as 200 MPa when the temperature is as low as -35°C. However, as stated in the previous section, the disjoining pressure is likely to be underestimated.

The evolution of percentages of each phase with the temperature is illustrated in Fig.(9.4).

Here, the percentages of each phase are defined as the volume fractions of each phase divided by initial porosity, that is, φ_i/ϕ_0, $i \in \{l, c, f\}$. As can be seen from the figure, the percentage of liquid water decreases with decreasing temperature, while both of the percentage of ice crystal and unfrozen water film increase with decreasing temperature. It is interesting to find that, the percentage of the unfrozen water film can reach as much as 10% when the temperature as low as -35°C. It can thus be inferred that, the effect of unfrozen water film will become more and more significant with the deceasing temperature because of its increasing volume fraction.

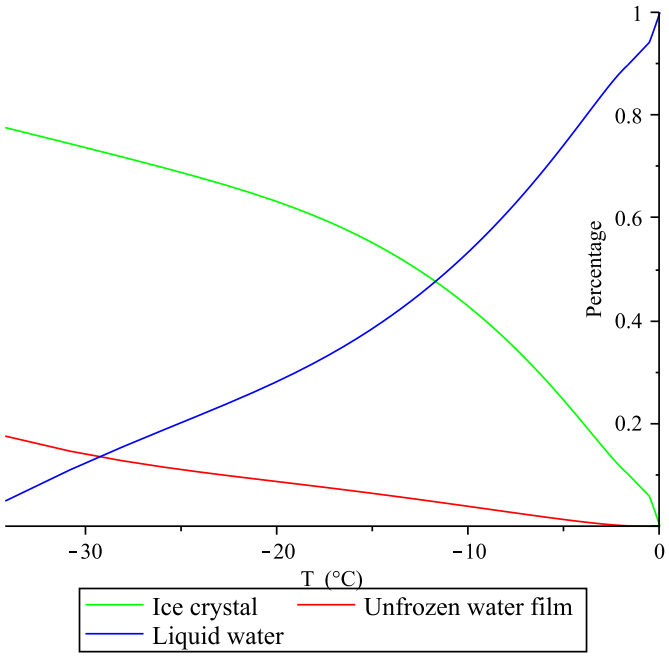

Figure 9.4: Evolution of the percentages of each phases with the temperature, the percentages of each phase are defined as their volume fractions divided by porosity.

The linear strains induced by equivalent pressure can be decomposed into two parts: strains induced by the liquid pressure ϵ_{P^l} and strains induced by the disjoining pressure ϵ_Π (see Eq.(9.5), recalling that the surface tension effect is disregarded owing to the assumption 7). The evolution of the linear strains with the temperature is depicted in Fig.(9.5) (a). As expected, owing to the increase of the liquid pressure and the disjoining pressure with the decreasing temperature (see Fig.(9.3)), the linear strains induced by liquid pressure and

disjoining pressure increase with decreasing temperature. Moreover, though the disjoining pressure may be underestimated, the linear strains induced by liquid pressure seems far greater than that induced by the disjoining pressure. Therefore, it can be inferred that, the liquid pressure plays a more dominant role than the disjoining pressure in the deformation of the undrained freezing porous medium under free swelling.

As shown in Eq.(9.5), the total linear strain (green curve) during freezing consists of two contributions: strains induced from equivalent pressure effect $\epsilon_{P^l} + \epsilon_{\Pi}$ and strains induced from thermal effect ϵ_{th}. The evolution of these two contributions with temperature is illustrated in Fig.(9.5) (b). As seen from this figure, the simulation results of the total strain (green curve) are comparable with the experimental results (black points) though there are still some discrepances between the two results. It should be noted that, at the temperatures ranging from 0°C to -9°C, the ice crystals will not form in the pore network of the cement paste owing to the bulk supercooling effect (lack of nucleus). Therefore, the total strains nearly arise from the thermal effect (ϵ_{th}) at this temperature range. When the temperature is lower than -9°C, the ice will form in the cement paste instantaneously. Hence, a huge liquid pressure and disjoining pressure will engender within the cement paste, which result in great strain of the cement paste.

Since the simulating thermal strains ϵ_{th} (blue dotted line) perfectly agree with the experimental results. Thus, according to Eq.(9.5), the discrepancy between the simulation result (green curve) and experimental results (black points) is likely to lie in the overestimation of liquid pressure (disjoining pressure is far smaller that liquid pressure as shown in Fig.(9.3)). The overestimation of the liquid pressure is probably led by the overestimation of ice content (volume fraction of ice) (as shown in Fig.(9.4)). Therefore, estimating the ice content from the pore size distribution derived from MIP and Gibbs-Thomson equation will be re-assessed.

Generally, it is more feasible to measure the volume fraction of ice crystal by means of TPM (with differential scanning calorimeter (DSC)) [32, 232] instead of MIP. That is because the drying process before MIP (NAD) will alter the microstructure of cement

paste [232]. On the contrary, TPM determines the pore size distribution in saturated porous media which can avoid the microstructural variation during the drying process [232]. Moreover, the stress induced by ice crystal is 10 times less than that exerted by mercury, which means TPM will alter microstructure less than MIP [232].

The pore size distributions of the mortar obtained by Mercury intrusion porosimetry (MIP), thermoporometry (TPM) and nitrogen adsorption/desorption (NAD) are compared and depicted in Fig.(9.6) by Sun et al. [232] [1]. As can be seen from this figure, the cumulative curve determined by TPM lies below that determined by MIP, which means that comparing to TPM, the porosity as well as pore size are enlarged by MIP [232]. Hence, estimating the ice content by means of pore size distribution derived from MIP will overestimate the ice content and then the total strains evaluated by the pore size distribution from MIP will be overestimated.

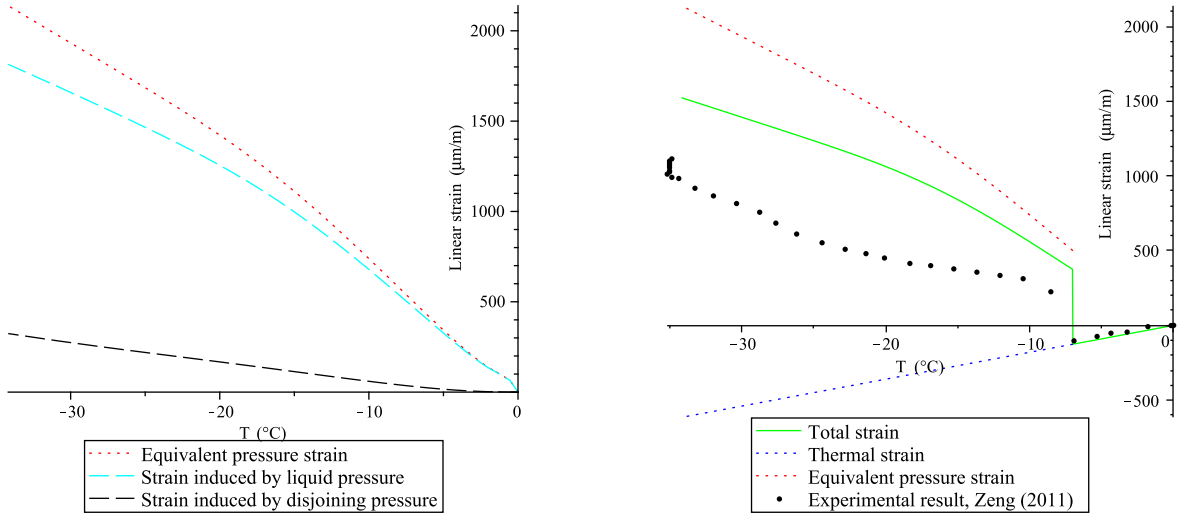

(a) Strains induced by each component of equivalent pressure

(b) Total strains induced by equivalent pressure and thermal effect

Figure 9.5: Evolution of the strains of the cement paste with the temperature during freezing process.

1. The old MIP (red dash-dot curve) was measured a year earlier than other samples (other curves), in this sample, the pore volume and the pores with radius < 12 nm are greater than those of the samples cured with the additional hydration time (other curves) [232].

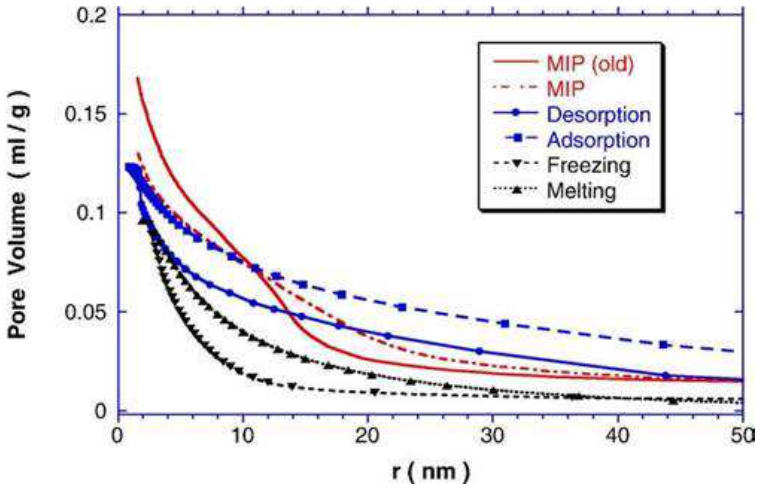

Figure 9.6: Comparison of pore size distributions of mortar derived by MIP, TPM and NAD, after Sun et al. [232].

9.7 Conclusion

Based on the local phase behaviors characterization, the micromechanics methodology seems effective to simulate the free swelling of cement paste under freezing. In this case, the total strains is composed of two parts: strains induced by thermal effect and strains induced by equivalent pressure. As supposed by Churaev et al. [45, 46, 49], the electrostatic and Van der Waals components of the disjoining pressure are negligible when compared with the structural component of the disjoining pressure of unfrozen water film. However, there is still lack of information about the structural component of the disjoining pressure of unfrozen water film. Therefore, the structural component of the disjoining pressure of the water film at room temperature is adopted in this model. The disjoining pressure of the unfrozen water film is likely to be underestimated owing to the temperature-dependent of the parameters of the structural component of the disjoining pressure (see Eq.(9.13)).

The simulating linear strains of the freezing cement paste under free swelling are comparable with the experimental results. The discrepancies between the two are likely to arise from the overestimation of the ice content, the latter is overestimated since the porosity as well as the pore sizes of the cementitious materials are enlarged during the MIP experiment.

Chapter 10

Conclusions

Based on the microstructure morphology (as shown in chapter 2 in part I) as well as the physical characterization of local behaviors, the main goal of this thesis is to study the transport properties and then freezing behavior of unsaturated porous media by means of micromechanics approach.

Part II

Micromechanics models for diffusion in unsaturated porous media are developed. The influences of the micromechanical scheme, the microstructure, the porosity ϕ, the volume fraction of the liquid layer and the constrictive factor δ of the liquid layer on the normalized homogenized diffusion coefficient are discussed in these models.

— The Self-Consistent scheme exhibits obvious percolation effect and is good for polycrystalline microstructure (e.g. granular material). The Mori-Tanaka scheme does not present percolation effect owing to connectivity of the matrix (here liquid water); it is well adapted to represent the matrix+inclusion microstructure.

— In two-scale microstructure models such as MT-SC (level I (local scale) and level II (macro scale) are estimated with Self-Consistent and Mori-Tanaka schemes, respectively) and SC-SC, the percolation effects decrease with pore volume fraction ϕ and ratio of macro pores α; the saturated homogenized diffusion coefficient $D^{hom}(Sr = 1)$ increases with ϕ and decreasing α. In MT-MT model, there is no percolation effect

and the saturated homogenized diffusion coefficient $D^{hom}(Sr = 1)$ increases with ϕ and decreasing α.

— The introduction of the liquid layer (the intergranular layer, the wetting layer and the water film) ensures the connectivity of liquid layer, even at low saturation degree. The liquid layer is accounted for in one-scale microstructure. When the local diffusion occurs in the liquid layer treated as an interface (2-D), with no volume fraction, the homogenized solute diffusion coefficient can be derived analytically. However, the real liquid layer is an interphase (3-D), the volume fraction of which can be accounted for in an enriched micromechanics model. The latter is thus able to characterize and take into account of the evolution of the thickness of the liquid layer during the desaturation process. When the homogenized diffusion coefficient is estimated with Mori-Tanaka scheme, the homogenized diffusion coefficient D^{hom} increases with the decreasing volume fraction of liquid layer. It also increases with δ and ϕ; when the homogenized diffusion coefficient is estimated with Self-Consistent scheme, the homogenized diffusion coefficient increases with volume fraction of liquid layer and also with δ and ϕ.

— Micromechanics model accounting for the local solute diffusion in the pore body water, the intergranular layer, the wetting film and the water film is developed for unsaturated glass beads, and sand. The simulation results of this micromechanics model agree well with the experimental results. At low saturation degree, the pore body water, the intergranular layers and the wetting layers are discontinuous, the solute diffusion is governed by the water film. At low saturation degree, from the simulation results, the homogenized diffusion coefficient will decrease by 4 to 5 orders of magnitude when comparing with the homogenized saturated diffusion coefficient.

A micromechanics model for the liquid permeability in unsaturated sandstone is developed. It is employed to predict the saturated intrinsic permeability and then the unsaturated relative permeability of Fontainebleau sandstone. The simulation results of saturated intrinsic permeability agree well with the experimental results and are comparable with

the modified Kozeny-Carman model for Fontainebleau sandstone. This micromechanics model is able to explain the D^2 dependence of the saturated intrinsic permeability coefficient according to the modified Kozeny-Carman model. This micromechanics model is also employed to estimate the relationship between the unsaturated permeability and saturation degree for Fontainebleau sandstone. The simulation results sound more comparable with the experimental results than Brooks-Corey's model and Van Genuchten's model.

Part III

The unfrozen water film between the ice crystal and the pore wall at local scale is specified and accounted for in the micromechanics model for unsaturated freezing porous media. From the physico-chemical point of view, an additional disjoining pressure is accounted for in the internal pressure. A first comprehensive micromechanics model for unsaturated freezing porous media is developed, which accounts for the thermal effect, the initial stress, the equivalent pressure (including liquid pressure, gas pressure, the membrane stress and the disjoining pressure). It is even possible to investigate the role of the disjoining pressure on the elastic properties of the unfrozen water film and then on the homogenized ones. However, because of lack of data on the dependence of the disjoining pressure on temperature, use is made of the first micromechanics model to study the free swelling of a freezing cement paste. The modelling results sound comparable with the experimental results though there are still some discrepancies. The discrepancies may lie in the overestimation of the ice content, which here is estimated by the pore size distribution by MIP and Gibbs-Thomson equation.

Bibliography

[1] http://en.wikipedia.org/wiki/gravel.

[2] http://en.wikipedia.org/wiki/porous medium.

[3] B. Aksoy. *Hydrophobic forces in free thin films of water in the presence and absence of surfactants*. PhD thesis, Virginia Polytechnic Institute and State University, 1997.

[4] M. Akyurt, G. Zaki, and B. Habeebullah. Freezing phenomena in ice-water systems. *Energy conversion and management*, 43(14):1773–1789, 2002.

[5] M. Antognozzi, A. Humphris, and M. Miles. Observation of molecular layering in a confined water film and study of the layers viscoelastic properties. *Applied Physics Letters*, 78(3):300–302, 2001.

[6] G. Archie. The electrical resistivity log as an aid in determining some reservoir characteristics. *Trans. AIMe*, 146(99):54–62, 1942.

[7] L. Arya, F. Leij, P. Shouse, and M. van Genuchten. Relationship between the hydraulic conductivity function and the particle-size distribution. *Soil Science Society of America Journal*, 63(5):1063–1070, 1999.

[8] M. Ashby and D. Jones. Engineering materials 2: An introductionto microstructures, processing and design. 2011.

[9] P. Atkins. Physical chemistry, 6th, 1998.

[10] S. Averjanov. About permeability of subsurface soils in case of incomplete saturation. *English Collection*, 7:19–21, 1950.

[11] S. Bakke and P. ? ren. 3-d pore-scale modelling of sandstones and flow simulations in the pore networks. *SPE Journal*, 2(2):136–149, 1997.

[12] S. Barer, N. Churaev, B. Derjaguin, O. Kiseleva, and V. Sobolev. Viscosity of non-freezing thin interlayers between the surfaces of ice and quartz. *Progress in Surface Science*, 40(1):371–378, 1992.

[13] P. Barraclough and P. Tinker. The determination of ionic diffusion coefficients in field soils. i. diffusion coefficients in sieved soils in relation to water content and bulk density. *Journal of Soil Science*, 32(2):225–236, 2006.

[14] J. Bear, B. Rubinstein, and L. Fel. Capillary pressure curve for liquid menisci in a cubic assembly of spherical particles below irreducible saturation. *Transport in porous media*, 89(1):63–73, 2011.

[15] D. Beard and P. Weyl. Influence of texture on porosity and permeability of unconsolidated sand. *AAPG Bulletin*, 57(2):349–369, 1973.

[16] J. Beaudoin and C. MacInnis. The mechanism of frost damage in hardened cement paste. *Cement and Concrete Research*, 4(2):139–147, 1974.

[17] M. Bellissent-Funel, J. Lal, and L. Bosio. Structural study of water confined in porous glass by neutron scattering. *The Journal of chemical physics*, 98:4246, 1993.

[18] F. Bergaya and G. Lagaly. General introduction: clays, clay minerals, and clay science. *Developments in Clay Science*, 1:1–18, 2006.

[19] M. Biot. General theory of three-dimensional consolidation. *Journal of applied physics*, 12(2):155–164, 1941.

[20] M. Blunt, D. Fenwick, and D. Zhou. What determines residual oil saturation in three-phase flow? In *SPE/DOE Improved Oil Recovery Symposium*, 1994.

[21] M. Blunt, M. J. King, and H. Scher. Simulation and theory of two-phase flow in porous media. *Physical Review A*, 46(12):7680, 1992.

[22] M. J. Blunt, M. D. Jackson, M. Piri, and P. H. Valvatne. Detailed physics, predictive capabilities and macroscopic consequences for pore-network models of multiphase flow. *Advances in Water Resources*, 25(8):1069–1089, 2002.

[23] S. Boggs. *Principles of sedimentology and stratigraphy*, volume 784. Prentice Hall Upper Saddle River, NJ, USA:, 1995.

[24] T. Bourbié, O. Coussy, and B. Zinszner. Acoustics of porous media: Gulf publ, 1987.

[25] T. Bourbie and B. Zinszner. Hydraulic and acoustic properties as a function of porosity in fontainebleau sandstone. *Journal of Geophysical Research*, 90(B13):11524–11, 1985.

[26] I. Bourg, G. Sposito, and A. Bourg. Modeling cation diffusion in compacted water-saturated sodium bentonite at low ionic strength. *Environmental science & technology*, 41(23):8118–8122, 2007.

[27] C. Boutin. Study of permeability by periodic and self-consistent homogenisation. *European Journal of Mechanics-A/Solids*, 19(4):603–632, 2000.

[28] D. Boyarskii, V. Tikhonov, and N. Y. Komarova. Model of dielectric constant of bound water in soil for applications of microwave remote sensing. *Progress In Electromagnetics Research*, 35:251–269, 2002.

[29] R. H. Brooks and A. T. Corey. Hydraulic properties of porous media. *Hydrology Papers, Colorado State University*, (March), 1964.

[30] I. Brovchenko and A. Oleinikova. *Interfacial and confined water*. Elsevier Science, 2008.

[31] P. G. Bruch. Laboratory study of evaporative fluxes in homogeneous and layered soils. 2008.

[32] M. Brun, A. Lallemand, J.-F. Quinson, and C. Eyraud. A new method for the simultaneous determination of the size and shape of pores: the thermoporometry. *Thermochimica Acta*, 21(1):59–88, 1977.

[33] A. Buchwald. Determination of the ion diffusion coefficient in moisture and salt loaded masonry materials by impedance spectroscopy. In *3rd Int. PhD Symposium*, volume 11, 2000.

[34] T. Bunsri, M. Sivakumar, and D. Hagare. Applications of hydraulic properties models on microscopic flow in unsaturated porous media. *Journal of Applied Fluid Mechanics*, 2(2):1–11, 2009.

[35] N. Burdine. Relative permeability calculations from pore size distribution data. *Journal of Petroleum Technology*, 5(3):71–78, 1953.

[36] G. Campbell and S. Shiozawa. Prediction of hydraulic properties of soils using particle-size distribution and bulk density data. *Indirect methods for estimating the hydraulic properties of unsaturated soils. University of California, Riverside*, pages 317–328, 1992.

[37] G. S. Campbell. A simple method for determining unsaturated conductivity from moisture retention data. *Soil Science*, 117(6):311–314, 1974.

[38] J. D. Campbell. *Pore pressures and volume changes in unsaturated soils*. PhD thesis, University of Illinois at Urbana-Champaign, 1973.

[39] S. Cariou. *Couplage hydro-mécanique et transfert dans l'argilite de Meuse/Haute-Marne: approches expérimentale et multi-échelle*. PhD thesis, Ecole des Ponts ParisTech, 2010.

[40] C. Carlos Jr. *Microscopic observations of internal frost damage and salt scaling*. PhD thesis, University of California, Berkeley, 2009.

[41] S. Chatterji and J. Jeffery. Studies of early stages of paste hydration of different types of portland cements. *Journal of the American Ceramic Society*, 46(6):268–273, 1963.

[42] E. C. Childs, N. Collis-George, E. Childs, and N. Collis-George. The permeability of porous materials. *Proceedings of the Royal Society of London. Series A. Mathematical and Physical Sciences*, 201(1066):392–405, 1950.

[43] H. Christenson, D. Gruen, R. Horn, and J. Israelachvili. Structuring in liquid alkanes between solid surfaces: Force measurements and mean-field theory. *The Journal of chemical physics*, 87:1834, 1987.

[44] N. Churaev. Surface forces and physicochemistry of surface phenomena. *Russian chemical reviews*, 73(1):25–36, 2004.

[45] N. Churaev, S. Bardasov, and V. Sobolev. On the non-freezing water interlayers between ice and a silica surface. *Colloids and Surfaces A: Physicochemical and Engineering Aspects*, 79(1):11–24, 1993.

[46] N. Churaev, S. Bardasov, and V. Sobolev. Disjoining pressure of thin nonfreezing water interlayers between ice and silica surface. *Langmuir*, 10(11):4203–4208, 1994.

[47] N. Churaev and B. Derjaguin. Inclusion of structural forces in the theory of stability of colloids and films. *Journal of colloid and interface science*, 103(2):542–553, 1985.

[48] N. Churaev and V. Sobolev. Disjoining pressure of thin unfreezing water layers between the pore walls and ice in porous bodies. *Colloid Journal*, 64(4):508–511, 2002.

[49] N. Churaev, V. Sobolev, M. Setzer, R. Auberg, and H. Keck. Disjoining pressure of water films in frozen materials. In *International RILEM Workshop on Frost Resistance of Concrete*, pages 97–103. RILEM Publications SARL, 2002.

[50] N. Churaev, V. Sobolev, and V. Starov. Disjoining pressure of thin nonfreezing interlayers. *Journal of colloid and interface science*, 247(1):80–83, 2002.

[51] T. Ciach and E. Swenson. Morphology and microstructure of hydrating portland cement and its constituents i. changes in hydration of tricalcium aluminate alone and in the presence of triethanolamine or calcium lignosulphonate. *Cement and Concrete Research*, 1(2):143–158, 1971.

[52] J. Conca and J. Wright. Diffusion and flow in gravel, soil, and whole rock. *Hydrogeology Journal*, 1(1):5–24, 1992.

[53] J. Conca, J. Wright, et al. Diffusion coefficients in gravel under unsaturated conditions. *Water Resour. Res*, 26(5):1055–1066, 1990.

[54] G. Constantinides. *Invariant mechanical properties of calcium-silicate-hydrates (CHS) in cement-based materials: instrumented nanoindentation and microporomechanical modeling*. PhD thesis, Massachusetts Institute of Technology, 2006.

[55] A. T. Corey. The interrelation between gas and oil relative permeabilities. *Producers monthly*, 19(1):38–41, 1954.

[56] O. Coussy. *Poromechanics*. Wiley, 2004.

[57] O. Coussy. Poromechanics of freezing materials. *Journal of the Mechanics and Physics of Solids*, 53(8):1689–1718, 2005.

[58] O. Coussy. *Mechanics and physics of porous solids*. Wiley, 2011.

[59] O. Coussy and P. Monteiro. Unsaturated poroelasticity for crystallization in pores. *Computers and Geotechnics*, 34(4):279–290, 2007.

[60] O. Coussy and P. Monteiro. Poroelastic model for concrete exposed to freezing temperatures. *Cement and Concrete Research*, 38(1):40–48, 2008.

[61] M. CRWMS. Invert diffusion properties model. Technical report, ANL-EBS-MD-000031, Las Vegas, Nevada, 2000.

[62] K. Culligan, D. Wildenschild, B. Christensen, W. Gray, M. Rivers, and A. Tompson. Interfacial area measurements for unsaturated flow through a porous medium. *Water Resour. Res*, 40(12):W12413, 2004.

[63] E. Dana and F. Skoczylas. Gas relative permeability and pore structure of sandstones. *International Journal of Rock Mechanics and Mining Sciences*, 36(5):613–625, 1999.

[64] E. Dana and F. Skoczylas. Experimental study of two-phase flow in three sandstones. i. measuring relative permeabilities during two-phase steady-state experiments. *International journal of multiphase flow*, 28(11):1719–1736, 2002.

[65] E. Dana and F. Skoczylas. Experimental study of two-phase flow in three sandstones. ii. capillary pressure curve measurement and relative permeability pore space capillary models. *International journal of multiphase flow*, 28(12):1965–1981, 2002.

[66] J. Dane and A. Klute. Salt effects on the hydraulic properties of a swelling soil. *Soil Science Society of America Journal*, 41(6):1043–1049, 1977.

[67] H. Darcy. Les fontaines publiques de la ville de dijon, 1856. *Dalmont, Paris*, 70.

[68] J. Dash, H. Fu, and J. Wettlaufer. The premelting of ice and its environmental consequences. *Reports on Progress in Physics*, 58(1):115, 1999.

[69] J. Dash, A. Rempel, and J. Wettlaufer. The physics of premelted ice and its geophysical consequences. *Reviews of modern physics*, 78(3):695, 2006.

[70] G. de Vera, M. A. Climent, E. Viqueira, C. Antón, and C. Andrade. A test method for measuring chloride diffusion coefficients through partially saturated concrete. part ii: The instantaneous plane source diffusion case with chloride binding consideration. *Cement and concrete research*, 37(5):714–724, 2007.

[71] B. Derjaguin and N. Churaev. On the question of determining the concept of disjoining pressure and its role in the equilibrium and flow of thin films. *Journal of Colloid and Interface Science*, 66(3):389–398, 1978.

[72] B. Derjaguin and N. Churaev. The theory of frost heaving. *Journal of Colloid and Interface Science*, 67(3):391–396, 1978.

[73] B. Derjaguin and N. Churaev. Flow of nonfreezing water interlayers and frost heaving. *Cold Regions Science and Technology*, 12(1):57–66, 1986.

[74] B. Derjaguin, N. Churaev, and V. Muller. Surface forces. *Consultants Bureau, New York*, 1987.

[75] B. Derjaguin and E. Obuchov. Colloid j., moscow 1, 385, 1935. *Acta phys.-chim. URSS*, 5(1), 1936.

[76] B. Deryagin and N. Churaev. Structure of water in thin layers. *Langmuir*, 3(5):607–612, 1987.

[77] B. Deryagin, N. Churaev, and Z. Zorin. Structure and properties of boundary layers of water. *Russian Chemical Bulletin*, 31(8):1507–1518, 1982.

[78] A. Doerr, M. Tolan, J. Schlomka, and W. Press. Evidence for density anomalies of liquids at the solid/liquid interface. *EPL (Europhysics Letters)*, 52(3):330, 2007.

[79] L. Dormieux, L. Jeannin, and N. Gland. Homogenized models of stress-sensitive reservoir rocks. *International Journal of Engineering Science*, 2011.

[80] L. Dormieux, L. Jeannin, and J. Sanahuja. Effective hydraulic and mechanical properties of heterogeneous media with interfaces. *Multiscale Methods in Computational Mechanics*, pages 179–194, 2011.

[81] L. Dormieux and D. Kondo. Approche micromécanique du couplage perméabilité–endommagement. *Comptes Rendus Mecanique*, 332(2):135–140, 2004.

[82] L. Dormieux, D. Kondo, and F. Ulm. *Microporomechanics*. Wiley New York, 2006.

[83] L. Dormieux, E. Lemarchand, and J. Sanahuja. Comportement macroscopique des matériaux poreux à microstructure en feuillets. *Comptes Rendus Mécanique*, 334(5):304–310, 2006.

[84] P. M. Doyen. Permeability, conductivity, and pore geometry of sandstone. *Journal of Geophysical Research*, 93(B7):7729–7740, 1988.

[85] F. A. Dullien et al. *Porous media: fluid transport and pore structure*, volume 2. Academic press San Diego, 1992.

[86] M. Dunn, J. Dore, and P. Chieux. Structural studies of ice formation in porous silicas by neutron diffraction. *Journal of crystal growth*, 92(1-2):233–238, 1988.

[87] A. El Bied, J. Sulem, F. Martineau, et al. Microstructure of shear zones in fontainebleau sandstone. *International Journal of Rock Mechanics and Mining Sciences*, 39(7):917–932, 2002.

[88] H. I. Ene and E. Sanchez-Palencia. Equations et phénomenes de surface pour lécoulement dans un modele de milieu poreux. *J. Mécanique*, 14(1):73–108, 1975.

[89] J. Eriksson and B. Toshev. Disjoining pressure in soap film thermodynamics. *Colloids and Surfaces*, 5(3):241–264, 1982.

[90] D. Everett. The thermodynamics of frost damage to porous solids. *Transactions of the Faraday Society*, 57:1541–1551, 1961.

[91] D. Everett and J. Haynes. Colloid science, 1the chemical society. *Burlington House, London*, 1973.

[92] G. Ewing. Thin film water. *The Journal of Physical Chemistry B*, 108(41):15953–15961, 2004.

[93] A. Fabbri. *Physico-mécanique des matériaux cimentaires soumis au gel-dégel*. PhD thesis, Université de Marne la Vallée, 2006.

[94] G. Fagerlund. Determination of pore-size distribution from freezing-point depression. *Matériaux et construction*, 6(3):215–225, 1973.

[95] G. H. Fancher and J. A. Lewis. Flow of simple fluids through porous materials. *Industrial & Engineering Chemistry*, 25(10):1139–1147, 1933.

[96] M. Fang, P. Sokol, J. Jehng, and W. Halperin. Neutron diffraction study of cement. *Journal of Porous Materials*, 6(2):95–99, 1999.

[97] M. Faraday. Note on regelation. *Proceedings of the Royal Society of London*, 10:440–450, 1859.

[98] T. Fen-Chong. *Durabilité sous percolation et/ou cristallisation confinée en milieu poreux*. PhD thesis, Université Paris-Est, 2008.

[99] T. Fen-Chong and A. Fabbri. Freezing and thawing porous media: experimental study with a dielectric capacitive method. *Comptes Rendus Mecanique*, 333(5):425–430, 2005.

[100] L. Fisher, R. Gamble, and J. Middlehurst. The kelvin equation and the capillary condensation of water. 1981.

[101] L. Fisher and J. Israelachvili. Direct experimental verification of the kelvin equation for capillary condensation. 1979.

[102] L. R. Fisher and J. N. Israelachvili. Experimental studies on the applicability of the kelvin equation to highly curved concave menisci. *Journal of Colloid and Interface Science*, 80(2):528–541, 1981.

[103] R. Fisher. On the capillary forces in an ideal soil; correction of formulae given by wb haines. *The Journal of Agricultural Science*, 16(03):492–505, 1926.

[104] D. Fredlund, A. Xing, and S. Huang. Predicting the permeability function for unsaturated soils using the soil-water characteristic curve. *Canadian Geotechnical Journal*, 31(4):533–546, 1994.

[105] D. G. Fredlund and A. Xing. Equations for the soil-water characteristic curve. *Canadian Geotechnical Journal*, 31(4):521–532, 1994.

[106] M. D. Fredlund, D. G. Fredlund, and G. Wilson. Prediction of the soil-water characteristic curve from grain-size distribution and volume-mass properties. In *Proc., 3rd Brazilian Symp. on Unsaturated Soils*, volume 1, pages 13–23. Rio de Janeiro, 1997.

[107] J. Fripiat, M. Letellier, P. Levitz, J. Thomas, J. Fripiat, M. Letellier, P. Levitz, and J. Thomas. Interaction of water with clay surfaces [and discussion]. *Philosophical Transactions of the Royal Society of London. Series A, Mathematical and Physical Sciences*, 311(1517):287–299, 1984.

[108] J. Gao, R. Szoszkiewicz, U. Landman, E. Riedo, et al. Structured and viscous water in subnanometer gaps. *Physical Review B*, 75(11):115415, 2007.

[109] W. Gardner. Some steady-state solutions of the unsaturated moisture flow equation with application to evaporation from a water table. *Soil science*, 85(4):228–232, 1958.

[110] S. Garrault, E. Finot, E. Lesniewska, and A. Nonat. Study of csh growth on c 3 s surface during its early hydration. *Materials and structures*, 38(4):435–442, 2005.

[111] L. Gelb, K. Gubbins, R. Radhakrishnan, and M. Sliwinska-Bartkowiak. Phase separation in confined systems. *Reports on Progress in Physics*, 62:1573, 1999.

[112] S. Ghabezloo. Association of macroscopic laboratory testing and micromechanics modelling for the evaluation of the poroelastic parameters of a hardened cement paste. *Cement and Concrete research*, 40(8):1197–1210, 2010.

[113] A. Giraud, Q. V. Huynh, D. Hoxha, and D. Kondo. Application of results on eshelby tensor to the determination of effective poroelastic properties of anisotropic rocks-like composites. *International journal of solids and structures*, 44(11):3756–3772, 2007.

[114] A. Giraud, Q. V. Huynh, D. Hoxha, and D. Kondo. Effective poroelastic properties of transversely isotropic rock-like composites with arbitrarily oriented ellipsoidal inclusions. *Mechanics of Materials*, 39(11):1006–1024, 2007.

[115] C. T. Gomez, J. Dvorkin, and T. Vanorio. Laboratory measurements of porosity, permeability, resistivity, and velocity on fontainebleau sandstones. *Geophysics*, 75(6):E191–E204, 2010.

[116] J. Gonçalvès, P. Rousseau-Gueutin, G. de Marsily, P. Cosenza, and S. Violette. What is the significance of pore pressure in a saturated shale layer? *Water Resources Research*, 46(4):W04514, 2010.

[117] J. Gonçalvès and J. Trémosa. Estimating thermo-osmotic coefficients in clay-rocks: I. theoretical insights. *Journal of colloid and interface science*, 342(1):166–174, 2010.

[118] P. Grathwohl. Diffusion in natural porous media: contaminant transport, sorption/desorption and dissolution kinetics (pod). 1998.

[119] A. T. d. C. Guimarães, M. A. Climent, G. d. Vera, F. J. Vicente, F. T. Rodrigues, and C. Andrade. Determination of chloride diffusivity through partially saturated portland cement concrete by a simplified procedure. *Construction and Building Materials*, 25(2):785–790, 2011.

[120] W. Haines. Studies in the physical properties of soils: Ii. a note on the cohesion developed by capillary forces in an ideal soil. *The Journal of Agricultural Science*, 15(04):529–535, 1925.

[121] M. Han, S. Youssef, E. Rosenberg, M. Fleury, and P. Levitz. Deviation from archies law in partially saturated porous media: wetting film versus disconnectedness of the conducting phase. *Physical Review E*, 79(3):031127, 2009.

[122] Z. Hashin. The elastic moduli of heterogeneous materials, 1960.

[123] A. Helba, M. Sahimi, L. Scriven, and H. Davis. Percolation theory of two-phase relative permeability. *SPE reservoir engineering*, 7(1):123–132, 1992.

[124] R. Horn, D. Smith, and W. Haller. Surface forces and viscosity of water measured between silica sheets. *Chemical Physics Letters*, 162(4):404–408, 1989.

[125] C.-H. Hsieh. *Vapor pressure lowering in porous media*. PhD thesis, Stanford University, 1980.

[126] Q. Hu, T. J. Kneafsey, J. J. Roberts, L. Tomutsa, and J. S. Wang. Characterizing unsaturated diffusion in porous tuff gravel. *Vadose Zone Journal*, 3(4):1425–1438, 2004.

[127] Q. Hu and J. Wang. Aqueous-phase diffusion in unsaturated geologic media: a review. 2003.

[128] R. Hunter. Foundations of colloid science (pod). 2000.

[129] S. Irmay. On the hydraulic conductivity of unsaturated soils. *Transactions, American Geophysical Union*, 35:463–467, 1954.

[130] T. Ishizaki, M. Maruyama, Y. Furukawa, and J. Dash. Premelting of ice in porous silica glass. *Journal of crystal growth*, 163(4):455–460, 1996.

[131] J. Israelachvili. Measurement of the viscosity of liquids in very thin films. *Journal of colloid and interface science*, 110(1):263–271, 1986.

[132] J. Israelachvili. Intermolecular and surface forces: With applications to colloidal and biological systems (colloid science), 1992.

[133] J. Israelachvili. *Intermolecular and surface forces*. Academic press, 1998.

[134] J. Israelachvili and R. Pashley. The hydrophobic interaction is long range, decaying exponentially with distance. 1982.

[135] J. Israelachvili and R. Pashley. Molecular layering of water at surfaces and origin of repulsive hydration forces. 1983.

[136] H. Jennings. A model for the microstructure of calcium silicate hydrate in cement paste. *Cement and Concrete Research*, 30(1):101–116, 2000.

[137] H. Jennings. Refinements to colloid model of csh in cement: Cm-ii. *Cement and Concrete Research*, 38(3):275–289, 2008.

[138] M. Juenger, V. Lamour, P. Monteiro, E. Gartner, and G. Denbeaux. Direct observation of cement hydration by soft x-ray transmission microscopy. *Journal of materials science letters*, 22(19):1335–1337, 2003.

[139] W. A. Jury, W. R. Gardner, W. H. Gardner, et al. *Soil physics.* John Wiley and Sons, Inc., 1991.

[140] K. Kaneko. Determination of pore size and pore size distribution: 1. adsorbents and catalysts. *Journal of membrane science*, 96(1):59–89, 1994.

[141] W. Kemper. Water and ion movement in thin films as influenced by the electrostatic charge and diffuse layer of cations associated with clay mineral surfaces. *Soil Science Society of America Journal*, 24(1):10–16, 1960.

[142] D. Kissel. *Adsorption and viscosity measurement of interfacial and nanoconfined water using surface and shear acoustic wave techniques*. 2008.

[143] J. Klein, U. Raviv, S. Perkin, N. Kampf, L. Chai, and S. Giasson. Fluidity of water and of hydrated ions confined between solid surfaces to molecularly thin films. *Journal of Physics: Condensed Matter*, 16(45):S5437, 2004.

[144] A. Klute and J. Letey. The dependence of ionic diffusion on the moisture content of nonadsorbing porous media. *Soil Science Society of America Journal*, 22(3):213–215, 1958.

[145] M. A. Knackstedt, A. P. Sheppard, and W. Pinczewski. Simulation of mercury porosimetry on correlated grids: Evidence for extended correlated heterogeneity at the pore scale in rocks. *Physical review E*, 58(6):R6923–R6926, 1998.

[146] F. O. Koenig. On the thermodynamic relation between surface tension and curvature. *The Journal of Chemical Physics*, 18:449, 1950.

[147] A. Kornyshev and S. Leikin. Fluctuation theory of hydration forces: The dramatic effects of inhomogeneous boundary conditions. *Physical Review A*, 40(11):6431, 1989.

[148] T. Kozaki, K. Inada, S. Sato, and H. Ohashi. Diffusion mechanism of chloride ions in sodium montmorillonite. *Journal of contaminant hydrology*, 47(2):159–170, 2001.

[149] S. Krishnapillai and N. Ravichandran. A statistical model for the relative hydraulic conductivity of water phase in unsaturated soils. *Open Journal of Urology*, 2.

[150] K. Kröhn. New conceptual models for the resaturation of bentonite. *Applied clay science*, 23(1):25–33, 2003.

[151] R. Kunze, G. Uehara, and K. Graham. Factors important in the calculation of hydraulic conductivity. *Soil Science Society of America Journal*, 32(6):760–765, 1968.

[152] M. Lebeau, J. Konrad, L. Alfonso, A. Lobbrecht, R. Price, M. Troldborg, W. Nowak, N. Tuxen, P. Bjerg, R. Helmig, et al. A new capillary and thin film flow model for predicting the hydraulic conductivity of unsaturated porous media. *Water Resour. Res*, 46(W12554):W12554, 2010.

[153] E. Lemarchand. *Contribution de la Micromécanique à l'étude des phénomènes de transport et de couplage poromécanique dans les milieux poreux: Application aux phénomènes de gonflement des géomatériaux*. PhD thesis, Ecole des Ponts ParisTech, 2001.

[154] E. Lemarchand, C. A. Davy, L. Dormieux, W. Chen, and F. Skoczylas. Micromechanics contribution to coupled transport and mechanical properties of fractured geomaterials. *Transport in porous media*, 79(3):335–358, 2009.

[155] Y. Leng and P. Cummings. Fluidity of hydration layers nanoconfined between mica surfaces. *Physical review letters*, 94(2):26101, 2005.

[156] R. Lenormand, C. Zarcone, and A. Sarr. Mechanisms of the displacement of one fluid by another in a network of capillary ducts. *J. Fluid Mech*, 135(34):337–353, 1983.

[157] E. C. Leong and H. Rahardjo. Permeability functions for unsaturated soils. *Journal of Geotechnical and Geoenvironmental Engineering*, 123(12):1118–1126, 1997.

[158] D. R. Lide. Crc handbook of physics and chemistry, 2001.

[159] P. Lim, S. Barbour, and D. Fredlund. The influence of degree of saturation on the coefficient of aqueous diffusion. *Canadian geotechnical journal*, 35(5):811–827, 1998.

[160] W. Lindquist and A. Venkatarangan. Investigating 3d geometry of porous media from high resolution images. *Physics and Chemistry of the Earth, Part A: Solid Earth and Geodesy*, 24(7):593–599, 1999.

[161] W. B. Lindquist, A. Venkatarangan, J. Dunsmuir, and T.-f. Wong. Pore and throat size distributions measured from synchrotron x-ray tomographic images of fontainebleau sandstones. *Journal of Geophysical Research: Solid Earth (1978–2012)*, 105(B9):21509–21527, 2000.

[162] L. Liu, M. Krack, and A. Michaelides. Density oscillations in a nanoscale water film on salt: Insight from ab initio molecular dynamics. *Journal of the American Chemical Society*, 130(27):8572–8573, 2008.

[163] P. Low. Viscosity of interlayer water in montmorillonite. *Soil Science Society of America Journal*, 40(4):500–505, 1976.

[164] A. Majumdar and I. Mezic. Instability of ultra-thin water films and the mechanism of droplet formation on hydrophilic surfaces. *Journal of heat transfer*, 121(4):964–971, 1999.

[165] S. Marčelja and N. Radić. Repulsion of interfaces due to boundary water. *Chemical Physics Letters*, 42(1):129–130, 1976.

[166] R. Martin. *Adsorbed water on clay: a review*. Massachusetts Institute of Technology, 1960.

[167] G. Mavko, T. Mukerji, and J. Dvorkin. The rock physics handbook, edn, 2009.

[168] G. Mavko and A. Nur. The effect of a percolation threshold in the kozeny-carman relation. *Geophysics*, 62(5), 1997.

[169] M. McBride. A critique of diffuse double layer models applied to colloid and surface chemistry. *Clays and Clay minerals*, 45(4):598–608, 1997.

[170] P. McGuiggan and R. Pashley. Molecular layering in thin aqueous films. *The Journal of Physical Chemistry*, 92(5):1235–1239, 1988.

[171] B. K. MEHTA, S. Shiozawa, and M. Nakano. Measurement of molecular diffusion of salt in unsaturated soils. *Soil science*, 159(2):115, 1995.

[172] J. Mitchell and K. Soga. Fundamentals of soil behavior. *J. Wiley.(or previous editions by Mitchell, JK without the*, 2005.

[173] V. Mitlin and M. Sharma. A local gradient theory for structural forces in thin fluid films. *Journal of colloid and interface science*, 157:447–447, 1993.

[174] K. Morishige and K. Kawano. Freezing and melting of water in a single cylindrical pore: The pore-size dependence of freezing and melting behavior. *The Journal of chemical physics*, 110:4867, 1999.

[175] Y. Mualem. Hysteretical models for prediction of the hydraulic conductivity of unsaturated porous media. *Water resources research*, 12(6):1248–1254, 1976.

[176] Y. Mualem, A. Klute, et al. Hydraulic conductivity of unsaturated soils: prediction and formulas. *Methods of soil analysis. Part 1. Physical and mineralogical methods*, pages 799–823, 1986.

[177] S. Nakashima. Diffusivity of ions in pore water as a quantitative basis for rock deformation rate estimates. *Tectonophysics*, 245(3):185–203, 1995.

[178] G. Narsilio, O. Buzzi, S. Fityus, T. Yun, and D. Smith. Upscaling of navier–stokes equations in porous media: Theoretical, numerical and experimental approach. *Computers and Geotechnics*, 36(7):1200–1206, 2009.

[179] C. Nguyen and D. Do. A new method for the characterization of porous materials. *Langmuir*, 15(10):3608–3615, 1999.

[180] T. Olesen, P. Moldrup, and J. Gamst. Solute diffusion and adsorption in six soils along a soil texture gradient. *Soil Science Society of America Journal*, 63(3):519–524, 1999.

[181] D. Or, M. Tuller, et al. Flow in unsaturated fractured porous media: Hydraulic conductivity of rough surfaces. *Water Resources Research*, 36(5):1165–1177, 2000.

[182] D. Or and J. Wraith. Temperature effects on soil bulk dielectric permittivity measured by time domain reflectometry: A physical model. *Water Resources Research*, 35(2):371–383, 1999.

[183] P. Oren. Pore-scale network modelling of waterflood residual oil recovery by immiscible gas flooding. In *SPE/DOE Improved Oil Recovery Symposium*, 1994.

[184] P. Øren and S. Bakke. Process based reconstruction of sandstones and prediction of transport properties. *Transport in Porous Media*, 46(2):311–343, 2002.

[185] P. Oren, J. Billiotte, and W. Pinczewski. Mobilization of waterflood residual oil by gas injection for water-wet conditions. *SPE Formation Evaluation*, 7(1):70–78, 1992.

[186] P. Øren and W. Pinczewski. The effect of film flow on the mobilization of waterflood residual oil by gas flooding. In *European IOR Symposium, Stavanger*, pages 21–23, 1991.

[187] P. E. Oren and W. V. Pinczewski. The effect of wettability and spreading coefficients on the recovery of waterflood residual oil by miscible gasflooding. *SPE Formation Evaluation*, 9(2):149–156, 1994.

[188] A. P. Oron and B. Berkowitz. Flow in rock fractures: The local cubic law assumption reexamined. *Water Resources Research*, 34(11):2811–2825, 1998.

[189] R. Papendick and G. Camprell. Theory and measurement of water potential. *Water potential relations in soil microbiology*, (waterpotentialr):1–22, 1981.

[190] R. Pashley. Hydration forces between mica surfaces in electrolyte solutions. *Advances in Colloid and Interface Science*, 16(1):57–62, 1982.

[191] L. Paterson, S. Painter, M. A. Knackstedt, and W. Val Pinczewski. Patterns of fluid flow in naturally heterogeneous rocks. *Physica A: Statistical Mechanics and its Applications*, 233(3):619–628, 1996.

[192] L. Paterson, S. Painter, X. Zhang, and V. Pinczewski. Simulating residual saturation and relative permeability in heterogeneous formations. In *SPE Annual Technical Conference and Exhibition*, 1996.

[193] V. Penttala. Freezing-induced strains and pressures in wet porous materials and especially in concrete mortars. *Advanced cement based materials*, 7(1):8–19, 1998.

[194] V. Penttala and F. Al-Neshawy. Stress and strain state of concrete during freezing and thawing cycles. *Cement and Concrete Research*, 32(9):1407–1420, 2002.

[195] G. Pereira, W. Pinczewski, D. Chan, L. Paterson, and P. Øren. Pore-scale network model for drainage-dominated three-phase flow in porous media. *Transport in Porous media*, 24(2):167–201, 1996.

[196] S. Perkin, L. Chai, N. Kampf, U. Raviv, W. Briscoe, I. Dunlop, S. Titmuss, M. Seo, E. Kumacheva, and J. Klein. Forces between mica surfaces, prepared in different ways, across aqueous and nonaqueous liquids confined to molecularly thin films. *Langmuir*, 22(14):6142–6152, 2006.

[197] G. Peschel and K. Adlfinger. Viscosity anomalies in liquid surface zones: Iv. the apparent viscosity of water in thin layers adjacent to hydroxylated fused silica surfaces. *Journal of Colloid and Interface Science*, 34(4):505–510, 1970.

[198] A. Peters and W. Durner. A simple model for describing hydraulic conductivity in unsaturated porous media accounting for film and capillary flow. *Water Resources Research*, 44(11):W11417, 2008.

[199] F. Pettijohn, P. Potter, and R. Siever. *Sand and sandstone*. Springer, 1987.

[200] L. Porter, W. Kemper, R. Jackson, and B. Stewart. Chloride diffusion in soils as influenced by moisture content. *Soil Science Society of America Journal*, 24(6):460–463, 1960.

[201] T. Powers and R. Helmuth. Theory of volume changes in hardened portland-cement paste during freezing. In *Highway Research Board Proceedings*, 1953.

[202] T. Powers and T. Willis. The air requirement of frost resistant concrete. In *Highway Research Board Proceedings*, 1949.

[203] D. Rasmussen and A. MacKenzie. Clustering in supercooled water. *The Journal of Chemical Physics*, 59:5003, 1973.

[204] U. Raviv, S. Giasson, J. Frey, and J. Klein. Viscosity of ultra-thin water films confined between hydrophobic or hydrophilic surfaces. *Journal of Physics: Condensed Matter*, 14(40):9275, 2002.

[205] U. Raviv, P. Laurat, and J. Klein. Fluidity of water confined to subnanometre films. *Nature*, 413(6851):51–54, 2001.

[206] J. Reinson, D. Fredlund, and G. Wilson. Unsaturated flow in coarse porous media. *Canadian geotechnical journal*, 42(1):252–262, 2005.

[207] E. M. Renkin. Filtration, diffusion, and molecular sieving through porous cellulose membranes. *The Journal of general physiology*, 38(2):225–243, 1954.

[208] L. A. Richards. Capillary conduction of liquids through porous mediums. *Physics*, 1(5):318–333, 1931.

[209] I. Richardson. The nature of csh in hardened cements. *Cement and Concrete Research*, 29(8):1131–1147, 1999.

[210] I. Richardson. The nature of the hydration products in hardened cement pastes. *Cement and Concrete Composites*, 22(2):97–113, 2000.

[211] M. Romkens and R. Bruce. Nitrate diffusivity in relation to moisture content of non-adsorbing porous media. *Soil Science*, 98(5):332–337, 1964.

[212] R. M. Roque-Malherbe. *Adsorption and diffusion in nanoporous materials*. CRC PressI Llc, 2007.

[213] W. Rose. Volumes and surface areas of pendular rings. *Journal of Applied Physics*, 29(4):687–691, 1958.

[214] D. Rowell, M. Martin, and P. Nye. The measurement and mechanism of ion diffusion in soils iii. the effect of moisture content and soil-solution concentration on the self-diffusion of ions in soils. *Journal of Soil Science*, 18(2):204–221, 1967.

[215] A. Sadeghi, D. Kissel, and M. Cabrera. Estimating molecular diffusion coefficients of urea in unsaturated soil. *Soil Science Society of America Journal*, 53(1):15–18, 1989.

[216] E. Samson and J. Marchand. Modeling the transport of ions in unsaturated cement-based materials. *Computers & Structures*, 85(23):1740–1756, 2007.

[217] J. Sanahuja, L. Dormieux, and G. Chanvillard. Modelling elasticity of a hydrating cement paste. *Cement and Concrete Research*, 37(10):1427–1439, 2007.

[218] K. Saxton, W. Rawls, J. Romberger, and R. Papendick. Estimating generalized soil-water characteristics from texture. *Soil Science Society of America Journal*, 50(4):1031–1036, 1986.

[219] A. Scheidegger. *The physics of flow through porous media*. University of Toronto Press, 1974.

[220] G. Scherer. Crystallization in pores. *Cement and Concrete research*, 29(8):1347–1358, 1999.

[221] E. Schulson, I. Swainson, T. Holden, and C. Korhonen. Hexagonal ice in hardened cement. *Cement and concrete research*, 30(2):191–196, 2000.

[222] M. Setzer. Mechanical stability criterion, triple-phase condition, and pressure differences of matter condensed in a porous matrix. *Journal of colloid and interface science*, 235(1):170–182, 2001.

[223] M. Setzer. Micro-ice-lens formation in porous solid. *Journal of colloid and interface science*, 243(1):193–201, 2001.

[224] M. Setzer. Development of the micro-ice-lens model. In *International RILEM Workshop on Frost Resistance of Concrete*, pages 133–145. RILEM Publications SARL, 2002.

[225] S. Shang, R. Horne, and H. Ramey Jr. Experimental study of water vapor adsorption on geothermal reservoir rocks, 1994.

[226] W. Smith and J. Hashemi. Foundations of materials science and engineering. 2006.

[227] R. M. Sok, M. A. Knackstedt, A. P. Sheppard, W. Pinczewski, W. Lindquist, A. Venkatarangan, and L. Paterson. Direct and stochastic generation of network models from tomographic images; effect of topology on residual saturations. *Transport in porous media*, 46(2-3):345–371, 2002.

[228] D. Steytler and J. Dore. Neutron diffraction studies of water in porous silica. *Molecular Physics*, 56(5):1001–1015, 1985.

[229] A. Sumner, E. Menke, Y. Dubowski, J. Newberg, R. Penner, J. Hemminger, L. Wingen, T. Brauers, and B. Finlayson-Pitts. The nature of water on surfaces of laboratory systems and implications for heterogeneous chemistry in the troposphere. *Physical Chemistry Chemical Physics*, 6(3):604–613, 2004.

[230] Z. Sun. *Mechanism of frost damage to concrete*. PhD thesis, Princeton University, 2010.

[231] Z. Sun and G. W. Scherer. Effect of air voids on salt scaling and internal freezing. *Cement and Concrete Research*, 40(2):260–270, 2010.

[232] Z. Sun and G. W. Scherer. Pore size and shape in mortar by thermoporometry. *Cement and Concrete Research*, 40(5):740–751, 2010.

[233] T. Takamuku, M. Yamagami, H. Wakita, Y. Masuda, and T. Yamaguchi. Thermal property, structure, and dynamics of supercooled water in porous silica by calorimetry, neutron scattering, and nmr relaxation. *The Journal of Physical Chemistry B*, 101(29):5730–5739, 1997.

[234] J. Taplin. A method for following the hydration reaction in portland cement paste. *Australian Journal of Applied Science*, 10(3):329–345, 1959.

[235] A. Tchistiakov. Physico-chemical aspects of clay migration and injectivity decrease of geothermal clastic reservoirs. In *Proceedings World Geothermal Congress, Kyushu-Tohoku, Japan, May*. Citeseer, 2000.

[236] K. Terzaghi. The shearing resistance of saturated soils and the angle between the planes of shear. In *Proceedings of the 1st International Conference on Soil Mechanics and Foundation Engineering*, volume 1, pages 54–56, 1936.

[237] M. Thommes, G. Lu, and X. Zhao. Physical adsorption characterization of ordered and amorphous mesoporous materials. *Nanoporous materials: science and engineering*, page 317, 2004.

[238] T. Tokunaga. Hydraulic properties of adsorbed water films in unsaturated porous media. *Water Resources Research*, 45(6):W06415, 2009.

[239] T. Tokunaga. Physicochemical controls on adsorbed water film thickness in unsaturated geological media. *Water Resources Research*, 47(8):W08514, 2011.

[240] T. Tokunaga, K. Olson, and J. Wan. Moisture characteristics of hanford gravels bulk, grain-surface, and intragranular components. *Vadose Zone Journal*, 2(3):322–329, 2003.

[241] T. Tokunaga and J. Wan. Water film flow along fracture surfaces of porous rock. *Water Resources Research*, 33(6):1287–1295, 1997.

[242] T. Tokunaga, J. Wan, and S. Sutton. Transient film flow on rough fracture surfaces. *Water Resources Research*, 36(7):1737–1746, 2000.

[243] M. Tuller and D. Or. Hydraulic conductivity of variably saturated porous media: Film and corner flow in angular pore space. *Water resources research*, 37(5):1257–1276, 2001.

[244] M. Tuller and D. Or. Unsaturated hydraulic conductivity of structured porous media a review of liquid configuration–based models. *Vadose Zone Journal*, 1(1):14–37, 2002.

[245] F.-J. Ulm, G. Constantinides, and F. Heukamp. Is concrete a poromechanics materials?a multiscale investigation of poroelastic properties. *Materials and structures*, 37(1):43–58, 2004.

[246] J. J. Valenza, II. *Mechanism for salt scaling*. PhD thesis, Princeton University, 2005.

[247] M. T. Van Genuchten. A closed-form equation for predicting the hydraulic conductivity of unsaturated soils. *Soil Science Society of America Journal*, 44(5):892–898, 1980.

[248] J. Van Schaik, W. Kemper, and S. Olsen. Contribution of adsorbed cations to diffusion in clay-water systems. *Soil Science Society of America Journal*, 30(1):17–22, 1966.

[249] E. Verwey and J. T. G. Overbeek. Theory of the stability of lyophobic colloids. 1948. *Amserdam: Elsevier*.

[250] G. Wardeh, M. A. Mohamed, and E. Ghorbel. Analysis of concrete internal deterioration due to frost action. *Journal of Building Physics*, 35(1):54–82, 2011.

[251] G. Wardeh and B. Perrin. Freezing–thawing phenomena in fired clay materials and consequences on their durability. *Construction and building materials*, 22(5):820–828, 2008.

[252] G. Wardeh and B. Perrin. Numerical modelling of the behaviour of consolidated porous media exposed to frost action. *Construction and Building Materials*, 22(4):600–608, 2008.

[253] D. Warncke and S. Barber. Diffusion of zinc in soil: Ii. the influence of soil bulk density and its interaction with soil moisture. *Soil Science Society of America Journal*, 36(1):42–46, 1972.

[254] L. G. Wilson. *Monitoring in the vadose zone: a review of technical elements and methods*, volume 1. Environmental Monitoring Systems Laboratory, Office of Research and Development, US Environmental Protection Agency, 1980.

[255] G. Wind. A field experiment concerning capillary rise of moisture in a heavy clay soil. *Netherlands Journal of Agricultural Science*, 3:60–69, 1955.

[256] M. Wyllie and A. Gregory. Fluid flow through unconsolidated porous aggregates. *Industrial & Engineering Chemistry*, 47(7):1379–1388, 1955.

[257] S. Xu, G. Scherer, T. Mahadevan, and S. Garofalini. Thermal expansion of confined water. *Langmuir*, 25(9):5076–5083, 2009.

[258] N. Yesiller, J. L. Hanson, and D. K. Cohen. Characterization of surface topography of sand. 2005.

[259] R. Yong and B. Warkentin. *Soil properties and behaviour*, volume 5. 1975.

[260] C. Yu, A. Richter, A. Datta, M. Durbin, and P. Dutta. Observation of molecular layering in thin liquid films using x-ray reflectivity. *Physical review letters*, 82(11):2326–2329, 1999.

[261] S. Yuster. Theoretical considerations of multiphase flow in idealized capillary systems. In *Proc., 3rd World Petroleum Congress*, volume 2, pages 437–445, 1951.

[262] Q. Zeng. Poromechanical behavior of cement-based materials subjected to freeze-thaw actions with salts: modeling and experiments. 2011.

[263] Q. Zeng, T. Fen-Chong, P. Dangla, and K. Li. A study of freezing behavior of cementitious materials by poromechanical approach. *International Journal of Solids and Structures*, 48(22):3267–3273, 2011.

[264] Z.-Y. Zhou and H. Mihashi. Micromechanics model to describe strain behavior of concrete in freezing process. *Journal of Materials in Civil Engineering*, 20(1):46–53, 2008.

[265] B. Zuber. *Vers une modélisation du comportement des matériaux cimentaires exposés au gel*. 2006.

[266] B. Zuber and J. Marchand. Modeling the deterioration of hydrated cement systems exposed to frost action: Part 1: Description of the mathematical model. *Cement and Concrete Research*, 30(12):1929–1939, 2000.

[267] B. Zuber and J. Marchand. Predicting the volume instability of hydrated cement systems upon freezing using poro-mechanics and local phase equilibria. *Materials and structures*, 37(4):257–270, 2004.

Appendix A

Physical properties of water film

A.1 Viscosity of the water film

A quantitative knowledge about the viscosity of water film is vital to transport (such as hydraulic conductivity and diffusion) in unsaturated porous media. Nevertheless, though there are numerous publications about the viscosity of confined water film [5, 12, 43, 76, 77, 124, 131, 141, 143, 155, 163, 197, 204, 205], the knowledge about the viscosity of water film (or confined water layer) is still controversy and in debated.

First, it should be noted that, most of the experiments and modellings of viscosity of interlayer are carried out on the confined water layer between two similarly charged parallel solid surface (e.g. silica, mica) [76, 77, 141, 205]. However, water film which is an asymmetrical system, has two distinct interfaces: solid-water film and gas-water film interfaces. Generally, the surface charge of two interfaces are negative, therefore, we can infer that, due to the similar charge interfaces and confined state, water film can be treated as interlayer. Therefore, the viscosity of the interlayer confined between two negatively charged surface can be reasonably assumed to be similar to that of the water film.

The viscosity of water is temperature-dependent, for the purpose of discussing the modification of viscosity induced by surface forces, all temperatures of the water film are considered to be room temperature. In the follows, the viscosity of the water film measured by indirect and direct experiment will be presented and discussed.

A.1.1 Indirect measurement of viscosity

The principle of the indirect measurement is based on the classic Poiseuille flow equation. In the early 1970's, Derjaguin et al. [76, 77] carried out the flow experiment through the altra-thin quartz capillaries (0.03 to 10 μm), the applied external pressures and velocities of flow were measured simultaneously, by means of the Poiseuille equation, the viscosity of the confined capillary water is found to be elevated to as much as 40%(with respect to that of bulk water) at the capillaries of 0.04 μm in radius.

With the water flow experiment as well as theory of absolute reaction rates for the viscosity, Low et al. [163] estimated the viscosity of Na-montmorillonite at various water content, it was found that the viscosity of the confined water film is greater than that of bulk water and increases exponentially with decreasing water content. Based on this

conclusion, Or et al. [182] established an empirical relationship to estimate the viscosity of the confined water film in terms of the distance from the solid surface:

$$\eta(y,T) = \eta_0 \exp(\frac{a^*}{yT}) \tag{A.1}$$

where η_0 is the viscosity of the bulk water, y is the normal distance from solid surface (in nm), a^* is a constant whose value is 162.1 nm.K as proposed by Or et al. [182], T is the temperature (in K).

From the aforementioned indirect experiments for the viscosity of confined water film, we can conclude that, confined in the hydrophilic surfaces, with the decrease of its thickness, the water film shows an elevated viscosity (with respect to that of bulk water).

A.1.2 Direct measurement of viscosity

The principle of the direct measurement of viscosity of confined water film (considered as Newtonian flow) is in accordance with its mechanical definition [108]:

$$F = \eta(h)\frac{\partial v_x}{\partial y}A \tag{A.2}$$

where y axis is the axis normal to the water film (along the thickness of water film), F is the shear force along x direction, x orthogonal to the y axis, v_x is the velocity of water film flow, A is the the surface area applied on the water film.

For the direct measurement of the viscosity of the water film under confinement, there are following two totally different arguments based on distinct experimental devices.

By means of the high-resolution atomic force microscope (AFM), Li et al. [108] estimated the viscosities of the confined purified water films between the hydrophilic surfaces (mica and glass). In these experiments, the normal and lateral forces encountered by a nanosize Si tip when approaching a solid surface in purified water are measured directly and simultaneously, the viscosities of sub-nanometre confined water films show orders of magnitude increase with bulk viscosity of water (e.g. 4 orders of magnitude higher than that of bulk water when the thickness of the water film is about 0.5 nm). This result was confirmed by viscosity measurement of the confined sub-nanometre pure water film with the other sophisticated apparatus-transverse dynamic force microscope (TDFM), more commonly known as shear force microscope [5].

Nevertheless, these results could not be reproduced in the subnanometer confined water films between hydrophilic surfaces with surface force apparatus (SFA) [124, 131, 143, 204, 205]. These experiments were performed by two crossed hydrophilic cylinders by means of measuring the normal and lateral forces directly and simultaneously. From the measured results, it is found that, the viscosity of the pure water film confined in mica [131, 204] or silica [124], even when confined to 1.0 ± 0.3 nm thick, is close to (within a ratio of 3) or the same as viscosity of the bulk water. The similar conclusions were derived when the confined water films are in low and high concentration electrolyte solution [143, 205].

For the above two distinct conclusions about the viscosities of the confined water films, owing to their similar experimental principle as Eq.(A.2), the disparity may lie in the different experimental devices. In fact, Perkin and Klein [196] attributed the abnormal higher viscosity of confined water film to the contaminated surface of the hydrophilic mica

surface during the sample processing, which is not convinced because not only mica solid surfaces but also silica surfaces [124] are employed in the experiments.

On the other way, Kissel [142] attributed the anomalous higher viscosity to the using of nanosize Si tapered tip probe (which is actually the difference between SFA and AFM - TDFM device). To prove his proposal, Kissel carried out measurement of the viscosity of water film with shear acoustic wave technique in which there is no probe. It was found that, the viscosity of confined water film between hydrophilic surfaces is close to viscosity of bulk water.

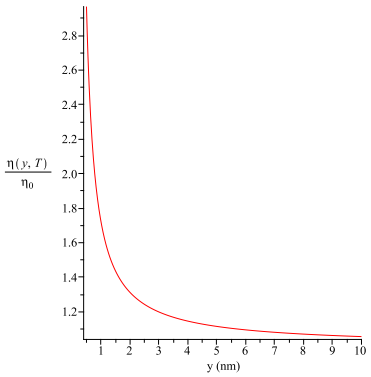

Figure A.1: The variation of viscosity within confined water film, calculated with Eq.(A.1) at temperature T= 298 K.

A.2 Structure and Density of water film on hydrophilic surface

As early as 1960s, using pycnometer as well as X-ray diffraction techniques, Martin et al. [166] investigated the structure and density of adsorbed water film on the sodium montmorillonite as a function of water content. It was found that, at lower water content, when the thickness of water film adsorbed on the sodium montmorillonite particle is less than three molecular layers (about 1 nm), the structure of which is significantly modified as well as the density of which is greater than that of normal water, while beyond 1nm from the solid surface, the structure and the density of water film is slightly different from those of bulk water. Since then, various of studies including experiments [78, 260] and molecular dynamics simulation (MD) [30, 162, 257], have been performed to verify the variation of density of water film near the hydrophilic solid surface. By MD simulations [162] of water film on the NaCl crystal system, it has been found that, due to the normal arrangement of the water dipoles to the hydrophilic solid surface, the structure of the water film differs from that of bulk water. Furthermore, the density of water film exhibits pronounced oscillations in the normal direction of surface at several water film layers. The maximum density in the first layer of water film (in vicinity of solid surface) is at 1.4 g/cm^3, about 40% higher than that of bulk liquid water. Likewise, the density maximum in the second layer is about 25% greater than bulk water. The oscillations become less pronounced when the thickness of the water film is greater than about 1nm (three or four layers of water molecules), and

the bulk liquid water density of 1 g/cm^3 is thus recovered [162]. The MD simulation of the water film-crystalline silica system carried out by Xu et al. & Scherer [257] has the similar results.

In summary, by the aformentioned experimental and simulation results: we can conclude that the structure of water film shows layer structure and discrete in nature in the first several layers of water molecules ($<$ 1 nm). The water dipoles arrange normally to the hydrophilic solid surface, which is distinct from structure of the bulk water [162]. Due to this structural modification, the density of water film in first several layers shows oscillations [162]. More over, the water films has a higher density than that of bulk water [162]. However, when the thickness of the water film is greater than 1 nm, the structure of such water films shows less modified, the oscillations and the variation of the density show slightly and can be neglected [257].

A.3 Thermodynamic definition of disjoining pressure

Due to the overlapping of the boundary layers, an additional work originates from the repulsive or attractive surface force have to be applied. In essence, the disjoining pressure $\Pi(h)$ is a local physical term. Within the thermodynamic framework, it can be defined as the variation of the Gibbs free energy ∂G associated with the change of thickness of water film ∂h. Where the chemical potential μ_i of the i-th dissolved substance, temperature T and pressure P remaining constant [3, 44, 50, 74]:

$$\Pi(h) = -(\frac{\partial G}{\partial h})_{T,P,\mu_i} \tag{A.3}$$

Using the Eq.(A.3), Erikson et al. [89] derived the following classic Gibbs-Duhem equation for the water film:

$$2d\gamma + S^f dT + \Pi(h)dh + 2\sum_i \Gamma_i^f d\mu_i = 0 \tag{A.4}$$

where γ is the surface tension of the water film-gas interface; S^f is the excess entropy of water film surface; Γ_i^f is the surface excess potential for i-th dissolve substance. At constant chemical potential of each component and temperature, Eq.(A.4) could be reduced to as [3]:

$$\Pi(h) = -2(\frac{d\gamma}{dh})_{T,\mu_i} \tag{A.5}$$

Obviously, Eq.(A.5) relates the disjoining pressure of the water film with the variation of surface tension within the confined domain of characteristic size h.

A.4 Parameters for the disjoining pressure within the unfrozen water film

It has been found by Churaev et al. [45] that, the structural component of the disjoining pressure obeyed the exponent form such as Eq.(3.21).

To determine the disjoining pressure in unfrozen water film, Chureav et al. [50] performed an experiment to determine the fitting parameters for the disjoining pressure, which are shown in the following table:

Table A.1: Calculated parameters of disjoining pressure at different temperature ranges, after Churaev et al. [46].

Temperature t, ℃	K,×10MPa	λ, nm
Nonfreezing Interlayer between ice and the capillary wall with r=1.14 μ m		
-0.14	1.0	12
-0.33 to -0.42	1.4	7
-0.55 to -0.64	2.0	4.7
-0.82 to -1	2.7	3.7
Nonfreezing interlayer between ice and surface of silica particles with r=56 nm		
-0.27	1.1	7.3
-0.67	1.4	3.4

As stated by Churaev et al.[46], the parameters K and λ are temperature-dependent. From the Table(A.1), it can be found that, the value K increases and the value λ decreases with decreasing temperature [46]. It was also found by Churaev et al. [46] that the parameters K and λ are the same order for hydrophilic surface of mica, quartz, silica and glass at room temperature.

To describe all of the experimental results in all temperature ranges (for example: -0.14 to -1℃), a two exponential-term formula such as Eq.(3.22) is employed. As proposed by Churaev et al.[50], the disjoing pressure in the nonfreezing interlayer between ice and capillary wall at the temperature: -0.14 to -1 ℃can be fitted by the equation (22) as well as the paramters can be determined as: $K_1 = 22.6 \pm 8.2$ MPa, $\lambda_1 = 3.1$ nm, $K_2 = 4.9 \pm 1.4$ MPa, $\lambda_2 = 5.3$ nm [50].

Appendix B

Determining average concentration tensors of each phase

B.1 Eshelby's problem in Linear Diffusion within unsaturated porous media

This section proposes a micromechanics analysis of solute diffusion process occurring in unsaturated porous media. "Unsaturated" has to be understood in the sense that diffusion occurs in a liquid phase that does not fully occupy the available (connected) pore space of porous media. Two practical situation are concerned with this theoretical approach: 1- freezing processes where the pore space is made up of a liquid water phase, a solid water phase (ice crystals) and gaseous phase; and 2- usual desaturation process with gas and liquid saturating the pore space.

Diffusion process is assumed to be well described by Ficks law at the microscopic scale. Similar to that introduced in Section(4.3), the diffusion in unsaturated porous media (as shown in the morphological schematic as Fig.(4.17)) is governed by the formulas such as [82]:

$$\begin{cases} \mathrm{div}_z \underline{j}^\gamma = 0 & \forall \underline{z} \in \Omega \\ \underline{j}^\gamma(\underline{z}) = -D(\underline{z}) \underline{\mathrm{grad}}_z \rho^\gamma & \forall \underline{z} \in \Omega \\ \rho^\gamma(\underline{z}) = \underline{H} \cdot \underline{z} & \text{when} \quad |z| \to \infty \end{cases} \tag{B.1}$$

$$D(\underline{z}) = \begin{cases} 0 & \forall \underline{z} \in \Omega^s \\ 0 & \forall \underline{z} \in \Omega^g \\ D^\gamma & \forall \underline{z} \in \Omega^{pw} \\ D^\gamma & \forall \underline{z} \in \Omega^{ig} \\ D^\gamma & \forall \underline{z} \in \Omega^{wl} \\ D_f^\gamma & \forall \underline{z} \in \Omega^f \end{cases} \tag{B.2}$$

where Ω^s ,Ω^g, Ω^{pw}, Ω^{ig}, Ω^{wl} and Ω^f are the solid, the gas, the pore body water, the intergranular layer, the wetting layer and the water film domains within REV.

The average diffusive flux in a REV consists of four contributions: the pore body water,

the intergranular layer, the wetting layer and the water film, it gives:

$$\underline{J}^{\gamma} = \langle \underline{j}^{\gamma} \rangle_{\Omega} = -\sum_{i} \varphi_i D_i^{\gamma} \langle \underline{\mathrm{grad}} \rho^{\gamma} \rangle_{\Omega_i} \quad i \in \{l, f, wl\} \tag{B.3}$$

where we introduced the volume average definitions for average concentration coefficients of each phase:

$$\overline{A}_i = \frac{1}{|\Omega_i|} \int_{\Omega_i} \underline{\mathrm{grad}} \rho^{\gamma} \mathrm{dV} \quad i \in \{g, s, pw, ig, f, wl\} \tag{B.4}$$

B.2 Solutions of auxiliary Eshelby-type problems: diffusion case

Let us introduce the fictitious uniform concentration gradient $\underline{H}_0$. Estimates for the homogenized diffusion coefficient is sought in the framework of the self-consistent scheme by considering three different morphologies: solid phase-water film-wetting layer spherical composite inclusion, pore body water inclusion and gaseous phase inclusion. They are assumed to sufficiently account for local phases distribution. Here, the auxiliary Eshelby-type problems can be classified into following four subproblems.

Subproblem 1 is dedicated to the introduction of specific morphology: the intergranular layer, the wetting layer and the water film surrounding on an impermeable solid inclusion. Subproblem 2 is a particular case of subproblem 1: the intergranular and the wetting layer are disregarded, water film is surrounded the impermeable solid inclusion. Subproblem 3 and 4 allow us to account for a fully diffusive pore body water phase and a non-diffusive gaseous phase. All these problems are derived within the assumption of local and global isotropy together with the morphological assumption that the pore space is made up of pores in spherical shape.

B.2.1 Subproblem 1: the intergranular layer, the wetting layer and the water film surrounded the impermeable solid inclusion

Let us first consider the auxiliary problems of a composite spherical inclusion embedded in a reference medium behaving as the sought macroscopic one (shown as C_0 in Fig.(B.1)). Whatever the practical problem of interest, as shown in Fig.(B.1), the impermeable core is characterized by a diffusion coefficient equal to 0 (solid or gaseous phase, shown as C_4). The three shells are the intergranular layer C_1 (solute diffusion coefficient is D^{γ}), the wetting layer C_2 (solute diffusion coefficient is D^{γ}) and the water film phase C_3 (solute diffusion coefficient is D_f^{γ}).

As shown in Fig.(B.1), in the framework of spherical coordinates, whose origin is taken in the centre of the spherical core. The solute concentration fields exhibit cylindrical symmetry with respect to $\mathbf{e}_3$. Thus, the concentration field is therefore sought in the form ($\cos\theta = \underline{e}_r \cdot \underline{e}_3$):

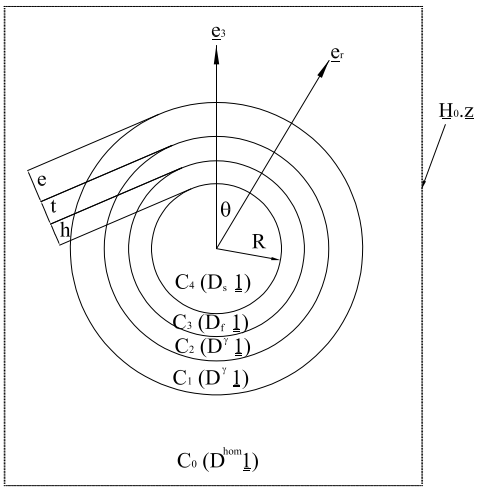

Figure B.1: Schematic illustration of the spherical composite inclusion with three shells; C_i denotes $i-th$ domain, the quantity in the bracket is solute diffusion coefficient within i-th domain, $i \in \{\ 0,\ 1,\ 2,\ 3{,}4\ \}$; in this case $D_s \to 0$, $\underline{H}_0$ is the fictitious uniform concentration gradient; e, t and h are the thicknesses of the intergranular layer, the wetting layer and the water film, respectively.

$$\begin{cases} r \le R: \ \rho^{\gamma}(r) = B_1 r\cos\theta & (a) \\ R \le r \le R+h: \ \rho^{\gamma}(r) = (F_2 + \dfrac{B_2}{r^2})\cos\theta & (b) \\ R+h \le r \le R+t: \ \rho^{\gamma}(r) = (F_3 + \dfrac{B_3}{r^2})\cos\theta & (c) \\ R+t \le r \le R+e: \ \rho^{\gamma}(r) = (F_4 + \dfrac{B_4}{r^2})\cos\theta & (d) \\ R+e \le r: \ \rho^{\gamma}(r) = (F_5 + \dfrac{B_5}{r^2})\cos\theta & (e) \end{cases} \tag{B.5}$$

where $\underline{H}_0 = H_0\mathbf{e}_3$, e, t and h are the thicknesses of the intergranular layer, the wetting layer and the water film, respectively, R is the radius of the solid core. Accordingly, the solute concentration gradient field in the 3 dimensional problem can be presented as:

$$\begin{cases} r \le R: \ \underline{\mathrm{grad}}\rho^{\gamma}(r) = B_1\underline{e}_3 & (a) \\ R \le r \le R+h: \ \underline{\mathrm{grad}}\rho^{\gamma}(r) = (F_2 - \dfrac{2B_2}{r^3})\cos\theta\underline{e}_r - (F_2 + \dfrac{B_2}{r^3})\sin\theta\underline{e}_\theta & (b) \\ R+h \le r \le R+t: \ \underline{\mathrm{grad}}\rho^{\gamma}(r) = (F_3 - \dfrac{2B_3}{r^3})\cos\theta\underline{e}_r - (F_3 + \dfrac{B_3}{r^3})\sin\theta\underline{e}_\theta & (c) \\ R+t \le r \le R+e: \ \underline{\mathrm{grad}}\rho^{\gamma}(r) = (F_4 - \dfrac{2B_4}{r^3})\cos\theta\underline{e}_r - (F_4 + \dfrac{B_4}{r^3})\sin\theta\underline{e}_\theta & (d) \\ R+e \le r: \ \underline{\mathrm{grad}}\rho^{\gamma}(r) = (F_5 - \dfrac{2B_5}{r^3})\cos\theta\underline{e}_r - (F_5 + \dfrac{B_5}{r^3})\sin\theta\underline{e}_\theta & (e) \end{cases} \tag{B.6}$$

To determine the 9 unknown constants F_i and B_i ($i \in \{1,2,3,4,5\}$), several boundary conditions should be considered. Adsorption phenomena (adsorption for solid cores) or mass exchange are prevented at the interfaces (at $r = R$, $r = R + h$, $r = R + t + h$ and $r = R + h + t + e$). In all, the solute concentration is assumed to be continuous and diffusive flux is assumed to be in balance at these interfaces, the boundary condition can be expressed as:

$$\begin{cases} \lim\limits_{r \to R_i^+} \rho^\gamma = \lim\limits_{r \to R_i^-} \rho^\gamma & (a) \\ (\underline{j}^\gamma \cdot \underline{e}_r)_{r=R_i} = 0 \qquad i \in \{1,2,3,4\} & (b) \end{cases} \tag{B.7}$$

where $R_1 = R$, $R_2 = R + h$, $R_3 = R + h + t$ and $R_4 = R + h + t + e$.

From Eq.(B.7), it can be found that there are 8 identical relations. Another identical relation can be derived at infinite boundary, that is:

$$\lim_{r \to \infty} \rho^\gamma = \underline{H}_0 \cdot \underline{z} \Longrightarrow F_5 = H_0 \tag{B.8}$$

Thus, the 9 unknown constants F_i and B_i ($i \in \{1,2,3,4,5\}$) can be determined from 9 identical relations. The following approximations can be made:

$$\frac{\varphi_f}{\varphi_s} = \frac{R_2^3 - R_1^3}{R_1^3} \qquad \frac{\varphi_{wl}}{\varphi_s + \varphi_f} = \frac{R_3^3 - R_2^3}{R_2^3} \qquad \frac{\varphi_f + \varphi_{wl} + \varphi_{ig}}{\varphi_s} = \frac{R_4^3 - R_1^3}{R_1^3} \tag{B.9}$$

where φ_s, φ_f, φ_{wl} and φ_{ig} are the volume fractions of solid phase, water film and wetting layers, respectively.

Consequently, combining Eq.(B.4) and Eq.(B.6) and Eq.(B.9), the average concentration tensors of each phase $\overline{A}_i$ ($i \in \{g, s, pw, ig, f, wl\}$) can be estimated.

B.2.2 Subproblem 2: water film surrounded on the impermeable inclusion

The schematic representation of the water film surrounded on the impermeable spherical inclusion is illustrated in Fig.(B.2).

Similarly, the average concentration coefficients $\overline{A}_i$ ($i \in \{s, f\}$) can be derived as those shown in Subsection(B.2.1). Here, we omit the deduction. The average concentration tensors for solid phase and water film are listed as:

$$\overline{A}_s = \frac{9}{2} \frac{D^{hom}(\varphi_s + \varphi_f)}{3D^{hom}\varphi_s + 2D^{hom}\varphi_f + D_f^\gamma \varphi_f} H_0 \tag{B.10}$$

$$\overline{A}_f = \frac{2}{3} \overline{A}_s \tag{B.11}$$

B.2.3 Subproblem 3: pore water spherical inclusion

The schematic morphological representation of pore water can be depicted in Fig.(B.3). For saturated pores, we consider the problem as a spherical inhomogeneity embedded in an infinite reference medium having the diffusion properties of the sought homogenized medium

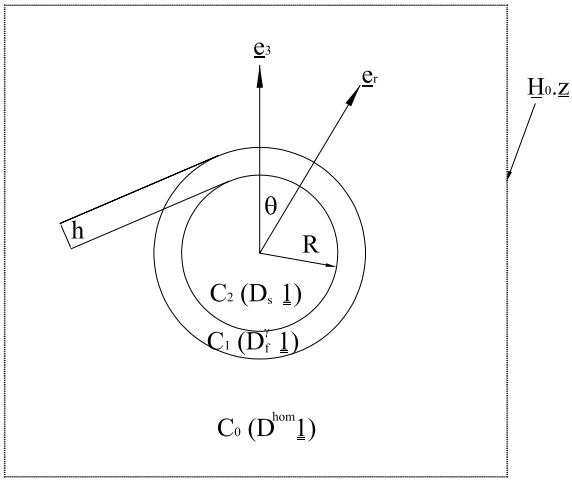

Figure B.2: Schematic illustration of the spherical composite inclusion with one shell, C_i denotes i-th domain, the quantity in the bracket is solute diffusion coefficient within i-th domain, $i \in \{0, 1, 2\}$, in this case $D_s \to 0$.

(as shown in Fig.(B.3)). The solute diffusion coefficient in saturated pores is denoted by D^γ.

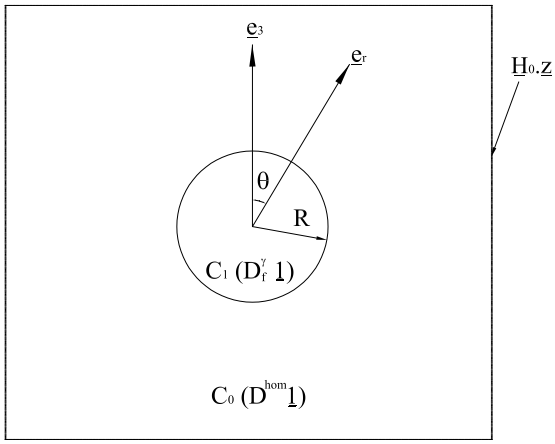

Figure B.3: Schematic illustration of the pore water spherical inclusion.

For the same uniform boundary conditions as in the previous subproblems, the average concentration tensor of pore water spherical inclusion can be obtained as the limit of the Eq.(B.11) when $\varphi_f \to 1$ as well as diffusion coefficient $D_f^\gamma = D^\gamma$, that is:

$$\overline{A}_l = \frac{3D^{hom}}{2D^{hom} + D^\gamma} H_0 \tag{B.12}$$

B.2.4 Subproblem 4: Gas spherical inclusion

The same reasoning may be used for the non-diffusive (gas or solid, depending upon the practical problem) phase with diffusion coefficient $D_f^\gamma \to 0$ and $\varphi_f \to 0$. Hence, according to the limit of Eq.(B.11), the concentration gradient of the solid phase (gas phase) is estimated by:

$$\overline{A}_g = \frac{3}{2} H_0 \tag{B.13}$$

The final step makes the link between the auxiliary problem with the fictitious uniform boundary conditions in $\underline{H}_0$ and the real uniform boundary conditions in $\underline{H}$. This is realized owing to the average rule $\underline{H} = \langle \underline{\text{grad}} \rho^\gamma \rangle$ on the concentration gradient.

B.3 Solutions of auxiliary Eshelby-type problems: flow permeability case

Different from diffusion case, the permeability coefficient of fluid phase is size dependent, that is to say, the permeability of fluid flow is related to its magnitude of size. As presented previously, the morphological illustration of unsaturated sandstone can be shown as Fig. (6.2).

To estimate the homogenized pressure gradient $\boldsymbol{\nabla} P$, three auxiliary Eshelby problems should be determined, the boundary conditions in such auxiliary problems denote as $P \longrightarrow \boldsymbol{\nabla} P_0 \cdot \mathbf{z}$, when $\mathbf{z} \to \infty$. Here, $\boldsymbol{\nabla} P_0$ is the fictitious average pressure gradient which will be related to the true pressure gradient $\boldsymbol{\nabla} P$ with Eq.(6.10).

Similarly, all these problems are derived within the assumption of local and global isotropy together with the morphological assumption that the pore space is made up of pores in spherical shape.

Fig.(B.4) depicts the spherical composite inclusion with three shells (water film, wetting layer and intergranular pore water) in flow permeability problem. It should bear in mind that, the fluid flows in three shells are considered as poiseuille flows. Therefore, the intrinsic permeability coefficients of each layer can be expressed as: $K_{ig} = e^2/3$, $K_{wl} = t^2/3$, $K_f = h^2/3$.

In such case, the pressure field and pressure gradient field can be expressed as :

$$\begin{cases} r \le R: \ P = B_1 r \cos\theta & (a) \\ R \le r \le R+h: \ P = (F_2 + \dfrac{B_2}{r^2}) \cos\theta & (b) \\ R+h \le r \le R+t: \ P = (F_3 + \dfrac{B_3}{r^2}) \cos\theta & (c) \\ R+t \le r \le R+e: \ P = (F_4 + \dfrac{B_4}{r^2}) \cos\theta & (d) \\ R+e \le r: \ P = (F_5 + \dfrac{B_5}{r^2}) \cos\theta & (e) \end{cases} \tag{B.14}$$

where $\boldsymbol{\nabla} P_0 = \nabla P_0 \mathbf{e}_3$ and $\mathbf{e}_3$ is corresponding to the axis colinear to $\theta = 0$ as well as $\cos\theta = \mathbf{e}_3 \cdot \mathbf{e}_\theta$, the pressure and velocity fields exhibit a cylindrical symmetry with respect

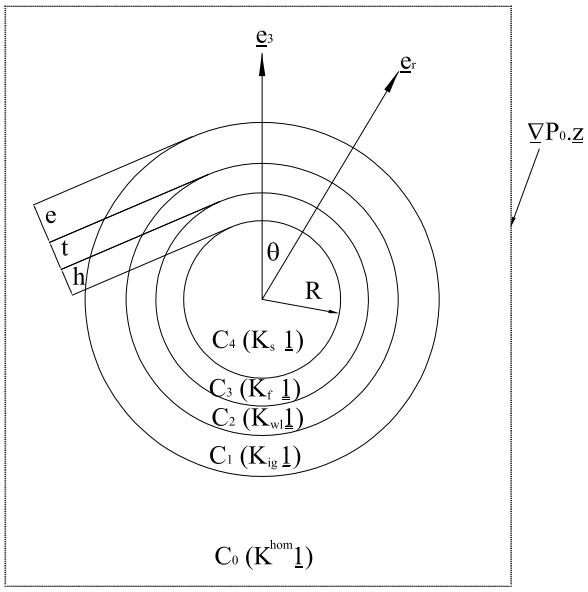

Figure B.4: Schematic illustration of the spherical composite inclusion with two shells in flow permeability problem; C_i denotes $i-th$ domain, the quantity in the bracket is permeability coefficient of i-th domain, $i \in \{\ 0,\ 1,\ 2,\ 3,\ 4\ \}$; in this case $K_s \to 0$; ∇P_0 is the fictitious uniform pressure gradient.

to $\mathbf{e}_3$; R denotes the radius of pore filled with gas. Accordingly, the pressure gradient field in the 3 dimensional problem can be presented as [79]:

$$\begin{cases} r \le R: & \underline{\text{grad}}P = B_1\underline{e}_3 & (a) \\ R \le r \le R+h: & \underline{\text{grad}}P = (F_2 - \dfrac{2B_2}{r^3})\cos\theta\underline{e}_r - (F_2 + \dfrac{B_2}{r^3})\sin\theta\underline{e}_\theta & (b) \\ R+h \le r \le R+t: & \underline{\text{grad}}P = (F_3 - \dfrac{2B_3}{r^3})\cos\theta\underline{e}_r - (F_3 + \dfrac{B_3}{r^3})\sin\theta\underline{e}_\theta & (c) \\ R+t \le r \le R+e: & \underline{\text{grad}}P = (F_4 - \dfrac{2B_4}{r^3})\cos\theta\underline{e}_r - (F_4 + \dfrac{B_4}{r^3})\sin\theta\underline{e}_\theta & (d) \\ R+e \le r: & \underline{\text{grad}}P = (F_5 - \dfrac{2B_5}{r^3})\cos\theta\underline{e}_r - (F_5 + \dfrac{B_5}{r^3})\sin\theta\underline{e}_\theta & (e) \end{cases} \tag{B.15}$$

The boundary condition at infinite gives:

$$\lim_{r\to\infty} P = \boldsymbol{\nabla} P_0 \cdot \mathbf{z} \qquad \Rightarrow \qquad \nabla P_0 = F_5 \tag{B.16}$$

With the pressure continuity and flow flux continuity, the other boundary condition can be expressed as:

$$\begin{cases} \lim\limits_{r\to R_i^+} P = \lim\limits_{r\to R_i^-} P & (a) \\ (\underline{v}_i \cdot \underline{e}_r)_{r=R_i} = 0 \qquad i \in \{1,2,3,4\} & (b) \end{cases} \tag{B.17}$$

where $R_1 = R$, $R_2 = R + h$, $R_3 = R + h + t$, $R_4 = R + h + t + e$, h , t and e are the thickness of water film, wetting layer and intergranular water layer, R is radius of solid grain (inclusion). From Eq.(B.16) and Eq.(B.17), we have 9 identical equations to solve 9 unknown constants: F_i and B_i ($i \in \{1,2,3,4\}$).

Therefore, the average concentration tensors of each phase within unsaturated porous media can be derived as Eq.(B.4):

$$\overline{A}_i(R) = \frac{1}{|\Omega_i|}\int_{\Omega_i} \underline{\mathrm{grad}} P \mathrm{dV} \quad i \in \{g, s, ig, f, wl\} \tag{B.18}$$

Combing Eq.(B.18) and Eq.(B.15), when the radius of the monodisperse solid grain is taken as R, we have the average concentration tensor for each phase $\overline{A}_i(R)$ ($i \in \{s, f, wl, ig\}$).

It can be found that the average concentration of the spherical composite are dependent significantly on the size of the wetting layer and water film. Therefore, considering the grain size distribution function f(R)($\int_{R_{min}}^{R_{max}} f(R)$ d R=1), it yield:

$$\varphi_s \overline{A}_s = (1-\phi)\int_{R_{min}}^{R_{max}} \overline{A}_s(R) f(R) \mathrm{d}R \tag{B.19}$$

$$\varphi_f \overline{A}_f = (1-\phi)\int_{R_{min}}^{R_{max}} \overline{A}_f(R) \frac{(R+h)^3 - R^3}{R^3} f(R) \mathrm{d}R \tag{B.20}$$

$$\varphi_{wl} \overline{A}_{wl} = (1-\phi)\int_{R_{min}}^{R_{max}} \overline{A}_{wl}(R) \frac{(R+h+t)^3 - (R+h)^3}{R^3} f(R) \mathrm{d}r \tag{B.21}$$

$$\varphi_{ig} \overline{A}_{ig} = (1-\phi)\int_{R_{min}}^{R_{max}} \overline{A}_{ig}(R) \frac{(R+h+t+e)^3 - (R+h+t)^3}{R^3} f(R) \mathrm{d}r \tag{B.22}$$

where R_{max} and R_{min} are the maximum and minimum radius of solid grains, ϕ is the porosity.

Correspondingly, the flow flux contributions of water film and wetting layer can be estimated by:

$$\underline{\overline{\mathrm{v}}}_f = K_f \varphi_f \overline{A}_f(R) = (1-\phi)\int_{R_{min}}^{R_{max}} \frac{h^2}{3\mu_f} \overline{A}_f(R) \frac{(R+h)^3 - R^3}{R^3} f(R) \mathrm{d}R \tag{B.23}$$

$$\underline{\overline{\mathrm{v}}}_{wl} = K_{wl} \varphi_{wl} \overline{A}_{wl}(R) = (1-\phi)\int_{R_{min}}^{R_{max}} \frac{t^2}{3\mu_0} \overline{A}_{wl}(R) \frac{(R+h+t)^3 - (R+t)^3}{R^3} f(R) \mathrm{d}R \tag{B.24}$$

$$\underline{\overline{\mathrm{v}}}_{ig} = K_{ig} \varphi_{ig} \overline{A}_{ig}(R) = (1-\phi)\int_{R_{min}}^{R_{max}} \frac{e^2}{3\mu_0} \overline{A}_{ig}(R) \frac{(R+h+t+e)^3 - (R+t+h)^3}{R^3} f(R) \mathrm{d}R \tag{B.25}$$

B.4 Solutions of auxiliary Eshelby-type problems: multi scale

Generally, most of the porous media exhibit multi scale microstructures: at local scale matrix is composed of spherical composite inclusion phase, small pore liquid and gas phase, the homogenized properties of matrix can be estimated with self-consistent scheme; at macro scale, the macro pores either filled with water or gaseous phase are embedded in the matrix, the homogenized properties can be estimated with Mori-Tanaka scheme.

B.4.1 Micro scale-with self-consistent scheme

The concentration tensors of each phase are estimated with self-consistent scheme in previous subsections. Using Eq.(4.14) and Eq.(6.25), the homogenized properties of matrix (D_m^γ) can be determined.

B.4.2 Macro scale-with Mori-Tanaka scheme

In the previous sections, the average concentration tensors are estimated based on the self-consistent scheme which is perfectly used to characterized the disordered morphology. The Mori-Tanaka scheme estimate in transport problem is based on the generalized Eshelby problem in which solid grains are surrounded by the matrix phase (e.x., liquid phase). Therefore, the average concentration tensors of each phase in Mori-Tanaka scheme can be derived from their corresponding ones in self consistent scheme by replacing D^{hom} with D_m^γ, it gives:

$$\overline{A}_m = H_1 \tag{B.26}$$

The average concentration tensors of pore water ($\overline{A}_{ml}$) and gas ($\overline{A}_{mg}$) in macro pores can be written as:

$$\overline{A}_{ml} = \frac{3D^{hom}}{2D^{hom} + D_m^\gamma} H_1 \tag{B.27}$$

$$\overline{A}_{mg} = \frac{3}{2} H_1 \tag{B.28}$$

where D_m^γ is the homogenized diffusion coefficient of matrix, H_1 is the fictitious uniform concentration (pressure) gradient applied on the boundary of REV.

Appendix C

Eshelby-type problems in poroelastic porous media under freezing

An extension of Eshelby's problem to microporoelasticity accounting for both heterogeneity of elastic properties and in-pore pressure (prestress) is given in Dormieux's work [82]. Here, the following derivation of Eshelby-based problem for the freezing porous media is based on his work.

C.1 Eshelby's problem coupled with prestress and inhomogeneity under freezing

When the pore inclusion (denoted as superscript I) is embedded in an infinite linear elastic solid medium applied on an uniform macroscopic strain $\boldsymbol{E}$ on the boundary, the physical formulas governing the stress field within this infinite solid can be expressed as [82]:

$$\begin{cases} \mathrm{div}\boldsymbol{\sigma} = 0 \\ \boldsymbol{\sigma} = \mathbb{C}^s : \boldsymbol{\varepsilon} - \boldsymbol{\kappa}^s \delta T + (\delta\mathbb{C} + \pi^I)\chi_I(\underline{z}) \\ \underline{\xi} = \boldsymbol{E}.\underline{z} \quad \text{when} \quad \underline{z} \to \infty \end{cases} \tag{C.1}$$

where $\delta\mathbb{C} = \mathbb{C}^I - \mathbb{C}^s = -\mathbb{C}^s$, $\boldsymbol{\kappa}^s$ is the volumetric dilation coefficient tensor of solid matrix, χ_I is the characteristic function of the domain of inclusion I. Processing as [82], the condition $\boldsymbol{\sigma}^I = \delta\mathbb{C} + \pi^I$ is taken to be constant, thus, both $\boldsymbol{\varepsilon}^I$ and prestress π^I are required to be uniform throughout I. Therefore, the following relations between $\boldsymbol{E}$, π^I and $\boldsymbol{\varepsilon}^I$ can be derived [82]:

$$\begin{cases} \boldsymbol{\sigma}^I = \delta\mathbb{C} + \pi^I \\ \boldsymbol{\varepsilon}^I = -\mathbb{P} : \boldsymbol{\sigma}^I + \boldsymbol{E} \end{cases} \tag{C.2}$$

Eliminating $\boldsymbol{\sigma}^I$ in Eq.(C.2) yields the expression for $\boldsymbol{\varepsilon}^I$ [82]:

$$\boldsymbol{\varepsilon}^I = (\mathbb{I} + \mathbb{P} : \delta\mathbb{C})^{-1} : (\boldsymbol{E} - \mathbb{P} : \pi^I) \tag{C.3}$$

with P tensor $\mathbb{P}$ [82]:

$$\mathbb{P} = \mathbb{S} : \mathbb{S}^s \tag{C.4}$$

where $\mathbb{S}^s$ is the compliance tensor of solid materix; $\mathbb{S}$ is the Eshelby tensor. In the case of spherical inhomogeneity embedded in an isotropic medium, the Eshelby tensor can be simplified as [82]:

$$\mathbb{S} = \alpha\mathbb{J} + \beta\mathbb{K} \tag{C.5}$$

with:

$$\alpha = \frac{3K^s}{3K^s + 4\mu^s}; \qquad \beta = \frac{6(K^s + 2\mu^s)}{5(3K^s + 4\mu^s)} \tag{C.6}$$

in which K^s and μ^s are the bulk modulus and shear modulus of the solid matrix.

C.2 Solution of Eshelby's problem with Mori-Tanaka scheme

To obtain the homogenized poroelastic properties of freezing porous media, a Mori-Tanaka scheme using the Eshelby's results will be introduced in this section [82]. The derivation of the poroelastic tensors lies in determining the average strain concentration tensor of pore space $\overline{\mathbb{A}}^p$. The pores within the freezing porous media are assumed to be spherical. The idea of Mori-Tanaka scheme is that, to capture the interaction between the pores, a fictitious macroscopic strains $\boldsymbol{E}_0$ is assumed to exert on the boundary at infinity. Here, $\boldsymbol{E}_0$ is set equal to the strain of the inhomogeneity continuum surrounding the inclusion (more precisely, $\boldsymbol{E}_0$ is equal to the average strain of matrix). More over, $\boldsymbol{E}_0$ should satisfied the micro-macro strain compatibility condition, $\overline{\boldsymbol{\varepsilon}} = \boldsymbol{E}$ [82].

Therefore, the uniform strain in the inclusion I is adopted as an estimated for the average strains $\overline{\boldsymbol{\varepsilon}}^p$ in the pore space of REV, and $\boldsymbol{E}_0$ is set equal to the average strain of matrix. In drained condition, it gives [82]:

$$\begin{cases} \overline{\boldsymbol{\varepsilon}}^p = \boldsymbol{\varepsilon}^I = (\mathbb{I} - \mathbb{S})^{-1} : \boldsymbol{E}_0 \\ \overline{\boldsymbol{\varepsilon}}^s = \boldsymbol{E}_0 \end{cases} \tag{C.7}$$

From Eq.(C.7) and micro-macro strain compatibility condition ($\overline{\boldsymbol{\varepsilon}} = \boldsymbol{E}$), it yields [82]:

$$\boldsymbol{E}_0 = ((1 - \phi_0)\mathbb{I} + \phi_0(\mathbb{I} - \mathbb{S})^{-1})^{-1} : \boldsymbol{E} \tag{C.8}$$

where ϕ_0 is the pore volume fraction (porosity).

From the relation: $\overline{\boldsymbol{\varepsilon}}^p = \overline{\mathbb{A}}^p : \boldsymbol{E}$, as well as combining Eq.(C.7) and Eq.(C.8), we have an expression for average strain concentration tensor of pore space [82]:

$$\overline{\mathbb{A}}^p = (\mathbb{I} - \mathbb{S})^{-1} : ((1 - \phi_0)\mathbb{I} + \phi_0(\mathbb{I} - \mathbb{S})^{-1})^{-1} \tag{C.9}$$

Therefore, from Eq.(8.34), the poroelastic tensors of freezing porous media can be expressed as [82]:

$$\mathbb{C}^{hom} = \mathbb{C}^s : (\mathbb{I} - \phi_0 \overline{\mathbb{A}}^p) = \mathbb{C}^s : [\mathbb{I} - \phi_0 (\mathbb{I} - \mathbb{S})^{-1} : ((1 - \phi_0)\mathbb{I} + \phi_0 (\mathbb{I} - \mathbb{S})^{-1})^{-1}] \tag{C.10}$$

$$\boldsymbol{\kappa}^{hom} = \boldsymbol{\kappa}^{hom} : (\mathbb{I} - \phi_0 \overline{\mathbb{A}}^p) = \boldsymbol{\kappa}^s : \mathbb{S}^s : \mathbb{C}^{hom} = \boldsymbol{\alpha}^s : \mathbb{C}^{hom} \tag{C.11}$$

$$\boldsymbol{B} = \phi_0 \mathbf{1} : \overline{\mathbb{A}}^p = \phi_0 \mathbf{1} : (\mathbb{I} - \mathbb{S})^{-1} : ((1 - \phi_0)\mathbb{I} + \phi_0 (\mathbb{I} - \mathbb{S})^{-1})^{-1} = \phi_0 \mathbf{1} : (\mathbb{I} - (1 - \phi_0)\mathbb{S})^{-1} \tag{C.12}$$

Appendix D

Levin's theorem in unsaturated microporoelastic freezing porous media

Levin's theorem requires us to extend the definition of the microscopic stress $\boldsymbol{\sigma}$, strain $\boldsymbol{\varepsilon}$ and displacement $\underline{\xi}$, respectively, from the solid domain Ω^s into the pore space Ω^f [82]. In addition to the linear elastic stress in the solid phase, microscopic stress within the pore space is considered to be uniform and and equal to $-P\mathbf{1}$, where P is the internal pressure within the pore space [82]. Treated as Levin theorem, the local stress field of the unsaturated freezing porous media can be expressed as the general affine form:

$$\boldsymbol{\sigma}(\underline{z}) = \begin{cases} \mathbb{C}^s \\ 0 \end{cases} : \boldsymbol{\varepsilon} + \begin{cases} \boldsymbol{\sigma}_0(\underline{z}) \\ -(p_0^{eq})\mathbf{1} \end{cases} + \begin{cases} -\boldsymbol{\kappa}^s \delta T \\ 0 \end{cases} + \begin{cases} 0 & \forall \underline{z} \in \Omega^s \\ p^{eq}\mathbf{1} & \forall \underline{z} \in \Omega^p \end{cases} \tag{D.1}$$

Obviously , there are four loading parameters in the freezing problems, they are: unifrom macroscopic strain tensor $\boldsymbol{E}$ applied on the boundary, initial prestress $\boldsymbol{\sigma}_0$, thermal stress tensor $\boldsymbol{\kappa}\delta T$ and prestress tensor $-p^{eq}\mathbf{1}$ (including the surface tension effect, internal pressure and disjoining pressure). The microscopic stress, strain and displacement which characterize the response of the REV to the four loading parameters, the macroscopic strain tensor $\boldsymbol{E}$, initial stress $\boldsymbol{\sigma}_0$, thermal stress tensor $\boldsymbol{\kappa}\delta T$ and the microscopic equivalent prestress filed $-p^{eq}\mathbf{1}$, satisfy [82]:

$$\begin{cases} \mathrm{div}\boldsymbol{\sigma} = 0 & \underline{z} \in \Omega \\ \boldsymbol{\sigma} = \mathbb{C} : \boldsymbol{\varepsilon} - p^{eq}\mathbf{1} - \boldsymbol{\kappa}\delta T & \underline{z} \in \Omega \\ \underline{\xi} = \boldsymbol{E} \cdot \underline{z} & \underline{z} \in \partial\Omega \end{cases} \tag{D.2}$$

Given the linearity of the problem with respect to $\boldsymbol{E}$ and p^{eq}, $\boldsymbol{\sigma}_0$ and $\boldsymbol{\kappa}\delta T$, it is convenient to decompose the problem into four loading cases:

Loading case 1: $\boldsymbol{E} \neq 0$, $\boldsymbol{\sigma}_0 = 0$, $\delta T = 0$, $p^{eq} = 0$. The physical quantities obey the following formulas:

$$\begin{cases} \mathrm{div}\boldsymbol{\sigma}^{'} = 0 & \underline{z} \in \Omega \\ \boldsymbol{\sigma}^{'} = \mathbb{C} : \boldsymbol{\varepsilon}^{'} & \underline{z} \in \Omega \\ \underline{\xi}^{'} = \boldsymbol{E} \cdot \underline{z} & \underline{z} \in \partial\Omega \end{cases} \tag{D.3}$$

The microscopic strain field of loading case 1 problem is:

$$\boldsymbol{\varepsilon}^{'}(\underline{z}) = \mathbb{A}(\underline{z}) : \boldsymbol{E} \tag{D.4}$$

The macroscopic stress $\boldsymbol{\Sigma}^{'}$ is:

$$\boldsymbol{\Sigma}^{'} = \overline{\boldsymbol{\sigma}^{'}} = \mathbb{C}^{hom} : \boldsymbol{E} \tag{D.5}$$

where, $\mathbb{C}^{hom}$ is the homogenized elasticity tensor of drained porous media.

Loading case 2: $\boldsymbol{\sigma}_0 \neq 0$, $\boldsymbol{E} = 0$, $\delta T = 0$, $p^{eq} = 0$. The physical quantities obey the following formulas:

$$\begin{cases} \mathrm{div}\boldsymbol{\sigma}^{''} = 0 & \underline{z} \in \Omega \\ \boldsymbol{\sigma}^{''} = \mathbb{C}(\underline{z}) : \boldsymbol{\varepsilon}^{''} + \boldsymbol{\sigma}_0 & \underline{z} \in \Omega \\ \underline{\xi}^{''} = \underline{0} & \underline{z} \in \partial\Omega \end{cases} \tag{D.6}$$

The solution to Eq.(D.6) is $\underline{\xi}^{''} = 0$ and $\boldsymbol{\sigma}^{''} = \boldsymbol{\sigma}_0$. Therefore, we have:

$$\boldsymbol{\Sigma}^{''} = \overline{\boldsymbol{\sigma}^{''} : \mathbb{A}} = \overline{\boldsymbol{\sigma}_0 : \mathbb{A}} = \boldsymbol{\Sigma}_0 \tag{D.7}$$

Loading case 3: $\delta T \neq 0$, $\boldsymbol{\sigma}_0 = 0$, $\boldsymbol{E} = 0$, $p^{eq} = 0$. The physical quantities obey the following formulas:

$$\begin{cases} \mathrm{div}\boldsymbol{\sigma}^{'''} = 0 & \underline{z} \in \Omega \\ \boldsymbol{\sigma}^{'''} = \mathbb{C} : \boldsymbol{\varepsilon}^{'''} - \boldsymbol{\kappa}\delta T & \underline{z} \in \Omega \\ \underline{\xi}^{'''} = \underline{0} & \underline{z} \in \partial\Omega \end{cases} \tag{D.8}$$

The macroscopic stress $\boldsymbol{\Sigma}^{'''}$ is:

$$\boldsymbol{\Sigma}^{'''} = \overline{\boldsymbol{\sigma}^{'''}} = \overline{\mathbb{C} : \boldsymbol{\varepsilon}^{'''} - \boldsymbol{\kappa}\delta T} = -\overline{\boldsymbol{\kappa} : \mathbb{A}}\delta T = -\boldsymbol{\kappa}^{hom}\delta T \tag{D.9}$$

Loading case 4: $p^{eq} \neq 0$, $\boldsymbol{\sigma}_0 = 0$, $\boldsymbol{E} = 0$, $\delta T = 0$. The physical quantities obey the following formulas:

$$\begin{cases} \mathrm{div}\boldsymbol{\sigma}^{''''} = 0 & \underline{z} \in \Omega \\ \boldsymbol{\sigma}^{''''} = \mathbb{C} : \boldsymbol{\varepsilon}^{''''} - p^{eq}\mathbf{1} & \underline{z} \in \Omega \\ \underline{\xi}^{''''} = \underline{0} & \underline{z} \in \partial\Omega \end{cases} \tag{D.10}$$

The macroscopic stress $\boldsymbol{\Sigma}^{'''}$ may be derived by:

$$\boldsymbol{\Sigma}^{''''} = \overline{p^{eq}\mathbf{1} : \mathbb{A}} = -\overline{p^{eq}}\phi_0\mathbf{1} : \overline{\mathbb{A}}^{p} = -P^{eq}\boldsymbol{B} \tag{D.11}$$

The macroscopic stress of the freezing porous media can be expressed as:

$$\boldsymbol{\Sigma} = \boldsymbol{\sigma}^{'} + \boldsymbol{\sigma}^{''} + \boldsymbol{\sigma}^{'''} + \boldsymbol{\sigma}^{''''} = \mathbb{C}^{hom} : \boldsymbol{E} + \boldsymbol{\Sigma}_0 - \boldsymbol{\kappa}^{hom}\delta T - \delta P^{eq}\boldsymbol{B} \tag{D.12}$$